

PART I: THE ORIGIN OF TSUNAMIS  
EXCITED BY LOCAL  
EARTHQUAKES

PART II: BROADBAND WAVEFORM  
OBSERVATION OF LOCAL  
EARTHQUAKES

Thesis by

Kuo-Fong Ma

In Partial Fulfillment of the Requirements  
for the Degree of  
Doctor of Philosophy

California Institute of Technology

Pasadena, California

1993

(Submitted Jan. 18, 1993)

Contents

© 1993  
Kuo-Fong Ma  
ALL RIGHTS RESERVED

## Acknowledgments

My initial interest in seismology was inspired by Prof. Jeen-Hwa Wang at the Institute of Earth Sciences, Academia Sinica, Taiwan. His friendship and advice have meant much these past few years.

Working at Caltech has been a wonderful experience for me. I have met many people who are full of wisdom and have much enthusiasm for science. I thank all the staff, faculty and students of the divisions for making my stay pleasant. Particular thanks go to Hiroo Kanamori, my advisor, for providing me with guidance while doing scientific research. I admire his attitude as a scientist and his insight for solving questions in a simple but meaningful way. I also would like to express my appreciation to Leon Teng at USC for his advice concerning my stay in the USA.

I have learned a lot from Kenji Satake about doing seismology using a new technique with tsunami data. Without him, part I of this thesis would not have been completed. I also thank Minoru Takeo for the use of his computer programs. Discussions with David Wald, Hong Kie Thio, Doug Dreger, Brad Woods, Laura Jones and Monica Kohler have been very useful. I thank Craig Scrinver and Blair Zajac for solving my problems with the computers, and Shawn Larson for his MPLOT graphics package. I also thank Weishi Huang, Linda Rowan, Xiaodong Song, Shingo Watada, and Lian-She Zhao.

I have enjoyed conversations with the staff. I thank Ann Freeman, my American Mom, for sharing my feeling and secrets, and Pat Kelly for proofreading this thesis. The aerobics team in the Seismo. Lab., Cheryl Contopulos, Laura Jones, Monica Kohler, and Marilee Manley, make my day full of energy. The pictures from Helen Qian leave my family with a lot of memories.

Special thanks to my husband, Jiunn-Ren Lin, for his encouragement and sharing of the care of the kids and housework. Our stay in the USA these past 5 years has been a special time for us. We started our family here and will go back home with two Ph.D.'s and two lovely daughters, Denise and Kimberly.



## Abstract

Kuo-Fong Ma

California Institute of Technology 1992

The origins of tsunamis excited by the 1989 Loma Prieta, the 1906 San Francisco, and 1975 Kalapana, Hawaii, earthquakes were examined in part I. Since tsunamis are mainly caused by vertical deformation under the sea-floor, the tsunami data allows us to constrain the vertical motion of the sea-floor during the earthquake and to determine the excitation mechanism of the tsunami.

The first arrival of the observed tsunami from the 1989 Loma Prieta, California, earthquake observed at Monterey was about 10 min. after the origin time of the earthquake. The synthetic tsunami computed for the uniform dislocation model determined from seismic data can explain the arrival time, polarity, and amplitude of the beginning of the tsunami but the period is too long. We tested other fault models with more localized slip distribution. None of the models could explain the observed period. The residual waveform, the observed minus the synthetic waveform, begins as a downward motion at about 18 min. after the origin time of the earthquake, and could be interpreted as due to a secondary source near Moss Landing. The volume of sediments involved in the slumping is

approximately  $0.012 \text{ km}^3$ . We conclude that the most likely cause of the observed tsunami is the combination of the vertical uplift of the sea floor due to the main faulting and a localized slumping near Moss Landing.

The observation of tsunami excited by the 1906 San Francisco earthquake is curious because this earthquake is generally believed to be a strike-slip earthquake for which tsunamis are not usually expected. We show that the tsunami was caused by a local subsidence associated with a bend of the San Andreas fault offshore from the Golden Gate; no vertical fault motion was involved during the 1906 San Francisco earthquake.

The 1975 Kalapana, Hawaii, earthquake was accompanied by large tsunamis which were well recorded at several tide-gauge stations around the Hawaii islands. To examine the source of the tsunamis associated with the earthquake, we computed synthetic tsunamis for three tide-gage stations, Hilo, Honolulu and Kahului, using various dislocation models, Hilina fault models and slump models. Crustal deformation data were used to constrain the dislocation models. We could find a combination of a dislocation model for the earthquake and a Hilina fault model which can explain the observed crustal deformation inland fairly well. However, the tsunamis computed for this combined model are too early in first arrivals and too small in amplitudes. The residual tsunamis, observed-synthetic, are not very different from the observed tsunamis and can be interpreted with a slump model which involves an uplift of 100~110 cm over an area of about  $2500\sim 3000 \text{ km}^2$  offshore. The total volume of displaced water associated with the slumping is about  $2.5\sim 3 \text{ km}^3$ .

The recent deployment of TERRAscope, a broadband and wide dynamic range seismic network in Southern California, provided us with a capability of recording complete waveforms of nearby earthquakes. These waveform data allow us to determine the overall faulting mechanisms, seismic moments, depths, stress drops, and the attenuation

characteristics of the crust. In part II, I investigated the waveforms of local earthquakes recorded at TERRAScope stations to understand the characteristics of the earthquake sequences.

The Pasadena earthquake ( $M_L=4.9$ ) of 3 December, 1988, occurred at a depth of 16 km, probably on the Santa Monica-Raymond fault. Prior to this event, no earthquake larger than magnitude 4 had been recorded in this area since 1930. We determined the focal mechanisms and seismic moment of 9 aftershocks by combining the first-motion data and the waveform data of P, SV, and SH waves recorded at Pasadena TERRAScope station, since the first-motion data for most of the aftershocks are too sparse to determine the mechanism. The average orientations of the P and T axes of the aftershocks are consistent with the strike of the Raymond fault. The ratio of cumulative seismic moment of the aftershocks to the seismic moment of the main shock is significantly smaller than commonly observed.

The mechanisms and seismic moments of the Sierra Madre earthquake ( $M_L=5.8$ ) of 28 June, 1991, sequence were determined using the same techniques that was applied in the 1988 Pasadena earthquake sequence. Most events located within 5 km west of the mainshock are similar to the mainshock in waveform. The mechanisms thus determined are thrust. Some events have high stress drops between 100 to 1000 bars; the mainshock is one of them. For other larger events, including the two largest aftershocks, the stress drops are between 10 to 100 bars. A few events located east of the mainshock have waveforms different from the mainshock and have strike-slip mechanisms. The ratio of cumulative seismic moments of the aftershocks to seismic moment of the mainshock is smaller than that of most events in California. The average  $Q_\beta$  values along the paths from

the hypocenters of the Sierra Madre and the Pasadena earthquake to PAS are about 130 and 80 respectively.

The 1992 Landers earthquake is the largest event to have occurred in Southern California since 1952. We examined the waveforms of the aftershocks recorded at PFO TERRAScope station to see the correlation of the waveform and mechanisms determined from surface wave inversion. Since the depths of the events are usually not determined very well, the amplitude ratio of surface wave to body wave was used to examine the accuracy of the depths determined with various methods. Most of the events which occurred to the south of the mainshock epicenter have similar waveforms and mechanisms. Only a few events occurred to the north of the mainshock epicenter where large slip occurred during the mainshock. These events have dissimilar waveforms and mechanisms. A near vertical distribution of the aftershock extending to a depth of 15 km, or even deeper is found at about 18 km to the south of the Landers earthquake epicenter. About 72% of the total energy of the aftershocks were released from the region to the south of the mainshock epicenter. The ratio of cumulative seismic moment of the aftershock to that of mainshock is less than 1/100.

# Table of Contents

<b>Part I: The Origin of Tsunamis Excited by Local Earthquakes</b>	<b>1</b>
<b>1 The Origin of Tsunami Excited by the 1989 Loma Prieta Earthquake-Faulting or Slumping-</b>	<b>7</b>
1.1 Abstract.....	7
1.2 Introduction .....	8
1.3 Data .....	10
1.4 Method.....	10
1.5 Fault Model .....	14
1.6 Results.....	14
1.7 Conclusions.....	25
<b>2 The Origin of Tsunami Excited by the 1906 San Francisco Earthquake</b>	<b>27</b>
<b>3 The Tsunamis Excited by the 1975 Kalapana, Hawaii, Earthquake</b>	<b>35</b>
3.1 Abstract.....	35
3.2 Introduction .....	36
3.3 Data .....	41
3.4 Method.....	41
3.5 Results and Discussions.....	46
3.5.1 Dislocation Model .....	46
3.5.2 Hilina Fault Model .....	61
3.5.3 Slumping Model.....	72
3.6 Conclusions.....	82
<b>References of Part I</b>	<b>84</b>
<b>Part II: Broadband Waveform Observation of Local Earthquakes</b>	<b>88</b>
<b>4 Aftershock Sequence of the December 3, 1988, Pasadena Earthquake (M<sub>L</sub>=4.9)</b>	<b>92</b>
4.1 Abstract.....	92

4.2	Introduction .....	93
4.3	Data .....	95
4.4	Method.....	101
4.5	Results.....	106
4.6	Conclusions.....	114
<b>5</b>	<b>Broadband Waveform Observation of the June 28, 1991, Sierra Madre Earthquake Sequence (<math>M_L=5.8</math>)</b>	<b>115</b>
5.1	Abstract.....	115
5.2	Introduction .....	116
5.3	Data .....	119
5.4	Method .....	128
5.5	Results.....	132
	5.5.1 Focal Mechanism and Seismic Moment Determination .....	132
	5.5.2 Q and Stress Drops Determination .....	139
5.6	Conclusions.....	148
<b>6</b>	<b>Broadband Waveform Observation of the 1992 Joshua Tree-Landers Earthquake Sequence (<math>M_w=7.3</math>)</b>	<b>150</b>
6.1	Abstract.....	150
6.2	Introduction .....	151
6.3	Data .....	155
6.4	Results.....	158
	6.4.1 Waveform and Mechanism Correlation.....	158
	6.4.2 Examination of Accuracy of Depth Determination.....	187
	6.4.3 Variation of Energy Release and Mechanism on the Fault Plane .....	205
6.5	Conclusions.....	210
	<b>Conclusions of Part II.....</b>	<b>212</b>
	<b>References of Part II.....</b>	<b>216</b>

## List of Tables

4.1	The main shock and nine aftershocks of the Pasadena earthquake sequence..	96
4.2	The seismic moment of the main shock, and cumulative seismic moment of the aftershocks for 13 earthquake sequences in California .....	112
5.1	The mainshock and 21 aftershocks of the Sierra Madre earthquake.....	121
6.1	53 aftershocks of the Joshua Tree and Landers earthquakes .....	159
6.2	Depths of the events .....	201

## List of Figures

1.1	Locations of the fault, the tide gauge station, and the epicenter of the main shock of the 1989 Loma Prieta earthquake .....	9
1.2	Observed and detrended tsunami records .....	11
1.3	Bathymetry and area for tsunami computation.....	12
1.4	Vertical crustal deformation .....	15
1.5	Inverse tsunami travel time isochrons .....	17
1.6	Snapshots of the computed tsunami .....	19
1.7	Comparison of the synthetic and observed tsunamis .....	21
1.8	Residual waveform .....	22
1.9	Vertical displacement beneath the sea-floor .....	23
1.10	Comparison of the synthetics and residual waveform .....	24
1.11	Comparison of the combined synthetic and observed tsunamis .....	25
2.1	Tide gage record at Fort Point, San Francisco.....	28
2.2	Bathymetry near the Golden Gate.....	30
2.3	Inverse tsunami travel-time isochrons .....	31
2.4	Vertical displacements of the sea-floor .....	32
2.5	Comparison of the synthetic and observed tsunamis .....	33
2.6	The numerical simulation of the vertical sea-floor deformation .....	34
3.1	Locations of the fault, tide-gauge stations, epicenter, and bathymetry .....	40
3.2	Observed and detrended tsunami records .....	42
3.3	Vertical crustal deformation .....	47
3.4	Inversion travel time isochrons.....	48
3.5	Comparison of the synthetic and observed tsunamis .....	50
3.6	Observed leveling data .....	51
3.7	Comparison of three vertical crustal deformations with the observed deformation inland and average required uplift offshore .....	53
3.8	Comparison of the synthetic and observed tsunamis .....	55
3.9	Comparison of the vertical crustal deformation with the observed deformation inland and average required uplift offshore .....	56
3.10	Comparison of the synthetic and observed tsunamis.....	59
3.11	Comparison of the combined vertical ground deformations and the observed deformation inland and required uplift offshore .....	62



3.12	Comparison of the combined vertical ground deformations and the observed deformation inland and required uplift offshore .....	65
3.13	Comparison of the synthetic and observed tsunamis.....	68
3.14	Comparison of the combined synthetic tsunamis with the observed tsunamis	69
3.15	The observed horizontal displacement .....	70
3.16	Comparison of the residual and observed tsunamis.....	73
3.17	Area for the tsunami computation of the three slumping models .....	75
3.18	Comparison of the synthetic and residual tsunamis .....	76
3.19	Comparison of the synthetic and residual tsunamis .....	77
3.20	Comparison of the synthetic and residual tsunamis .....	79
4.1	Seismicity before and after the December 3, 1988, Pasadena earthquake .....	94
4.2	Rotated displacement records of the mainshock .....	97
4.3	The mechanisms of the main shock .....	98
4.4	Rotated displacement records of the 9 aftershocks in 3 groups.....	99
4.5	Comparison of the focal mechanisms determined from the first motion data alone and the combined (first-motion and waveform) data .....	104
4.6	The mechanism and the corresponding synthetics obtained from the first motion data and the combined data .....	107
4.7	The spatial distribution of the focal mechanisms of the main shock and the aftershocks of the Pasadena earthquake sequence.....	109
4.8	Equal-area projection of the P and T axes on the lower hemisphere .....	110
4.9	Logarithm of cumulative aftershock seismic moment plotted as a function of logarithm of the seismic moment of the main shock .....	113
5.1	Seismicity after the June 28, 1991, Sierra Madre earthquake .....	118
5.2	Rotated displacement records of the mainshock and 21 aftershocks in 5 groups .....	123
5.3	Rotated displacements recorded by portable instrument at MWC station.....	129
5.4	Comparison of the focal mechanisms determined from the first motion data alone and the combined (first-motion and waveform) data .....	133
5.5	The spatial distribution of the focal mechanisms of the main shock and the aftershocks of the Sierra Madre earthquake sequence.....	141
5.6	Comparison of the observed pulse width (SH waves) and those computed for different stress drops and Q values .....	145
5.7	Comparison of the observed pulse width (SH waves) and those computed for different stress drops and Q values .....	147
6.1	Seismicity after the Joshua Tree-Landers earthquake .....	153
6.2	Rotated displacement records and mechanisms of the Joshua Tree and Landers earthquakes.....	159
6.3	Locations of the aftershocks .....	163
6.4	Rotated displacement records of the aftershocks in Group 1.....	164
6.5	The mechanisms of the events in Group 1 .....	169
6.6	Rotated displacement records of the aftershocks in Group 2.....	171
6.7	The mechanisms of the events in Group 2.....	173

6.8	Rotated displacement records of the aftershocks in Group 3.....	174
6.9	The mechanisms of the events in Group 3 .....	179
6.10	Rotated displacement record and mechanism of Group 4 .....	180
6.11	Rotated displacement records of the aftershocks in Group 5.....	181
6.12	The mechanisms of the events in Group 5.....	183
6.13	Rotated displacement records of the aftershocks in Group 6.....	184
6.14	The mechanisms of the events in Group 6 .....	185
6.15	Rotated displacement records of the aftershocks in Group 7.....	186
6.16	The mechanisms of the events in Group 7 .....	188
6.17	Depths distribution along the fault.....	189
6.18	Transverse and radial components of the synthetic waveforms at various depths.....	194
6.19	Seismograms with transverse component of event 1, 3 and 4 of Group 1 ....	196
6.20	Comparison of the amplitude ratios of observed and synthetic .....	198
6.21	Comparison of the depths from the relocated catalog of Caltech-USGS SCSN and surface wave inversion.....	200
6.22	Mechanisms variation and energy released along the fault .....	208

## Part I

# The Origin of Tsunamis Excited By Local Earthquakes

A “tsunami” is a gravity wave in an ocean caused mainly by earthquakes or submarine landslides. Although infrequent, tsunamis have been responsible for great loss of life and extensive destruction of property. Tsunamis generally occur in the Circum-Pacific belt. In the United States, Alaska, the Hawaiian Islands, and part of the west coast have suffered considerable tsunami hazards.

Although tsunamis are generally thought to be caused by vertical deformation under the sea-floor associated with earthquakes, the detailed excitation mechanisms are still unknown. For example, some earthquakes, such as the 1946 Aleutian, the 1975 Kalapana, Hawaii, and the 1929 Grand Banks earthquakes have had anomalously large tsunamis relative to their magnitudes. These earthquakes are called “tsunami earthquakes” (Kanamori 1972). This is in contrast to “tsunamigenic earthquakes” which are earthquakes with significant tsunamis. Whether these tsunami earthquakes were caused by faulting or submarine landslides has been a subject of debates. The study of tsunami waveforms can help us understand better the nature of the tectonic deformation under the

sea-floor during an earthquake and the origin of the tsunamis and possible mechanisms of the earthquakes.

Tsunami waveforms, like seismic data, contain information not only on the source but also the propagation path. The propagation velocity of a tsunami depends only on water depth as far as a tsunami is regarded as a linear long-wave. Aida (1969) used numerical modeling to study tsunamis caused by the 1964 Niigata, Japan, and the 1968 Tokachi-Oki, Japan, earthquakes. The tsunami waveforms computed numerically were in satisfactory agreement with those observed at tide-gauge stations. Hwang et al. (1970, 1972a,b) simulated the tsunamis resulting from the Alaska earthquake of March 27, 1964, and the Chilean earthquake of May 22, 1960. They developed a numerical model of generation and trans-oceanic propagation of tsunamis using hydrodynamic equations in a spherical coordinate system. Aida (1978) showed that the observed tsunami heights can be explained in the first approximation by seismic fault models. In recent studies, Satake (1987, 1989) showed that the slip distribution on the fault plane of large submarine earthquakes can be determined by inversion of tsunami waveforms.

Tsunami waveforms have been computed either analytically for a uniform depth (Takahashi 1942; Kajiura 1963) or numerically for actual topography (Aida 1978; Satake 1985). The basic equations of motion for tsunami computation are

$$\frac{\partial u}{\partial t} + u \frac{\partial u}{\partial x} + v \frac{\partial u}{\partial y} - fv = -g \frac{\partial H}{\partial x} - \frac{ru(u^2 + v^2)^{1/2}}{(H + D - \eta)} \quad (1)$$

$$\frac{\partial v}{\partial t} + u \frac{\partial v}{\partial x} + v \frac{\partial v}{\partial y} + fu = -g \frac{\partial H}{\partial y} - \frac{rv(u^2 + v^2)^{1/2}}{(H + D - \eta)} \quad (2)$$

where  $u$  and  $v$  are the velocity components in the directions of the coordinates,  $x$  and  $y$ ;  $H$

is the water level elevation relative to still water;  $f$  is the Coriolis parameter,  $g$  is the acceleration of gravity,  $\eta$  is bottom displacement,  $r$  is the coefficient of bottom friction, and  $D$  is water depth prior to source displacement. The Coriolis's force and frictional force resulting from viscosity can be ignored because the period of waves considered is relatively short and a deep sea region is considered primarily in this study. If the amplitude of a tsunami is small compared to the water depth, the advection terms:  $u \frac{\partial u}{\partial x}$ ,  $v \frac{\partial u}{\partial y}$ ,  $u \frac{\partial v}{\partial x}$ , and  $v \frac{\partial v}{\partial y}$  can also be neglected so that the equation of motion becomes linear (Murty1977) as

$$\frac{\partial u}{\partial t} = -g \frac{\partial H}{\partial x} \quad (3)$$

$$\frac{\partial v}{\partial t} = -g \frac{\partial H}{\partial y} \quad (4)$$

The phase velocity  $c$  of a small amplitude, or linear, gravity wave is given as (Lamb 1932),

$$c = \sqrt{(g/k) \tanh kD} = \sqrt{(g\lambda / 2\pi) \tanh(2\pi D / \lambda)} \quad (5)$$

where  $k$  is the wavenumber, and  $\lambda$  is the wavelength. If  $D/\lambda$  is small, the velocity in (5) becomes  $\sqrt{gD}$ , which corresponds to a long-wave approximation. If  $D/\lambda$  is larger than 0.3, the phase velocity becomes  $\sqrt{g\lambda/2\pi}$ , which shows dispersive character. This corresponds to a deep water or short wave approximation. In general tsunami propagation in open sea can be treated adequately by a linear theory, but both phase and amplitude dispersions will be important for tsunami propagation on the continental shelf. In the very shallow coastal areas, the amplitude dispersion dominates. However, if we consider moderate tsunamis caused by local earthquakes, the traveling distance of the tsunami is

short and its amplitude is much smaller than the water depth, so that the dispersions of phase and amplitude can be ignored and linear long-wave approximation will be adequate. Since the tide gauge is usually located in shallow water, runup effect is serious for large tsunamis, and interpretation of tsunami waveforms recorded with tide gauges would be difficult. In this thesis, I investigate tsunamis with moderate amplitudes observed at short distances using a long-wave linear equation for tsunami computation.

In the following three chapters, I investigated tsunamis with moderate amplitudes recorded at nearby tide-gauge stations during the 1989 Loma Prieta, California (Chapter 1), 1906 San Francisco, California (Chapter 2), and 1975 Kalapana, Hawaii (Chapter 3) earthquakes. For these events, the long distance dispersion and tsunami runup effects can be ignored. Since the amplitudes of the observed tsunamis of the 1989 Loma Prieta, 1906 San Francisco and 1975 Kalapana earthquakes are about  $10^1$  to  $10^2$  cm and are much smaller than the water depth, about  $10^4$  to  $10^5$  cm, and the wavelengths of the tsunamis, about 10 km, are much larger than the water depth, the long-wave approximation is valid in the present study and the associated error is less than several percent. Satake et al. (1988) studied tide-gauge response to tsunamis and showed that the tide-gauge response is important only for tsunamis with periods less than 5 min. Since the periods of the observed tsunamis of the three events are about 15 min., I did not correct for the response of the tide-gauge in this study. Since the bathymetry is usually very well known, I computed tsunami waveforms using a finite-difference method for actual bathymetry.

For the 1989 Loma Prieta earthquake (Chapter 1), I investigated the tsunami recorded at Monterey, California, during the 1989 Loma Prieta earthquake ( $M_w=6.9$ ). I computed synthetic tsunamis for various fault models to understand the possible cause of the observed tsunamis. The synthetic tsunamis computed for various dislocation models can

explain the arrival time and the amplitude of the very beginning of the observed tsunami, but the period of the synthetic tsunami is too long. The most likely cause of the tsunami observed at Monterey is the combination of the vertical uplift of the sea-floor owing to the main faulting and a localized slumping triggered by the earthquake.

For the 1906 San Francisco earthquake (Chapter 2), I investigated the tsunami observed at Fort Point in San Francisco Bay during that earthquake (M~8). Since tsunamis are mainly caused by the vertical deformation under the sea-floor, I determined the vertical motion of the sea-floor from the observed tsunami data and show that the tsunami was caused by a local subsidence associated with the bend of the San Andreas fault offshore from the Golden Gate; no vertical fault motion is necessary to explain the observed tsunami.

The mechanism of the 1975 Kalapana earthquake has been a subject of much debate. Ando (1979) and Furumoto and Kovach (1979) suggested a fault model with a nearly horizontal fault plane at a depth of about 10 km. Recently, Eissler and Kanamori (1987) proposed a slump model for the generation of long-period surface waves, but Wyss and Kovach (1988) argued for a nearly horizontal thrust faulting. By using the side-looking sonar system GLORIA (Geologic Long-Range Inclined Asdic), Moore et al. (1989) showed that slumps and debris avalanche deposits are common features surrounding the Hawaiian Islands. The 1975 Kalapana earthquake was accompanied by large tsunamis which were well recorded by several tide-gauge stations around the Hawaiian Islands. These data provide an important clue to the mechanism of this earthquake. In Chapter 3, I synthesized tsunamis for various fault models determined from seismic data and slump models to understand the origin of the observed tsunami, and the mechanism of the earthquake. I computed synthetic tsunamis at three tide gauge stations, Hilo, Kahului and

Honolulu for fault models located on the south flank of Kilauea volcano and in the Hilina fault system, and for slump models. The deformation caused by the dislocation models and Hilina fault models has little contribution to the observed tsunamis, although it can explain the observed deformation inland fairly well. To explain the observed tsunamis a large-scale slumping along the east rift zone of Kilauea volcano is required.

Chapters 2 and 3 have been published. Chapter 4 is under preparation for publication. As such, each chapter is intended to be self-contained, complete with an abstract, methodology, results and conclusions. Hence, some redundancies exist between the chapters.



## Chapter 1

# The Origin of Tsunami Excited By The 1989 Loma Prieta Earthquake —Faulting or Slumping—

### 1.1 Abstract

We investigated the tsunami recorded at Monterey, California, during the 1989 Loma Prieta earthquake ( $M_w=6.9$ ). The first arrival of the tsunami was about 10 min after the origin time of the earthquake. Using an elastic half-space, we computed vertical ground displacements for many different fault models for the Loma Prieta earthquake, and used them as the initial condition for computation of tsunamis in Monterey Bay. The synthetic tsunami computed for the uniform dislocation model determined from seismic data can explain the arrival time, polarity, and amplitude of the beginning of the tsunami. However, the period of the synthetic tsunami is too long compared with the observed. We tested other fault models with more localized slip distribution. None of the models could explain the observed period. The residual waveform, the observed minus the synthetic waveform,

begins as a downward motion at about 18 min after the origin time of the earthquake, and could be interpreted as resulting from a secondary source near Moss Landing. If the large scale slumping near Moss Landing suggested by an eyewitness observation occurred about 9 min after the origin time of the earthquake, it could explain the residual waveform. To account for the amplitude of the observed tsunami, the volume of sediments involved in the slumping is approximately  $0.012 \text{ km}^3$ . Thus the most likely cause of the tsunami observed at Monterey is the combination of the vertical uplift of the sea floor due to the main faulting and a large-scale slumping near Moss Landing.

## 1.2 Introduction

The Loma Prieta earthquake ( $M_w=6.9$ ) which occurred in the Santa Cruz Mountains, in central California, on October 18, 1989, excited tsunamis in nearby Monterey Bay. Figure 1.1 shows the location of the fault, epicenter and the tide-gauge station at Monterey. Nearfield tsunamis are relatively rare in the United States. The 1906 San Francisco earthquake (Lawson et al. 1910), the 1927 Lompoc earthquake, the 1964 Alaskan earthquake, and the 1975 Kalapana earthquake are among the few examples. Since large earthquakes near the coast, either onshore or offshore, can cause serious tsunami hazards, we investigated the tsunami excited by the Loma Prieta earthquake in an attempt to understand the generation mechanism of such nearfield tsunamis.

We will show that two elements contributed to tsunami excitation-the vertical deformation of the sea floor caused by faulting and the secondary submarine slumping presumably caused by shaking.

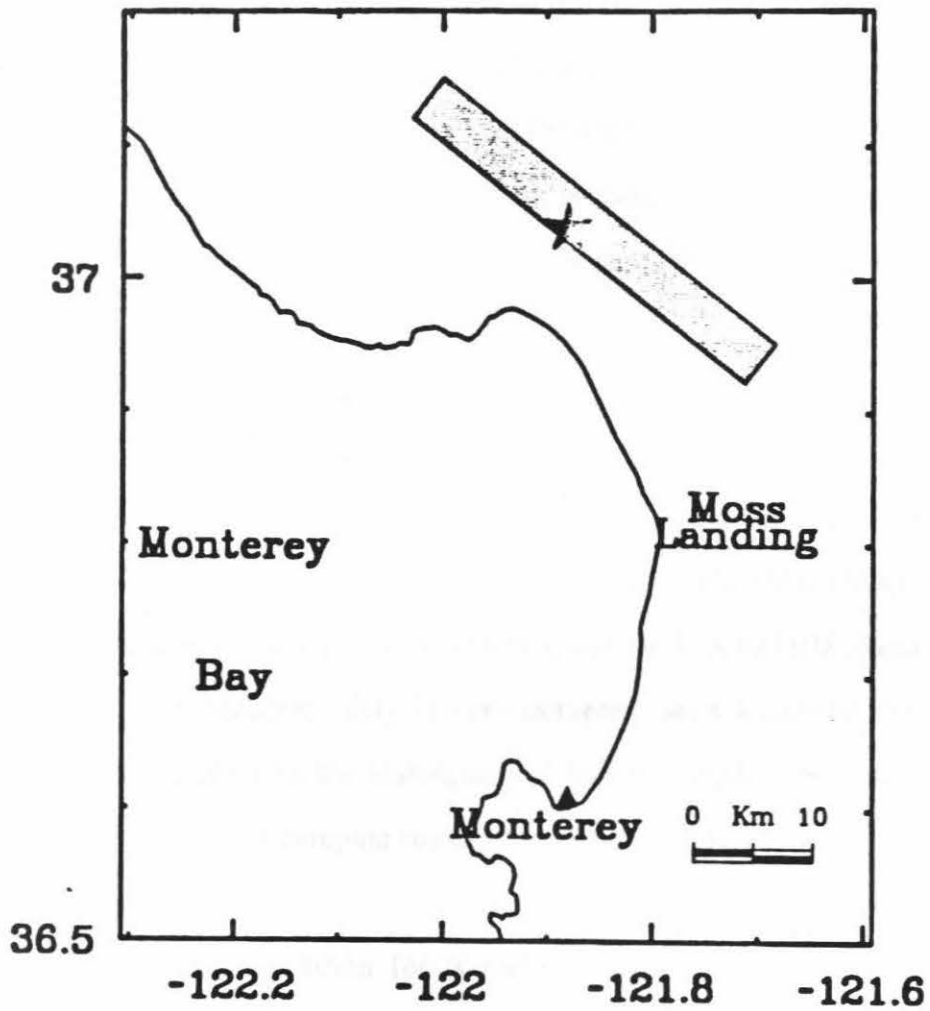


Figure 1.1: Locations of the fault (shaded strip) and the tide gauge station (solid triangle). The star indicates the epicenter of the main shock of the 1989 Loma Prieta earthquake.

## 1.3 Data

Figure 1.2a shows the tsunami recorded on the tide gauge in Monterey Bay. Schwing et al. (1990) describe this instrument as a bubble gauge. We digitized and detrended the record. Figure 1.2b shows the detrended record for one hour starting from the origin time of the earthquake. The first arrival of the tsunami is about 10 minutes after the origin time of the earthquake, and the peak-to-peak amplitude is about 40 cm.

## 1.4 Method

Tsunami waveforms are computed either analytically for the case of uniform depth (e.g., Takahashi 1942; Kajiura 1963; Ward 1982; Comer 1984; Okal 1988), or numerically for actual bathymetry (Hwang et al. 1972a; Houston 1978; Aida 1978; Satake 1985). Since the bathymetry in Monterey Bay is very complex, with a canyon running northeast to southwest (Figure 1.3), the assumption of uniform depth is not valid. We used a finite difference method to compute tsunamis in the bay using the actual bathymetry which is known very accurately.

As the initial condition for tsunami computation, we used the vertical ground displacement caused by faulting. For this computation, we used Okada's (1985) program which computes ground deformations caused by faulting in an homogeneous half-space. Since the source process time of the earthquake is less than 10 seconds and the water depth is much smaller than the scale length of the ground deformation, we assumed that the water surface is uplifted instantaneously exactly in the same way as the bottom deformation. The

a.

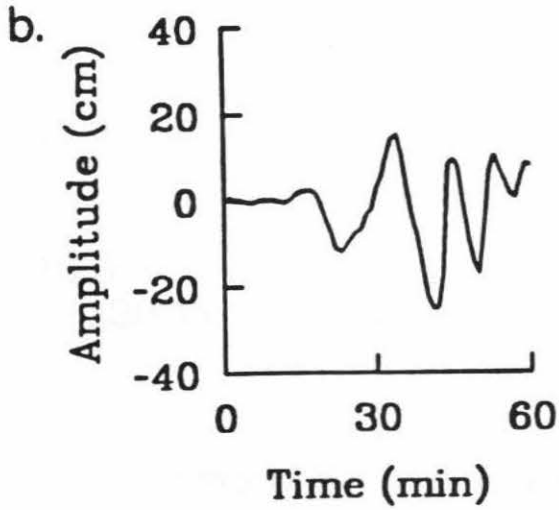
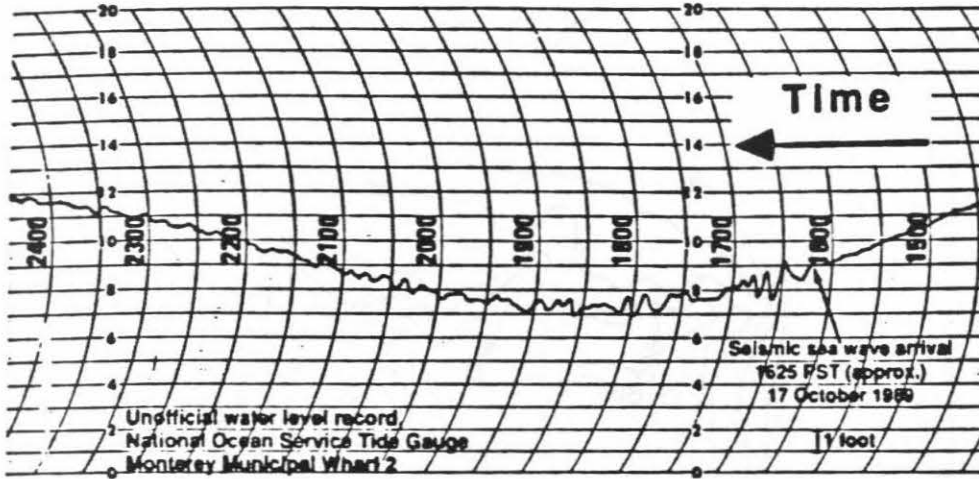


Figure 1.2 a): Tsunami recorded on the tide gauge at Monterey (after Schwing et al. 1990). b): Detrended tsunami record for one hour starting from the origin time of the earthquake.

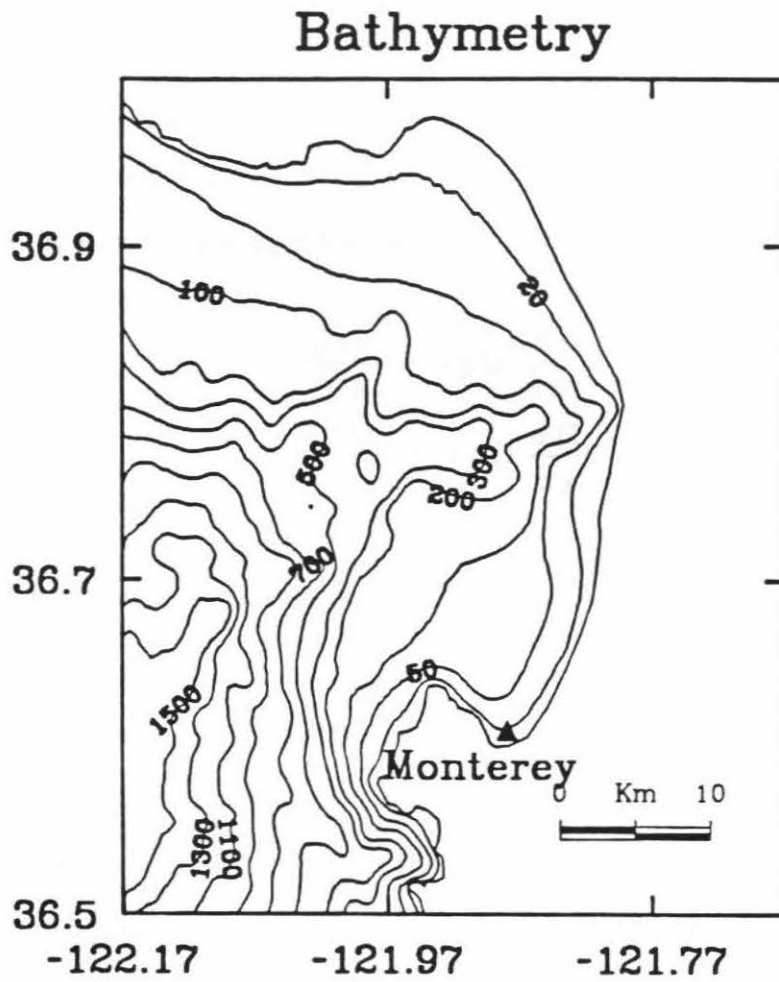


Figure 1.3. The bathymetry in Monterey Bay and the area over which the tsunami computation is made. The contour lines indicate the water depths in meters.

amplitude of the tsunami is of the order of 10 cm and is much smaller than the water depth, about 100 m. Also the wavelength of the tsunami, about 10 km in the bay, is much longer than the water depth. Hence we can use the vertically integrated linear long-wave equation and continuity equation as basic equations of tsunami propagation. In a Cartesian coordinate system (x, y) these equations are given by

$$\begin{aligned}\frac{\partial Q_x}{\partial t} &= -gD \frac{\partial H}{\partial x} \\ \frac{\partial Q_y}{\partial t} &= -gD \frac{\partial H}{\partial y}\end{aligned}$$

and

$$\frac{\partial H}{\partial t} = -\frac{\partial Q_x}{\partial x} - \frac{\partial Q_y}{\partial y} ,$$

where  $Q_x$  and  $Q_y$  are the flow rate obtained by integrating the velocity vertically from the bottom to the surface in the x and y directions respectively, g is the acceleration of gravity, D is the water depth, and H is the water height above the average surface. These equations are solved with a finite difference method. The bathymetry in Monterey Bay and the area for which the computation is made are shown in Figure 1.3. The grid size is 1/4 min, which is about 400 m and 500 m in the x and y directions, respectively, and the number of grid points is about 14,400. The time step of computation is 2 sec which is chosen to satisfy the stability condition for the finite difference calculation. Since the bathymetry is known in detail, the tsunami can be computed very accurately.

## 1.5 Fault Model

The fault model of the Loma Prieta earthquake has been determined very well using seismic, geodetic, and aftershock data. Kanamori and Satake (1990) inverted teleseismic body- and surface-wave data and obtained a mechanism with dip= $70^{\circ}$  SW, rake= $138^{\circ}$ , and strike= $N128^{\circ}$  E. The seismic moment is  $3 \times 10^{26}$  dyne-cm ( $M_W=6.9$ ). The total length of the aftershock area is about 40 km, and the main shock is located near the center of the aftershock (U.S.G.S. staff, 1990), which suggests bilateral faulting. Kanamori and Satake (1990) suggested a uniform fault model having a fault length,  $L$ , of 35 km. The coseismic slip on the fault is 238 cm, if the fault width,  $W$ , is assumed to be 12 km. Lisowski et al. (1990) compared the observed geodetic data with several dislocation fault models; their preferred fault model has a fault length of 37 km and fault width of 13.3 km. The coseismic slip on the fault is 204 cm. The focal mechanism has dip= $70^{\circ}$  SW, rake= $144^{\circ}$ , and strike= $N44^{\circ}$  W. The total seismic moment determined from geodetic data is the same as that determined from seismic data by Kanamori and Satake (1990).

## 1.6 Results

We first computed the vertical crustal deformation for the uniform seismic fault model ( $L=35$  km,  $W=12$  km, and  $D=238$  cm) determined by Kanamori and Satake (1990), and used it as the initial condition for tsunami computation. Figure 1.4 shows the location of



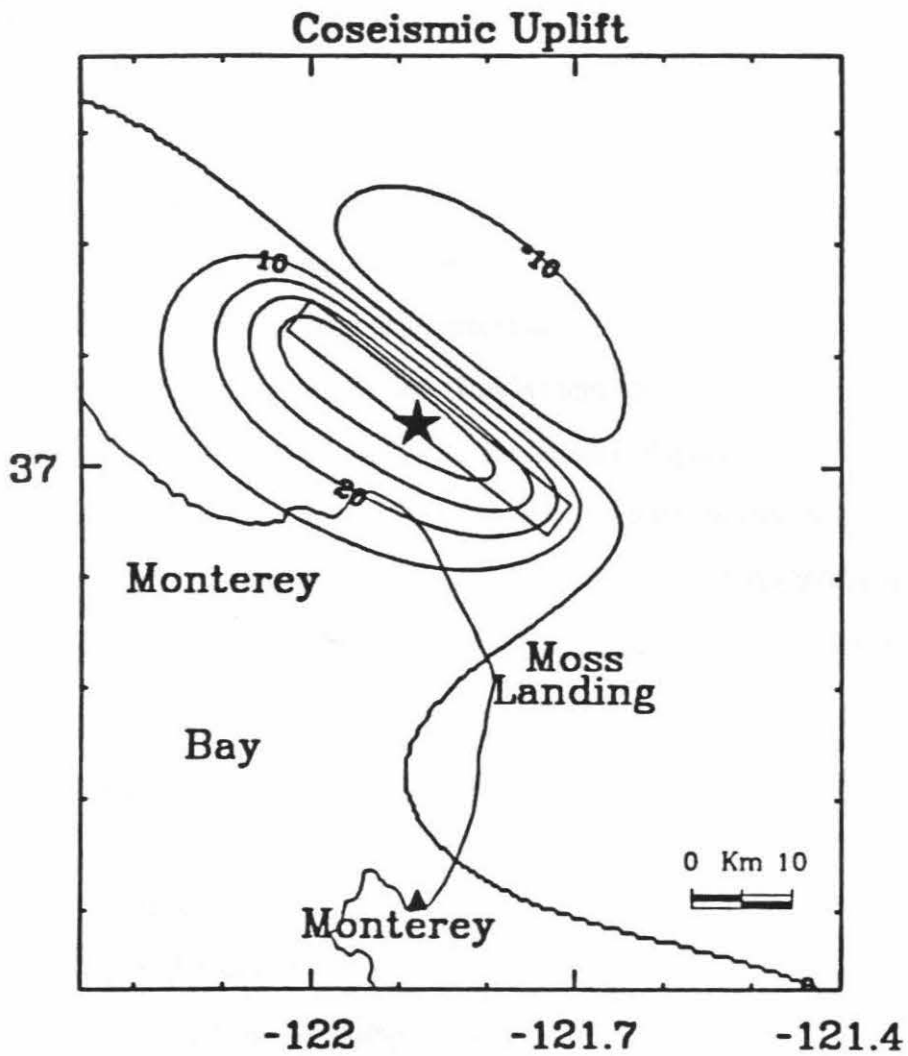


Figure 1.4. Vertical crustal deformation with 10 cm contour interval for uniform seismic fault model ( $L=35$  km,  $W=12$  km, and  $D=238$  cm).

the fault and the vertical crustal deformation. The displacement beneath the sea floor, a maximum of 25 cm, is responsible for tsunami generation.

To see the contribution of the sea-floor displacement to the observed tsunami, we computed an inverse travel-time diagram by placing a source at the tide-gauge station, and propagating tsunamis backward into the bay. Figure 1.5 shows the inverse tsunami travel times every 2 min. The isochron at 10 min is close to the southern edge of the displacement field defined by the 0 cm contour line. This is consistent with the onset time of the tsunami at 10 min after the origin time of the earthquake. Figure 1.6 shows the snapshots of computed tsunamis at 5, 10, 15, 20, 25, and 30 min after the origin time.

Figure 1.7a compares the synthetic tsunami computed for this model with the observed. The synthetic tsunami can explain the arrival time, polarity, and amplitude of the beginning of the observed tsunami. However, the period of the synthetic tsunami is too long compared with the observed.

The reason for the long period of the synthetic tsunami is that the sea floor deformation caused by faulting is very broad. If the slip on the fault is more localized than that in the model used in the above computation, the period of the synthetic tsunami could be decreased. To test this, we computed tsunamis for three localized sources and for the geodetic fault model obtained by Lisowski et al. (1990) for comparison.

In the first case we localized the entire slip in the northwestern half of the fault (fault length=17.5 km). In the second case, the slip is localized in the southeastern half (fault length=17.5 km). In the third case, we localized the displacement in the bottom half of the fault plane (fault length=35 km, width=6 km). In all of these cases, the seismic moment is the same as for the uniform model. These cases represent the three extreme cases of localized sources. The fourth model is taken from Lisowski et al. (1990). Figures 1.7b to

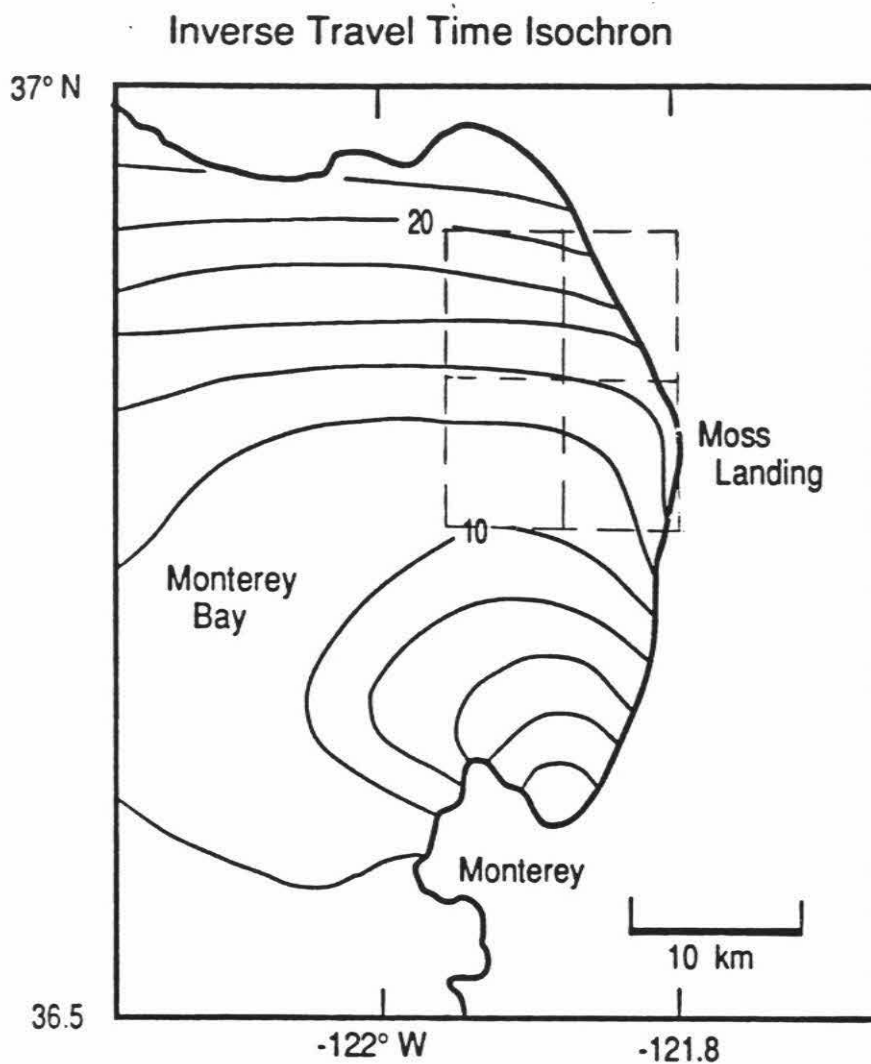
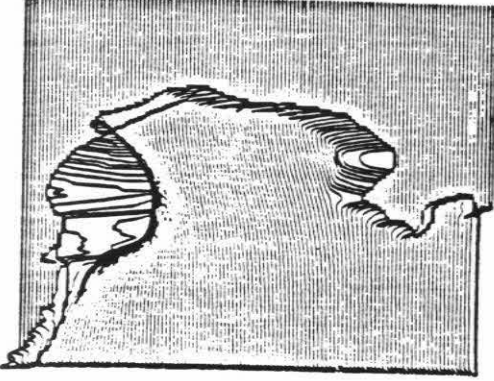


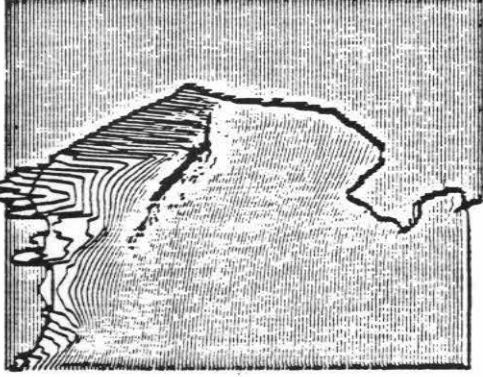
Figure 1.5 Inverse tsunami travel time isochrons. The contour lines indicate the tsunami wavefronts at every 2 min. The dash box indicates the area for inversion computation.

Figure 1.6. Snapshots of the computed tsunami computed for the fault model at 5, 10, 15, 20, 25, and 30 min.

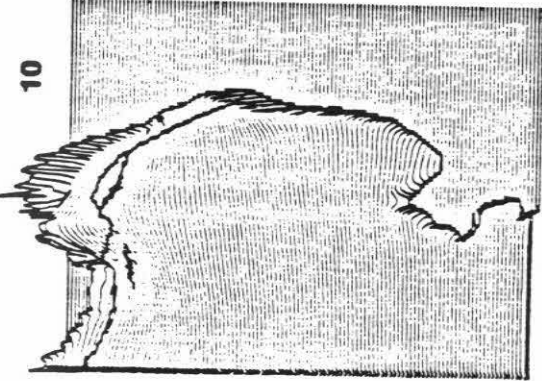
15



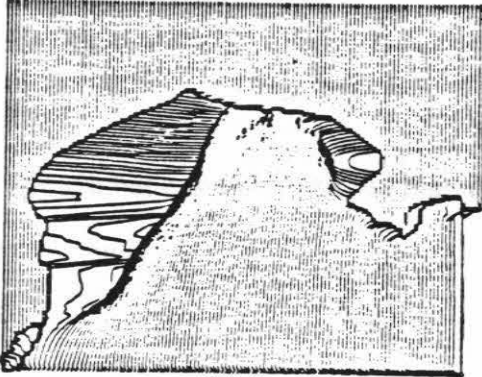
30



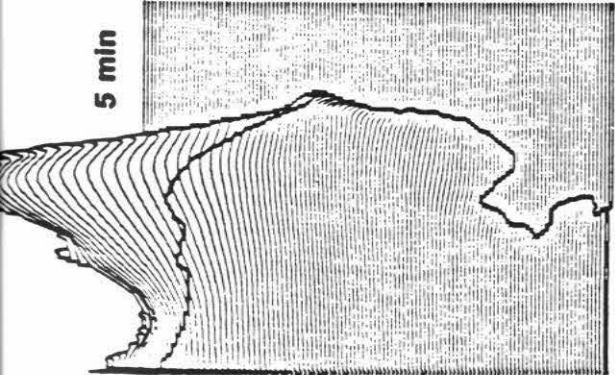
10



25



5 min



20

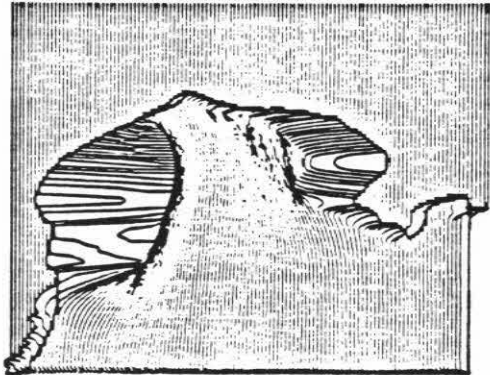
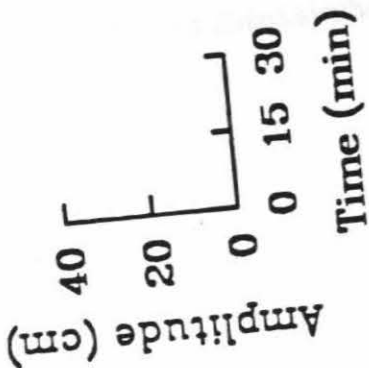


Figure 1.7 a), b), c), d), e): Comparison of the synthetic tsunami (dashed line) computed for various fault models with the observed (solid line).

----- Synthetic  
—— Observed

c SE Half



b NW Half



e "Geodetic"



a Uniform Fault



d Bottom Half



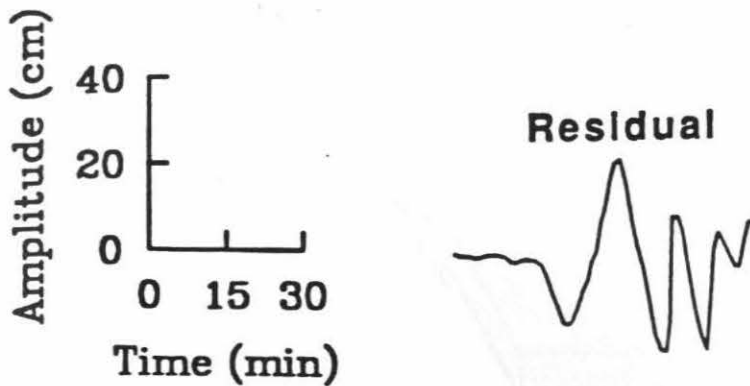


Figure 1.8 The residual waveform (observed minus synthetic waveform for uniform fault model)

1.7e compare the synthetics for these cases with the observed. The waveform of the synthetics is not very different from that for the uniform model. This result indicates that the displacement field caused by faulting is smoothed out in Monterey Bay, and it is not possible to explain the short period of the observed tsunami.

Thus the difference in the period suggests that a secondary source may be responsible for the tsunami observed at Monterey. To explore this possibility, we computed the residual waveform, e.g., the observed minus the synthetic waveforms. The residual waveform, shown in Figure 1.8, begins as a downward motion at about 18 min after the origin time of the earthquake. Figure 1.5 shows that the isochron at 18 min is slightly north of Moss Landing. Schwing et al. (1990) suggest the possibility of large-scale slumping near Moss Landing. Sea level fell by 1 m or more near Moss Landing soon after the earthquake. This sea level change is larger than the change expected from solely the direct effect of faulting. The inverse travel time curve shown in Figure 1.5 suggests that if



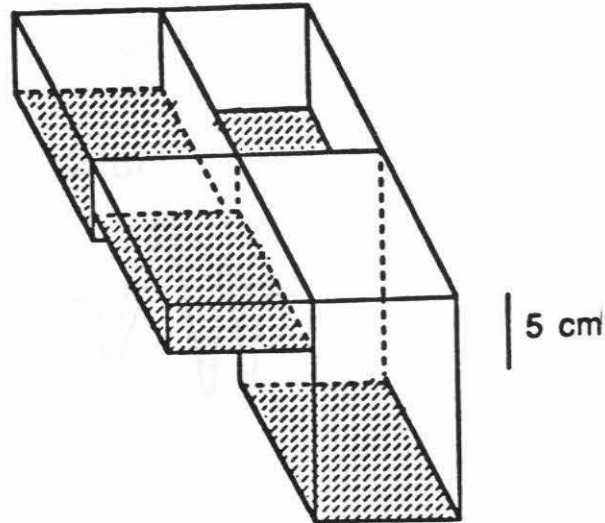


Figure 1.9 The sea-floor displacement obtained from the inversion of observed tsunami.

this slumping occurred 9 min after the earthquake, the arrival time of the residual tsunami shown in Figure 1.8 could be interpreted as due to the slumping at Moss Landing.

To determine more details of the secondary source responsible for the tsunami, we divided the sea-floor into 4 blocks ( $8 \times 10 \text{ km}^2$  each) as shown in Figure 1.5. Due to the time delay of the secondary source, we shifted the residual waveform by 9 minute and inverted the shifted residual tsunami waveform to determine the displacement for each block. The inversion is formulated as

$$\sum_{j=1}^{N_b} A_j(t_i) x_j = b(t_i) \quad i=1, \dots, N_t, \quad (2)$$

where  $N_b$  and  $N_t$  are number of the blocks and time steps,  $A_j(t_i)$  is the tsunami amplitude at time  $t_i$  due to a unit displacement at the  $j$ th block,  $x_j$  is the displacement at the  $j$ th block, and  $b(t_i)$  is the observed tide gauge record at time  $t_i$ .

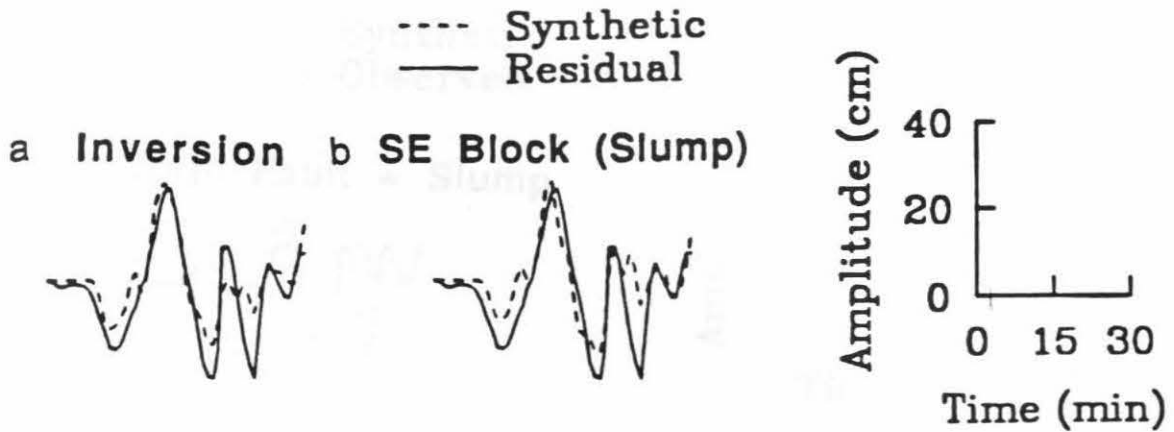


Figure 1.10 a, b): Comparison of the residual waveform (solid line) with the synthetics (dash line) for the displacement field obtained from the inversion and computed for a 15 cm subsidence at the southeastern block shown in (a).

The displacement  $x_j$  for each block is estimated with a linear least squares inversion of equation (2).

Figure 1.9 shows the vertical displacement of the sea floor determined by the inversion. The displacement shows an isolated subsidence at the southeastern block near Moss Landing, which is consistent with our assumption. The synthetic tsunamis computed for the displacement field shown in Figure 1.9 and for a subsidence in the southeastern block only were shown in Figure 1.10a and 1.10b, respectively. Both can explain the period and the amplitude of the shifted residual tsunami. The SE block near Moss Landing has a subsidence of about 15 cm over an area of 80 km<sup>2</sup>. Figure 1.11 compares the synthetic waveform computed for faulting and slumping combined with the observed.

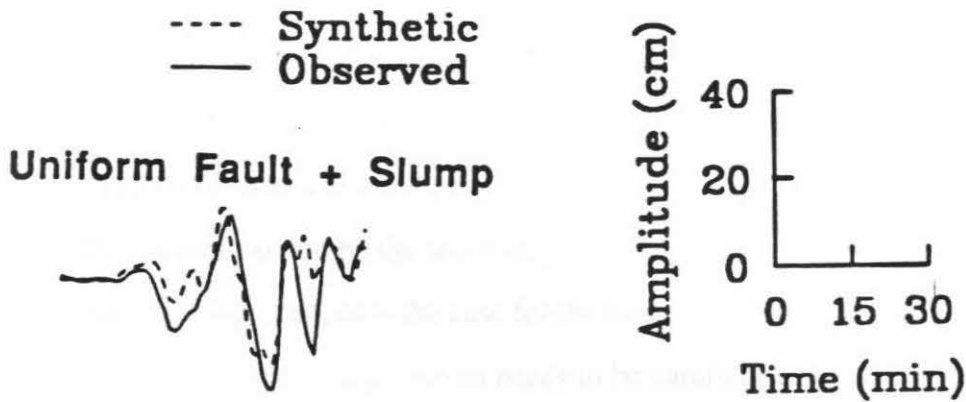


Figure 1.11: Comparison of the synthetic tsunami (dashed line) computed for faulting and slumping combined with the observed (solid line).

A slump may be most adequately modelled by a sudden subsidence followed by a gradual uplift. However, the details are unknown. If the later uplift was gradual, the tsunami source could be modelled using a single subsidence source. If this is the case, our result suggests that the volume of sediments involved in the slumping is approximately  $0.012 \text{ km}^3$ . However, this estimate depends on the details of the slumping. Unfortunately, from the single observation we cannot determine further details.

## 1.7 Conclusions

The uniform fault model determined from seismic data can explain the arrival time, polarity, and amplitude of the beginning of the observed tsunami, but the period of the synthetic tsunami is too long. We tested fault models with a wide range of nonuniform slip distribution, but none of them could explain the observed period satisfactorily. This

suggests that a secondary source is required to explain the tsunami observed at Monterey. The residual waveform, the observed minus synthetic waveform computed for the seismic source, suggests that the most likely secondary source is a sediment slumping near Moss Landing; evidence for such a slumping has been reported by an eyewitness.

Since the tsunami excited by the secondary source can be more extensive than that by the earthquake faulting itself, as is the case for the Loma Prieta earthquake, the possibility of tsunamis caused by secondary sources needs to be carefully evaluated in assessing the tsunami potential of nearshore earthquakes.

## Chapter 2

# The Origin of Tsunami Excited by the 1906 San Francisco Earthquake

Lawson et al. (1910) reported a tsunami observed at Fort Point in San Francisco Bay (Figure 2.1a) during the 1906 San Francisco earthquake (M~8). This observation is curious because the San Francisco earthquake is generally believed to be a strike-slip earthquake for which tsunamis are not usually expected. However, the recent Loma Prieta earthquake which occurred on a part of the rupture zone of the San Francisco earthquake unexpectedly had a significant component of vertical fault motion, and suggested the possibility that the San Francisco earthquake also had some vertical fault motions. To investigate this possibility, we analyzed the tsunami observed at Fort Point. Since tsunamis are primarily caused by vertical motion of the sea floor, we can constrain the extent of vertical component of fault motion using tsunami data. We show that the tsunami was caused by a local subsidence associated with a bend of the San Andreas fault offshore from the Golden Gate; no vertical fault motion was involved during the 1906 San Francisco earthquake.

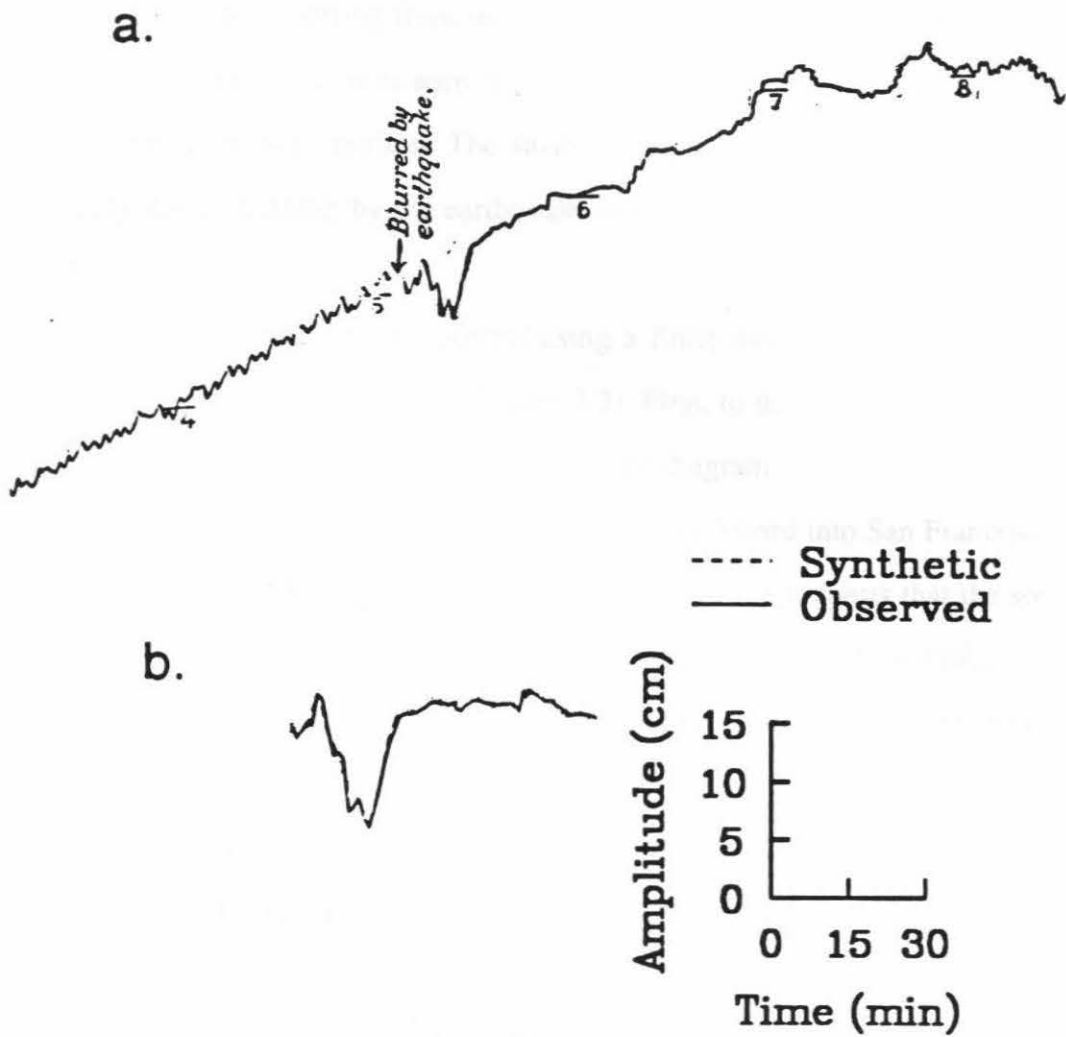


Figure 2.1 a): Tide gage record at Fort Point, San Francisco (after Lawson et al. 1910).

b): The detrended tsunami waveform starting from the origin time of the earthquake.

We first removed the tide from the original record. Figure 2.1b shows the detrended record for one hour starting from the origin time of the earthquake. A depression of the water level of about 10 cm is seen about 7 to 8 min after the origin time. The waveform shows only downward motion. The small motion immediately after the earthquake is probably due to shaking by the earthquake (Lawson et al. 1910), and is ignored in this analysis.

We computed tsunami waveforms using a finite difference method and the actual bathymetry of San Francisco Bay (Figure 2.2). First, to determine the source location of the tsunami, we computed an inverse travel-time diagram by placing a source at the Fort Point tide-gage station, and propagating tsunamis backward into San Francisco Bay. The inverse travel time isochron at 8 min shown in Figure 2.3 suggests that the source of the tsunami is probably a subsidence that occurred east of the San Andreas fault.

To determine more details of the seafloor deformation responsible for the tsunami, we divided the sea-floor into 15 blocks ( $4 \times 5 \text{ km}^2$  each) as shown in Figure 2.3, and inverted the observed tsunami waveform to determine the displacement for each block. The inversion is formulated as

$$\sum_{j=1}^{N_b} A_j(t_i) x_j = b(t_i) \quad i=1, \dots, N_t, \quad (1)$$

where  $N_b$  and  $N_t$  are number of the blocks and time steps, where  $A_j(t_i)$  is the tsunami amplitude at time  $t_i$  due to a unit displacement at the  $j$ th block,  $x_j$  is the displacement at the  $j$ th block, and  $b(t_i)$  is the observed tide gage record at time  $t_i$ . The displacement  $x_j$  for each block is estimated with a linear least squares inversion of equation (1).

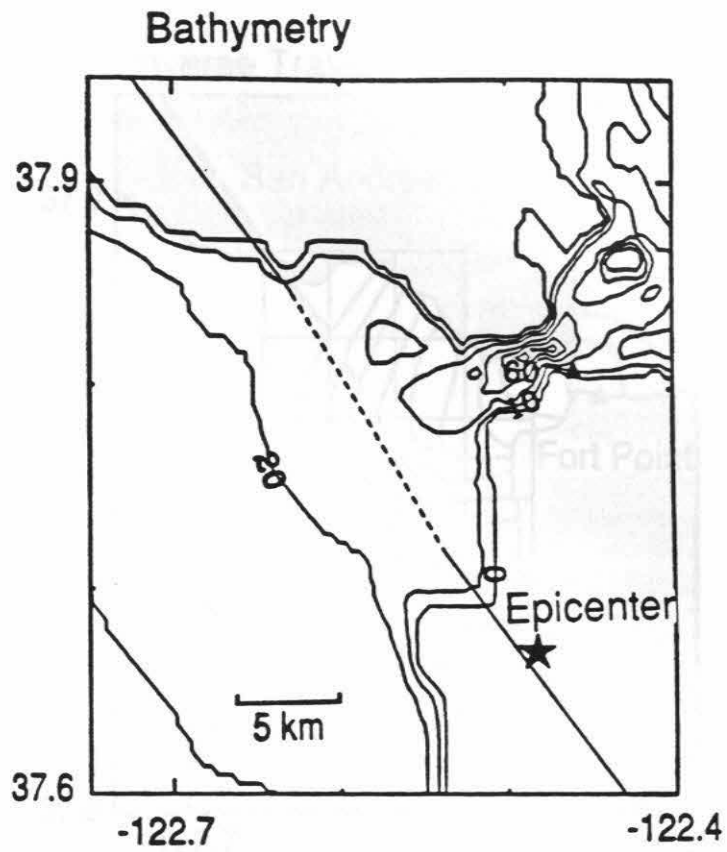


Figure 2.2 Bathymetry near the Golden Gate. The contour lines are given at 0, 10, 20, 40, 60, and 80 m.



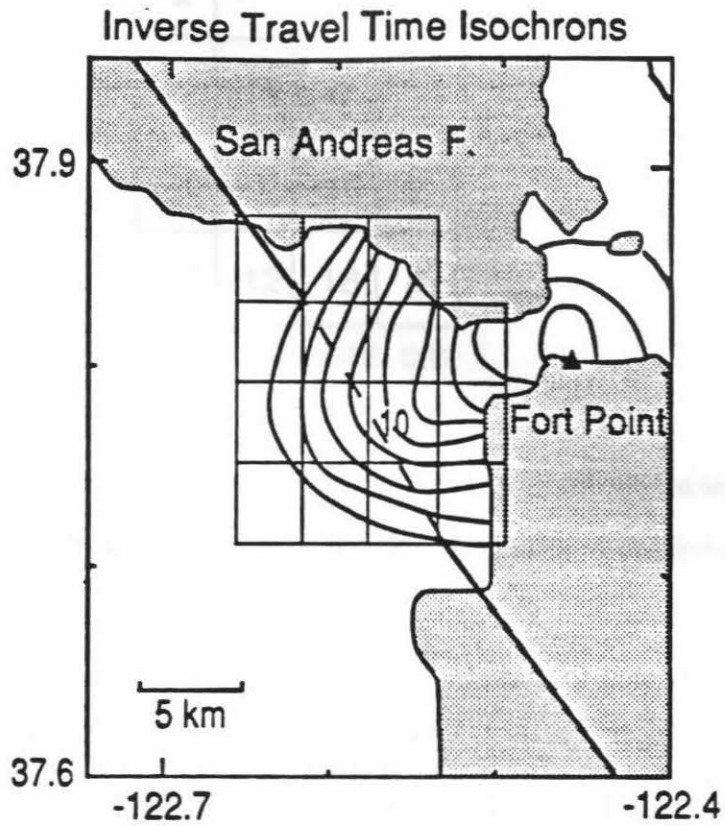


Figure 2.3 Inverse tsunami travel-time isochrons from Fort Point . Contour intervals are 2 min.

-2	-7	-22	
12	-15	-4	1
-15	-1	-10	2
-17	-12	-18	4

Displacement, cm

Figure 2.4. Vertical displacements (in cm) in the boxed areas shown in Figure 2.3 obtained from tsunami data by inversion. The negative values indicate subsidence.

Figure 2.4 shows the vertical displacement of seafloor determined by the inversion. The displacement is mostly subsidence. The synthetic tsunami computed for the displacement field shown in Figure 2.5 can explain the period and the amplitude of the observed tsunami. The subsidence averaged over the 15 blocks is about 7 cm.

The San Andreas fault exhibits a right-stepping bend offshore from the Golden Gate as shown in Figure 2.3. For this geometry, a right-lateral strike-slip fault yields a subsidence between the straight segments even if the slip is purely horizontal. Although the exact magnitude and distribution of the vertical displacement depends on the details of fault geometry, a simple numerical calculation (Figure 2.6) shows that the ratio of the vertical displacement to the horizontal slip ranges from 0.01 to 0.03 for a vertical strike-slip fault extending to a depth of 12 km. Since the horizontal slip during the 1906 San Francisco earthquake is estimated to be about 6 m along this segment (Lawson et al., 1910; Thatcher,

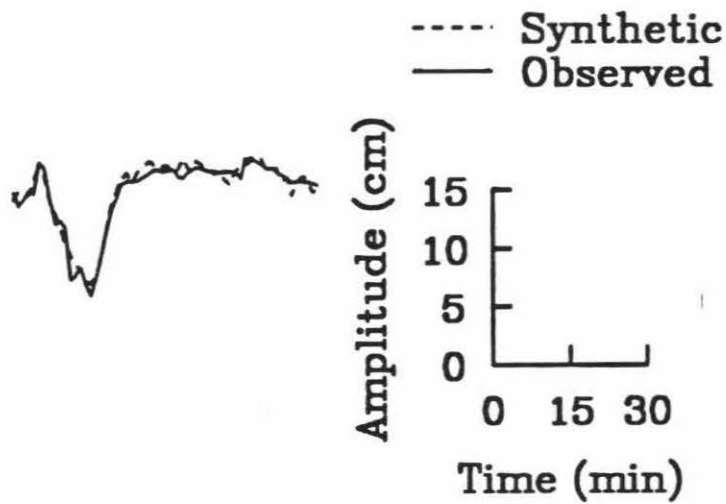


Figure 2.5: Comparison of the synthetic tsunami waveform computed for the displacement field shown in Figure 2.4.

1975), a subsidence of about 10 cm is expected near the bend, which is consistent with that determined from the observed tsunami waveform. This agreement suggests that the cause of the tsunami is due to the local subsidence associated with the right-stepping bend of the San Andreas fault offshore from the Golden Gate, and no vertical fault motion was involved during the 1906 San Francisco earthquake.

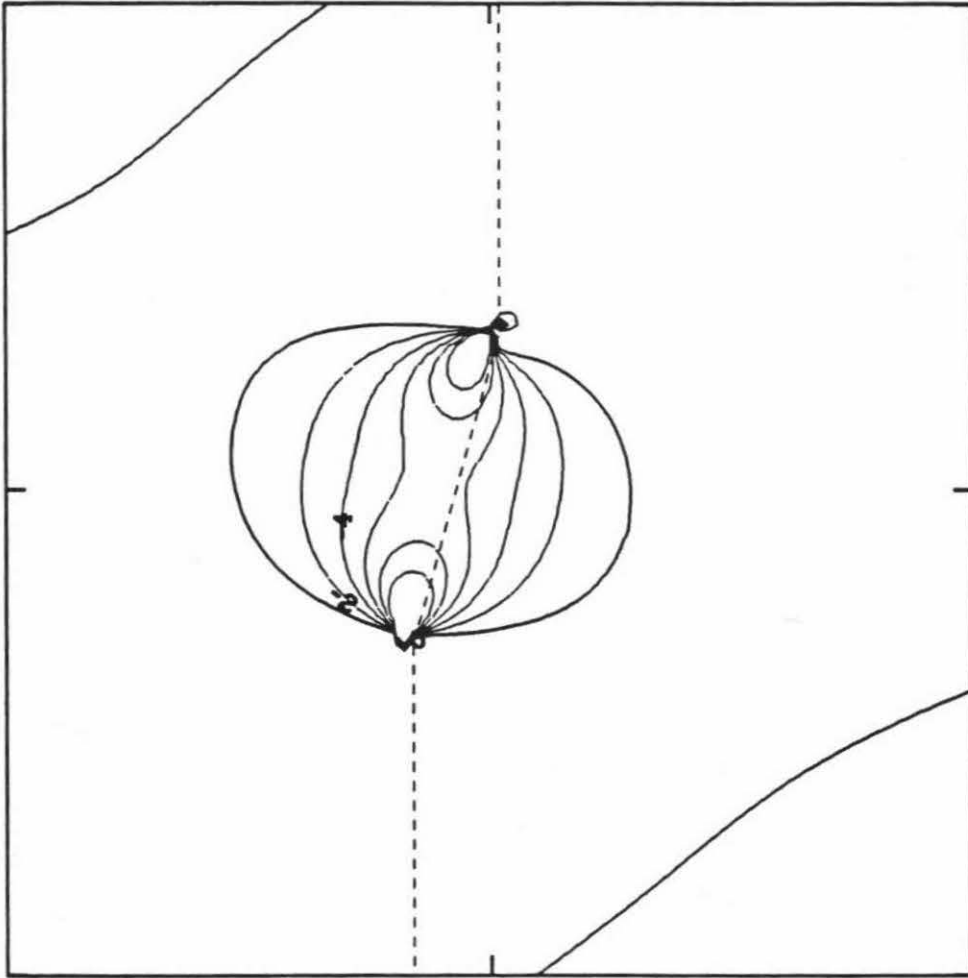


Figure 2.6 The numerical simulation of the vertical sea-floor deformation for a vertical strike-slip fault extending to a depth of 12 km and horizontal slip of 6 m along the geometry of San Andreas fault near the Golden Gate (dash line). Contour intervals are 2 cm. The negative values indicate subsidences.

## Chapter 3

# Tsunamis Excited by the 1975 Kalapana, Hawaii, Earthquake

### 3.1 Abstract

We investigated the waveforms of the tsunamis recorded at three tide-gage stations, Hilo, Kahului, and Honolulu from the 1975 Kalapana, Hawaii, earthquake. We computed synthetic tsunamis at the three tide-gage stations, Hilo, Kahului and Honolulu for various models to examine the source of the tsunamis associated with the earthquake. The arrival times and the amplitudes of the synthetic tsunamis computed for Ando's fault model (strike= $N70^{\circ}E$ , dip= $20^{\circ}SE$ , rake= $-90^{\circ}$ , fault depth=10 km) are about 10 min earlier and 5 times smaller than those of the observed tsunamis, respectively. We tested other modified seismic fault models with different dip angles and fault depths. A dislocation fault model with northwest dip direction yields larger amplitudes of tsunami than that with southeast dip direction. A dislocation fault model with shallower fault depth produces later first arrivals than that with a deeper fault depth. However, the synthetic tsunamis for the extreme fault model (strike= $N70^{\circ}E$ , dip= $10^{\circ}NW$ , rake= $90^{\circ}$  and fault depth=3 km) are still

too early in the arrival times and too small in amplitudes compared with the observed tsunamis. Since the displacements caused by the dislocation models can explain only the general trend of the observed geodetic data but not the steep gradient inland near the coast observed by leveling, we computed the ground deformation caused by the Hilina fault to see whether the slip on the Hilina fault system can explain the observed deformation inland. The deformation from the combination of the seismic dislocation model (strike=N70°E, dip=10°SE, rake=-90° and fault depth=3 km) and the Hilina fault model (strike=N60°E, dip=70°SE, rake=-90° and fault depth=3.5 km) can explain the observed displacement inland fairly well. However, the tsunamis computed for the composite fault model are still too early in first arrivals and too small in amplitudes. The residual tsunamis (observed-computed tsunamis) are not very different from the observed tsunamis and can be interpreted by a slump model with a propagating uplift offshore with 4 min duration. To explain the observed tsunamis, the propagating slump model is required to have an average uplift of 110 cm over an area of about 3000 km<sup>2</sup> which is consistent with the interpretation that the 1975 Kalapana earthquake was caused by a large-scale slumping due to gravitational instability of the south flank of Kilauea volcano.

## 3.2 Introduction

Large earthquakes near the coast either onshore or offshore are usually accompanied by tsunamis. Tsunami records contain not only the information on the source but also the effects of propagation path. The propagation velocity of tsunami depends only on water depth as far as a tsunami is regarded as a linear long-wave. Since the bathymetry is

generally very well-known, the propagation effect can be evaluated more precisely for tsunamis than seismic waves by means of numerical computation.

Aida (1969) used numerical modeling to study tsunamis caused by the 1964 Niigata, Japan, and 1968 Tokachi-Oki, Japan, earthquakes. The computed tsunamis from his numerical experiment were satisfactory in the comparison of the waveforms at tide-gage station. Hwang et al. (1970, 1972a,b) simulated the tsunami due to the Alaska earthquake of March 1964, the Chilean earthquake of May 1960, and the Andreanof earthquake of 1957. They developed a numerical model for generation and trans-oceanic propagation of tsunamis based on hydrodynamic equations in a spherical coordinate system. Aida (1978) showed that the observed tsunami height can be explained in the first approximation by seismic fault models. Recent studies, Satake (1987, 1989) showed that the slip distribution on the fault plane of large submarine earthquakes can be determined using inversion of tsunami waveforms. By inverting the observed tsunamis excited by the 1989 Loma Prieta and 1906 San Francisco, California, earthquakes, Ma et al. (1991a,b) obtained the vertical sea-floor deformation during the earthquakes and discussed the possible origins of the observed tsunamis.

The Kalapana, Hawaii, earthquake occurred at about 04:47:30 Hawaiian Standard Time (14:47:30, GMT) on 29 November 1975 (Tilling et al., 1976) with a magnitude of 7.1. The location given by Hawaii Volcano Observatory (HVO) was at 19°20'N, 155°02'W, and a depth of 5-7 km. This earthquake affected most of the south flank of Kilauea volcano between the southwest rift zone and the east rift zone and was accompanied by large tsunamis which caused significant damage. The tsunamis were observed at several locations along the coast. A severe tsunami reached a maximum height of 14.6 m at Halape

beach, where two campers were killed. Similar large earthquakes accompanied by tsunamis previously occurred in this region of the island in 1868 and 1823.

The 1975 Kalapana earthquake is the largest Hawaiian earthquake instrumentally recorded and several studies have been done using seismic, aftershock, geodetic as well as tsunami data. However, there are still some debates about the mechanism of this earthquake. From the analysis of seismic waves, tsunami and crustal deformation data, Ando (1979) suggested a normal fault mechanism with strike= N70°E; dip= 20°SSE; fault length= 40 km; width= 20-30 km; depth= 10 km; slip= 5.5-3.7 m. On the basis of teleseismic and local seismic data, Furumoto and Kovach (1979) suggested that this earthquake has an overthrust mechanism with dip 4° to the NW and strike of N64°E. From the radiation pattern of long-period surface waves, Eissler and Kanamori (1987) proposed a near-horizontal single force mechanism which represents slumping rather than faulting. The single force is oriented opposite to the direction of the inferred slumping on the south flank of Kilauea volcano. However, Wyss and Kovach (1988) argued for a nearly horizontal thrust faulting.

A large static deformation caused by the earthquake was observed along the coast. Coseismic subsidence was observed along 50 km of the south coast between the rift zone. Lipman et al. (1985) observed horizontal extensions steadily increasing seaward over the south flank and ground cracking along 25 km of the Hilina fault system. Swanson et al. (1976) noted that the entire south flank of Kilauea is mobile and has undergone extensions of several meters in the last century previous to the 1975 Kalapana earthquake. Bryan and Johnson (1991) analyzed the earthquake mechanisms on the island of Hawaii from 1986 to 1989 and suggested that Kilauea's south flank is mobile and moving seaward. Hatori (1976) estimated the possible tsunami-generating area of the 1975 Kalapana earthquake by



using tsunami ray-tracing method and obtained an average uplift of 1 m over an area of 2200 km<sup>2</sup> of sea-floor. Ando (1979) computed synthetic tsunamis at Hilo tide gauge station using his seismic fault models. His synthetics have too small amplitudes compared with the observed. Cox (1980) noted that the timing marks on the marigrams of the tide gauge stations had an error of about 0-6.5 minutes, which Hatori (1976) and Ando (1979) did not take into consideration in their interpretation.

Since the 1975 Kalapana earthquake was accompanied by large tsunamis which were well recorded at several tide-gauge stations around the Hawaii Islands, these tsunami data provide us with a good opportunity to study the mechanism of the earthquake. In this thesis, I computed synthetic tsunamis at three tide gauge stations, Hilo, Kahului and Honolulu for various models to examine the mechanism of the tsunami generated by this earthquake. Figure 3.1 shows the bathymetry in the area and the locations of the three tide-gauge stations. We first compared the crustal deformations inland computed for various dislocation models to the observed leveling data associated with the 1975 Kalapana earthquake obtained by Lipman et al. (1985). A fault model for the Hilina fault system was added to the dislocation model. We found that a combination of a dislocation model and Hilina fault model can explain the observed deformation inland but not the observed tsunami.

To explain the tsunamis a large uplift of the sea floor was required. We consider this uplift as a result of a large-scale slumping. We tested several slump models which are represented by uplift of the sea floor. We will show that the tsunamis were mainly caused by a large-scale slumping extending to the sea-floor. The large-scale slumping is caused by the gravitaional sliding of the entire south flank of the Kilauea volcano.

# Bathymetry

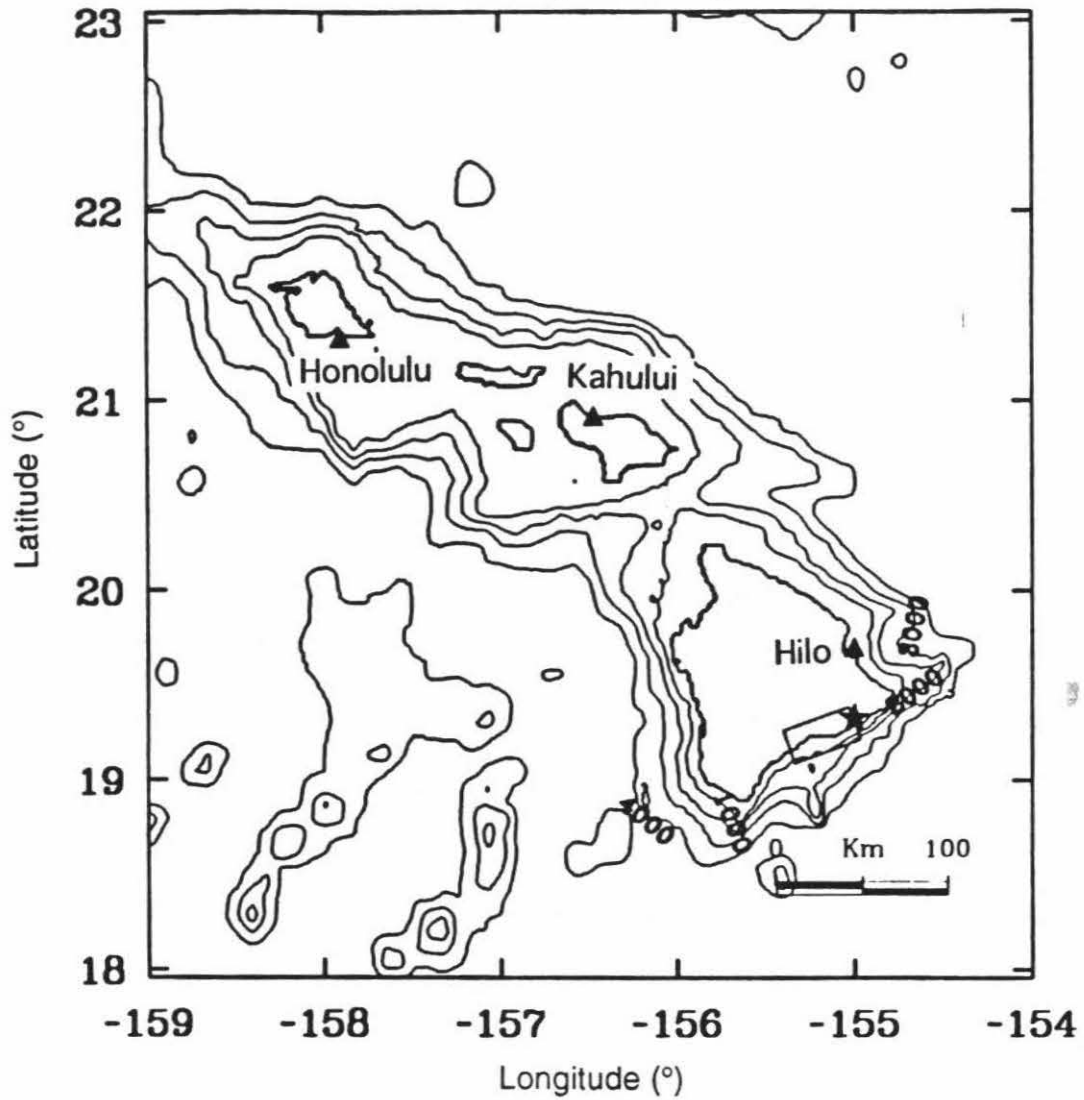


Figure 3.1: Locations of the fault (shaded strip) and the three tide-gauge stations (solid triangle). The star indicates the epicenter of the mainshock of the 1975 Kalapana earthquake. The bathymetry around Hawaii islands is shown by contour lines in meters.

### 3.3 Data

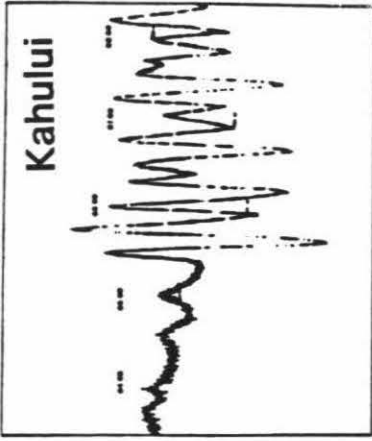
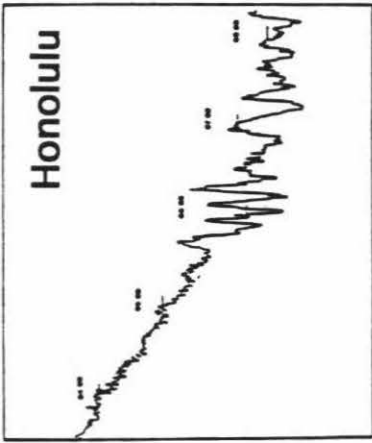
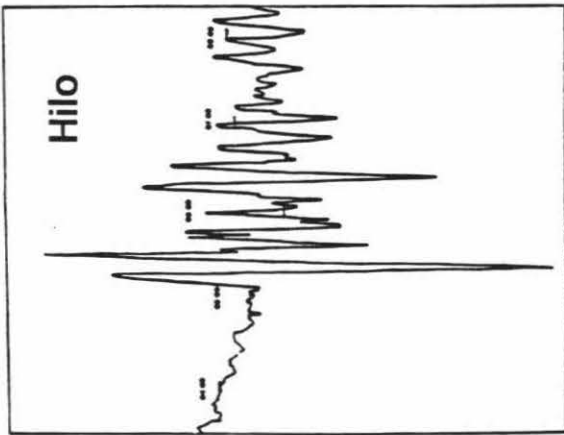
Figure 3.2a shows the tsunamis recorded at three tide gage stations, Hilo, Honolulu, and Kahului during the earthquake (Cox 1980). According to the gage-time corrections made by Cox (1980), the average timing errors were 0, -0.5, and 6.5 minutes for Hilo, Honolulu, and Kahului tide-gage stations respectively. The positive and negative signs indicate the advance and delay of the tide-gage clocks. These corrections were obtained by checking the clocks on the day before and after the earthquake occurred. Applying the gage-time corrections to the tide-gage records, we digitized and detrended the records for one and half hours starting from the origin time of the earthquake. Figure 3.2b shows the time-corrected detrended records. Since the records at the three tide gage stations show very noisy background, the tsunamis' first arrivals are defined as times when distinct upward motions were observed as indicated on Figure 3.2b. The first arrivals of tsunamis at Hilo, Honolulu, and Kahului tide gage stations are about 23, 48 and 49 minutes, respectively, after the origin time of the earthquake with an error of about 2 minutes. The peak to peak amplitudes for the corresponding tide gage stations are about 180, 15 and 85 cm, respectively.

### 3.4 Method

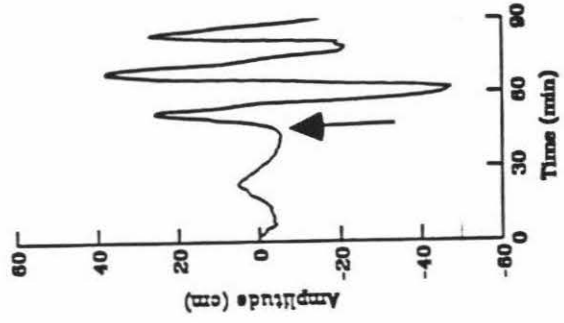
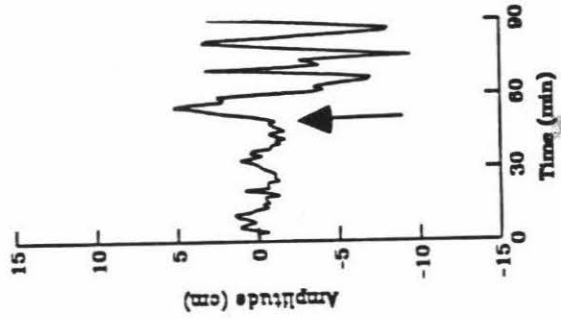
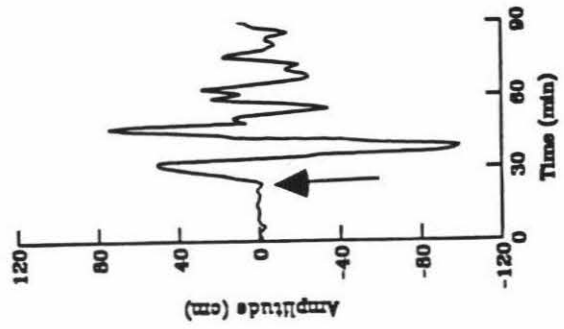
Tsunami waveforms have been computed either analytically for a uniform depth (Takahashi 1942; Kajiura 1963) or numerically for an actual topography (Aida 1978; Satake 1985). Since the bathymetry is very-well known and has a very significant effect on tsunami propagation (Satake 1987), we computed tsunamis using actual topography. To

Figure 3.2 (a): Tsunamis recorded on the tide gauge stations at Hilo, Honolulu, and Kahului, respectively. (b): The corresponding detrended tsunami records for one and a half hours starting from the origin time of the earthquake of the three tide-gauge stations.

a.



b.



compute tsunami propagation effects, we used long-wave linear equations. If the amplitude of a tsunami is small compared to the water depth, the advection term can be neglected so that the equation of motion becomes linear (Murty 1977; Introduction of the thesis). The phase velocity  $c$  of a small amplitude, or linear, gravity wave is given as (Lamb 1932),

$$c = \sqrt{(g/k) \tanh kD} = \sqrt{(g\lambda/2\pi) \tanh(2\pi D/\lambda)} \quad (1)$$

where  $g$  is the gravitational acceleration,  $k$  is the wavenumber,  $D$  is the water depth, and  $\lambda$  is the wavelength. If  $D/\lambda$  is small, the velocity in (1) becomes  $\sqrt{gD}$ . This corresponds to a long-wave approximation. If  $D/\lambda$  is larger than 0.3, the phase velocity becomes  $\sqrt{g\lambda/2\pi}$ , which shows dispersive character. This corresponds to a deep water or short wave approximation. Since the amplitude of the observed tsunami in this study, 1 m, is much smaller than the water depth, about  $10^2$ - $10^3$  m, and the wavelength of the tsunami is much larger than the water depth, the long-wave approximation is valid in the present study and the associated error is less than several percent.

We used the vertically integrated linear long-wave equation and continuity equation as basic equations for tsunami propagation. In Cartesian coordinate system  $(x,y)$  these equations are given by

$$\begin{aligned} \frac{\partial Q_x}{\partial t} &= -gD \frac{\partial H}{\partial x} \\ \frac{\partial Q_y}{\partial t} &= -gD \frac{\partial H}{\partial y} \end{aligned} \quad (2)$$

and

$$\frac{\partial H}{\partial t} = -\frac{\partial Q_x}{\partial x} - \frac{\partial Q_y}{\partial y} \quad (3)$$

where  $Q_x$  and  $Q_y$  are the flow rate in the  $x$  and  $y$  directions, respectively, obtained by integrating the velocity vertically from the bottom to the surface,  $g$  is the acceleration of gravity,  $D$  is the water depth, and  $H$  is the water height above the average surface. The area for tsunami computation,  $5^\circ \times 5^\circ$ , is also shown in Figure 3.1. The grid space for the finite difference computation is 1 min, which is about 1.85 km and 1.76 km in the  $x$  and  $y$  directions, respectively. This grid size is chosen to be less than one-eighth of the source size to prevent numerical dispersion (Satake, 1987). The total number of grid points is 90,000. The time step of the computation is 2 sec which is chosen to satisfy the stability condition for the finite difference calculation (Aida, 1969).

The velocity of a tsunami, or linear long-wave, is much smaller than any kind of seismic waves or rupture velocity of the fault. Kajiura (1970) discussed the energy exchange between the bottom and the water on the basis of the long-wave approximation and showed that if the deformation is completed in less than several minutes it can be treated as an abrupt change. If the source process time of the earthquake is less than a few minutes, we can assume that the water surface is uplifted in exactly the same way as the sea floor. This uplift of the water surface can be used as the initial condition for computation of tsunami propagation. We used the vertical component of the ground deformation caused by faulting as the initial condition for tsunami computation. If the source process is much longer than several minutes, only part of the bottom deformation contributes to tsunami generation.

## 3.5 Results and Discussions

### 3.5.1 Dislocation Model

In the tsunami computation, we used the fault model determined by Ando (1979) as a reference model. We first computed the vertical crustal deformation for Ando's fault model, shown in Figure 3.3, and used it as the initial condition for tsunami computation. The maximum uplift of the sea floor is about 50 cm, the maximum subsidence inland is about 150 cm. The average uplift over the deformation area under the sea floor is about 20 cm. We call the deformation area beneath the sea-floor a "tsunami source area," since it is the area responsible for tsunami generation.

To see the contribution of the sea-floor deformation to the observed tsunamis, we computed an inverse travel-time diagram by the finite difference method by putting a source at the three tide gauge stations, Hilo, Honolulu, and Kahului, respectively, and propagating tsunamis backward into the sea. Figure 3.4 shows the inverse travel time isochrons near the source area at every minute from 20 to 25 minutes, 45 to 50 minutes, and 40 to 50 minutes for Hilo, Honolulu, and Kahului tide gage stations, respectively. The isochrons corresponding to the three tide gauge stations meet each other at 24 minutes, 49 minutes, and 48 minutes, for Hilo, Honolulu and Kahului, respectively. These times are close to the onset time of the observed tsunami at each station. Hereafter, we called these isochrons onset time isochrons. The 0 cm contour line of the vertical crustal deformation of the fault model is far away from the intersection of the onset time isochrons for Hilo, Honolulu, and Kahului tide-gauge stations. This indicates that the first arrivals of the synthetic tsunamis from Ando's fault model would be too early compared with the observed.



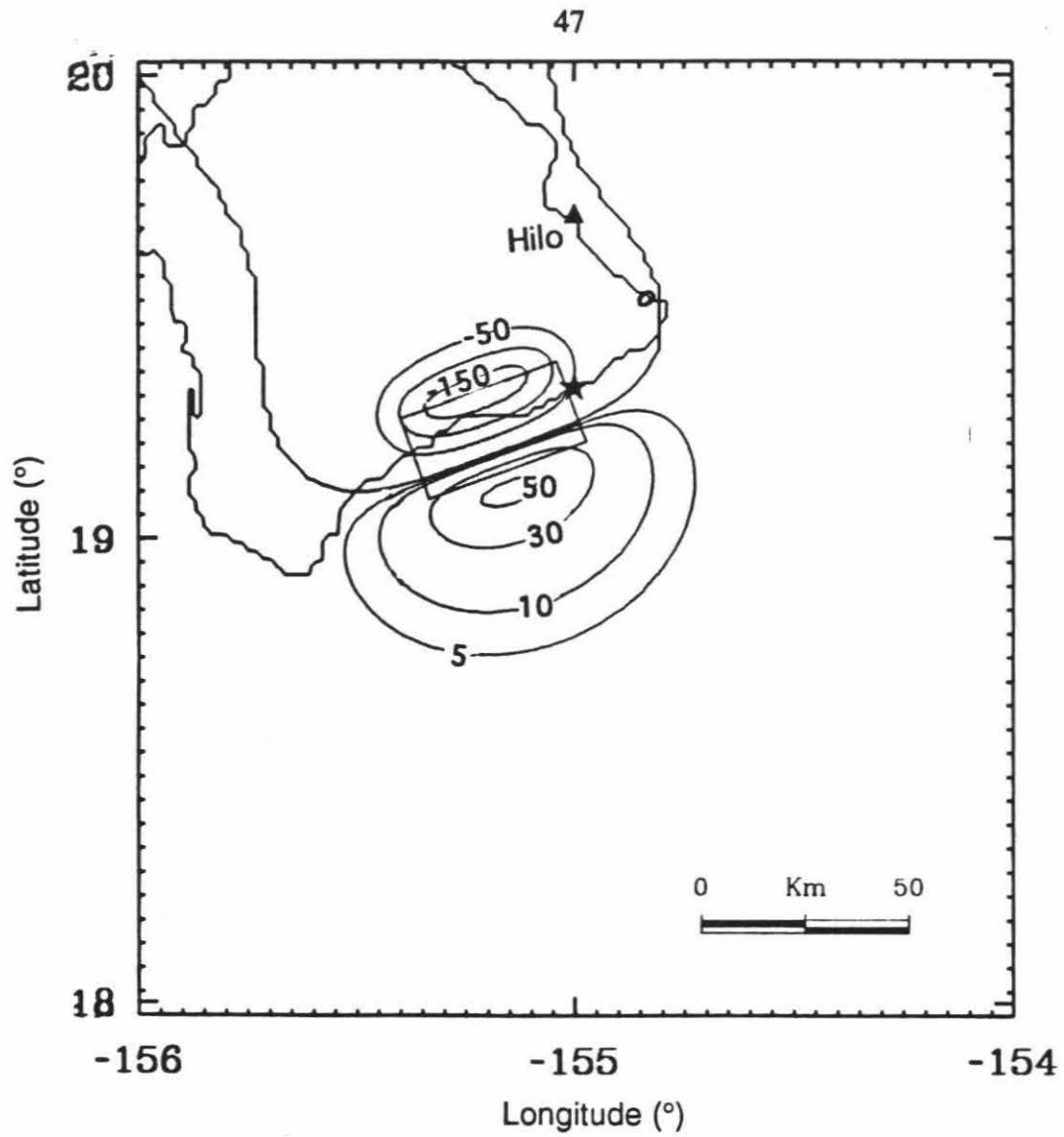


Figure 3.3: Vertical crustal deformation for Ando's fault model. The contour lines indicate the displacement in cm.

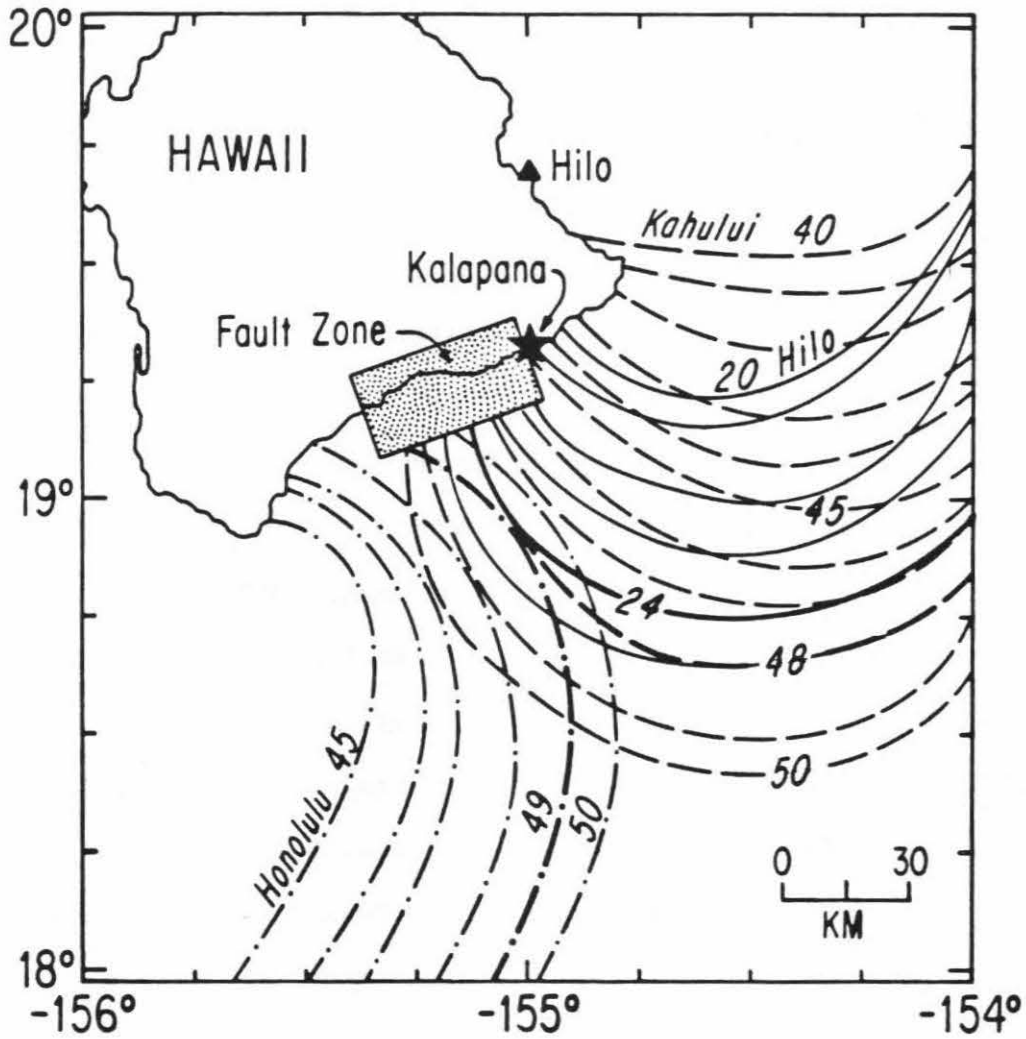


Figure 3.4: Inverse travel time isochrons at every minute near source area. The solid, dash-dot, and dashed curves indicate the tsunami wavefronts at every minute from 20 to 25 min, 45 to 50 min, and 40 to 50 min for Hilo, Honolulu, and Kahului stations, respectively. The bold curves indicate the onset time isochrons. The asterisk indicates the epicenter of the earthquake. The shaded area represents the fault zone.

Figure 3.5 compares the synthetic tsunamis computed for this fault model with the observed. The synthetics are too early in arrival time, as we expected, and too small in amplitudes compared with the observed. The first arrival times of the synthetics are about 10 minutes early. The peak to peak amplitudes of the synthetics are about 1/5 of the observed. This suggests that about an average of 100 cm uplift over the tsunami source area could be required to explain the amplitude of the observed tsunamis.

To investigate the difference between the synthetics and the observed, we compared the vertical crustal deformation computed for various dislocation fault models with the observed displacement inland obtained by Lipman et al. (1985). Figure 3.6, taken from Lipman et al. (1985), shows the elevation changes associated with the earthquake. The maximum displacement occurred at Halape with the subsidence of 3.5 m. The amount of subsidence along the south flank of Kilauea decreases abruptly to the west of Halape and more gradually to the east. Figure 3.7 shows a displacement profile along AA' which passes Halape where the maximum subsidence was observed. The first trough of the displacement profile is associated with the summit of the Kilauea volcano. The steep gradient near A' is located near the Hilina fault system, and is probably related to it. We examine if the tsunamis can be explained by modifying seismic dislocation models obtained by previous studies. We compared the vertical deformations computed for different seismic dislocation models with the observed deformation on land to obtain a dislocation model which can best explain the observed tsunamis. The cross section A'A'' in Figure 3.7 extends the line AA' to the seaward. From the comparison of the amplitudes of the synthetics from Ando's fault model to the observed tsunamis, we showed above that an average displacement of 100 cm offshore is required to explain the observed tsunamis. This average is shown in Figure 3.7.

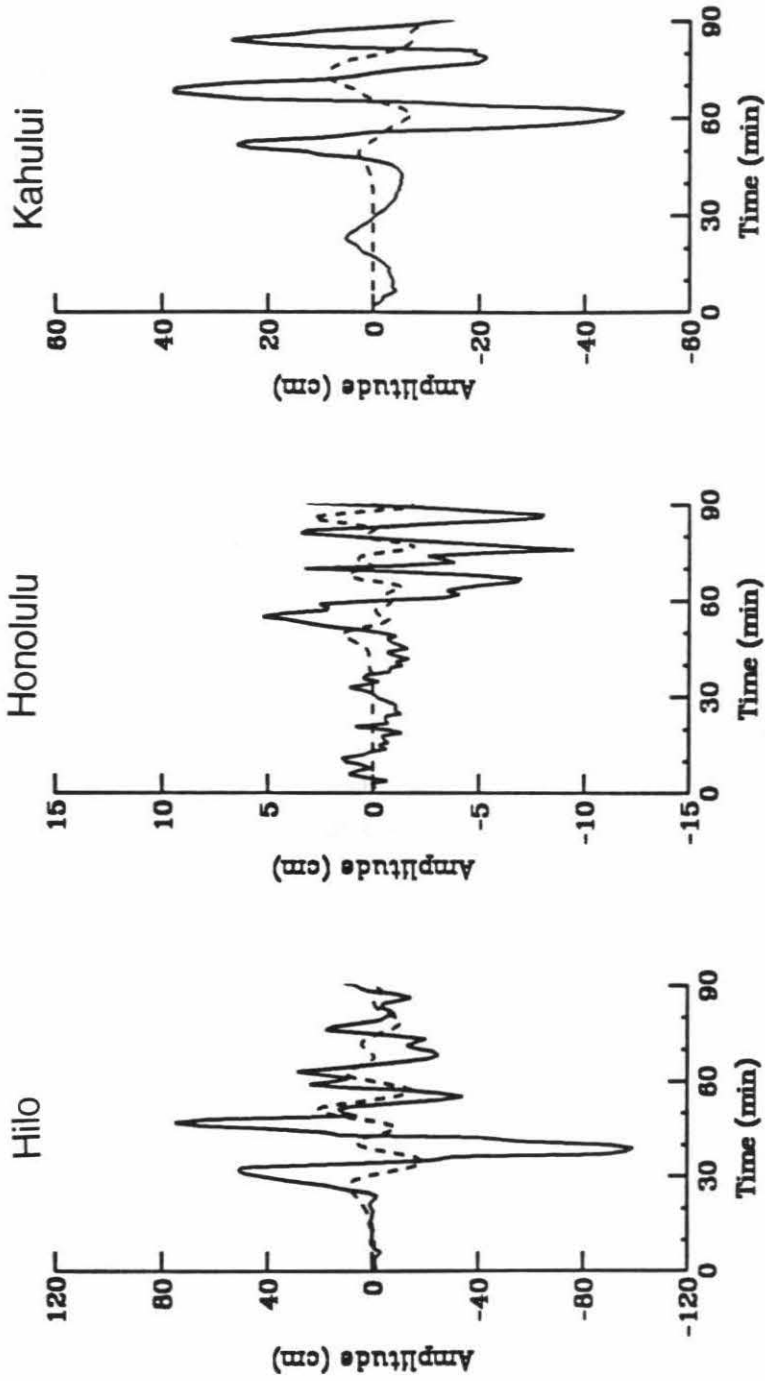
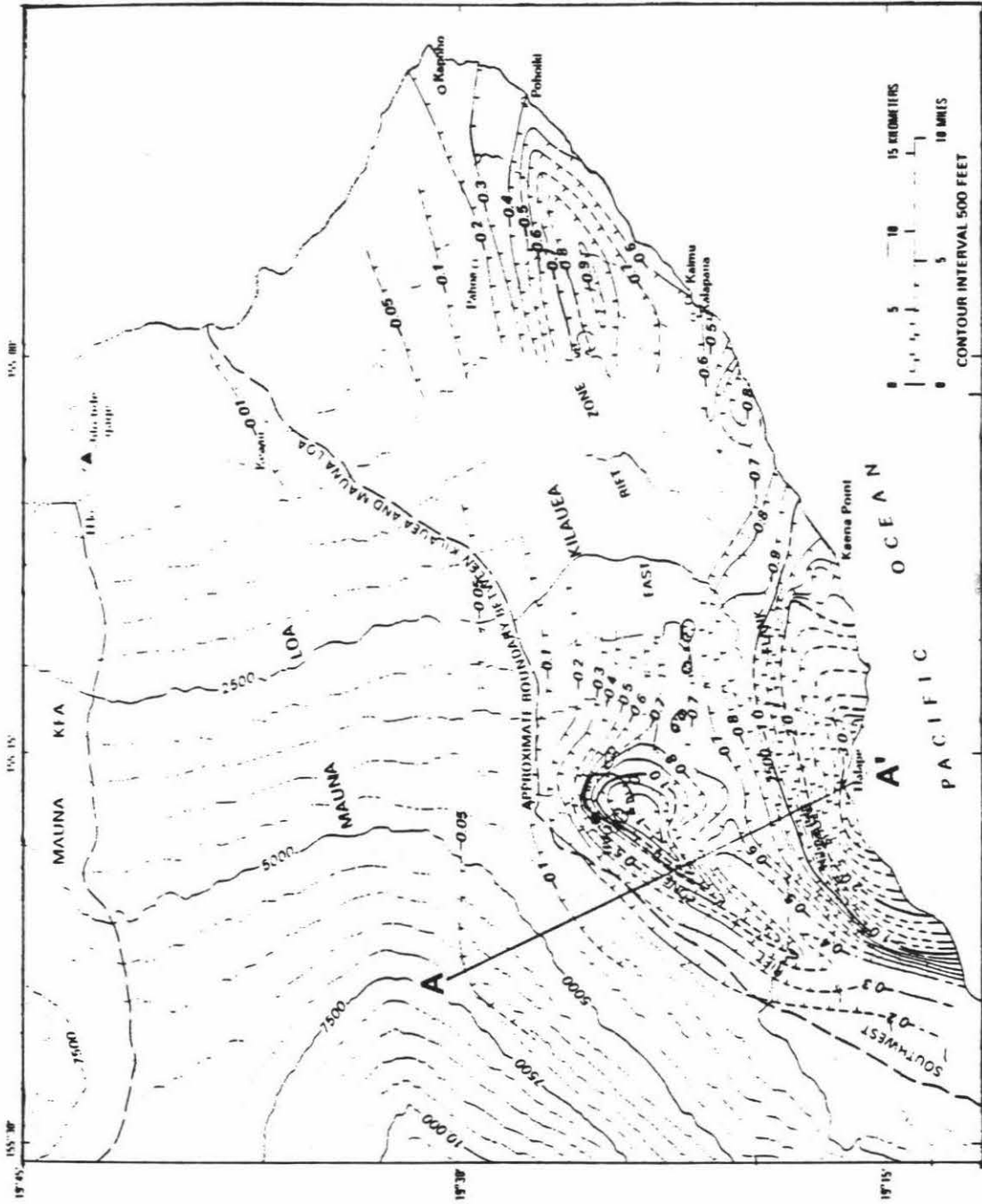


Figure 3.5: The comparison of the synthetic tsunamis (dashed line) computed for Ando's fault model with the observed (solid line).

Figure 3.6: The contour of the leveling data associated with the 1975 Kalapana earthquake (after Lipman et al. 1985) and the cross section line AA'. The contour lines indicate the uplift (positive) and subsidence (negative) in meters.



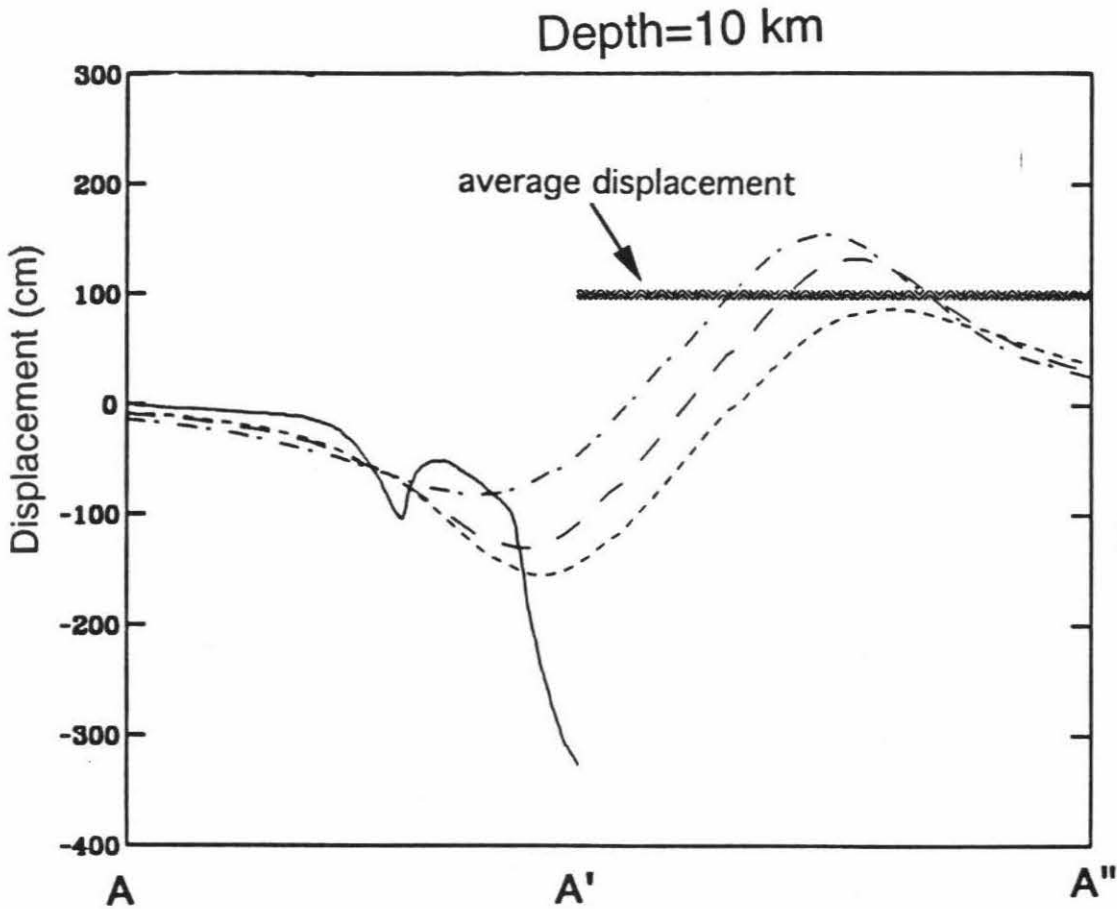


Figure 3.7: The comparison of the three vertical crustal deformations (short dashed, dashed, and dot-dashed line) computed from various fault models with dip directions  $10^{\circ}\text{SE}$ ,  $0^{\circ}$ , and  $10^{\circ}\text{NW}$ , respectively. The upper edge of the fault is at 10 km. The observed leveling data and average displacement offshore required to explain the observed tsunami are shown by solid and shaded line, respectively.

The dip angle of the fault model of the 1975 Kalapana earthquake is not very well determined. Ando (1979) suggested that this event is a normal fault event with dip  $20^{\circ}$ SE, while Furumoto and Kovach (1979) suggested that it is an overthrusting event with dip  $4^{\circ}$ NW. Given this uncertainty, we computed the vertical crustal deformation profile along AA" for fault models with dip angle of  $10^{\circ}$ SE,  $0^{\circ}$ , and  $10^{\circ}$ NW shown in Figure 3.7. The other parameters of the fault models were the same as Ando's model. The amount of subsidence decreases, but the amount of uplift increases as the dip direction changes from SE to NW. The model dipping southeast yields a maximum subsidence of about 150 cm, and maximum uplift of only 80 cm. In contrast, the model dipping northwest yields a maximum subsidence of 80 cm, and a maximum uplift of about 150 cm offshore. Except for the steep gradient inland close to the coast and near the summit of Kilauea volcano, the trend of subsidence profile inland for these fault models is similar to that of the observed deformation. Since the NW dipping fault model produces the largest amount of uplift offshore which is comparable to the required displacement on the sea-floor, we computed the synthetic tsunami for this fault model. Figure 3.8 compares the synthetics for this model to the observed. The synthetics are still too early in arrivals by about 10 min. This model yields larger amplitudes than Ando's fault model. The amplitude of the synthetic is close to that of the observed at Honolulu. However, they are still too small to compare with the observed at the other two stations.

To examine the effect of fault depth to the vertical crustal deformation, we computed the vertical crustal deformation for the upper edge of fault at depths of 3, 5, 7, and 10 km and dip angles of  $10^{\circ}$ SE,  $0^{\circ}$ , and  $10^{\circ}$ NW. Figure 3.9a, 3.9b and 3.9c show the vertical crustal deformation profiles along AA" for these models. The fault models with shallower fault



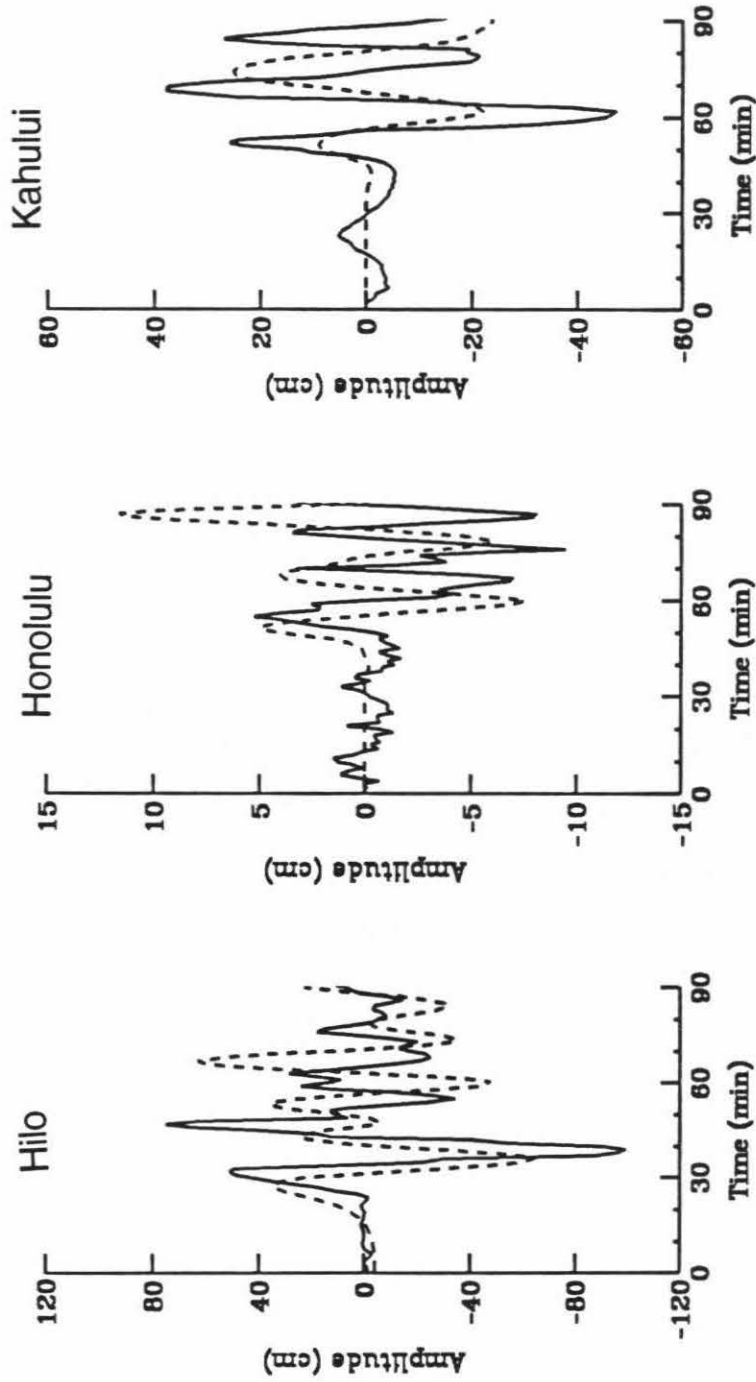
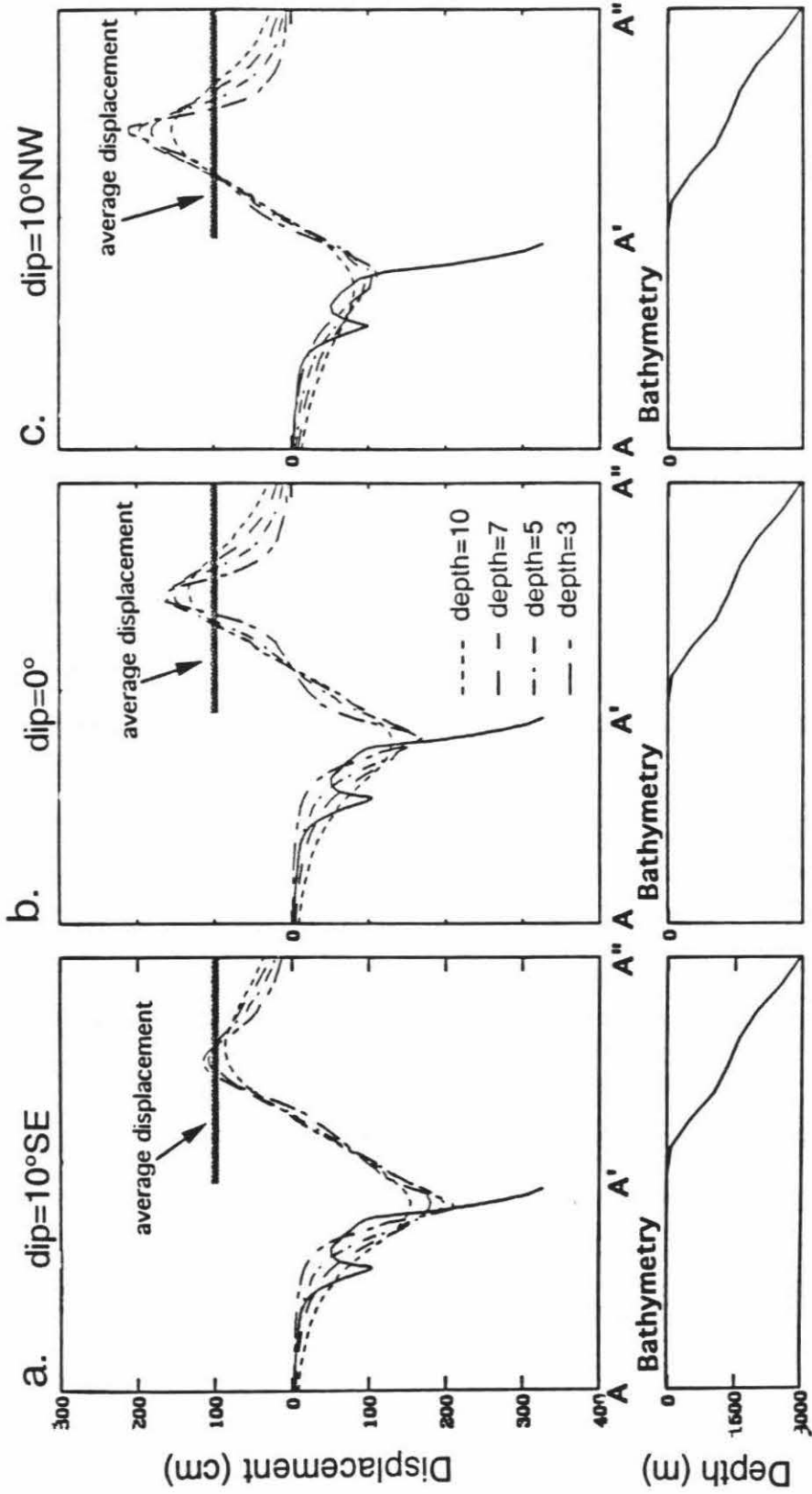


Figure 3.8: The comparison of the synthetic tsunamis (dash line) for a fault model with dip angle of  $10^{\circ}$ NW with the observed (solid line) for Hilo, Honolulu, and Kahului stations, respectively. The upper edge of the fault is at 10 km

Figure 3.9: The comparison of the vertical crustal deformation (dashed lines) for fault models with the upper edge of the fault at depths of 10, 7, 5, and 3 km, respectively, with the observed deformation (solid line) inland and average required uplift (shaded line) offshore. (a), (b), and (c) show the comparisons for fault models with dip angle of  $10^{\circ}\text{SE}$ ,  $0^{\circ}$ , and  $10^{\circ}\text{NW}$ , respectively. The bottom boxes indicate the bathymetry along the profile AA”.



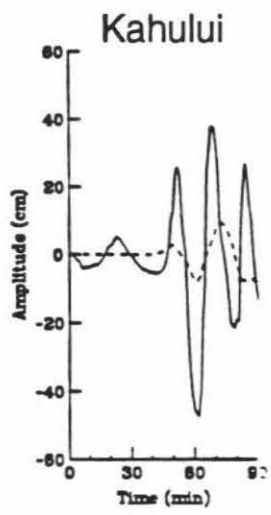
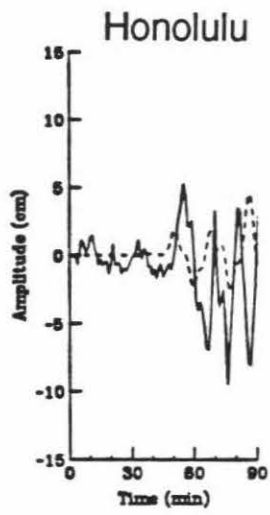
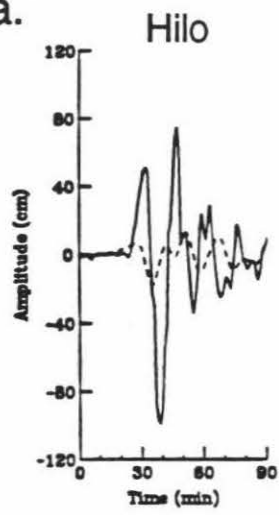
depths yield more rapidly changing patterns of subsidence on land and uplift on sea-floor regardless of the dip angles. The models with the upper edge of the fault at a depth of 3 km show similar displacement pattern inland to the observed, and the amount of the average displacement is more comparable to the estimated required uplift offshore. Figure 3.10a, 3.10b and 3.10c compare the synthetic tsunamis of the three extreme cases with the upper edge of fault at depth of 3 km and dip directions of  $10^{\circ}\text{SE}$ ,  $0^{\circ}$ , and  $10^{\circ}\text{NW}$ , respectively. The amplitude of the synthetics increases as the dip directions changes from southeast to northwest. The synthetics of the fault model with dip of  $10^{\circ}\text{NW}$  and a fault depth of 3 km are similar to those of the fault model with the same dip angle but at 10 km fault depth (Figure 3.8). Comparison of Figure 3.8 and Figure 3.10c, Figure 3.10c indicates later first arrivals of the synthetics. These computations suggest that the fault model with northwest dip direction yields larger amplitudes than that with southeast dip direction. The fault model with a shallower depth produces later first arrivals than deeper fault models. These comparisons indicate that shallow NW dipping model yields the arrivals close to the observation and displacement offshore comparable to the required uplift. Since the strike of the fault does not affect the pattern of the vertical crustal deformation, we did not test the fault models with different strikes.

Previous studies show that the largest dip angle of the fault model dipping NW for the 1975 Kalapana earthquake is  $4^{\circ}\text{NW}$  (Furumoto and Kovach 1979), and shallowest fault depth is 6 km (Wyss and Kovach 1988). Thus, the model (strike= $\text{N}70^{\circ}\text{E}$ , dip= $10^{\circ}\text{NW}$ , rake= $90^{\circ}$ , fault depth=3 km) used to compute the synthetics in Figure 3.10c is beyond the most extreme case. However, the synthetics from this model are still too early in arrivals and too small in amplitudes to compare with the observed tsunamis. This result suggests that the observed tsunamis could not be explained by the seismic dislocation model alone. The

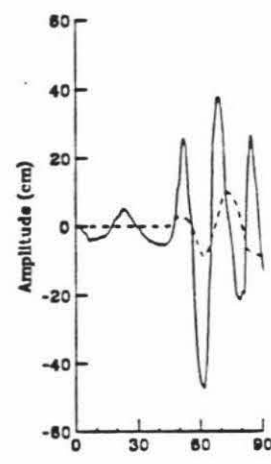
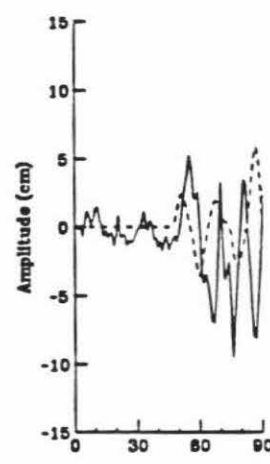
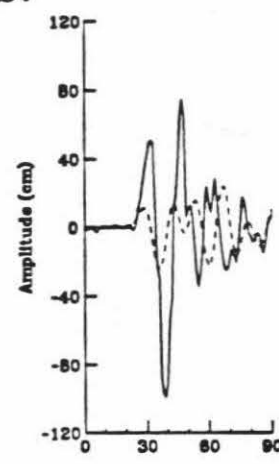
Figure 3.10: The comparison of the synthetic tsunamis (dashed line) computed for fault models with various dip angles and upper edge of the fault at depth of 3 km with the observed (solid line) for Hilo, Honolulu, and Kahului stations, respectively. (a), (b), and (c) show the comparisons for fault models with dip angle of  $10^{\circ}\text{SE}$ ,  $0^{\circ}$ , and  $10^{\circ}\text{NW}$ , respectively.

60

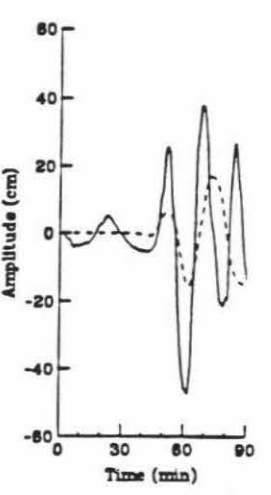
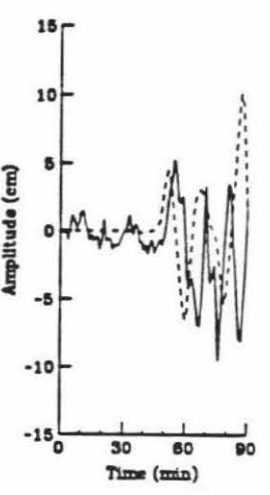
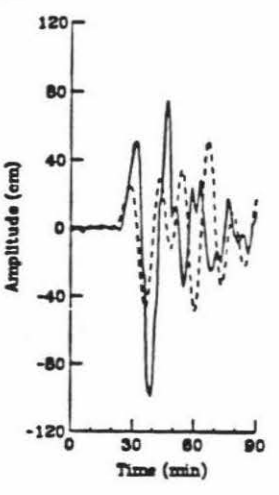
a.



b.



c.



crustal deformations caused by seismic dislocation models have too small uplift offshore. The area responsible for tsunami generation estimated from seismic fault models is too broad, and produces too early first arrivals of the synthetic tsunamis.

### 3.5.2 Hilina Fault Model

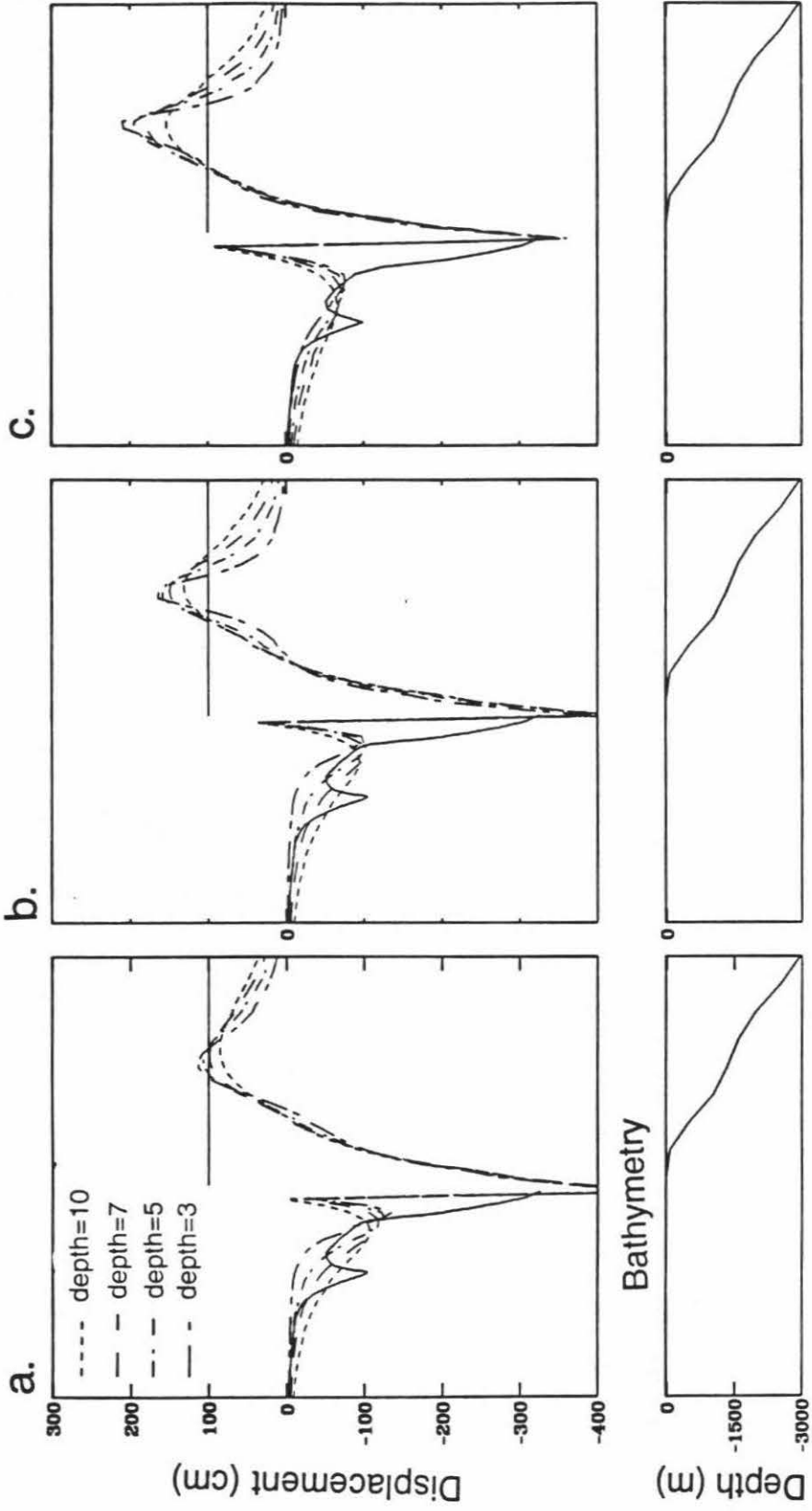
The deformation caused by seismic fault models could explain only the general trend of the observed deformation but not the steep gradient of the deformation inland near the Hilina fault system on the coast. We computed the crustal deformation caused by the Hilina fault and compared it with the observed to see whether the slip on the Hilina fault system can explain the observed steep gradient.

The Hilina Fault system is characterized by south-facing normal fault scarps as high as 500 m. The new faulting occurred during the earthquake extending about 25 km along the trend of the Hilina fault system, and individual faults have vertical displacement of as much as 1.5 m (Lipman et al. 1985).

The trace of the Hilina fault is very well defined. The Hilina fault zone is about 40 km long and 5 km wide, and has a strike of about  $60^{\circ}\text{NE}$  and a dip of about  $60^{\circ}\text{--}80^{\circ}\text{SE}$ . The depth of the fault is known to be very shallow. We first tested the Hilina fault model with faulting reaching the surface. Figure 3.11a, 3.11b, and 3.11c compared the combined deformation from the Hilina fault model and dislocation models (Figure 3.9a, 3.9b, and 3.9c) with the observed along AA". The displacement on the Hilina fault explain the steep slope of deformation profile inland near the coast. However, there is an obvious discontinuity of the displacement inland close to the coast. We tested Hilina fault models with various fault depths. As we increase the depth of the upper edge of the fault, the

Figure 3.11: The comparison of the combined vertical ground deformations (dashed lines) from the dislocation fault models with fault depths of 10, 7, 5, and 3 km and Hilina fault model with faulting through the surface with the observed deformation inland and required uplift offshore (solid line) along the profile AA". (a), (b), and (c) show the comparisons for fault models with dip angle of  $10^{\circ}\text{SE}$ ,  $0^{\circ}$ , and  $10^{\circ}\text{NW}$ , respectively. The bottom boxes indicate the bathymetry profile along AA".

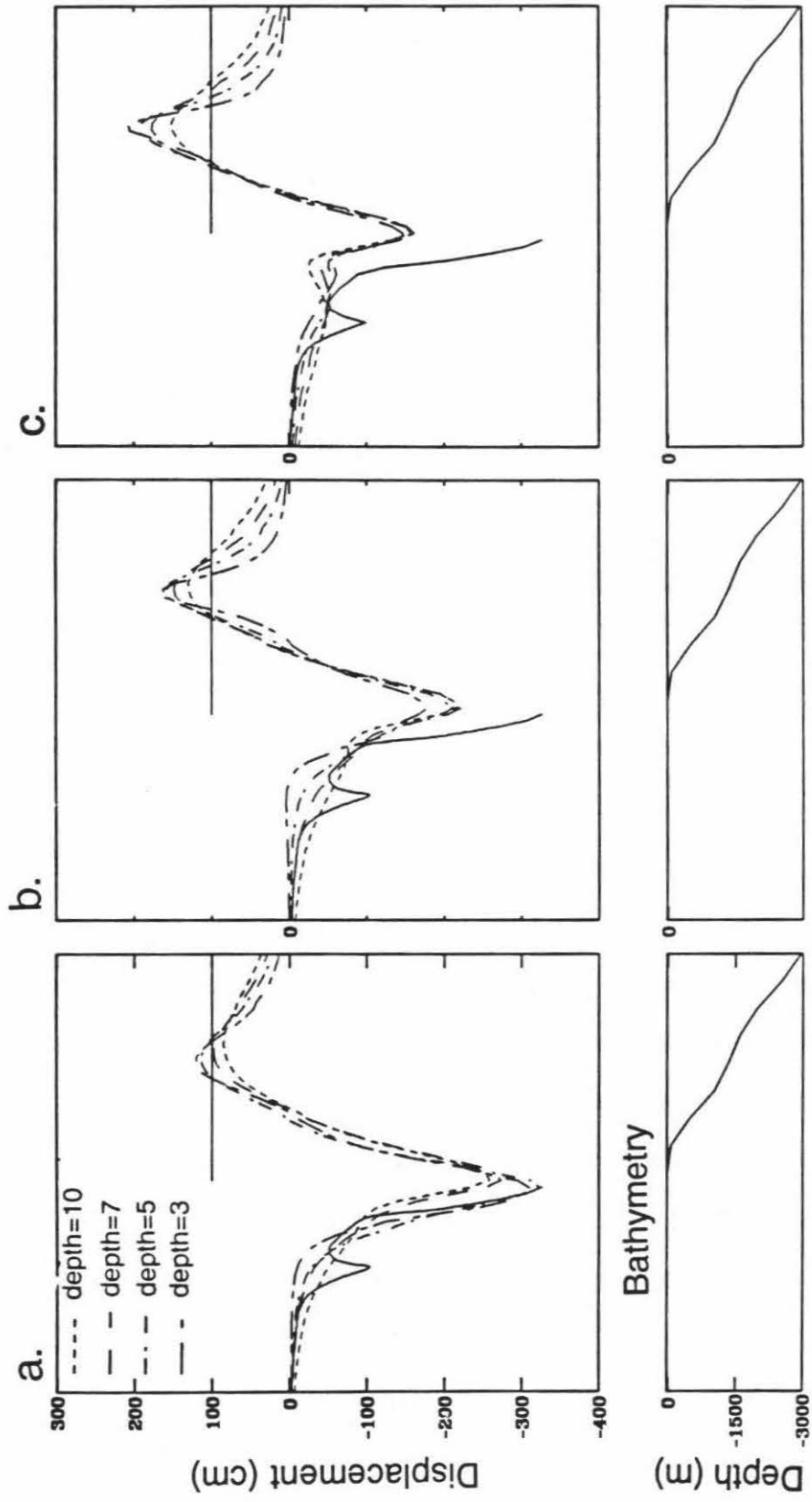




displacement caused by the Hilina fault model becomes smoother. Figure 3.12a, 3.12b, and 3.12c compared the combined deformation for the Hilina fault model with the upper edge of fault at a depth of 3.5 km and dislocation models (Figure 3.9a, 3.9b, and 3.9c) with the observed along AA". The maximum subsidence of the combined deformations decreases as the dip direction of the dislocation models changes from southeast to northwest. The combination of the displacement shown in Figure 3.12a can explain the steep gradient change of the observed data inland fairly well regardless of the depths of seismic dislocation models. They show about the right gradient of deformation and reach the observed maximum subsidence of about 300 m at the coast, while Figure 3.12b and 3.12c show more gentle gradients of deformation and smaller amount of subsidence on the coast compared with the observed. This suggests that the ground deformation inland associated with the 1975 Kalapana earthquake was caused by the combination of the dislocation model with dip  $10^{\circ}$ SE in the south flank of the Kilauea and Hilina fault model with the upper edge of the fault at a depth of 3.5 km. The displacement more inland is associated with the deformation near the summit of Kilauea volcano. Since it is difficult to distinguish the deformation from previous eruptions and by this earthquake, we did not attempt to match the deformation near the summit area.

The seismic dislocation model in the rift zone with strike of  $70^{\circ}$ NE, dip of  $10^{\circ}$ SE, rake of  $-90^{\circ}$  and slip of 5.5 m with the upper edge of the fault at a depth of 3–10 km combined with the Hilina fault model with strike of  $60^{\circ}$ NE, dip of  $70^{\circ}$ SE, rake of  $-90^{\circ}$  and slip of 5.5 m with the upper edge of the fault at a depth of 3.5 km can explain the observed displacement inland generally well. The depth of the seismic fault is difficult to determine from the crustal deformation data. In the following analysis we used the fault model with the upper edge of the fault at 3 km, since it produces the largest amount of uplift offshore,

Figure 3.12: The comparison of the combined vertical ground deformations (dashed lines) from the dislocation fault models with fault depths of 10, 7, 5, and 3 km and the Hilina fault model with the upper edge of the fault at a depth of 3.5 km with the observed deformation inland and required uplift offshore (solid line) along the profile AA". (a), (b), and (c) show the comparisons for fault models with dip angle of 10°SE, 0°, and 10°NW, respectively. The bottom boxes indicate the bathymetry profile along AA".



and the largest tsunamis compared with the models with larger depths. This model is used as the extreme dislocation model that excites tsunamis most efficiently.

Figure 3.13 compares the tsunamis excited only by the slip on the Hilina fault with the observed. The contribution of the Hilina fault to tsunami excitation is very little. They show a downward first motion at Hilo station. Figure 3.14 compares the tsunamis computed for the combination of the extreme dislocation model and the Hilina fault model with the observed. Although the combination of the extreme dislocation model and the Hilina fault model can explain the observed ground displacement on land, the synthetic tsunamis for this model are still too early in arrivals and too small in amplitudes.

Lipman et al. (1985) showed that the extensional ground deformation related to the 1975 earthquake and associated normal faults was as much as 3.5 m vertically and 8 m horizontally on land. The maximum horizontal displacement occurred in the same area of south flank as the maximum subsidence (Figure 3.6 and 3.15). Combining these observations with the asymmetry of the deformation, the gradient of subsidence along the south flank of Kilauea which decreases more rapidly to the west of Halape than to the east, they suggested that the initial earthquake triggered a sequence of deformation that migrated westward along the Hilina fault system. The ratio of horizontal to vertical displacement associated with the 1975 Kalapana earthquake suggests a gravitational slump or blockglide interpretation. Lipman et al. (1985) also observed some new ground breakages in the Hilina fault system which were as much as 1 m along the southwestern but minimal along the eastern part of the Hilina fault system; none was found near the epicenter. Widening of many cracks occurred within the Hilina fault system, which indicated significant horizontal extension. The patterns of ground breakage along the Hilina fault system and the leveling contours showing the maximum gradients of subsidence in the same area also offer

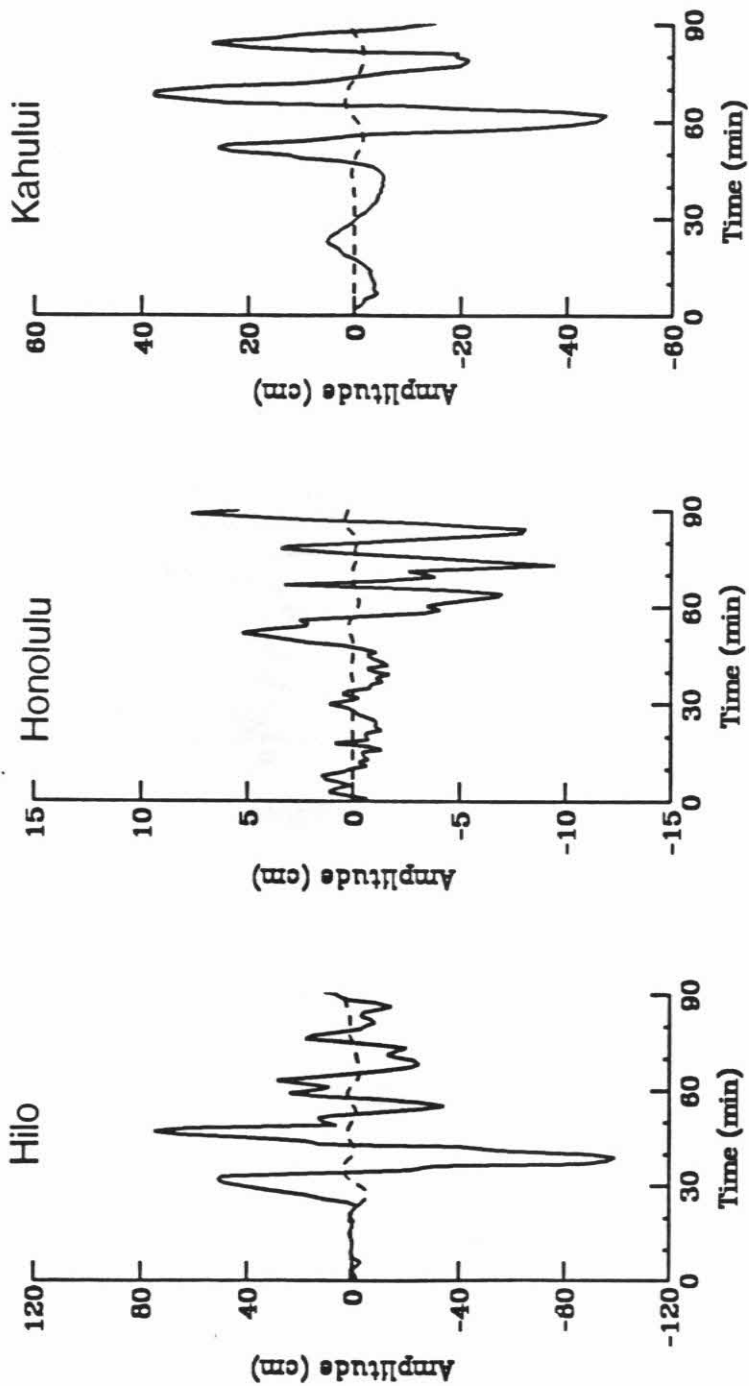


Figure 3.13: The comparison of the synthetic tsunamis (dashed line) for Hilo, Honolulu, and Kahului, respectively, at depth of 3.5 km with the observed (solid line) for Hilo, Honolulu, and Kahului, respectively.

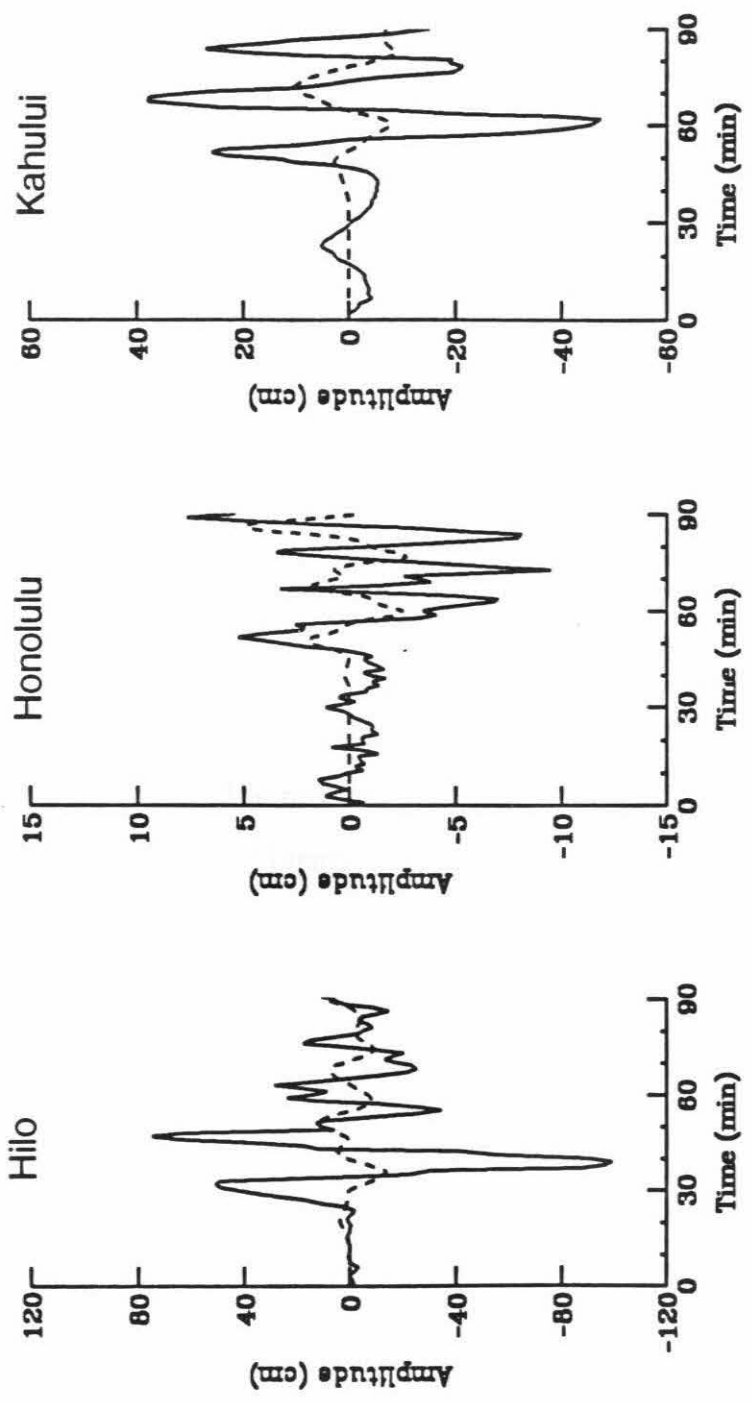
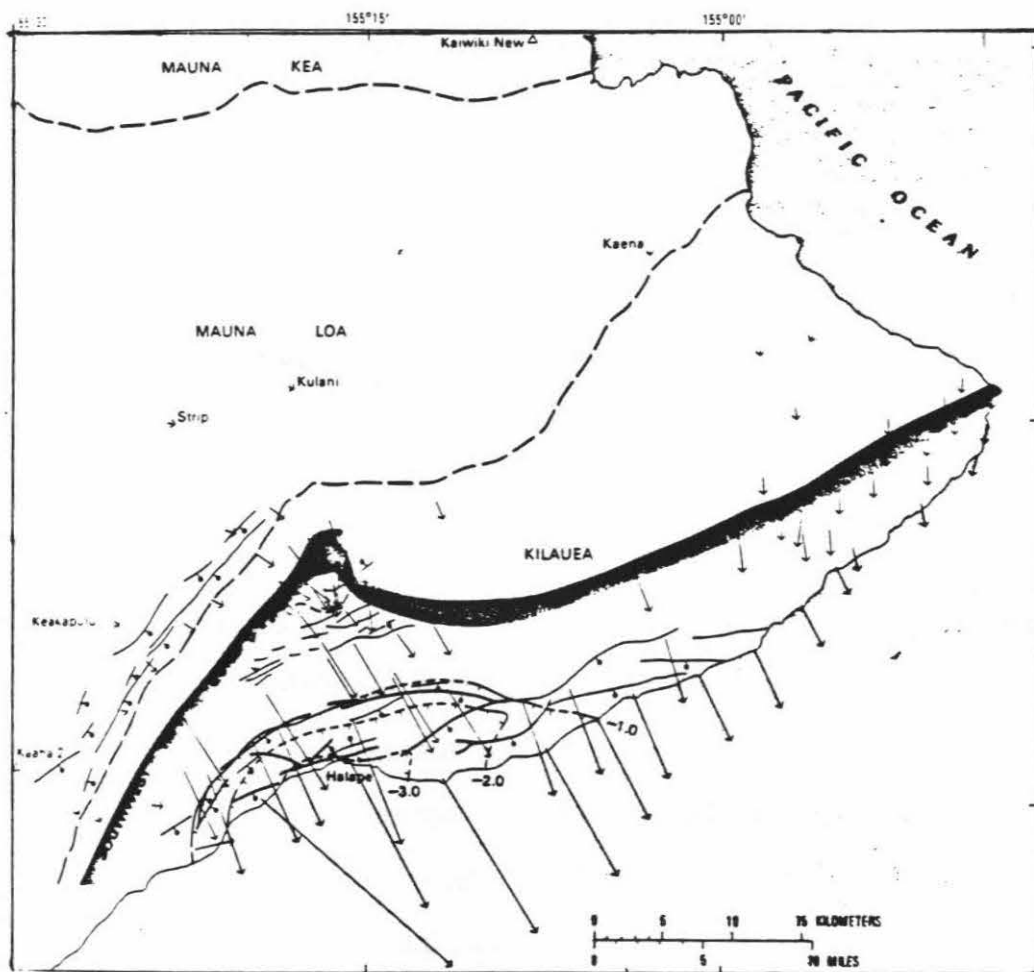


Figure 3.14: The comparison of the combined synthetic tsunamis (dash line) computed from dislocation fault model (dip=10°SE, and depth=3 km) and Hilina fault model (depth=3.5 km) with the observed tsunamis (solid line) for Hilo, Honolulu, and Kahului stations, respectively.

Figure 3.15: The observed horizontal displacement associated with the 1975 Kalapana earthquake (after Lipman et al. 1985).



## HORIZONTAL DISPLACEMENTS

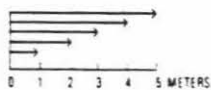


## EXPLANATION

— FAULT 0.5-1.5m OF 1975 OFFSET—Bar and ball on downthrown side

— OTHER MAJOR FAULTS—Bar and ball on downthrown side

— -2.0 — SUBSIDENCE CONTOURS IN METERS 1974-1976 — Machures show direction of increasing subsidence



convincing evidence that much of the earthquake-related deformation involved seaward gravitational slumping or block sliding.

### 3.5.3 Slump Model

To investigate the mechanism responsible for tsunami excitation, we subtracted the synthetic tsunami computed for the combination of the extreme dislocation model and the Hilina fault model from the observed. We call the difference the residual tsunami. Figure 3.16 compared the residual tsunamis with the observed. The residual tsunamis are not very different from the observed. This means that the tectonic deformation associated with seismic faulting and the Hilina fault contributes little to the observed tsunamis; some other mechanism must be responsible for tsunami generation. The residual tsunamis show very small downward motion in the very beginning which is about 10 minutes earlier than the distinct upward motion of the observed tsunami at Hilo station. The downward motions are very small compared with the distinct upward motions and are almost in the noise level, especially for Honolulu and Kahului stations. The small downward motions in the beginning of the residual tsunamis are probably related to the subsidence along the coast. The large upward motions are associated with the uplift of the sea floor. We assume that this uplift is due to slumping on the south flank of Kilauea volcano. Hereafter we call the models that involve an uplift of the sea floor, slump models. In slump model computations, we try to estimate the source area responsible for the residual tsunamis and the amount of uplift. We considered three different slump models.

Since the first downward motions of the residual tsunamis are almost in the background noise level, in slumping model I, we ignored the subsidence along the coast and considered

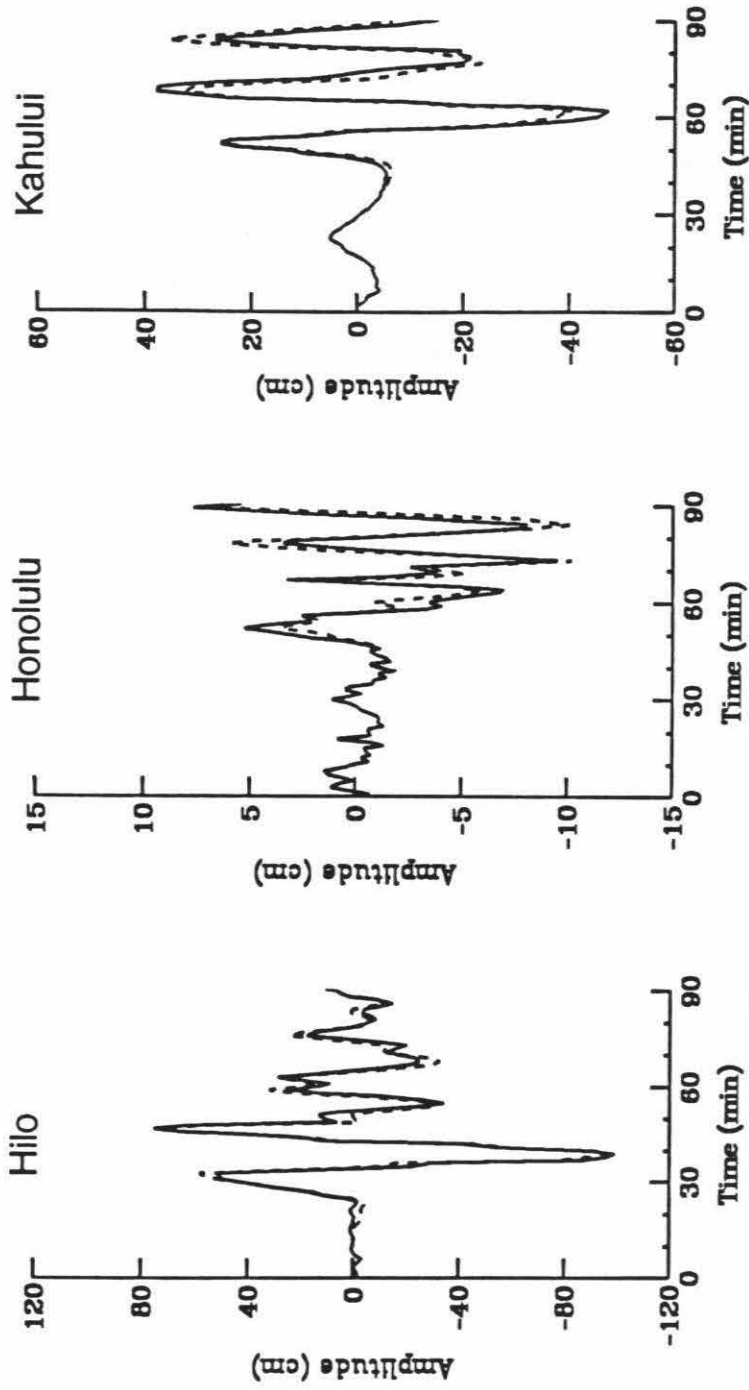


Figure 3.16: The comparison of the residual tsunamis, observed-combined tsunamis, (dash line) with the observed (solid line) for Hilo, Honolulu, and Kahului stations, respectively.

only the uplift due to slumping over the sea-floor. We assumed that the slumping occurred simultaneously with the generation of the distinct large upward motion of tsunamis. According to the inverse travel-time isochron diagram in Figure 3.4, the source area responsible for the slumping could be estimated from the area surrounded by the three onset time isochrons, which correspond to the first distinct upward motions at the three tide-gauge stations. The slumping area for this model is shown in Figure 3.17. The dimension of this area is 9'x9'. Figure 3.18 compares the computed tsunamis with an uplift of 100 cm over the source area with the residual tsunamis. The synthetics could explain the arrival time of the first large upward motion of the residual tsunamis, but the amplitudes and periods of the synthetics are in general too small compared with those of the residual tsunamis.

In slumping model II, we considered a propagating slumping source. We divided the source area into 12 blocks. Each block has an area of 9'x9'. We computed synthetic tsunamis with 100 cm subsidence along the coast and a 100 cm propagating uplift over the sea-floor. The amount of subsidence was taken from the average subsidence along the coast. We estimated the time lag for each block of the propagating uplift from the inverse travel time isochrons of the three tide-gauge stations. Figure 3.17 shows the area and time lag on each block for the propagating slumping model. Figure 3.19 compares the synthetics to the observed. The synthetics could not explain the small downward motions in the beginning of the residual tsunamis, even though we already included the subsidence along the coast. Again, since the small downward motions are in the noise level, they are difficult to model. The downward motion in the very beginning of Hilo station is probably associated with some small amount of subsidence on the eastern end of the island. If we ignore the small downward motions in the beginning of the residual tsunamis and

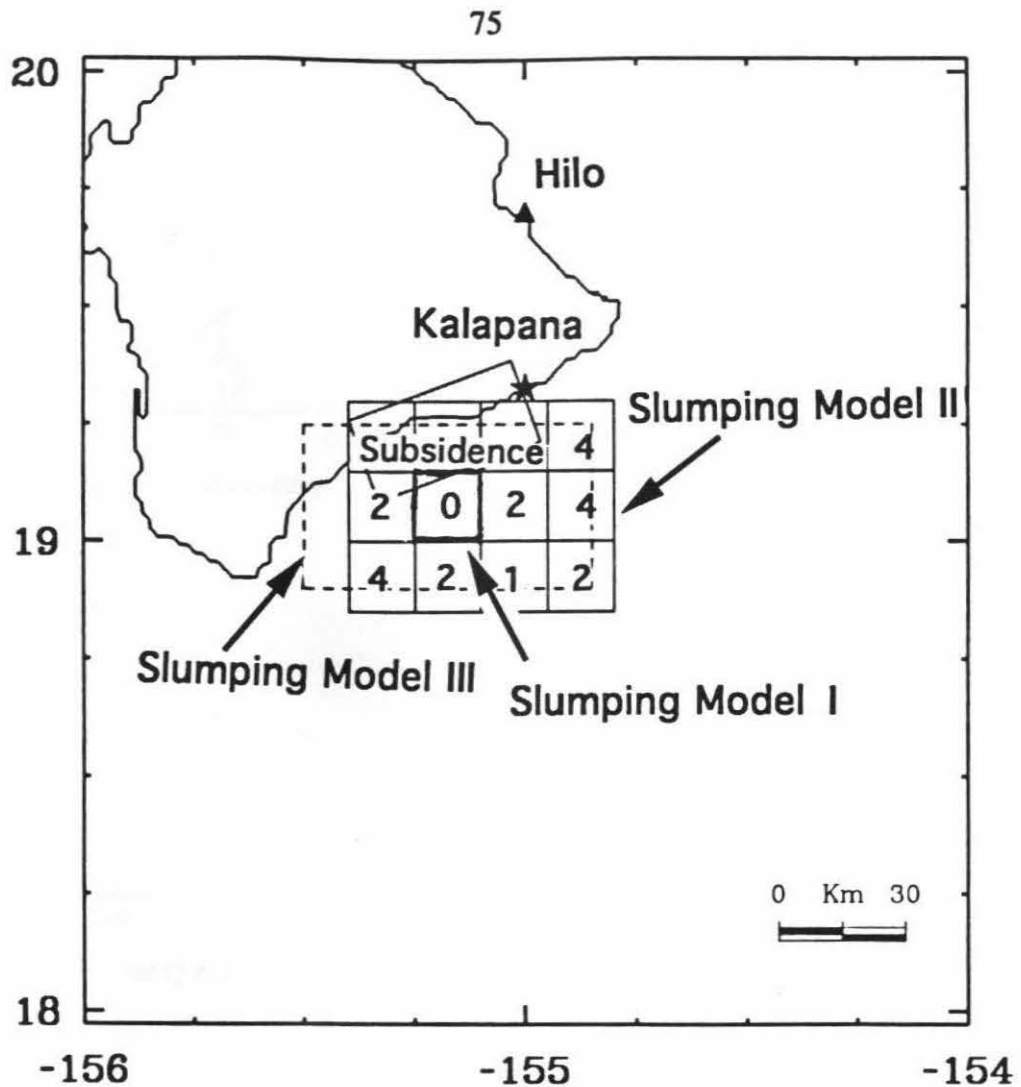


Figure 3.17: The area for the tsunami computation of the three slumping models. The small box in bold solid line indicates the slumping area of slumping model I. The big box in solid line indicates the slumping area for slumping model II. The numbers on each block for slumping model II represent the time lag of the propagating uplift of the slumping at each block. The box in dash line indicates the area for slumping model III.

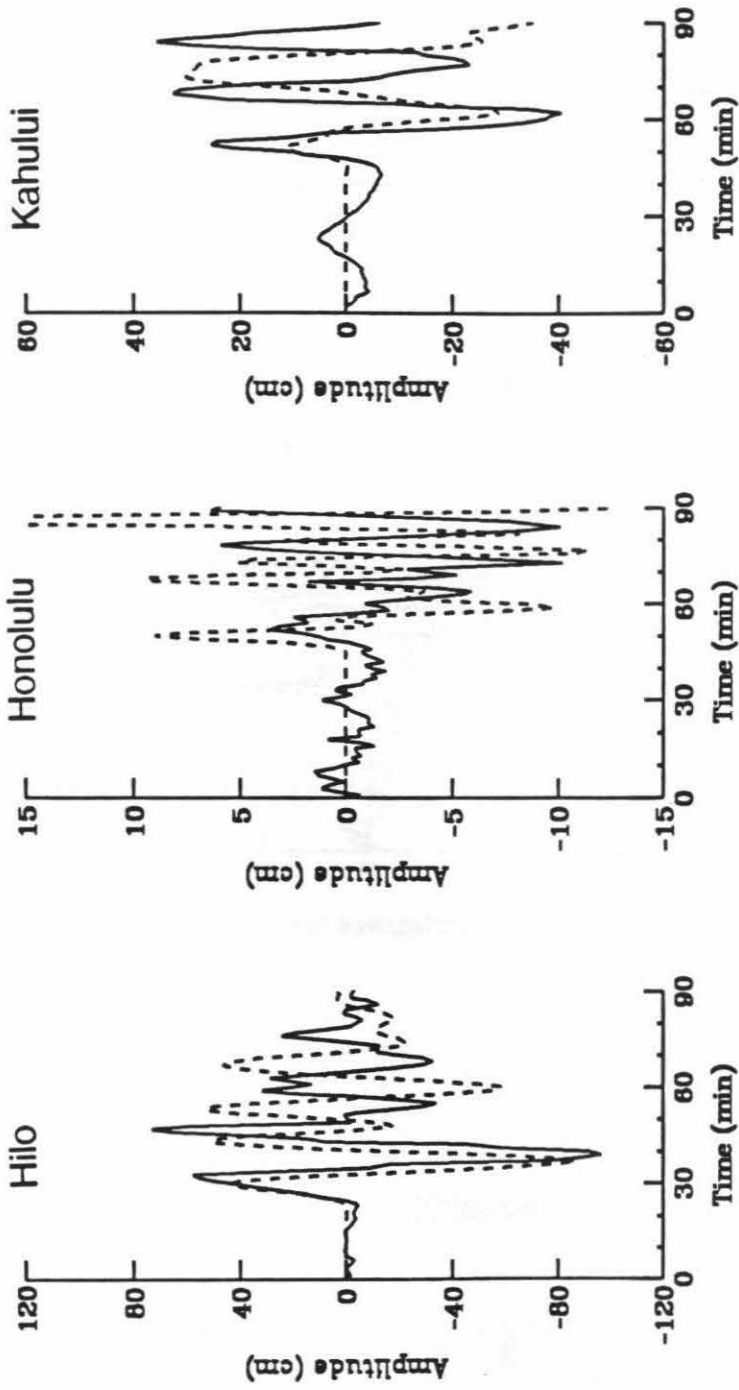


Figure 3.18: The comparison of the synthetic tsunamis (dashed line) for slumping model I with the residual tsunamis (solid line) for Hilo, Honolulu, and Kahului stations, respectively.

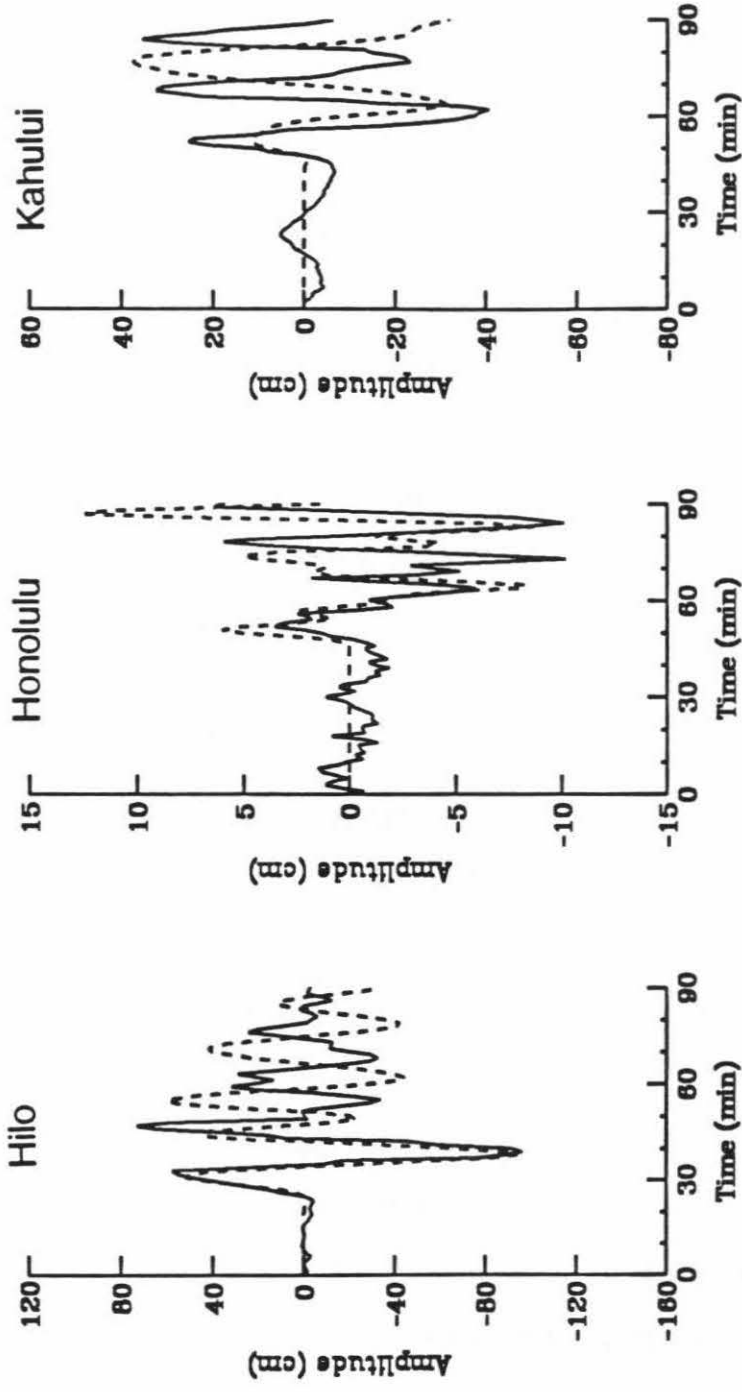


Figure 3.19: The comparison of the synthetic tsunami (dashed line) for slumping model II with the residual tsunami (solid line) for Hilo, Honolulu, and Kahului stations, respectively.

consider only the first cycle of the records, this propagating slumping model could explain the arrival times of the distinct upward motions, amplitudes and periods of the residual tsunamis generally well. From the uplifted area of the slumping model, we estimated that the volume of displaced water is about  $2.5 \text{ km}^3$ .

In slumping model III, the slumping was modeled by a sudden subsidence along the coast followed by simultaneous uplift over the offshore area with 4 min. duration. The source area for slumping model III is shown in Figure 3.17. The boundary of the area was based primarily on the tangents of the isochrons which are 4 min. earlier than the onset time isochrons of the three tide-gauge stations. We computed synthetic tsunamis by putting a unit amount of uplift in the source area. From the comparison of the amplitudes of synthetics to the observed tsunamis, the amount of uplift required to explain the observed tsunami at each station was determined. The amounts of uplift required for Hilo, Honolulu, and Kahului tide-gauge stations for this source region are 97 cm, 60 cm, and 180 cm, respectively.

Figure 3.20 compares the synthetics for the three tide-gauge stations to the residuals tsunami. If we only consider the first cycle of the tide-gauge records, the synthetics could explain the first arrivals, amplitudes, and the period of the residual tsunamis. The period of the synthetic tsunami for Kahului station is too long. The reason for that is still unknown. The uplift required for Kahului station is relatively large compared with that of Hilo and Honolulu stations. Because Honolulu and Kahului are far away from the source area, the observed tsunamis are considered to be more contaminated by the reflections from the coast. The results from the two stations are less reliable. If we take the average uplift obtained from the three stations, the uplift required over the sea floor is about 110 cm.



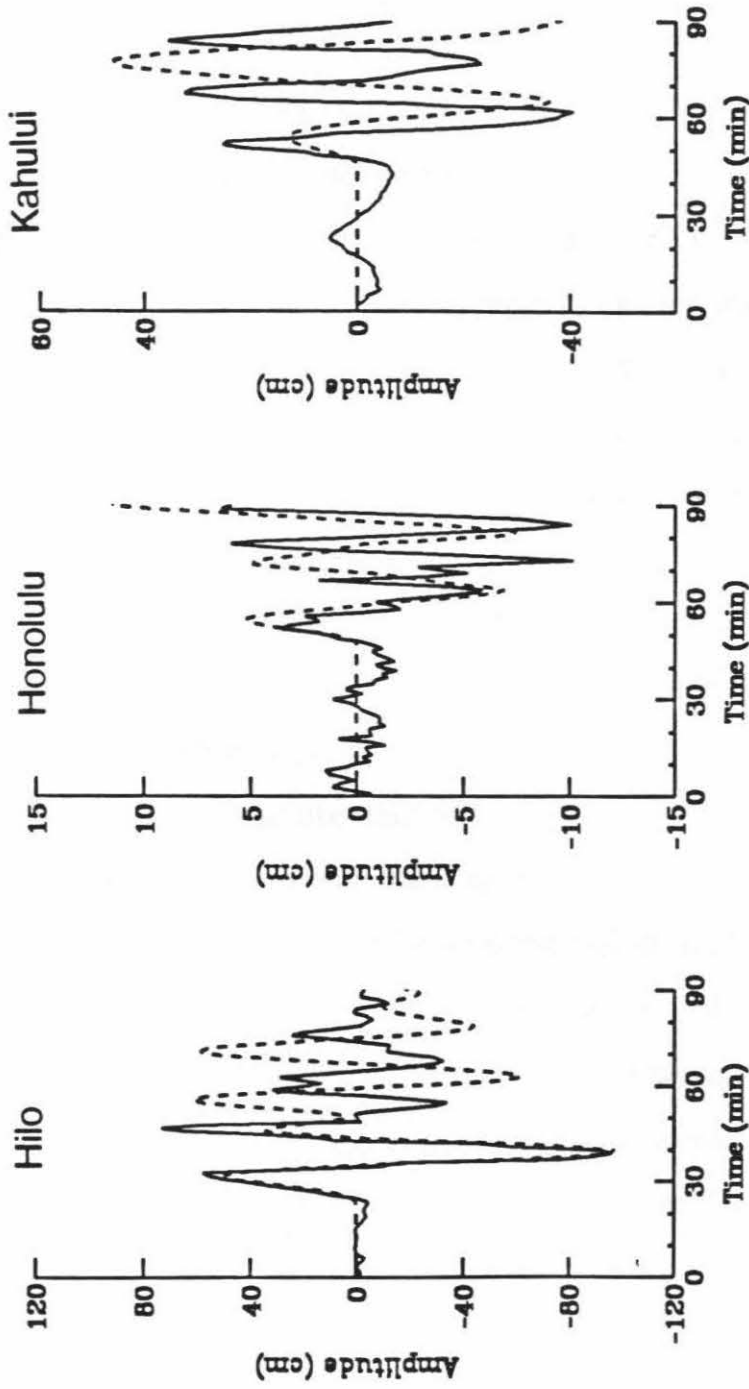


Figure 3.20: The comparison of the synthetic tsunamis (dashed line) for slumping model III with the residual tsunamis (solid line) for Hilo, Honolulu, and Kahului stations, respectively.

Thus, slump model III is required to have an average uplift of 110 cm over an area of about 3000 km<sup>2</sup> of sea floor. The volume of displaced water is about 3 km<sup>3</sup>. Hatori (1976) estimated that 1 m of uplift over an area of 2200 km<sup>2</sup> of sea floor is required to explain the tsunamis caused by the Kalapana earthquake. Lipman et al. (1985) measured the observed subsidence and seaward displacement associated with the 1975 Kalapana earthquake. The total volume of the deformation is 2 km<sup>3</sup>. The volume we obtained from the slumping model is comparable to these estimates by the previous studies.

We now compare the present result with the single force model of Eissler and Kanamori (1987). However, since the single force model was obtained from seismic radiation, it cannot be directly compared with the present result. We make a qualitative comparison in the following.

The single force is kinematic representation of southeastward slumping of a large block on the south flank of Kilauea. The northern half of this block is onland and the southern half is offshore (Figure 12 of Eissler and Kanamori 1987). Seaward sliding of the offshore part of this wedge-like structure would uplift the sea-floor over a large area. The pattern of uplift is consistent with that determined from tsunami data. Since the magnitude of the single force depends on the total mass of the sliding block, while tsunami excitation depends only on the area and the amount of uplift, no direct comparison can be made between the magnitude of the single force and tsunami excitation.

The overall size of the landslide can be presented as  $M \cdot D$  using centroid single force (CSF) model (Kawakatsu, 1989), where  $M$  and  $D$  are total mass of the landslide and sliding distance. If we assume a time function of the force to be a simple one-cycle sine wave with half-period  $\tau$ ,

$$f_0 s(t) = \begin{cases} f_0 \sin(\pi t / \tau) & 0 \leq t \leq 2\tau \\ 0 & t > 2\tau \end{cases}, \quad (4)$$

where  $f_0$  is the peak force, the overall size of the landslide can be written as

$$M \cdot D = \rho \cdot V \cdot D = f_0 \int_0^{2\tau} \left[ \int_0^t s(\tau) d\tau \right] dt = f_0 \int_0^{2\tau} \left[ \int_0^t \sin\left(\frac{\pi\tau}{\tau}\right) d\tau \right] dt = \frac{2f_0\tau^2}{\pi}, \quad (5)$$

where  $\rho$  and  $V$  are the density and total volume of the landslide. Eissler and Kanamori (1987) estimated  $f_0$  to be about  $1 \times 10^{15}$  N from long-period surface wave data. Then, they estimated  $D$  to be 80 to 2600 m for ranges of  $M$  and  $\tau$  from  $10^{15}$  to  $10^{16}$  kg and 50 to 90 sec, respectively. Kawakatsu (1989), using more data than Eissler and Kanamori (1987) and an inversion method, estimated  $D$  to be 37 to 370 m. Since the observed subaerial horizontal displacement increased from 1 m near the summit of Kilauea to 8 m at the coast, the above value of  $D$  suggests that the displacement continued to increase undersea as the slide block deteriorated into a massive sediment slump. How much vertical displacement is caused by this horizontal displacement depends on the details of slide geometry. If the slide is a simple wedge with a triangular shape with a slope  $\alpha$  the vertical displacement  $H$  is given by  $D \cdot \tan\alpha$ . Eissler and Kanamori's (1987) gravity slide model suggests  $\alpha = 5^\circ$ . However this slope results in  $H = 3$  to 227 m which is too large compared with the uplift estimated from tsunami data. If the average slope of offshore slump decreases,  $H$  can be reduced accordingly. Although large uncertainties are involved in the determination of  $f_0$  and  $\tau$  and the total volume and geometry of the slide mass are not known well, the above comparison appears to indicate that the magnitude of the single force is too large to be

consistent with the observed tsunami. Kawakatsu (1989) concluded that neither a double-couple nor single force model can explain the data completely satisfactorily, and suggested a combination of them. If part of the seismic radiation is due to faulting, then the magnitude of the single force can be reduced, and the resulting uplift can be made consistent with that estimated from tsunami data. However, this problem remains unresolved at present.

### 3.6 Conclusions

The synthetic tsunamis computed for Ando's dislocation model are too early in the first arrivals and too small in amplitudes. We tested various seismic fault models with different dip directions and fault depths, but none of them could explain the observed tsunamis. Since the crustal deformation caused by the dislocation models can explain only the general trend of the observed geodetic data but not the steep gradient inland near the coast observed by Lipman et al. (1985), we considered a Hilina fault model, in addition to the dislocation model from seismic data, to see whether slip on the Hilina fault can explain the observed displacement. The deformation from the combination of the seismic dislocation model with a strike of  $70^{\circ}\text{NE}$ , dip of  $10^{\circ}\text{SE}$ , rake of  $-90^{\circ}$  and slip of 5.5 m at a depth of 3~10 km and the Hilina fault model with a strike of  $60^{\circ}\text{NE}$ , dip of  $70^{\circ}\text{SE}$ , rake of  $-90^{\circ}$  and also slip of 5.5 m at depth of 3.5 km can explain the leveling data inland fairly well. However, the tsunamis computed for this composite fault model still cannot explain the arrival times and amplitudes of the observed tsunamis. This suggests that another mechanism is required to explain the observed tsunamis. The residual waveform, observed minus computed tsunamis for the composite fault model, is not very different from the observed tsunamis. We tested several different slump models to explain the residual tsunamis. We find that a

propagating slump model can explain the arrival times and amplitudes of the residual tsunamis very well. The total time duration for the propagating slump is about 4 minutes. The slump model has an average uplift of 110 cm over an area of about 3000 km<sup>2</sup>.

The result is consistent with the interpretation that the 1975 Kalapana earthquake was caused by large-scale slumping due to gravitational instability of the south flank of Kilauea volcano. However, whether this result is quantitatively consistent with the single force model determined from seismic data or not remains unresolved.

## References of Part I

- Aida, I., Numerical experiments for the tsunami propagation - the 1964 Niigata tsunami and the 1968 Tokachi-Oki tsunami, *Bull. Earthquake Res. Inst.*, **47**, 673-700, 1969.
- Aida, I., Reliability of a tsunami source model derived from fault parameters, *J. Phys. Earth*, **26**, 57-73, 1978.
- Ando, M., The Hawaii earthquake of November 29, 1975: Low dip angle faulting due to forceful injection of magma, *J. Geophys. Res.*, **84**, 7616-7626, 1979.
- Bryan C. J. and C. E. Johnson, Block Tectonics of the island of Hawaii from a focal mechanism analysis of basal slip, *Bull. Seismol. Soc. Am.*, **81**, 491-507, 1991.
- Comer, R. P., The tsunami mode of a flat earth and its excitation by earthquake sources, *Geophys. J. R. astr. Soc.*, **77**, p.1-27, 1984
- Cox, D. C., Source of the tsunami associated with the Kalapana (Hawaii) earthquake of November 1975, *Hawaii Inst. of Geophys.*, Univ. of Hawaii, Honolulu, Rep. **80-8**, 46 pp., 1980.
- Crosson, R. S. and E. T. Endo, Focal mechanisms of earthquakes related to the 29 November 1975 Kalapana, Hawaii, earthquake: The effect of structure models, *Bull. Seismol. Soc. Am.*, **71**, 713-729, 1981.
- Crosson, R. S. and E. T. Endo, Focal mechanisms and locations of earthquakes in the vicinity of the 1975 Kalapana earthquake aftershock zone 1970-1979: Implications for the tectonics of the south flank of Kilauea volcano, Hawaii, *Tectonics*, **1**, 495-542, 1982.
- Eissler, H. K. and H. Kanamori, A single-force model for the 1975 Kalapana, Hawaii, earthquake, *J. Geophys. Res.*, **92**, 4827-4836, 1987.

- Furumoto, A. S., and R. L. Kovach, The Kalapana earthquake of November 29, 1975: An intra-plate earthquake and its relation to geothermal processes, *Phys. Earth Planet. Inter.*, **18**, 197-208, 1979.
- Hatori, T., Wave source of the Hawaii tsunamis in 1975 and the tsunami behavior in Japan (in Japanese), *Zisin*, **2(29)**, 355-363, 1976.
- Houston, J. R., Interaction of tsunamis with the Hawaiian Islands calculated by a finite-element numerical model, *J. Phys. Ocean.*, p. 93-102, 1978.
- Hwang, L.-S., D. Divoky, and A. Yuen, Amchitka tsunami study, *Tetra Tech. Inc.*, Pasadena, Calif. Rep. TC-177, 84 p., 1970.
- Hwang, L.-S., H. L. Butler, and D. Divoky, Tsunami model: generation and open-sea characteristics, *Bull. Seismol. Soc. Am.*, **62**, 1579-1596, 1972a.
- Hwang, L.-S., H. L. Butler, and D. Divoky, Tsunami generation and propagation, *13th Int. Conf. Coastal Eng.* July 10-14, Vancouver, B. C. p.397-400, 1972b (Abstract).
- Kajiura, K., The leading wave of a tsunami, *Bull. Earthq. Res. Inst. Univ. Tokyo*, **41**, 535-571, 1963.
- Kajiura, K., Tsunami source, energy, and the directivity of wave radiation, *Bull. Earthq. Res. Inst. Univ. Tokyo*, **48**, 835-869, 1970.
- Kanamori, H., Mechanism of tsunami earthquakes, *Phys. Earth Planet. Inter.*, **6**, 346-359, 1972.
- Kanamori, H. and K. Satake, Broadband study of the 1989 Loma Prieta earthquake, *Geophys. Res. Lett.*, **17**, p. 1179-1182, 1990.
- Kawakatsu, H., Centroid single force inversion of seismic waves generated by landslides, *J. Geophys. Res.*, **94**, 12363-12374, 1989.
- Lamb, H., Hydrodynamics, *Cambridge University Press, Cambridge*, 738 pp., 1932.

- Lawson, A. C., G. K. Gilbert, H. F. Reid, J. C. Branner, A. O. Leuschner, G. Davidson, C. Burkhalter, and W. W. Campbell, The California earthquake of April 18, 1906, *Report of the state earthquake investigation commission, Carnegie Institution*, **2**, 369-373, 1910.
- Lipman, P.W., J. P. Lockwood, R. T. Okamura, D. A. Swason, and K. M. Yamashita, Ground deformation associated with the 1975 magnitude-7.2 earthquake and resulting changes in activity of Kilauea volcano, Hawaii, *U.S. Geol. Surv. Prof. Pap.*, **1276**, 45 pp., 1985.
- Lisowski, M., W. H. Prescott, J. C. Savage and M. J. Johnston, Geodetic estimate of coseismic slip during the 1989 Loma Prieta, California, earthquake, *Geophys. Res. Lett.*, **17**, 1437-1440, 1990.
- Ma, K.-F., K. Satake and H. Kanamori, The origin of tsunami excited by the 1989 Loma Prieta earthquake: Faulting or slumping, *Geophys. Res. Lett.*, **18**, 637-640, 1991a.
- Ma, K.-F., K. Satake and H. Kanamori, The tsunami excited by the 1906 San Francisco earthquake, *Bull. Seismol. Soc. Am.*, **81**, 1396-1397, 1991b.
- J. G. Moore, D. A. Clague, R. T. Holcomb, P. W. Lipman, W. R. Normark, and M. E. Torresan, Prodigious submarine landslides on the Hawaiian ridge, *J. Geophys. Res.*, **94**, 17465-17484, 1989.
- Murty, T. S., Seismic sea waves-tsunamis, *Bull. Fish. Res. Board Canada*, **198**, 1-337, 1977.
- Okada, Y., Surface deformation due to shear and tensile faults in a half-space, *Bull. Seismol. Soc. Am.*, **75**, 1135-1154, 1985.
- Okal, E. A., Seismic parameters controlling far-field tsunami amplitudes: A review, *Natural Hazards*, **1**, 67-96, 1988.
- Satake, K., The mechanism of the 1983 Japan sea earthquake as inferred from long-period surface waves and tsunamis, *Phys. Earthq. Planet. Inter.*, **37**, 249-260, 1985.



- Satake, K., Inversion of tsunami waveforms for the estimation of a fault heterogeneity: method and numerical experiments, *J. Phys. Earth*, **35**, 241-254, 1987.
- Satake, K., M. Okada, and K. Abe, Tide gauge response to tsunamis: Measurements at 40 tide gauge stations in Japan, *J. Marine Res.*, **46**, 557-571, 1988.
- Satake, K., Inversion of tsunami waveforms for the estimation of heterogeneous fault motion of large submarine earthquakes: the 1968 Tokachi-oki and 1983 Japan Sea Earthquakes, *J. Geophys. Res.*, **94**, 5627-5636, 1989.
- Schwing, F.B., J. G. Norton and C. H. Pilskaln., Earthquake and Bay, response of Monterey Bay to the Loma Prieta earthquake, *EOS*, **71**, 250-251, 1990.
- Swanson, D. A., W. A. Duffield, and R. S. Fiske, Displacement of the south flank of Kilauea volcano: The result of forceful intrusion of magma into the rift zones, *U.S. Geol. Surv. Prof. Pap.*, **963**, 39 pp., 1976.
- Takahashi, R., On seismic sea waves caused by deformation of the sea bottom, *Bull. Earthq. Res. Inst. Univ. Tokyo*, **20**, 377-400, 1942 (in Japanese).
- Thatcher, W., Strain accumulation and release mechanism of the 1906 San Francisco earthquake, *J. Geophys. Res.*, **80**, 4862-4872, 1975.
- Tilling, R. I., R. Y. Koyanagi, P. W. Lipman, J. P. Lockwood, J. G. Moore, and D. A. Swanson, Earthquake and related catastrophic events, Island of Hawaii, November 29, 1975: A preliminary report, *U.S. Geol. Surv. Circ.*, **740**, 33 pp., 1976.
- Ward, S.N., Earthquake mechanisms and tsunami generation: The Kuril Islands earthquake of 13 October, 1963, *Bull. Seismol. Soc. Am.*, **72**, 759-777, 1982.
- Wyss, M., R. L. Kovach, Comment on "A single force model for the 1975 Kalapana, Hawaii, earthquake" by Holly K. Eissler and Hiroo Kanamori, *J. Geophys. Res.*, **93**, 8078-8082, 1988.

## Part II

# Broadband Waveform Observation of Local Earthquakes

The recent deployment of TERRAScope in Southern California provided us with a capability of recording complete waveforms of local earthquakes. A TERRAScope station consists of a 3-component Wielandt-Streckeisen broadband seismometer and a Kinematics FBA-23 accelerometer. The overall dynamic range is about 200 db. The response of the broadband system is approximately flat in velocity over a period range from 0.2 to 370 sec. The sampling rate of the broadband and accelerograph systems are 20 and 80 to 100 samples per second, respectively. The system has recorded events on-scale with magnitude from 1.5 to 7.

The broadband waveforms contain information about the mechanism and stress drop of the events, and attenuation characteristics of the crust. The December 3, 1988, Pasadena,  $M_L=4.9$ , earthquake (Chapter 4) and June 28, 1991 Sierra Madre,  $M_L=5.8$ , earthquake (Chapter 5) occurred only about 5 and 16 km away from the Pasadena TERRAScope station, respectively, and the broadband waveform could be used to study the characteristics of the earthquake sequence. The June 28, 1992, Landers ( $M_w=7.3$ )

earthquake (Chapter 6) is the largest event in California since 1952. This earthquake occurred in a complex fault system and ruptured about 70 km to the north with surface slip as large as 6.5 m. The observation of the broadband waveform data allows us to study the energy release pattern during the entire earthquake sequence.

To study the source characteristics, the propagation effect must be removed from the waveform data. One approach is to use numerical methods to remove the path effect. This is not always easy, however, because the path effects are usually very complex, especially when the structure varies laterally. An alternative way is to use waveform similarity of the observed seismograms. This is somewhat similar to the empirical Green's function method widely used in strong-motion seismology (Hartzell, 1978). In general similarity of waveform suggests similar location and mechanism of the event. In this thesis, I will use this approach and classify the events for each earthquake sequence into several groups according to their waveforms and locations.

Since the first-motion data for small aftershocks are not always complete enough to determine the mechanisms using the conventional first-motion method, I applied an inversion method to the broadband waveform data and combined the results from first-motion data to determine the focal mechanisms. When the epicentral distance is short, P and S pulses are not strongly affected by the propagation effects along the path, and provide approximate source time functions. The waveforms can be inverted to determine the seismic moment and the three fault parameters (dip, rake, and strike). The pulse width of SH waves observed at short distances can be used to determine the stress drops and attenuation factor,  $Q$ , along the path from the hypocenter to station.

In chapter 4, I determined the focal mechanisms and seismic moments of 9 aftershocks of the 1988 Pasadena earthquake ( $M_L=4.9$ ). At the time of the event, only one station,

PAS, of the TERRAScope array was operational. This station is only about 4 km from the mainshock epicenter. It recorded high quality waveforms which are relatively free from contamination by propagation path effects. I inverted the waveforms recorded at PAS station and combined the result from the first-motion data to determine the focal mechanisms and seismic moments. The results in this study show that the aftershock mechanisms are, overall, consistent with left-lateral strike-slip motion on the Santa Monica-Raymond fault. The ratio of cumulative aftershock seismic moment to that of the mainshock is much smaller than that of most earthquakes in California.

Chapter 5 focuses on the June 28, 1991, Sierra Madre earthquake ( $M_L=5.8$ ). The PAS station is only about 16 km away from the mainshock epicenter. I applied the same technique I used for the 1988 Pasadena earthquake to determine the mechanisms and seismic moments of the mainshock and 21 aftershocks with magnitude equal to or larger than 1.5. For some events, good waveform data were also recorded with a portable instrument at Mount Wilson (MWC) which is only about 5 km from the mainshock epicenter. I inverted the waveforms recorded at PAS and MWC simultaneously to determine the focal mechanisms. I used the pulse widths of SH waves of the aftershocks to determine the average Q values along the path from the hypocenter to PAS station and stress drops of the events.

Chapter 6 focuses on the Joshua Tree-Landers earthquake sequence in 1992. We examined the depths and mechanisms of the aftershocks using the waveforms, and determined the spatial variation of the mechanisms and distribution of energy released along the fault. Only a few events occurred in the area where large slip occurred during the mainshock. The aftershocks between large asperities (zones with large slip during the mainshock rupture) show dissimilar waveforms and mechanisms suggesting

heterogeneities of the stress field in the area surrounding the asperities. During the aftershock sequence, most energy was released from the south of the mainshock epicenter. At one location, near vertical distribution of the aftershock, activity extending to a depth deeper than 15 km was found.

## Chapter 4

# Aftershock Sequence of the December 3, 1988 Pasadena Earthquake

### 4.1 Abstract

The Pasadena earthquake ( $M_L=4.9$ ) of 3 December, 1988, occurred at a depth of 16 km, probably on the Santa Monica-Raymond fault which is recognized as one of the most important faults in the Los Angeles basin for its potential seismic hazard. Prior to this event, no earthquake larger than magnitude 4 had been recorded since 1930 in this area. High-quality seismograms were recorded with the Pasadena very broadband (VBB) system (IRIS-TERRAScope station) not only for the main shock but also for the aftershocks at epicentral distances of 3 to 4 km. We determined the focal mechanisms of 9 aftershocks using these data, for most of the aftershocks the first-motion data are too sparse to determine the mechanism. We combined the first-motion data and the waveform data of P, SV, and SH waves recorded with the VBB instrument to determine the mechanism and seismic moment of 9 aftershocks. The average orientations of the P and T axes of the aftershocks are consistent with the strike of the Raymond fault. The ratio of the logarithm

of cumulative seismic moment of aftershocks to that of the seismic moment of the main shock is significantly smaller than commonly observed.

## 4.2 Introduction

The Pasadena earthquake ( $M_L=4.9$ ) occurred on 3 December 1988, at a depth of 16 km nearly directly beneath the Pasadena station. No earthquake with  $M_L>4$  had been recorded since 1930 in this area. High-quality seismograms were recorded with the broadband Pasadena IRIS-TERRAscope system for the main shock and nine aftershocks. Since the station is only about 4 km from the main shock epicenter, these records are relatively free from contamination by propagation path effects.

Figure 4.1 shows the locations of the main shock and the aftershocks taken from the catalog of the Caltech-USGS Southern California Seismic Network. Magistrale (1990) also determined the location of these events using a 3-D structure for the Los Angeles basin which resulted in generally good agreement with that from the catalog. Figure 4.1 includes earthquakes that occurred during the period January 1, 1988, to July 1, 1990. Jones et al. (1990) obtained the focal mechanisms of the main shock and four aftershocks which are large enough to allow mechanism determination from the first-motion polarities. They showed that the mechanisms of the main shock and the four aftershocks indicate left-lateral strike-slip motions on an east-northeast striking fault, and suggest that the Pasadena earthquake occurred on the Santa Monica-Raymond fault which has been recognized as one of the important faults in the Los Angeles basin. Since the entire extent of the Santa Monica-Raymond fault runs through the densely populated part of the Los Angeles basin, a large earthquake on this fault can cause a major seismic hazard. Kanamori et al. (1990)

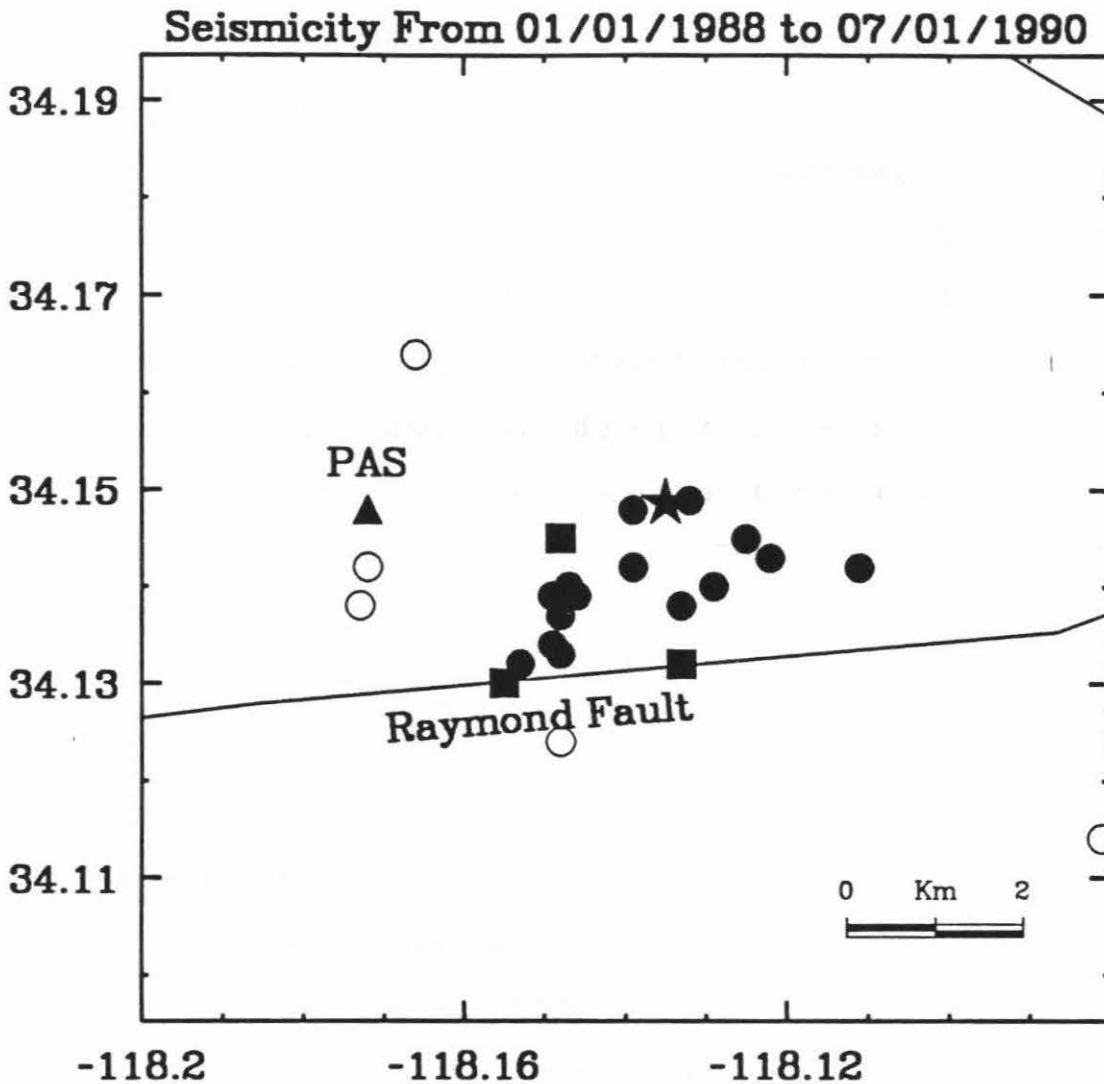


Figure 4.1 Seismicity before and after the December 3, 1988, Pasadena earthquake for the period from 1988 to July, 1990 from the catalog of the Caltech-USGS Southern California Seismic Network. The open circles, solid circles, and solid squares indicate the foreshocks, the aftershocks from December 3 to 31, 1988, and the other aftershocks, respectively. The star and the triangle indicate the main shock and the Pasadena station, respectively.



estimated the stress drop of the main shock to be an order of 1 kbar which is significantly higher than that of most large earthquakes.

In view of these unique characteristics of the Pasadena earthquake, we determined the focal mechanisms of the aftershocks. Since the first motion data for the aftershocks are too sparse to determine the mechanisms using the conventional first-motion method, we applied an inversion method to the broadband waveform data observed at Pasadena to determine the focal mechanisms. Since the epicentral distance is very short, P and S pulses can be inverted to determine the seismic moment and three fault parameters (dip, rake, and strike) using the method described by Kanamori (1989).

### 4.3 Data

Fifteen aftershocks were recorded by the Caltech-USGS Southern California Seismic Network during the period from December 3, 1989, to December 31, 1989, in the area. Of these, 9 events were recorded at the Pasadena station (Table 4.1). We rotated the broadband records into the transverse and radial components, and deconvolved them with the instrument response to obtain ground motion displacement records. In order to remove the large microseismic noise with periods of 4 to 8 sec, we high-pass filtered the records at 3 sec. Figure 4.2 shows the displacement record for the main shock and Figure 4.3 shows the mechanisms determined by Jones et al. (1990) from the first-motion data, and by Kanamori et al. (1990) using the waveform data. Figure 4.4 shows the displacement waveforms of the aftershocks in 3 groups. The events in group I (Figure 4.4a; events 2, 7 and 8) are very similar to the main shock in waveform. They show a small upward P-wave motion, and an S wave with negative (clockwise around the epicenter) transverse

No.	Date	Time	North Latitude (deg.)	West Longitude (deg.)	Z (km)	Dip	Rake	Strike	Mo ( $10^{19}$ dyne-cm)
0	881203	1138	34.149	118.135	15.4	90.0	9.0	249.0*	24000-46000
1	881203	1149	34.139	118.154	15.5	61.2	26.8	-98.9	2.58
2	881203	1156	34.145	118.133	15.2	68.8	11.0	-110.5	4.68
3	881203	1208	34.156	118.127	15.9	45.4	11.1	73.9	2.06
4	881203	1213	34.142	118.148	14.3	72.1	37.9	-131.3	10.40
5	881203	1215	34.141	118.148	15.0	88.0	-6.2	45.4	2.54
6	881203	1336	34.158	118.127	16.5	58.0	10.2	72.2	1.22
7	881203	1446	34.142	118.146	14.5	85.8	24.6	-109.3	0.76
8	881204	0801	34.145	118.135	15.1	82.8	-9.2	44.3	1.74
9	881208	0251	34.157	118.113	16.4	21.7	19.4	85.1	4.38

\* Kanamori et al (1990)

Table 4.1 The origin time, location, fault parameters, and seismic moment of the main shock and nine aftershocks of the Pasadena earthquake sequence.

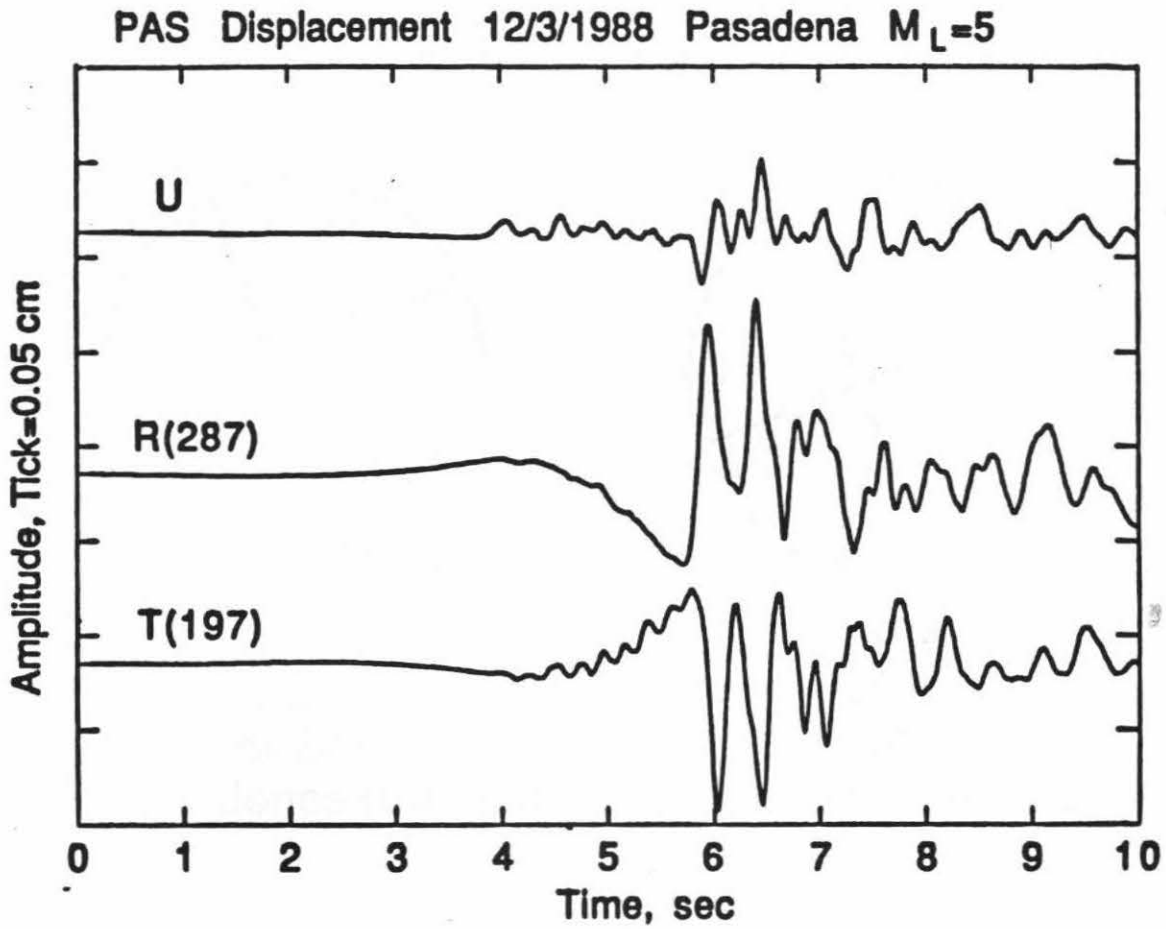
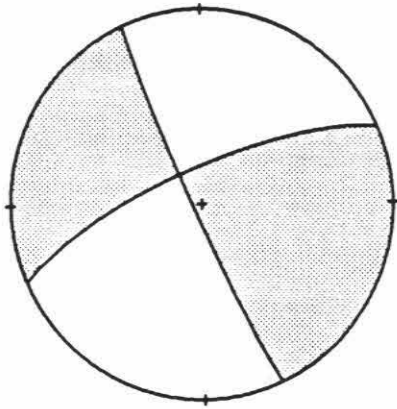
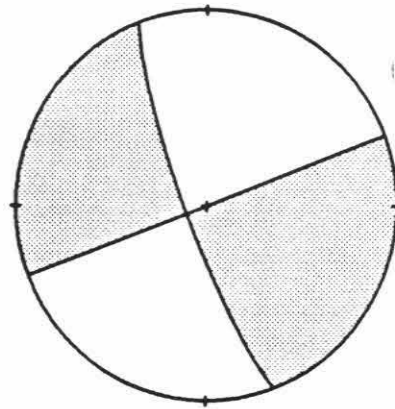


Figure 4.2 Rotated displacement records of the December 3, 1988, Pasadena earthquake obtained from the low-gain channel of the Pasadena system (high-pass-filtered at 5 sec).



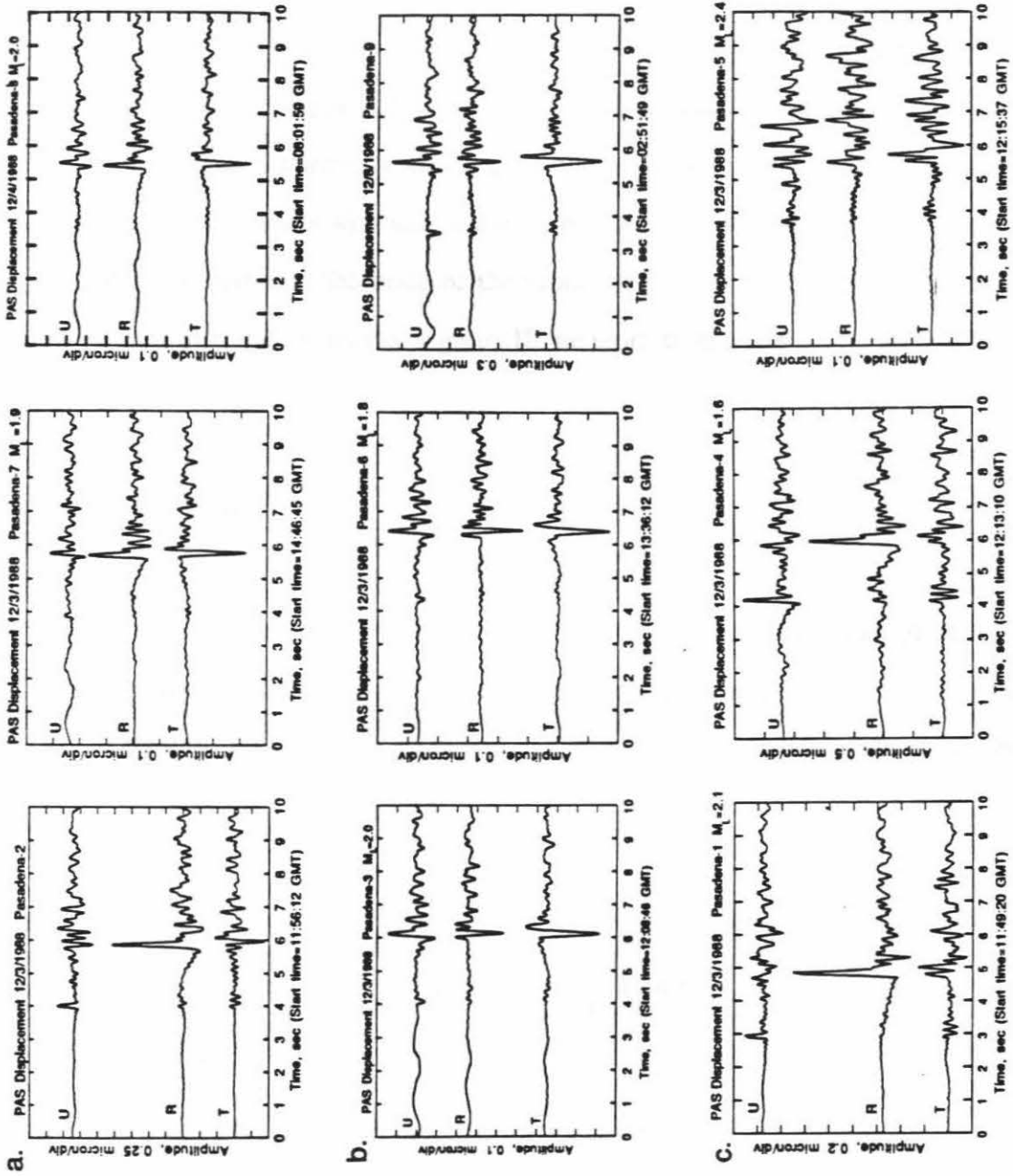
$\delta=75^\circ$   
 $\lambda=4^\circ$   
 $\phi=247^\circ$   
Jones et al. (1990)



$\delta=90^\circ$   
 $\lambda=9^\circ$   
 $\phi=249^\circ$   
Kanamori et al. (1990)

Figure 4.3 The mechanisms of the main shock determined by Jones et al. (1990) from the first-motion data, and by Kanamori et al. (1990) using the waveform data.

Figure 4.4 Rotated displacement records of the 9 aftershocks in 3 groups: (a). Group I: events 2, 7, and 8. (b) Group II: events 3, 6, and 9. (c) Group III: events 1, 4 and 5. The amplitude scale indicates the true ground motion amplitudes in microns



component and positive (away from the epicenter) radial component. This similarity suggests that the mechanisms of these events are similar to that of the main shock. The events in group II (Figure 4.4b; events 3, 6, and 9) have a downward P wave, and an S wave with negative transverse and radial components. Group III (Figure 4.4c; events 1, 4 and 5) has three events with very complex SH waveforms suggesting that the Pasadena station is located near the node of the radiation pattern of SH waves. In general, the waveforms of P and SV waves of group III are more similar to those of group I than group II.

## 4.4 Method

We used the method described in Kanamori (1989) and Kanamori et al. (1990) to determine the seismic moment and fault parameters (dip, rake, and strike). The P, SV, and SH far field displacements,  $U_r$ ,  $U_\theta$ , and  $U_\phi$ , from a double-couple point source are given by

$$\begin{bmatrix} U_r \\ U_\theta \\ U_\phi \end{bmatrix} = \frac{M_0 S(t)}{4\pi\rho\alpha^3} \begin{bmatrix} R^P \\ (\alpha/\beta)^3 R^{SV} \\ (\alpha/\beta)^3 R^{SH} \end{bmatrix}, \quad (1)$$

where  $s(t)$  and  $M_0$  are the unit moment rate function and the seismic moment, respectively. Here,  $\rho$ ,  $\alpha$ , and  $\beta$  are density, P velocity, and S velocity, and  $R^P$ ,  $R^{SV}$ , and  $R^{SH}$  are P-wave, SV-wave and SH-wave radiation patterns respectively. The radiation patterns are functions of the fault parameters: dip  $\delta$ , rake  $\lambda$ , and strike  $\phi$ . We used (1) to determine

$M_o$ ,  $\delta$ ,  $\lambda$ , and  $\phi$  from  $U_r$ ,  $U_\theta$ , and  $U_\phi$  estimated from the observed P, SV, and SH amplitudes and polarities.

Let  $U_P$ ,  $U_{SVZ}$ ,  $U_{SVR}$ , and  $U_{SH}$  be the displacements of the P wave on the vertical component, the SV wave on the vertical component, the SV wave on the radial component, and the SH wave on the tangential component, respectively, observed at the free surface. If we ignore the P-SV conversion at the free surface, then

$$\begin{aligned} U_r &= U_P / (2 \cos i_o) \\ U_\theta &= U_{SVZ} / (-2 \sin i_o) = U_{SVR} / (2 \cos i_o) \\ U_\phi &= U_{SH} / 2, \end{aligned} \quad (2)$$

where  $i_o$  is the incidence angle. The free-surface effect is approximated by a factor of 2 of amplification of the incidence wave. Since these events are very close to the station, this approximation is satisfactory. If P-SV conversion at the free surface is considered,  $U_{SVZ}$  and  $U_{SVR}$  become more complex functions of the incidence angle. Since the effect of the free surface is generally smaller on the vertical component than on the radial component, we usually estimate  $U_\theta$  from the vertical component. However, when  $U_{SVZ}$  is too small to measure, we used  $U_{SVR}$  to estimate  $U_\theta$ .

Because the number of parameters, 4, is larger than the number of data, 3, in equation (1), the solution is nonunique. We obtained the solution combining the waveform and first-motion data as follows.

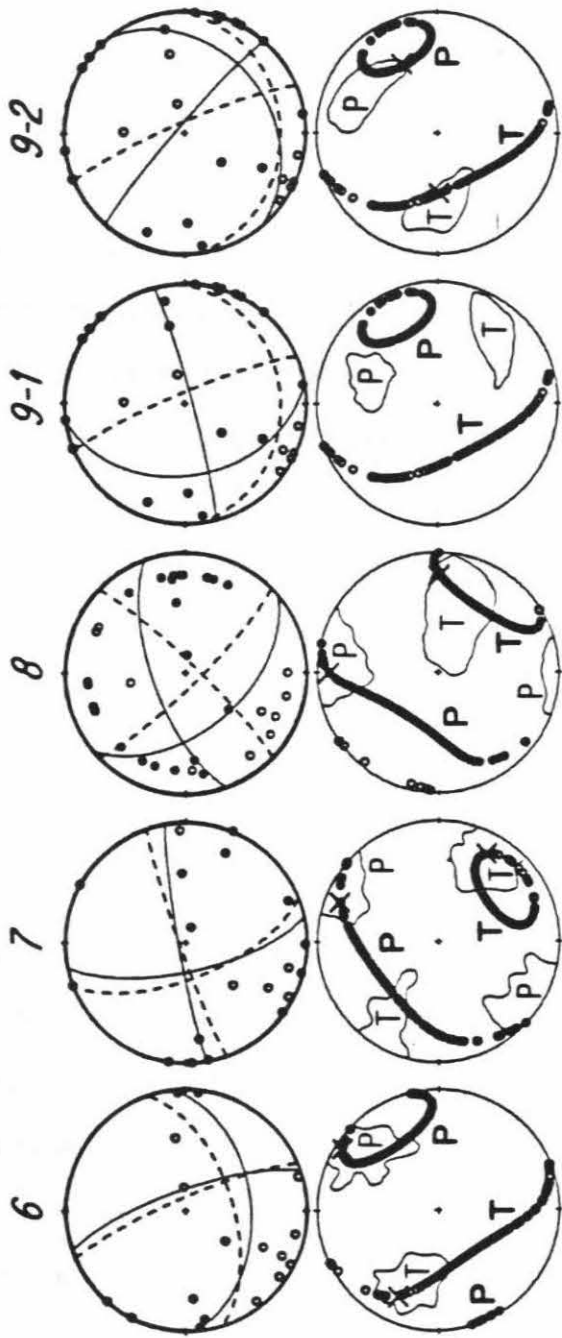
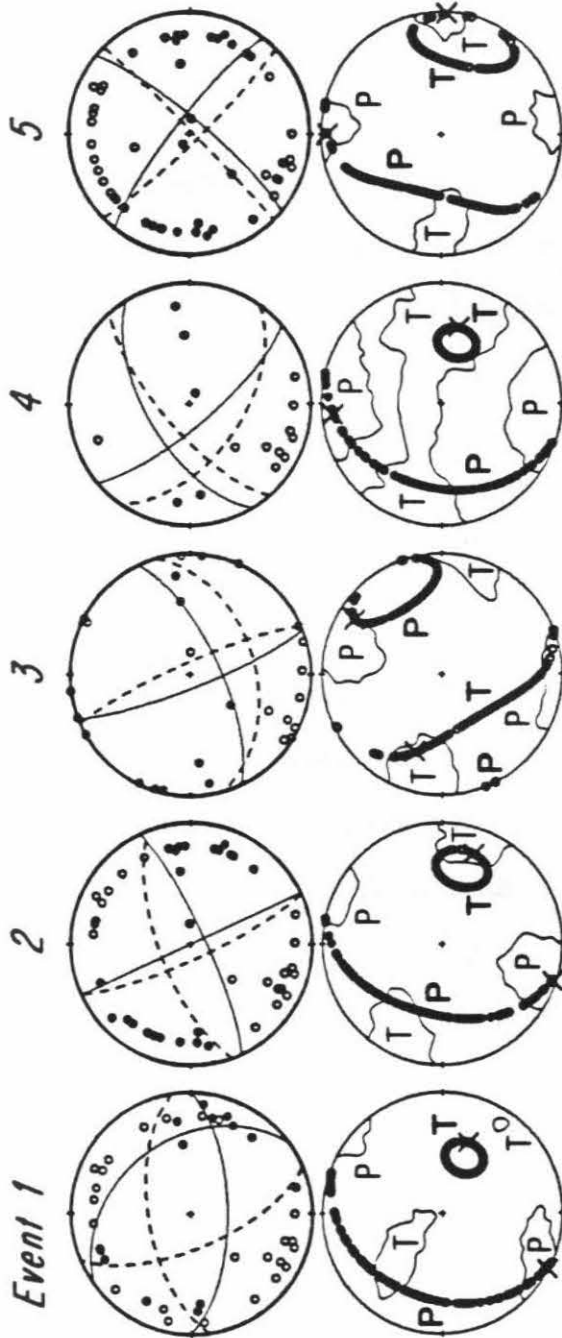
Although the solution of equation (1) is nonunique, we can determine the range of allowable solutions that explain the observed amplitudes and polarities of P, SV, and SH waves. Figure 4.5 shows the loci of the P and T axes (hereafter called the inversion P-T



loci) of the allowable solutions determined by inverting equation (1). Any solution with a pair of P and T axes on the loci yields the correct amplitudes and polarities of P, SV and SH waves.

Next we analyzed the first-motion data using the program FPFIT (Reasenber and Oppenheimer, 1985). The available first-motion data recorded by the Caltech-USGS Southern California Seismic Network of the nine aftershocks are shown in Figure 4.5 by equal area projection of the lower hemisphere. Because the magnitudes of the aftershocks are in the range of 1.5 to 2, the number of first-motion data available is small. For some events, compressional and dilatational first motions are mixed, suggesting ambiguous beginning of the first motion. The program FPFIT uses a grid-search procedure to find a mechanism by minimizing the normalized, weighted sum of the discrepancies between the observed and theoretical polarity at each station. The program also determines the ranges of P and T axes of mechanisms that fit the first-motion data equally well. These ranges, here called the first-motion P-T ranges, are shown in Figure 4.5. Since the quality of the first-motion data is limited, the allowable P-T ranges are generally large. Any solution in these ranges are considered acceptable. If the inversion P-T loci pass through the first-motion P-T ranges, any solution for which the P and T axes lie in the overlapping region can satisfy both the first-motion and waveform data. If the inversion P-T loci do not pass through the first-motion P-T ranges, we chose a point on the inversion P-T loci that is closest to the first-motion P-T ranges. Figure 4.5 shows the points we chose this way, and the resulting solutions (dashed curve); these solutions are compared with those (solid curve) picked by FPFIT using the first-motion data alone.

Figure 4.5 The first-motion data recorded by the Caltech-USGS Southern California Seismic Network and the focal mechanisms determined from the first motion data alone (solid curves) and the combined (first-motion and waveform) data (dashed curves) of the nine aftershocks of the 1988 Pasadena earthquake. The figure beneath the first-motion data shows the inversion P-T loci (heavy curve with bold face letters) and the first-motion P-T ranges. The cross symbols indicate the P and T axes of our preferred solution.



## 4.5 Results

For event 1, the inversion T axis locus does not pass through the first-motion T axis range. This means that no solution can explain both the first-motion and waveform data simultaneously. We chose a mechanism with the P axis located on the inversion P axis locus and in the middle of the first-motion P axis range as the solution. As shown in the mechanism diagram, this solution fits the first motion data satisfactorily.

For event 9, two mechanisms are obtained from the first-motion data. However, the waveform data are consistent only with the mechanism with a low angle plane dipping southeast (second solution in Figure 4.5).

Considering the ambiguities in the first-motion data, the mechanisms for other events thus determined are in general consistent with the first-motion data. Some first-motion data are inconsistent, but, for these small events, first motion is not always distinct, and some inconsistency is acceptable.

To illustrate the sensitivity of the waveform to the mechanism, we compared the synthetic waveforms of event 8, for instance, computed for the mechanism determined by the first-motion data only and by inversion. The waveform for the mechanism determined from the first-motion data.(Figure 4.6a) does not match the observed (Figure 4.4), while the waveforms computed for the mechanism obtained by inversion (Figure 4.6b) have the correct P to SH ratio. The waveform of the SV component is not explained very well, however. As mentioned earlier, the inversion is done using the first half cycle of the vertical component. The amplitude of the radial component is not used in the inversion. The vertical to radial ratio is solely determined by the incidence angle. Also the SV waveform

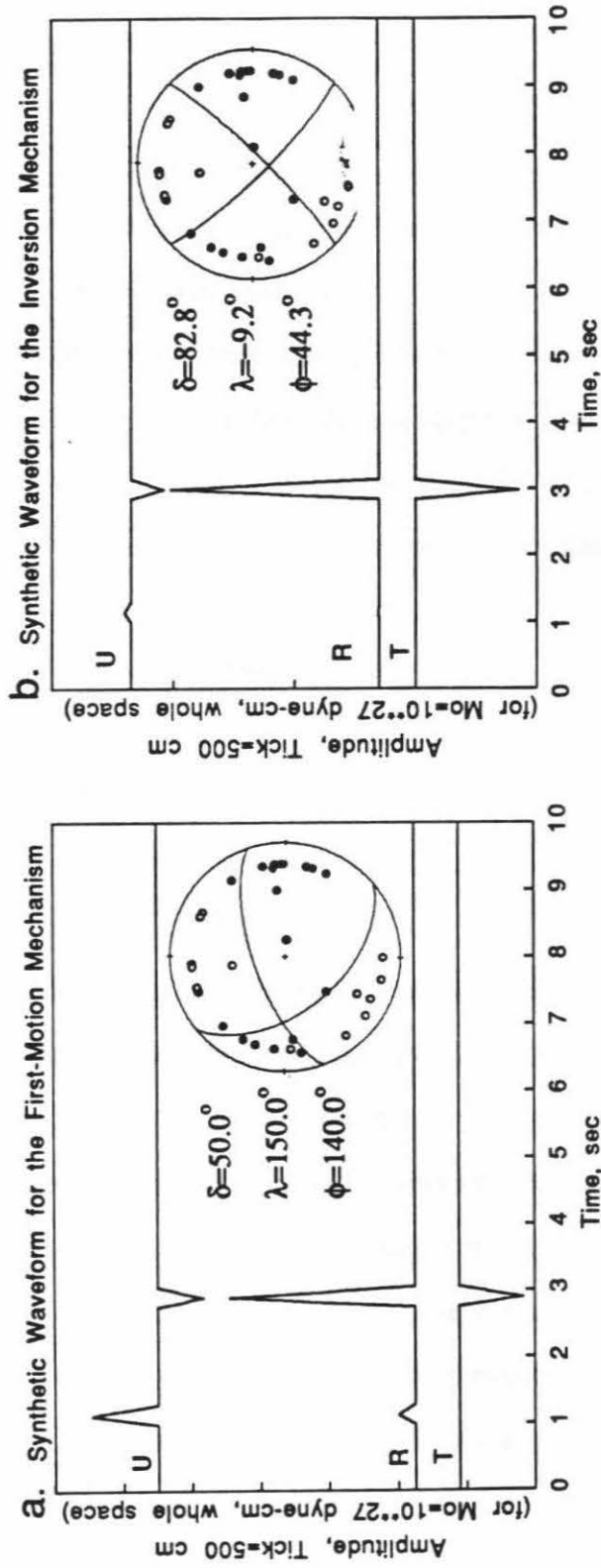


Figure 4.6a): The mechanism obtained from the first motion data of event 8 and the corresponding synthetics. b): The mechanism obtained from the combined (waveform and first-motion ) data of event 8 and the corresponding synthetics.

on the vertical component is double-sided. This is probably due to SV-P interaction caused by some structures near the surface. We have not been able to explain this feature satisfactorily with a half-space or a layered half space model. In our inversion, only gross amplitude ratio and polarity of P, SV and SH waves are used, and the second half cycle of the SV wave is not used. For some events, a small oscillatory P wave is observed on the transverse component. This might be due to structural heterogeneity near the Pasadena station. The details of these features are unknown.

Figure 4.7 shows the spatial distribution of the main shock and the aftershocks of the Pasadena earthquake sequence with focal mechanisms shown by equal area projections of the lower focal hemisphere. The locations are taken from Magistrale (1990). For group I, the solutions thus obtained are similar to that of the main shock. This is not surprising in view of the similarity of the waveforms. These solutions are in general consistent with the first-motion data with steep dipping planes. The average orientations of P and T axes are in southwest-northeastern and southeastern directions, respectively. For group II, the solutions were slightly different from that of the main shock. One of the nodal planes is shallowly dipping to the south, especially for event 9. The P and T axes have the average orientation of northeast and northwest, respectively. Since the waveforms of the events in group III are complex, the solution is less reliable than that for the events in groups I and II. The mechanism for event 5 is very similar to that of main shock, although the SH wave is almost on the node. The average orientations of P and T axes are similar to those of group I. The P and T axes of these events are shown in Figure 4.8.

The overall waveform similarity of events in group I, group III, and, to a lesser extent, group II to that of the main shock suggests that the mechanisms of the aftershock are similar to that of the main shock, and the result shown in Figure 4.7 is reasonable. The

## Pasadena Earthquakes

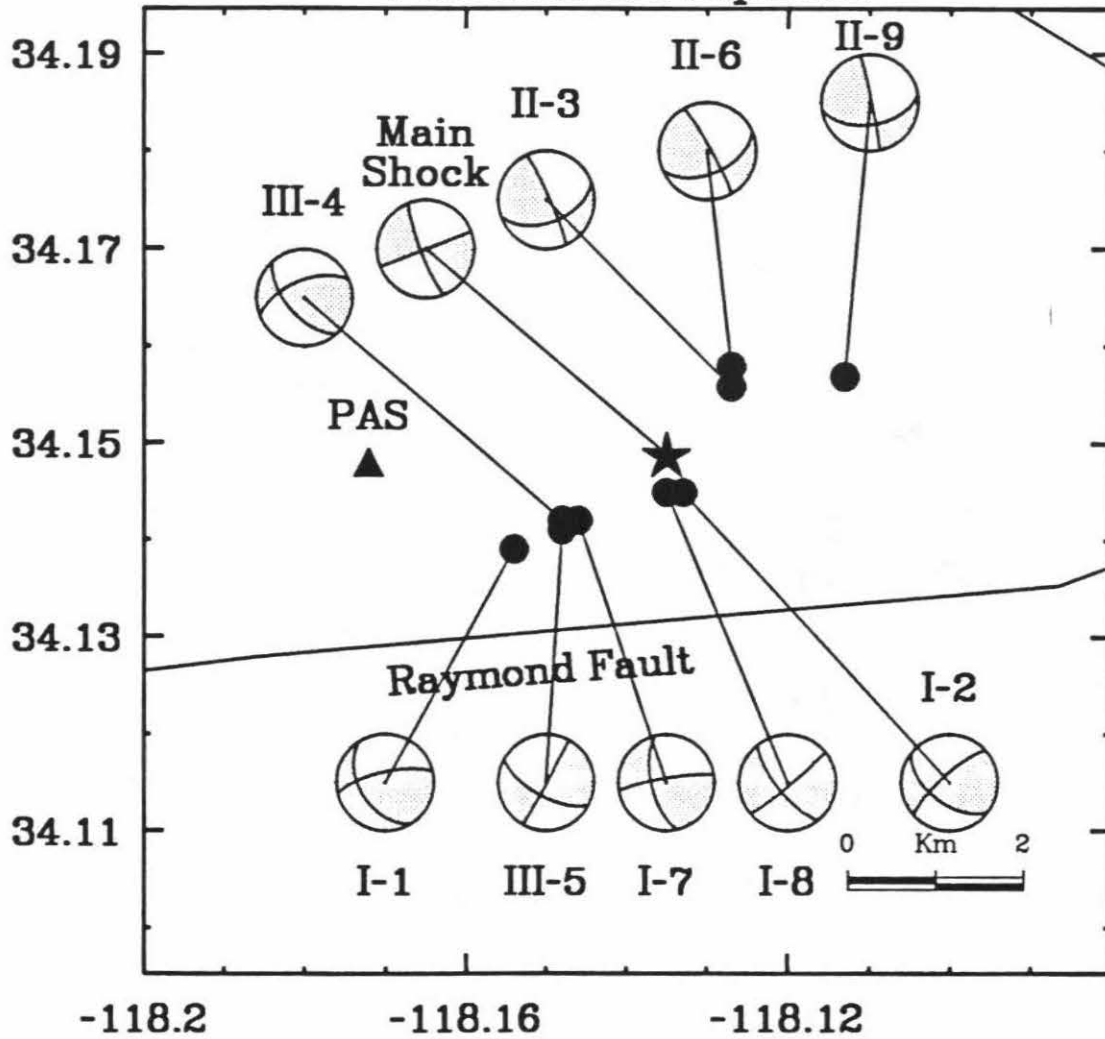


Figure 4.7 The spatial distribution of the main shock and the aftershocks of the Pasadena earthquake sequence with focal mechanisms shown by equal-area projections of the lower focal hemisphere with the locations from Magistrale (1990).

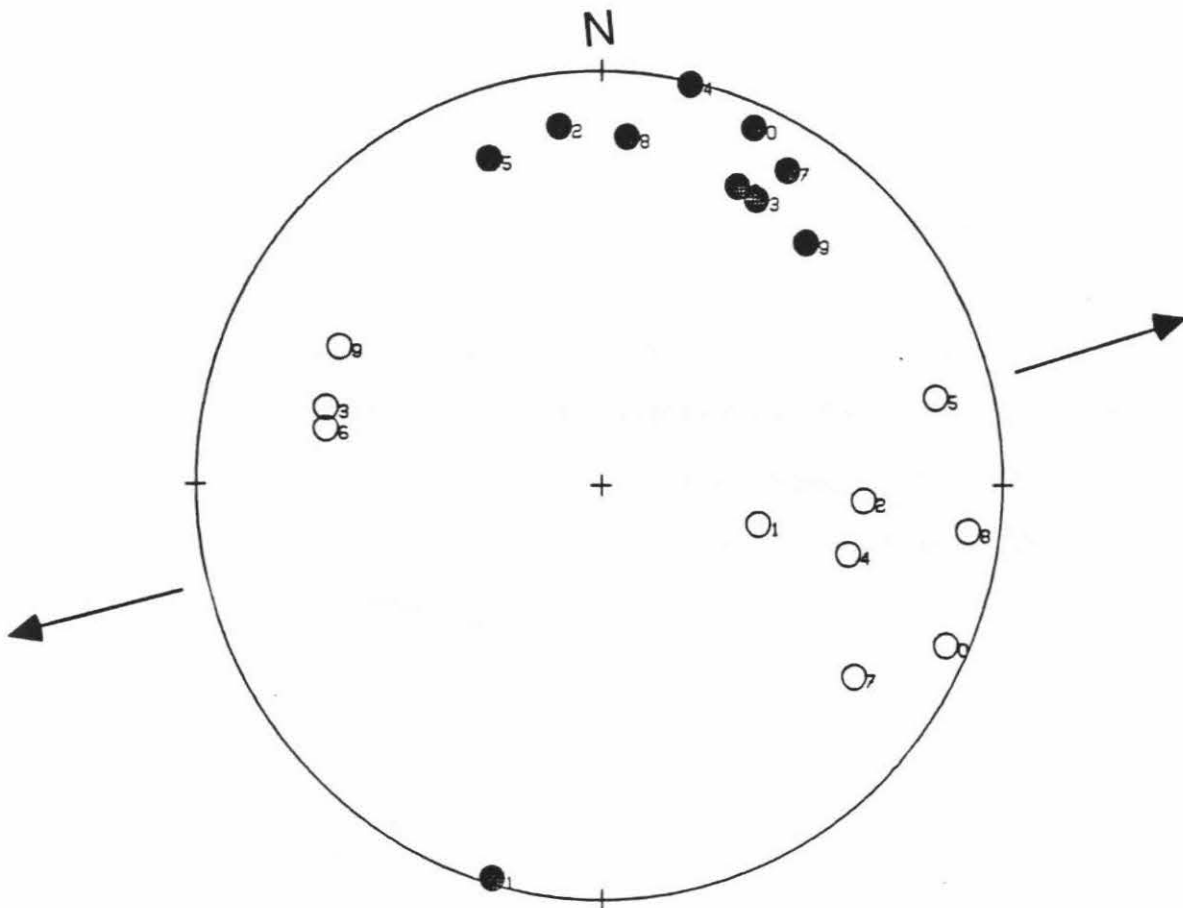


Figure 4.8 Equal-area projection of the P and T axes on the lower hemisphere. The solid circles and open circles indicate P and T axes respectively. The arrows indicate the average strike,  $N75^{\circ}E$ , of the Raymond fault.



average orientations of the P and T axes of the aftershocks (Figure 4.8) are consistent with the strike of the Santa Monica-Raymond fault (strike of N65°E to N85°E), in agreement with Jones et al. (1990).

The focal mechanisms and seismic moments of the aftershocks of the Pasadena earthquake thus determined are listed in Table 4.1. A remarkable feature of this sequence is that the aftershocks are very few and small. In order to demonstrate this, we compared the Pasadena earthquake sequence to 12 earthquake sequences in California shown in Table 4.2 and Figure 4.9. We calculated the cumulative aftershock seismic moment ( $\Sigma M_{0A}$ ) for these events. Except for the Pasadena earthquake sequence, the seismic moments of the aftershocks of the other events are estimated using the empirical relation,  $\log M_0 = 1.5 M_L + 16.1$ , where  $M_0$  is the seismic moment in dyne-cm, and  $M_L$  is the local magnitude (Thatcher and Hanks, 1973). In this calculation, we included all the aftershocks with magnitudes ( $M_{\text{main shock}} - 3.5$ ) or larger that occurred within one year after the main shock. For the Loma Prieta earthquake (Oct. 17, 1989) and the Upland earthquake (February 28, 1990), we included the aftershocks which occurred during the two weeks and six months after the main shock, respectively. The results thus obtained are listed in Table 4.2.

Figure 4.9 plots  $\log \Sigma M_{0A}$  against  $\log$  of the main shock moment,  $M_{0M}$ , for these events. The solid lines indicate the trend for constant ratios, 1,  $1/10^2$ , and  $1/10^4$ . Except for the Pasadena earthquake sequence, all the sequences have a ratio between 1 and  $1/100$ . The ratio for the Pasadena earthquake sequence is about  $1/1000$ , and is distinctly lower than the others.

Event	Date	M L	$M_{OM}^*$ ( $10^{25}$ dyne-cm)	$\sum M_{OA}$ ( $10^{25}$ dyne-cm)
San Fernando	Feb., 9, 1971	6.4	9.75	139.00
Imperial Valley	Oct., 15, 1979	6.6	6.00	46.50
Coalinga	May, 2, 1983	6.3	2.82	108.00
San Diego	June, 29, 1983	4.6	0.008	0.016
North Palm Spring	July, 8, 1986	5.9	1.70	4.35
Oceanside	July, 13, 1986	5.4	0.13	2.64
Whittier Narrows	Oct., 1, 1987	5.9	1.43	14.05
Superstition Hills	Nov., 24, 1987	6.1	7.20	8.50
Gorman	June, 10, 1988	5.4	0.13	0.67
Pasadena	Dec., 3, 1988	4.9	0.04	0.0015
Malibu	Jan., 19, 1989	5.0	0.032	0.95
Loma Prieta	Oct., 18, 1989	6.9	30.0	11.70
Upland	Feb., 28, 1990	5.2	0.17	2.97

\* footnote: average of the published values

Table 4.2 The seismic moment of the main shock, and the sum of the seismic moment of the aftershocks for 13 earthquake sequences in California.

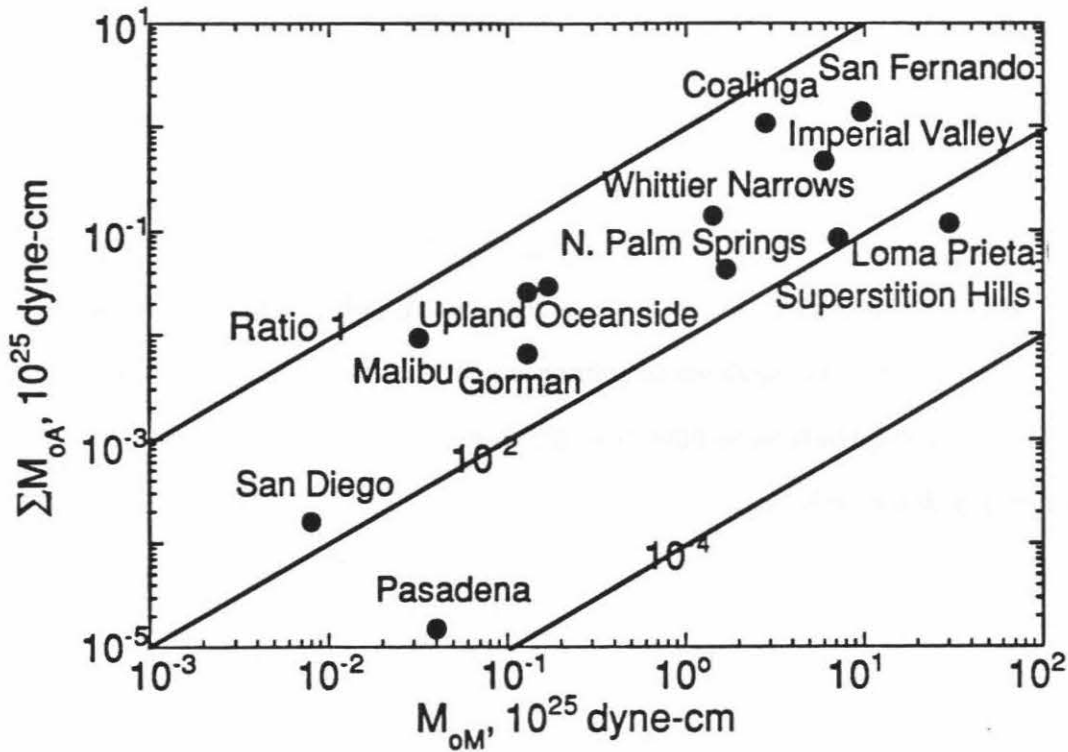


Figure 4.9 Logarithm of cumulative aftershock seismic moment plotted as a function of logarithm of the seismic moment of the main shock for the San Fernando ( $M_L=6.4$ ), 1971; Imperial Valley ( $M_L=6.6$ ), 1979; Coalinga ( $M_L=6.3$ ), 1983; San Diego ( $M_L=4.6$ ), 1983; North Palm Springs ( $M_L=5.9$ ), 1986; Oceanside ( $M_L=5.4$ ), 1986; Superstition Hills ( $M_L=6.1$ ), 1987; Whittier Narrows ( $M_L=5.9$ ), 1987; Gorman ( $M_L=5.4$ ), 1988; Pasadena ( $M_L=4.9$ ), 1988; Malibu ( $M_L=5.0$ ), 1989; Loma Prieta ( $M_L=6.9$ ), 1989; and Upland ( $M_L=5.2$ ), 1990 earthquake sequences. The solid lines indicate ratios of 1,  $1/10^2$ , and  $1/10^4$ .

Recent studies (e.g., Mendoza and Hartzell 1988; Schwartz et al. 1989; Choy and Dewey 1988) show that aftershocks generally do not occur in the regions where the main shock slip is large. Houston and Engdahl (1989) in their study of the 1986 Andreanof Islands earthquake, found that the moment release of the main shock occurred in regions of no or few aftershocks or preshocks. They suggest that the most moment release occurs from strong regions on the fault plane which are locked before or after the main shock. Kanamori et al. (1990) found that most of the main-shock energy of the Pasadena earthquake came from two strong asperities on the fault plane. We suggest that, before the main shock, the strain had accumulated there without producing any seismic events; during the main shock almost all the energy was released in a high-stress drop event, leaving little energy for aftershocks.

## 4.6 Conclusions

We determined the focal mechanisms of the Pasadena earthquake sequence by applying an inversion method to the waveform data. The first-motion data are combined in a systematic way with the waveform data to determine mechanisms that are consistent with both sets of data. The aftershock mechanisms are overall consistent with left-lateral strike-slip motion on the Santa Monica-Raymond fault, which is consistent with the result of Jones et al. (1990). The small ratio of the cumulative aftershock seismic moment to the main-shock seismic moment of the Pasadena earthquake is consistent with the high-stress drop model in which most of the energy was released from strong asperities.

## Chapter 5

# Broadband Waveform Observation of the June 28, 1991, Sierra Madre Earthquake Sequence ( $M_L=5.8$ )

### 5.1 Abstract

The Sierra Madre earthquake ( $M_L=5.8$ ) of 28 June, 1991, occurred at a depth of about 12 km, on the Clamshell-Sawpit fault in the San Gabriel Mountains. High-quality seismograms were recorded with TERRAScope not only for the mainshock but also for the aftershocks at epicentral distances of about 17 km. We determined the focal mechanisms and seismic moments of the mainshock and 21 aftershocks by combining the waveform and first-motion data. We classified the events into 5 groups according to the location and waveforms recorded at PAS. Most events located within 5 km west of the mainshock are similar to the mainshock in waveform. The mechanisms thus determined are thrust mechanisms. A few events located east of the mainshock have waveforms different from

the mainshock and have strike-slip mechanisms. The average  $Q\beta$  values along the paths from the hypocenters of the Sierra Madre and the Pasadena earthquake to PAS are about 130 and 80 respectively. The stress drop of the mainshock is about 500 bars. Most of the aftershocks have stress drops between 10 to 100 bars.

## 5.2 Introduction

The recent deployment of TERRAScope, a broadband and wide dynamic range seismic network in Southern California, provided us with a capability of recording complete waveforms of nearby earthquakes. These waveform data allow us to determine the focal mechanisms, seismic moments, stress drops and the attenuation characteristics of the crust. The mechanisms of regional earthquakes traditionally determined from P-wave first-motion data represent the very beginning of fault motion, but do not necessarily represent the overall fault motion. A combined use of broadband waveform data enables us to obtain the overall mechanism which explains the first-motion and waveform data.

The Sierra Madre earthquake ( $M_L=5.8$ ) sequence which occurred on 28 June 1991, at a depth of about 12 km and only about 16 km away from the Pasadena TERRAScope station provided us with a good opportunity to utilize broadband data for determining the overall characteristics of this sequence.

The PAS station recorded on-scale waveforms of the mainshock and the aftershocks. The focal mechanism of the mainshock determined from regional and local body waveforms is a thrust fault (Dreger and Helmberger 1991). The average slip is approximately 50 cm in a small rupture area of about 12 km<sup>2</sup> (Wald 1991). The aftershock distribution and the focal mechanism of the mainshock suggest that the Sierra Madre

earthquake was on the Clamshell-Sawpit fault in the south central part of the San Gabriel Mountains (Hauksson 1992).

The seismicity in the Los Angeles basin and the adjacent areas has been high for the last 4 years (Jones et al. 1991). From 1900 through 1986 no earthquake larger than magnitude 4.9 occurred in the San Gabriel Valley, while four earthquakes (the 1987 Whittier Narrows; the 1988 Pasadena; the 1990 Upland; and the 1991 Sierra Madre) with magnitude 4.9 or larger have occurred since 1987.

We determined the focal mechanisms and seismic moments of the mainshock and the aftershocks of the Sierra Madre earthquake sequence using the waveforms recorded with broadband instruments. Since these events are very close to the PAS station, the waveforms at PAS station allowed us to perform reliable source mechanism determinations. We inverted the waveform data of the mainshock and 21 aftershocks with magnitudes equal to or larger than 1.5 recorded at PAS in conjunction with the first-motion data from the Southern California Seismic Network. Just a few hours after the mainshock, Caltech installed a portable instrument at Mount Wilson (MWC), which is only 5 km away from the epicenter (Figure 5.1). This instrument provided good waveform data for some of the aftershocks. For these events, we inverted the waveforms recorded at PAS and MWC simultaneously. Also the waveforms recorded at PAS station allowed us to estimate the average Q values along the path from the hypocenter to PAS station and stress drops of the events.

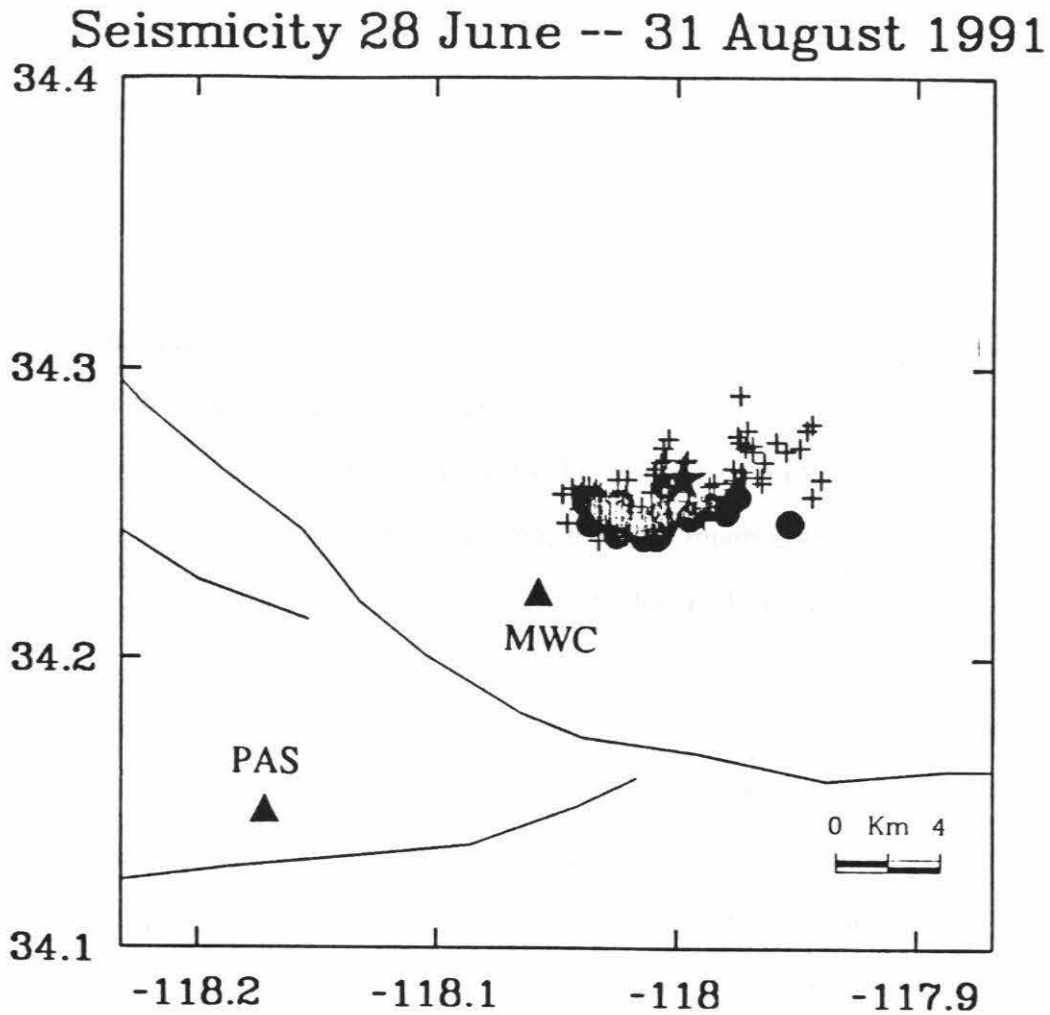


Figure 5.1: Seismicity during the time period from 28 June to 31 August in the area. Cross symbols and solid circles represent the aftershocks recorded by the Caltech-USGS Southern California Seismic Network and events with magnitude 1.5 or larger recorded by PAS TERRAScope station, respectively. The asterisk indicates the mainshock.



### 5.3 Data

One hundred and nine aftershocks were recorded by the Caltech-USGS Southern California Seismic Network (SCSN) during the period from 28 June 1991 to 31 August 1991 in the area shown in Figure 5.1. Of these, 22 events with a magnitude 1.5 or larger were recorded with the Pasadena (PAS) very broadband TERRAScope station (Table 5.1). We rotated the broadband records into the transverse and radial components, and deconvolved the instrument response from them to obtain ground motion displacement records. We high-pass filtered the records of the aftershocks at 0.33 Hz to remove the large microseismic noise with periods of 4 to 8 sec.

The portable instrument deployed by Caltech at Mount Wilson (MWC) station has a broadband Ranger seismometer with a flat velocity response from 0.05 to 20 Hz. In total, 26 aftershocks were recorded with the portable instrument at MWC. This instrument provided good waveform data for 6 of the aftershocks (Table 5.1). We rotated the records, and integrated them to obtain the displacement records. The records were high-pass filtered at a corner frequency of 0.5 Hz.

We classified the events into five groups according to the locations and the waveforms recorded at PAS station. The events in Group I (Figure 5.2a) are very similar to the mainshock in waveform. They show a small upward P-wave, and an S wave with large negative (clockwise around the epicenter) transverse component and negative (toward the epicenter) radial component. There are 9 events in Group I including the mainshock. This similarity suggests that the mechanisms of the events are similar to that of the mainshock.

Table 5.1: The origin time, location, fault parameters, and seismic moment of the mainshock and 21 aftershocks of the Sierra Madre earthquake in five groups. Stations used are indicated by a cross under the station name.

Event	Time (GMT)	Latitude (N)	Longitude (W)	Depth (km)	M	PAS	MWC	Dip (deg.)	Rake (deg.)	Strike (deg.)	Moment (dyne-cm)
<b>Group 1</b>											
0	6281443	34.263	-117.998	12.54	5.8	X		56.7	70.1	-127.6	2.70E+24
1	6281620	34.254	-118.034	12.09	1.6	X		59.6	119	111.1	1.27E+19
2	6281658	34.253	-117.987	11.13	3.3	X		61.2	53.3	-137.9	9.70E+20
3	6281700	34.250	-117.994	11.12	4	X		66.6	138.6	119.7	3.64E+22
4	6281755	34.255	-118.038	13.31	2.1	X		79.4	131.2	139.6	7.58E+19
5	6281950	34.247	-118.036	12.00	1.8	X		48.8	61.4	-114.9	1.31E+19
6	6302140	34.247	-118.025	11.40	2.2	X	X	35.561	109.58	-85.63	4.73E+19
7	7051536	34.254	-118.024	13.71	1.8	X	X	48.67	108.46	-95.66	2.40E+19
8	7070745	34.254	-118.038	13.26	1.7	X	X	51.94	39.09	-130.75	8.46E+18
<b>Group 2</b>											
1	6281459	34.254	-118.035	13.22	3.2	X		39.4	79.9	67.5	3.04E+21
2	6281513	34.250	-118.008	10.35	2	X		47	155.5	143.6	2.93E+19
3	6281517	34.260	-118.005	11.58	2.1	X		55.7	106.1	-94.5	1.64E+19
4	6281852	34.247	-118.010	11.08	3.1	X		60.1	145	131.6	7.87E+20
5	6300214	34.243	-118.025	10.94	2.3	X	X	58.5	106.93	-102.9	9.50E+20
<b>Group 3</b>											
1	6281553	34.243	-118.008	9.55	1.5	X		17.5	26.4	-157.9	2.49E+18
2	6281711	34.242	-118.014	11.19	2.2	X		30.4	10.8	-163.5	8.76E+19
3	7062254	34.242	-118.009	10.92	4	X	X	88.18	105.85	97.19	6.67E+21
<b>Group</b>											
1	6281716	34.249	-117.995	9.59	1.6	X	X	59.13	44.96	-146.31	3.52E+18
2	6291150	34.256	-117.975	9.48	1.5	X	X	56.3	29.83	-143.55	4.55E+18
<b>Group 5</b>											
1	6281537	34.251	-117.980	13.09	3.5	X		67.6	170.7	-74.1	7.21E+21
2	6281953	34.246	-118.006	10.39	1.9	X		75.7	-32.1	126.6	2.00E+19
3	8142150	34.248	-117.950	10.40	3	X		89.5	-171.5	-17.9	7.03E+20

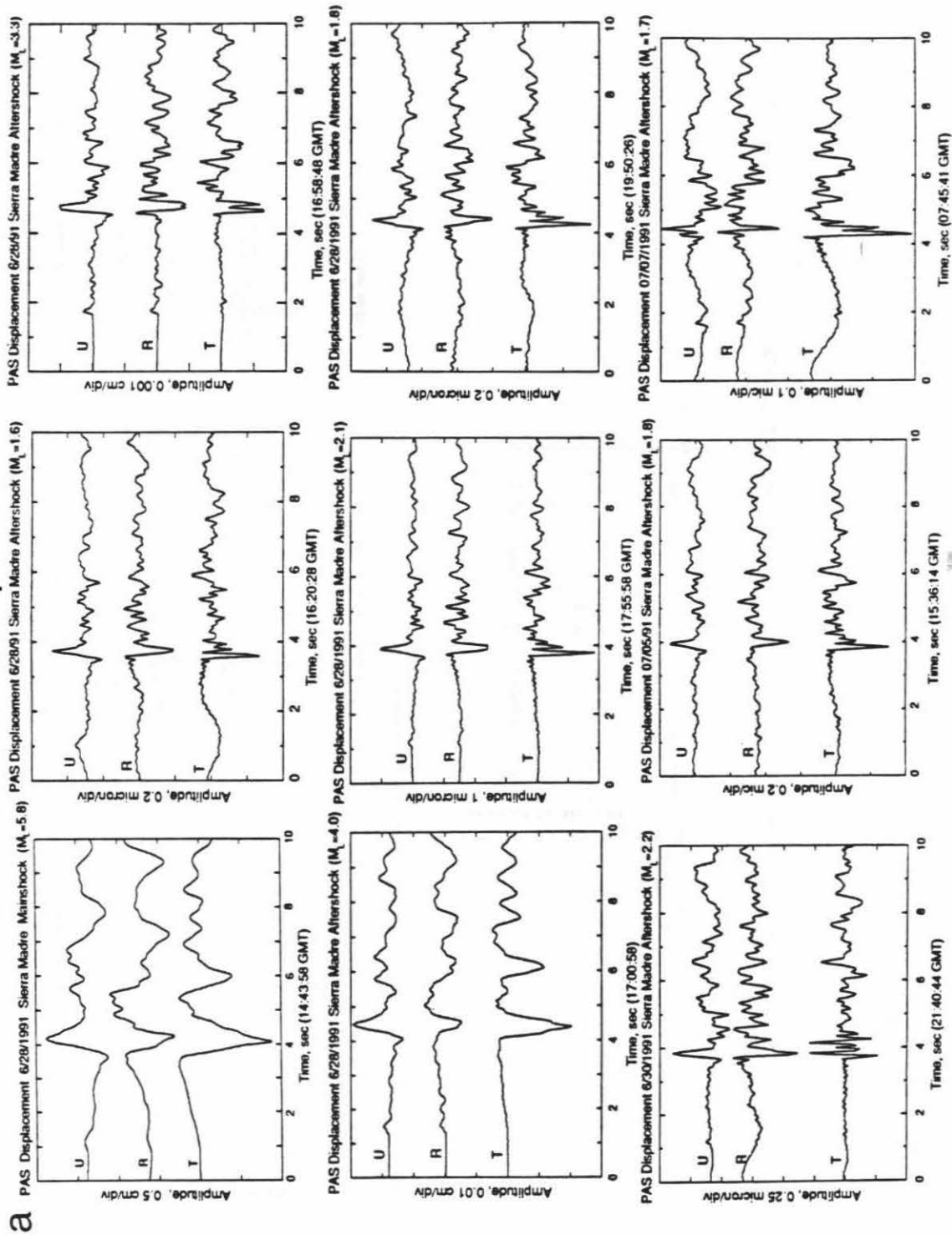
The waveform of event 3 in Group I is particularly similar to that of the mainshock. This is one of the largest aftershocks with a magnitude of 4.0. Other events in Group I have magnitudes 1.6 to 3.3. They show a downward double-peaked S wave on the tangential component. Event 6 has a nodal SH wave.

There are five events in Group II (Figure 5.2b) which are essentially similar to those of Group II, except that the P-wave shows a small downward motion. The small P waves in Group I and II suggest that the PAS station is close to the node of the P-wave radiation pattern. Group III (Figure 5.2c) has three events with distinct upward P wave motion, and an S wave with positive transverse component and negative radial component. Event 1 in this group is with a magnitude of only 1.5 and the record is very noisy. Group IV (Figure 5.2d) has two small events with magnitudes of 1.6 and 1.5. They also show noisy waveforms and the polarities of P and S wave motions are similar to those of Group I. However, the amplitude of the P wave on the vertical component is about the same as that of the S wave. Group V (Figure 5.2e) has three events. The waveforms of events 1 and 2 have different polarities of P, SV and SH from those of any other aftershocks. The waveforms of the third event in Group V are similar to those in Group II. However, the location of this event is farther east from the cluster of Group II (Figure 5.5).

The rotated displacement records for the 6 events recorded at MWC are shown in Figure 5.3. They show distinct P and S wave motions. Three events in Group I were recorded by the portable instrument. Since the MWC station is close to the nodes of the events, despite the similarity in waveforms of the events at PAS station, the waveforms of the three events at MWC are different.

Figure 5.2: Rotated displacement records of the mainshock and 21 aftershocks in 5 groups. The amplitude scale indicates the true ground motion amplitudes. a): Rotated displacement records of the mainshock and 8 aftershocks of Group I.

Group I



# Group II

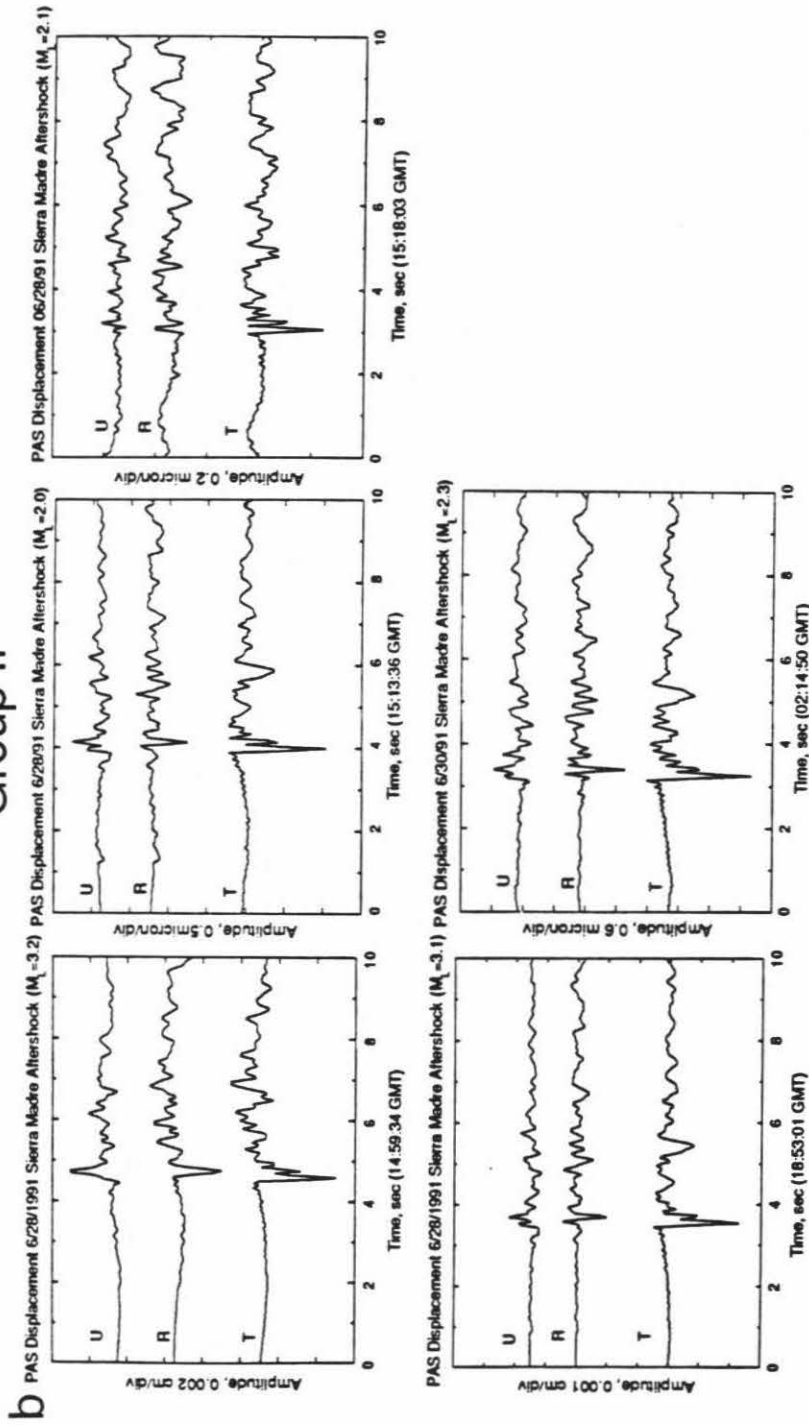


Figure 5.2b): Rotated displacement records of the 5 aftershocks of Group II.

## Group III

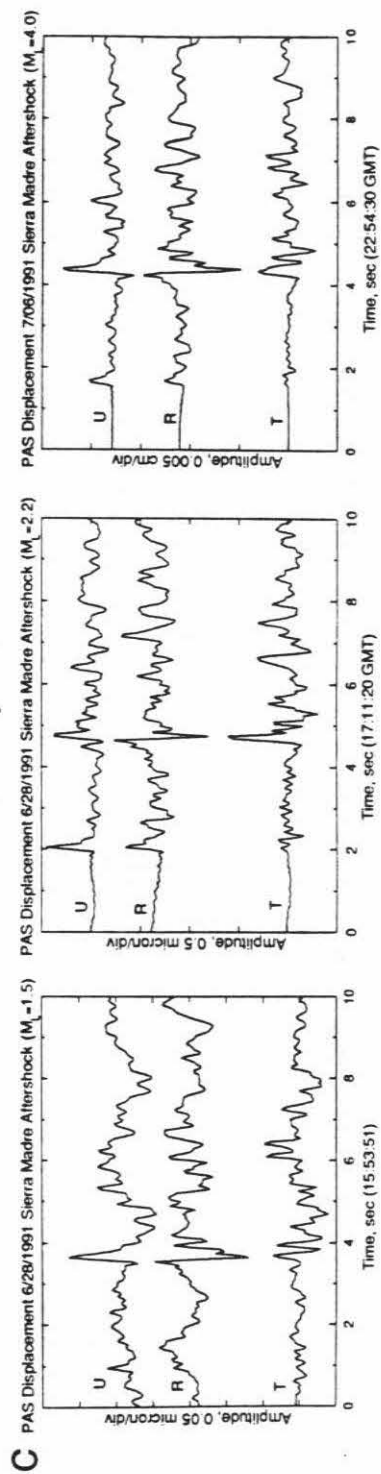
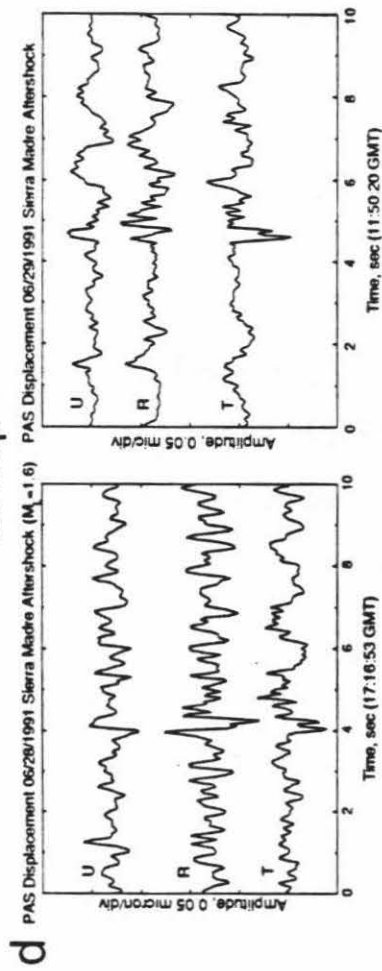


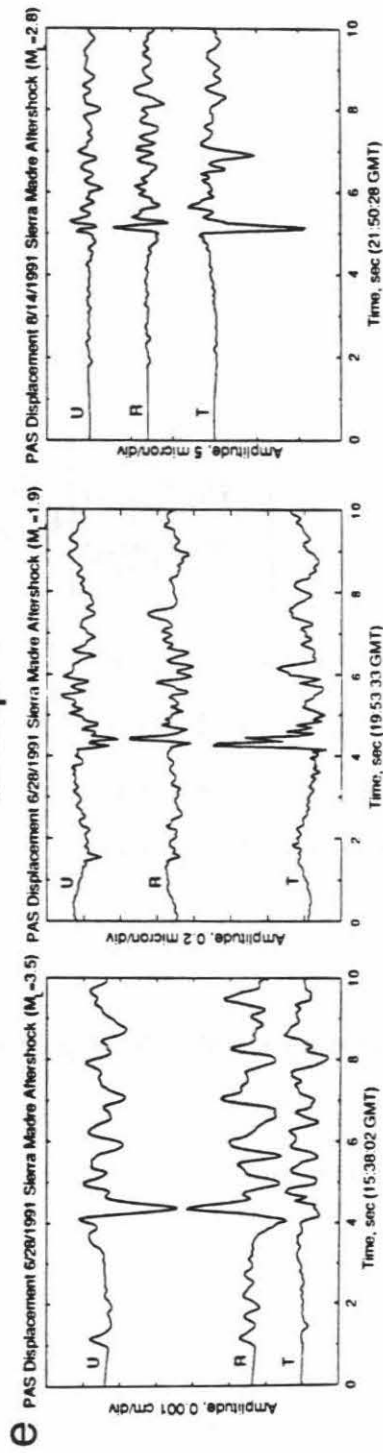
Figure 5.2c): Rotated displacement records of the 3 aftershocks of Group III.



## Group IV



## Group V



127

Figure 5.2d): Rotated displacement records of the 2 aftershocks of Group IV. e): Rotated displacement records of the 3 aftershocks of Group V.

## 5.4 Method

The method used in this study is essentially the same as that used by Ma and Kanamori (1991). The P, SV, and SH far-field displacements,  $U_r$ ,  $U_\theta$ , and  $U_\phi$ , from a double-couple point source are given by

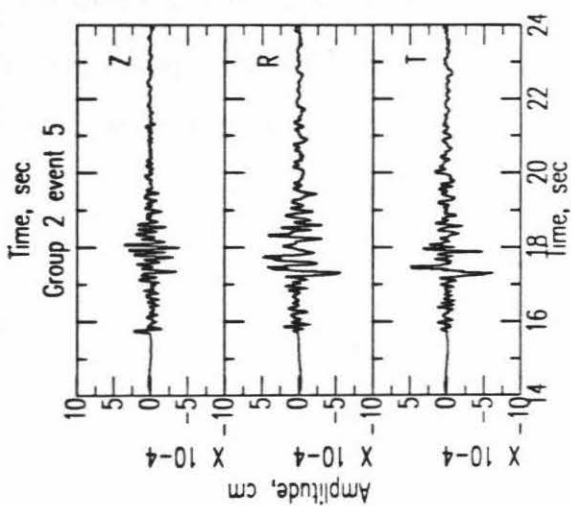
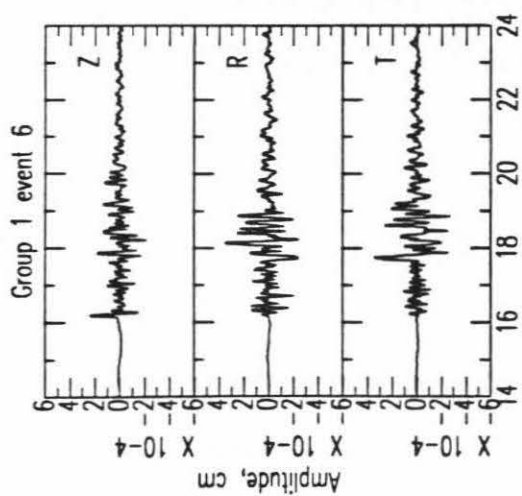
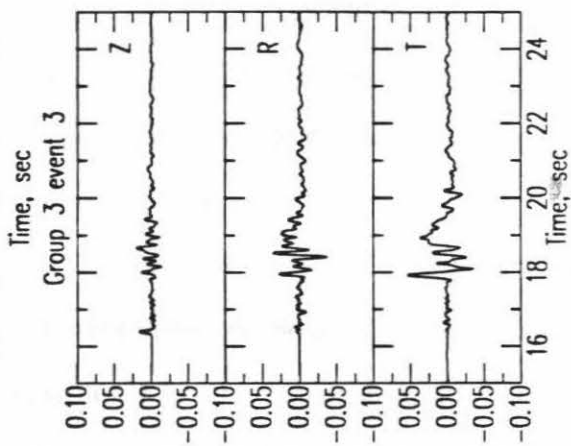
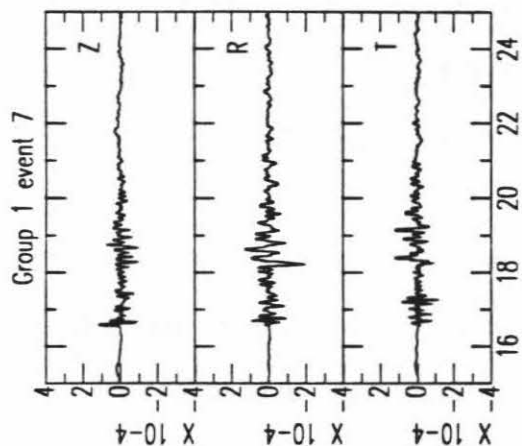
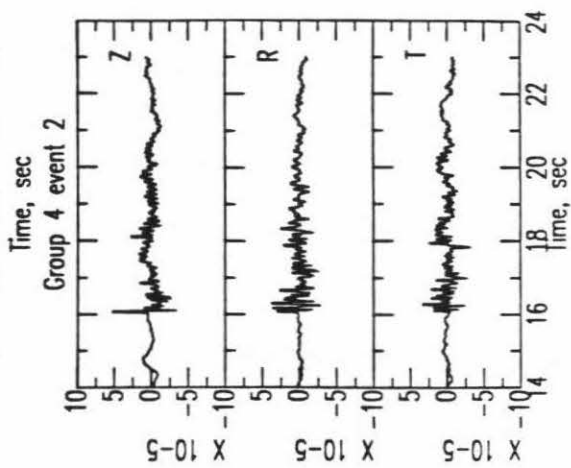
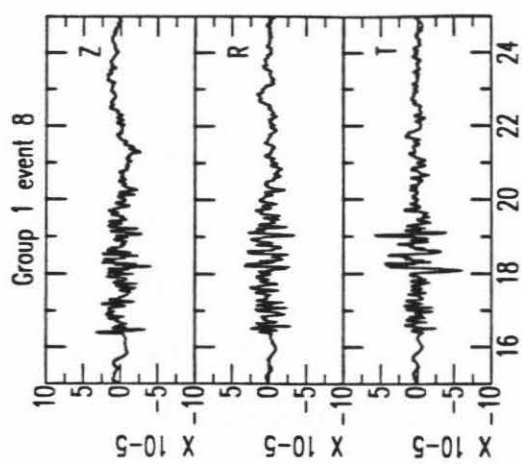
$$\begin{bmatrix} U_r \\ U_\theta \\ U_\phi \end{bmatrix} = \frac{M_0 s(t)}{4\pi\rho r\alpha^3} \begin{bmatrix} R^P \\ (\alpha/\beta)^3 R^{SV} \\ (\alpha/\beta)^3 R^{SH} \end{bmatrix}, \quad (1)$$

where  $s(t)$  and  $M_0$  are the unit moment rate function and the seismic moment, respectively. Here,  $\rho$ ,  $\alpha$ , and  $\beta$  are density, P velocity, and S velocity, and  $R^P$ ,  $R^{SV}$ , and  $R^{SH}$  are P-wave, SV-wave and SH-wave radiation patterns respectively. The radiation patterns are functions of the fault parameters: dip  $\delta$ , rake  $\lambda$ , and strike  $\phi$ . We use (1) to determine  $M_0$ ,  $\delta$ ,  $\lambda$ , and  $\phi$  from  $U_r$ ,  $U_\theta$ , and  $U_\phi$  estimated from the observed P, SV, and SH amplitudes and polarities.

Let  $U_P$ ,  $U_{SVZ}$ ,  $U_{SVR}$ , and  $U_{SH}$  be the displacements of P wave on the vertical component, the SV wave on the vertical component, the SV wave on the radial component, and the SH wave on the tangential component, respectively, observed at the free surface, then

$$\begin{aligned} U_r &= U_P / (2\cos i_0) \\ U_\theta &= U_{SVZ} / (-2\sin i_0) = U_{SVR} (2\cos i_0) \\ U_\phi &= U_{SH} / 2, \end{aligned} \quad (2)$$

Figure 5.3: Rotated displacement records for the 6 events recorded by portable instrument at MWC station. The amplitude scale indicates the true ground motion amplitude.



where  $i_0$  is the incidence angle. The free-surface effect is approximated by a factor of 2 of amplification of the incidence wave. If P-SV conversion at surface is considered,  $U_r$  and  $U_\theta$  become more complex functions of the incidence angle. Since the effect of the free surface is generally smaller on the vertical component than on the radial component, we estimated  $U_\theta$  from the vertical component.

In this study, we use only the stations which are close to the epicenter. The propagation effect is simple and the approximation mentioned above is satisfactory. If only one station is available, the number of parameters, 4, is larger than the number of data, 3, in equation (1), and the solution of (1) is nonunique; thus, we obtained the solution by combining the waveform and first-motion data. If there were more than one station available, the solution of (1) could be obtained without using the first-motion data.

We determined the loci of the P and T axes, here called the inversion P-T loci (Figure 5.4), which are consistent with the observed amplitudes and polarities of P, SV and SH waves. We combined the inversion P-T loci with the first-motion data recorded by SCSN (Figure 5.4), using the program FPFIT (Reasenber and Oppenheimer, 1985). The program FPFIT determines the mechanism and the range of P and T axes that fit the first-motion data equally well. These ranges are called the first-motion P-T ranges (Figure 5.4). If the inversion P-T loci pass through the first-motion P-T ranges, any solution for which the P and T axes lie in the overlapping region can satisfy both the first-motion and waveform data. If the inversion P-T loci did not pass through the first-motion P-T ranges, we chose a point on the inversion P-T loci that is closest to the first-motion P-T ranges. Since the magnitude of some of the aftershocks are in the range of 1.5 to 3, the number of first-motion data available is small. For some small events, compressional and dilatation

first motions are mixed, suggesting ambiguous beginning of the first motion. The first-motion P-T ranges of these events are not reliable. If we assumed that the events with similar waveforms and locations in the same group have similar mechanisms, we could use the first-motion P-T ranges of the largest event in the group for the smaller events with poor first-motion data. For some small events, an alternative mechanism was determined using the first-motion data of the largest event in the same group. If there are two or more broadband stations available, we can solve the equation (1) using the standard method of least squares.

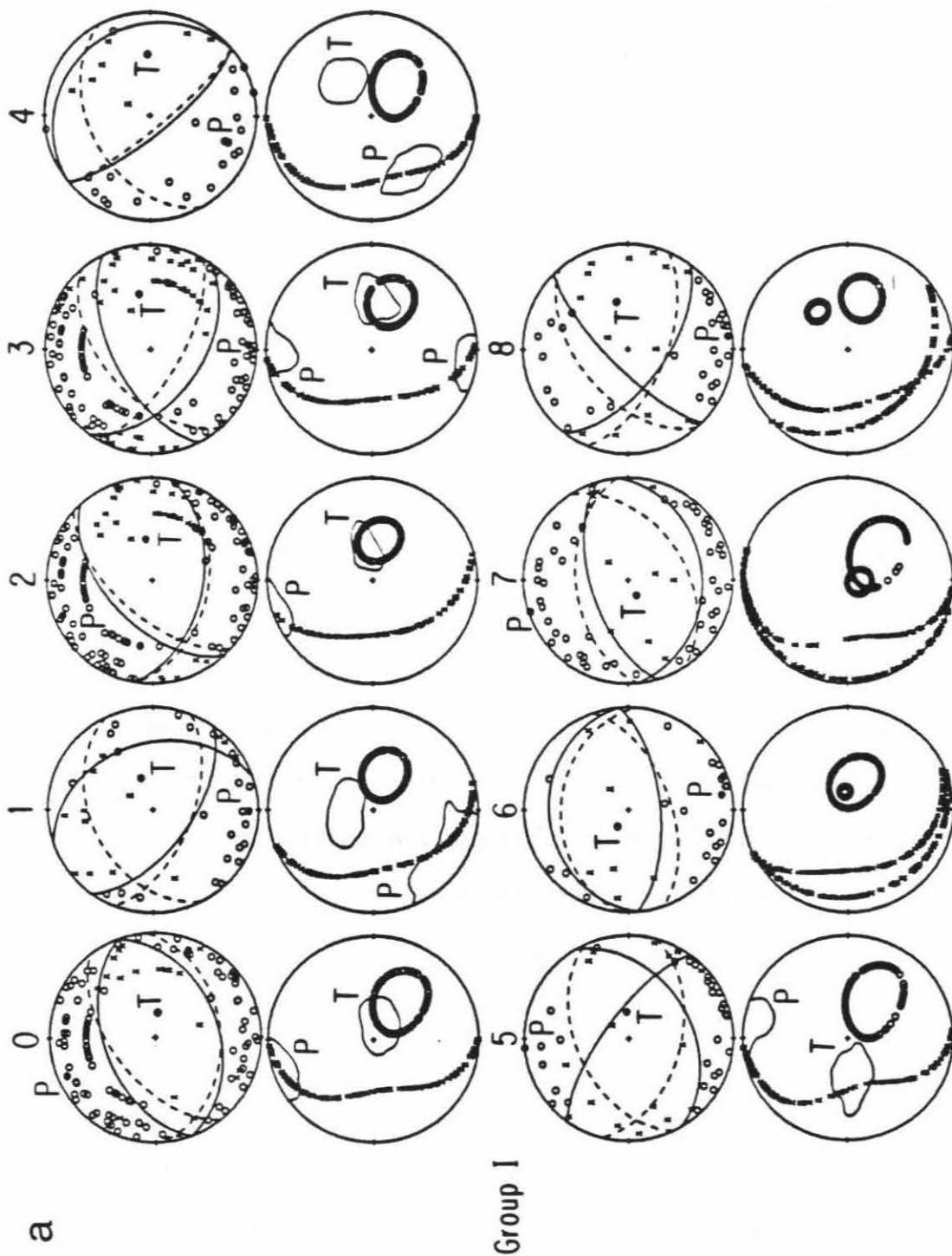
## 5.5 Results

### 5.5.1 Focal Mechanism and Seismic Moment Determination

The mechanisms determined from the method described above for Group I are shown in Figure 5.4a to compare with the solutions determined from the first-motion data alone. The mechanisms of event 6, 7 and 8 were determined from the waveform inversion of PAS and MWC stations. We also determined the mechanisms of event 6, 7 and 8 by combining the waveform and first motion data. The solutions are similar to that from inversion of waveforms at two stations; the difference is only  $5^\circ$  in strike.

The mechanisms of other events were determined by inverting the waveform at PAS and first motion data. Since the magnitude of event 4 and 5 are only about 2.1 and 1.8, the first motion data are sparse and less reliable. We also determined the mechanisms of these two events using first motion P-T ranges of the mainshock. The solutions thus obtained

Figure 5.4: The first-motion data recorded by the Caltech-USGS Southern California Seismic Network and the focal mechanisms determined from the first-motion data alone (solid curves) and the combined (first-motion and waveform) data (dashed curved) of the mainshock and 21 aftershocks of the 1991 Sierra Madre earthquake in five groups. The dot symbols indicate the P and T axes of our preferred solution. The figures beneath the first-motion data show the inversion P-T loci and the first-motion P-T ranges. The cross symbols and open circles indicate the compression and dilatation of first motions and P and T loci of inversion. a): The comparison of the mechanisms determined with our method and from first-motion data for mainshock and 8 aftershocks of Group I.





using first-motion P-T ranges of the mainshock are different by less than  $2^\circ$  in strike from those obtained using their own first motion P-T ranges. This is not surprising because of the similarities of the mechanisms of the mainshock and these events in Group I. The P and T axes of these mechanisms are close to or within the overlapping regions of inversion P-T loci and first-motion P-T ranges.

Except for events 1, 4 and 5, the mechanisms of the events in Group I thus determined are generally consistent with those from the first-motion data. These three events are very similar in waveforms (Figure 5.2a) and locations (Figure 5.5), but the first motions are very different, especially in the second quadrant. This difference indicates that the fault motion in the beginning was different from the overall fault mechanism. The solution from the waveform data represents the overall mechanism. In general, the mechanisms of the events in Group I thus obtained are similar to each other with a thrust fault mechanism.

The mechanisms obtained for Group II are shown in Figure 5.4b to compare with the solutions from the first-motion data alone. Except for event 3 and 5, the inversion P-T loci overlap with the corresponding first-motion P-T ranges. The solutions thus determined for these events can explain the waveform and first-motion data fairly well. The mechanisms for the three events are in general consistent with those from first motions. The P and T axes of the mechanism for event 3 were chosen from the point on the inversion P-T loci which is close to the first-motion P-T ranges. The resulting solution is very different from that from the first-motion data. Our solution has thrust fault mechanisms similar to those of the mainshock and other events in Group II. This event has mostly compressive first motions for the stations with azimuths from  $180$  to  $270^\circ$ , while the other events in Group II have mostly dilatational first motions in the same regions. This discrepancy suggests that either the first motions of the magnitude 2.1 event are not reliable, or the

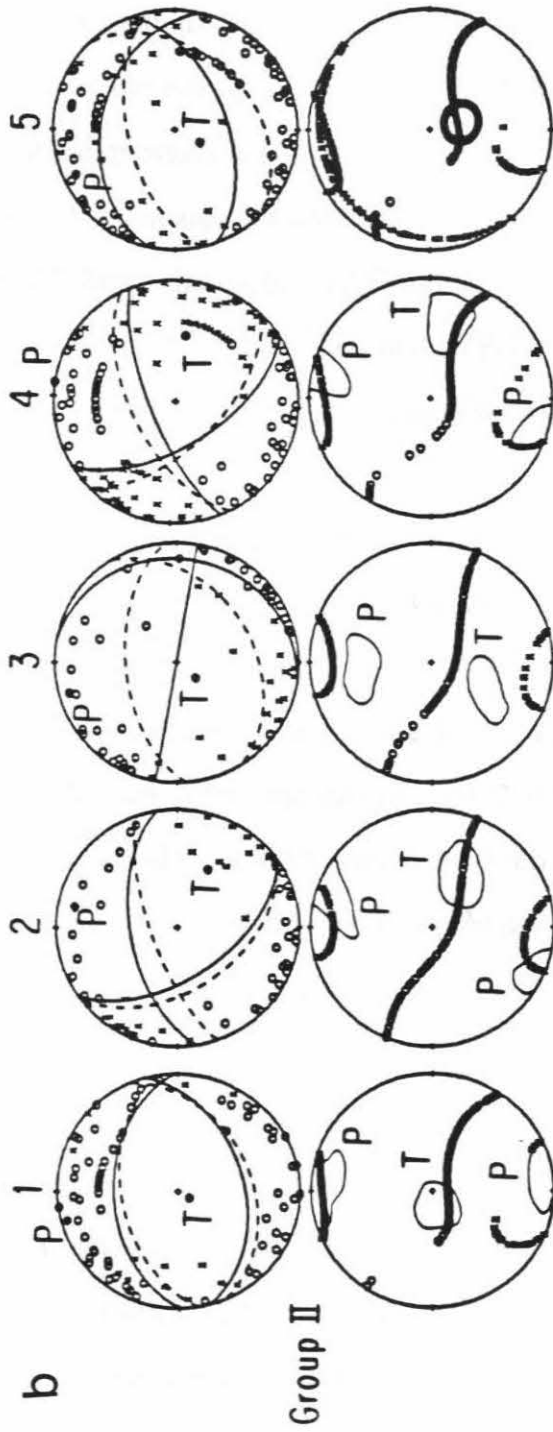


Figure 5.4b): The comparison of the mechanisms determined with our method and from first-motion data for 5 aftershocks of Group II.

beginning of fault motion is different from the overall faulting mechanism as we discussed for Group I. The mechanism for event 5 was determined from the waveform inversion of PAS and MWC stations. The solution is similar to that from first-motion data. The overall mechanisms of the events in Group II thus determined show thrust fault mechanisms similar to those of events in Group I.

Figure 5.4c compares our solutions with that from the first-motion data for the events in Group III. Since the event 1 of Group III is with a magnitude of only 1.5, the first motions are very sparse and the first-motion P-T ranges are very large. The solution from waveform inversion and first-motion data of the events in Group III show more strike-slip motion with a very steep fault plane.

The mechanisms for the two events in Group IV shown in Figure 5.4d were determined by inverting the waveforms at PAS and MWC stations. Since they are very small, the mechanisms from the first-motion data are not available. The waveform data at MWC station for event 1 are not available. Because of the similarity in waveforms and locations of the two events, the data of event 2 at MWC station were used in event 1 to combine with the data at PAS station to determine the mechanism of event 1. The mechanisms thus obtained for the events in Group V (Figure 5.4e) are similar to those from the first-motion data. These events have strike-slip mechanisms which are very different from that of any other aftershocks.

Figure 5.5 shows the spatial distribution of the main shock and the aftershocks of the Sierra Madre earthquake sequence with focal mechanisms shown in equal-area projections of the lower focal hemisphere. Most of the events (Group I and II) are located within 5 km west of the mainshock. They are similar to the mainshock in waveforms. The mechanisms thus determined for these events are thrust faulting and are essentially similar to that of the

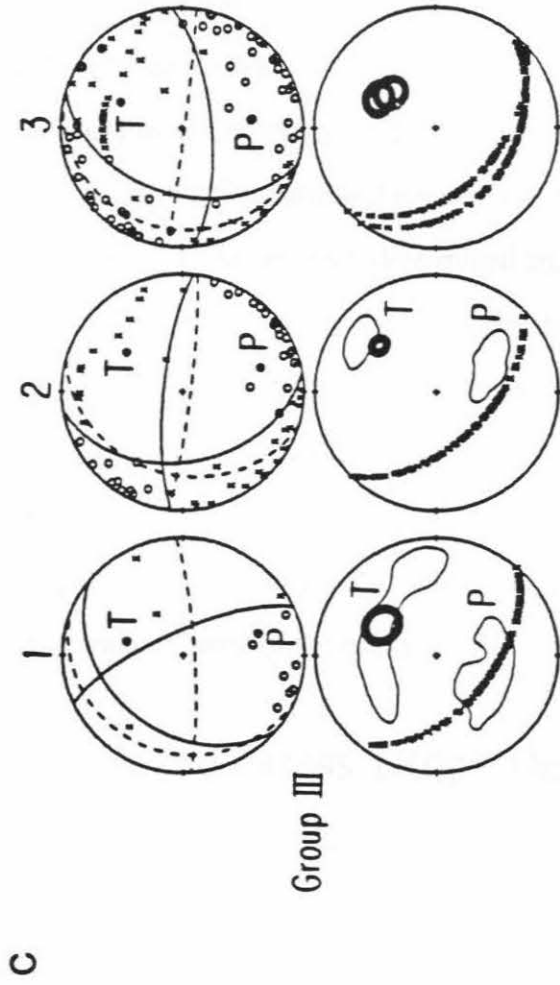


Figure 5.4c): The comparison of the mechanisms determined with our method and from first-motion data for 3 aftershocks of Group III.

mainshock. The events located right below the mainshock show the combination of strike-slip and thrust faulting mechanisms. A few aftershocks located to the east of the mainshock have strike-slip mechanisms. The location and mechanism of the mainshock and aftershocks suggest that the Sierra Madre earthquake sequence probably occurred on the Clamshell-Sawpit fault. The different mechanisms of some of the aftershocks indicate a complex structure of the fault (Hauksson and Jones 1991).

The focal mechanisms and seismic moments of the mainshock and aftershocks of the Sierra Madre earthquake thus determined are listed in Table 5.1. We compared the ratio of cumulative seismic moments of the aftershocks to that of the mainshock for the Sierra Madre earthquake sequence with the ratios for 13 other earthquake sequences in California. The method is similar to that of Ma and Kanamori (1991). The ratio for the Sierra Madre sequence is about 1/50 which is larger than the ratio, 1/1000, for the 1988 Pasadena earthquake sequence, but is smaller than that for most earthquakes in California. The average ratio of most of the events in California is about 1/5.

### 5.5.2 Q and Stress Drops Determination

The quality factor,  $Q$ , of the crust, a measure of the attenuation property, is an important parameter of the crust besides the seismic velocities for understanding wave propagation in the crust. Also the attenuation property provides information about the degree of fracture in the crust. The broadband waveform observed at short distance contains information about the source dimension and the attenuation characteristics of the medium along the path. Here we attempt to use broadband data observed at short distances to determine the attenuation property of the crust and stress drops of earthquakes. The stress drop which is determined

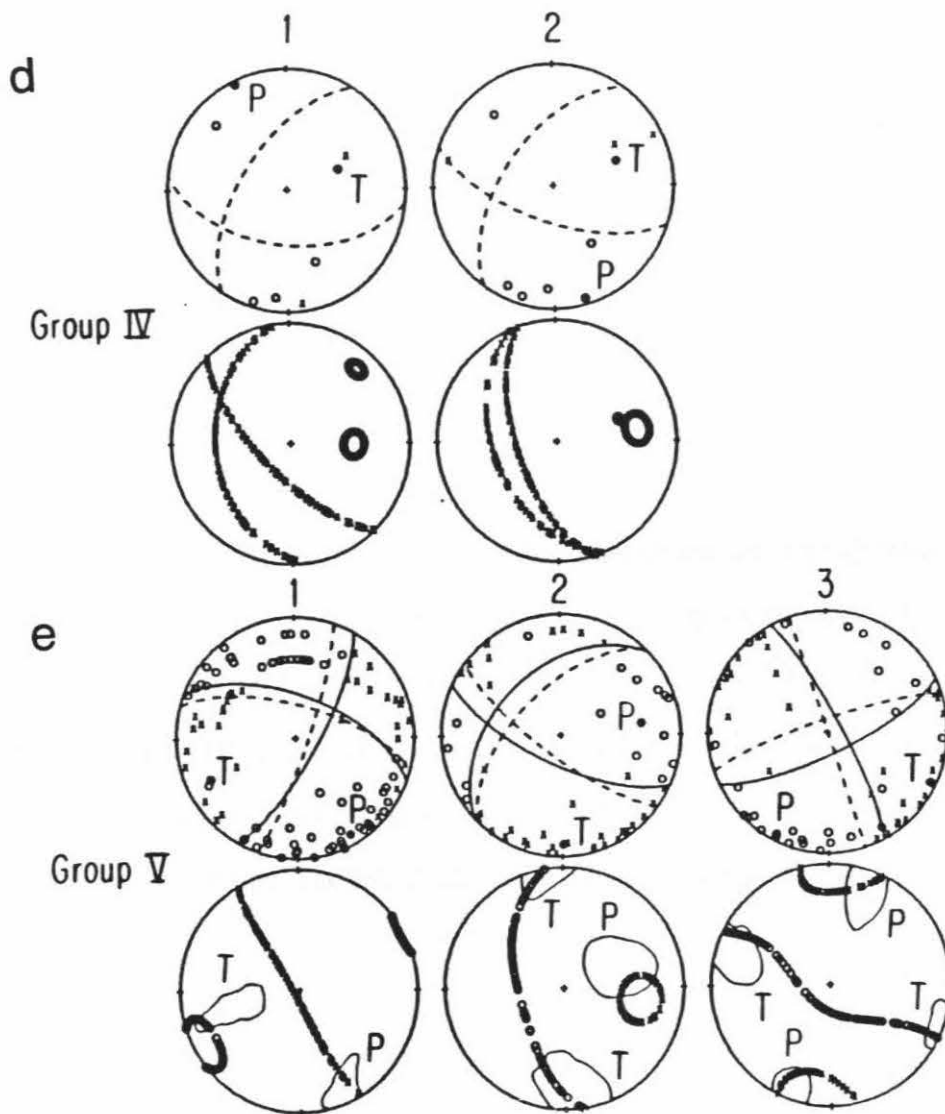


Figure 5.4d): The comparison of the mechanisms determined with our method and from first-motion data for 2 aftershocks of Group IV. e):The comparison of the mechanisms determined with our method and from first-motion data for 3 aftershocks of Group V.

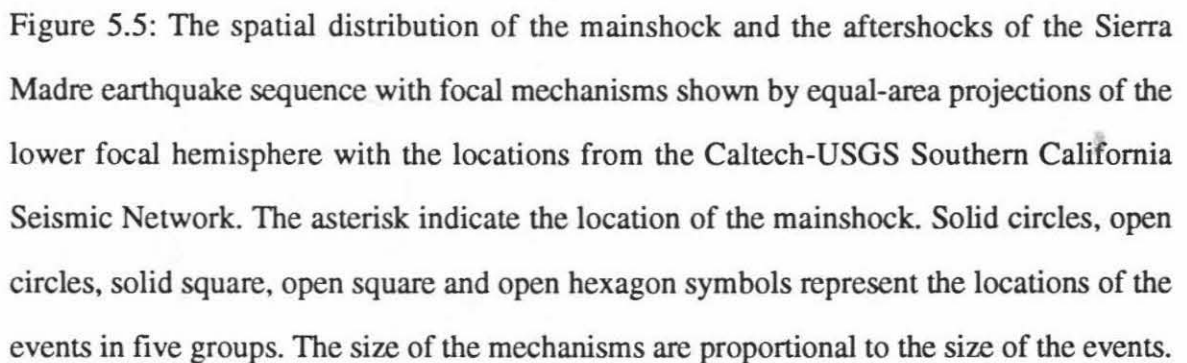
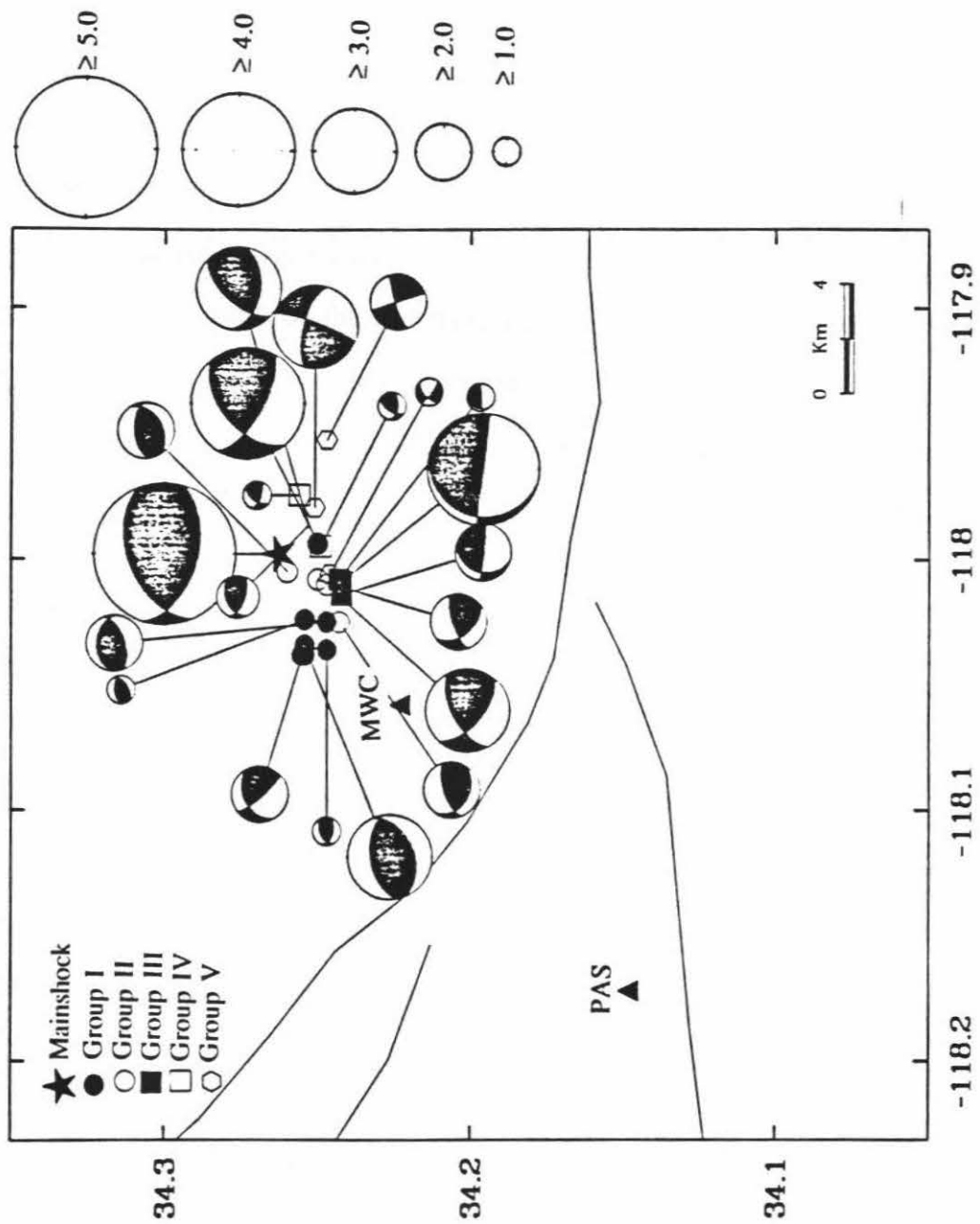


Figure 5.5: The spatial distribution of the mainshock and the aftershocks of the Sierra Madre earthquake sequence with focal mechanisms shown by equal-area projections of the lower focal hemisphere with the locations from the Caltech-USGS Southern California Seismic Network. The asterisk indicates the location of the mainshock. Solid circles, open circles, solid square, open square and open hexagon symbols represent the locations of the events in five groups. The size of the mechanisms are proportional to the size of the events.





from the seismic moment and the source dimension provides information about the state of stress in the fault zone. Although the detailed relationship between the tectonic stress field and earthquake stress drops is not known, stress drop is still a fundamental property of earthquakes and it is important to determine it for different tectonic provinces.

If there is no attenuation (i.e., if the medium is perfectly elastic), the width of the observed seismic pulse (P or S waves) is in general proportional to the source dimension. However, the actual waveform and pulse depend on the details of the rupture geometry and the pulse width depends on the various rupture parameters such as the rise time of local dislocation function, rupture length, rupture mode (unilateral, bilateral, etc.), and the source complexity. Nevertheless, on the average, one would expect a linear relationship between the pulse width and the source dimension, and many studies have been made using an average relationship between the pulse width and the source dimension. For example, Cohn et al. (1982), using a circular fault model of Brune (1970), obtained the relation

$$\tau = 2.62a/\beta, \quad (2)$$

where  $\tau$  is the source time duration in seconds,  $a$  is the radius in km and  $\beta$  is the shear velocity in the vicinity of the source. For a circular fault, the stress drop,  $\Delta\sigma$ , is written as

$$\Delta\sigma = \frac{7M_0}{16a^3} \quad (3)$$

(Eshelby 1957) where  $M_0$  is the seismic moment. Substituting  $\tau$  in (2) to (3). We obtain

$$\tau = \frac{5.69 \times 10^{-8} (M_o)^{1/3}}{(\Delta\sigma)^{1/3}} \quad (4)$$

for a shear velocity of 3.5 km/sec. As is evident from its derivation, equations (2), (3) and (4) should be considered valid only in average sense. Nevertheless equation (4) can be used to estimate average stress drops of regional events from the pulse width.

If attenuation is included, the pulse width of the observed waveform increases as  $Q$  decreases. For a given  $\tau$  and  $Q$ , we can compute the waveform at the station by convolving a triangle source time function with the Futterman  $Q$  operator (Futterman, 1962). Since the observed pulse shape is usually not a simple triangle function, we define the equivalent width  $W_e$  by the expression

$$W_e = \frac{\left[ \int f(t) dt \right]^2}{\int [f(t)]^2 dt} \quad (5)$$

where  $f(t)$  is the time history of the wavelet of which the pulse width is to be estimated. This expression is analogous to a similar expression used in Blackman and Tukey (1958) to define the effective width of a power spectrum.

Since most of the events for the Sierra Madre earthquake sequence are in the node of the radiation pattern of P wave, the P waves are usually small. To avoid the effect of P-SV conversion at the free surface, we measured the pulse width of S wave on the transverse components. The curves in Figure 5.6 show the relation between  $W_e$  and  $M_o$  for various stress drops and  $Q$ . If seismic moment is less than about  $10^{20}$  dyne-cm, the pulse width is essentially determined by  $Q$  and  $W_e$  tends to a constant value regardless of  $\Delta\sigma$ . We compared  $W_e$  computed for various values of  $Q$  and  $\Delta\sigma$  to that of the observed and

### Sierra Madre Earthquake Sequence

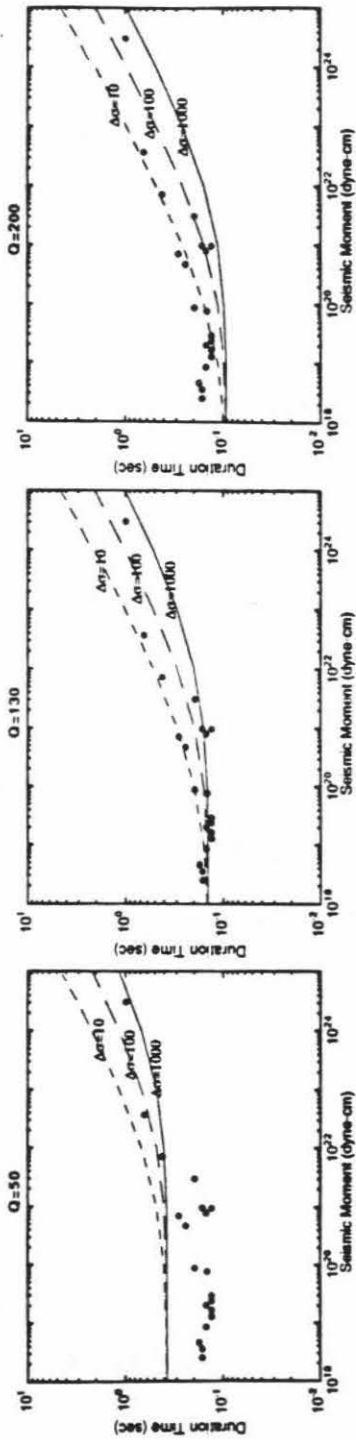


Figure 5.6: The comparison of the observed pulse width (SH waves) with those computed for three different stress drops 10, 100, and 100 bars and for three Q values  $Q=50$ , 130 and 200 for the Sierra Madre earthquake sequence.

determined the average  $Q$  along the path from the hypocenter to PAS and  $\Delta\sigma$  of the events.

For events with a seismic moment less than  $10^{20}$  dyne-cm, the observed data fit the curve for  $Q=130$ . Since we assumed that the observed pulse width of the S wave represent the narrowest pulse width at PAS after the consideration of  $Q$ , the  $Q$  value thus obtained is considered as a lower bound of  $Q_{\beta}$  along the path to the PAS station. The stress drop of the mainshock is about 500 bars. Most of the aftershocks with seismic moments larger than  $10^{20}$  dyne-cm have stress drops between 10 to 100 bars, which are much smaller than the stress drop of the mainshock and comparable to the stress drops of most earthquakes (Kanamori and Anderson, 1975).

We apply the same method to the 1988 Pasadena earthquake. This earthquake occurred only about 5 km away from the PAS station. Figure 5.7 shows the comparison of the observed and computed pulse widths for various stress drops of 10, 100, and 1000 bars for different  $Q$  values of 50, 80, and 200. The average  $Q_{\beta}$  of 80 can explain the observed data generally well for events with seismic moments less than  $10^{20}$  dyne-cm. Kanamori et al. (1990) suggested that the 1988 Pasadena earthquake was a double event and consisted of two asperities. From the comparison in Figure 5.7, we obtained a stress drop of about 800 and 1500 bars for the two asperities and one asperity, respectively. Since most of the aftershocks of the 1988 Pasadena earthquake have seismic moments less than  $10^{20}$  dyne-cm, the stress drops of the aftershocks are difficult to determine.

The different  $Q$  values obtained from the Sierra-Madre and Pasadena earthquake sequences may be caused by the structure underneath the PAS station. The path from the hypocenters of the events of the Pasadena earthquake sequence to the PAS station is within the fault zone of the Raymond fault, and the average  $Q_{\beta}$  may be small. Dreger (1992) used  $Q_{\beta}$  of 300 bars in his waveform modeling at PAS station for the two large aftershocks of

### Pasadena Earthquake Sequence

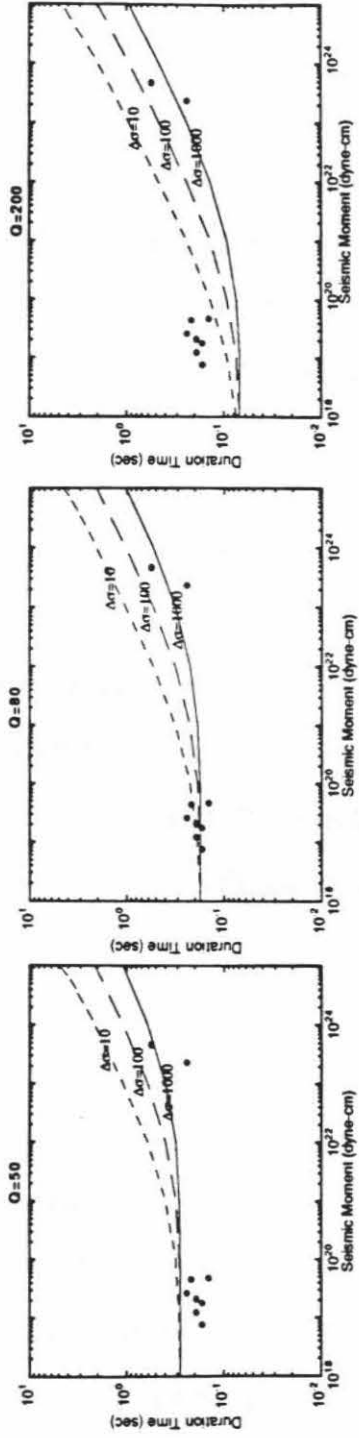


Figure 5.7: The comparison of the observed pulse width (SH waves) with those computed for three different stress drops 10, 100, and 100 bars and for three  $Q$  values  $Q=50$ , 80 and 200 for the Pasadena earthquake sequence.

the 1991 Sierra Madre earthquake. However, he suggested that the value of 300 bars might be too high.

## 5.6 Conclusions

We determined the focal mechanisms and seismic moments of the mainshock and 21 aftershocks of the June 28, 1991 Sierra Madre earthquake sequence by applying an inversion method to the waveform data with the first-motion data as constraints. We classified the events into different groups according to the location and waveform recorded at PAS station. The similarities in waveform of the events suggest similarities of the mechanisms and locations. Most of the aftershocks located within 5 km west of the mainshock are similar to the mainshock in waveform. The mechanisms thus determined for these events are essentially similar to that of the mainshock with thrust fault mechanism. A few aftershocks located to the east of the mainshock have strike-slip mechanisms and different waveforms. The mechanisms are overall consistent with thrust motion on the Clamshell-Sawpit fault, which is consistent with the result of Hauksson (1992). The small variation in mechanisms, especially to the east of the mainshock, of the aftershock suggests complexity of the structure. Some mechanisms from our waveform inversion are very different from those of first motion data. This suggests that the faulting mechanism in the beginning is different from the overall faulting.

The ratio of the cumulative aftershock seismic moment to the mainshock seismic moment of the Sierra Madre earthquake is smaller than that for most earthquakes in California. The average  $Q\beta$  values along the paths from the hypocenters of the Sierra Madre and Pasadena earthquake sequences to PAS station are about 130 and 80

respectively. The difference might be caused by the structure underneath the PAS station. The path for the 1988 Pasadena earthquake sequence is in the fault zone of the Raymond fault. The stress drop of the mainshock is about 500 bars. Most of the aftershocks have stress drops between 10 to 100 bars.

## Chapter 6

# Broadband Waveform Observation of the Joshua Tree-Landers Earthquake Sequence

### 6.1 Abstract

The Landers earthquake ( $M_w=7.3$ ) of 28 June, 1992 occurred at a depth of about 5~10 km and was preceded by the Joshua Tree ( $M_w=6.2$ ) earthquake of 23 April, 1992. TERRAScope stations recorded on-scale waveform data for many of the larger aftershocks of the two earthquakes. Since the PFO station (UCSD/TERRAScope station) is the closest among all the TERRAScope stations to the epicenters of the two mainshocks, it recorded the most complete aftershock data. We investigated the waveforms of broadband seismograms of the aftershocks ( $M_w \geq 3.5$ ) of the Joshua Tree and Landers earthquakes recorded at PFO and used the mechanisms, seismic moments, and depths of the events from surface wave inversion to examine the correlation between the waveforms and mechanisms. Since the depths were not determined very well, we examined the accuracy of depth determinations by comparing the amplitude ratio of surface wave to SH wave. In general, the events with similar waveforms and locations show similar mechanisms. The

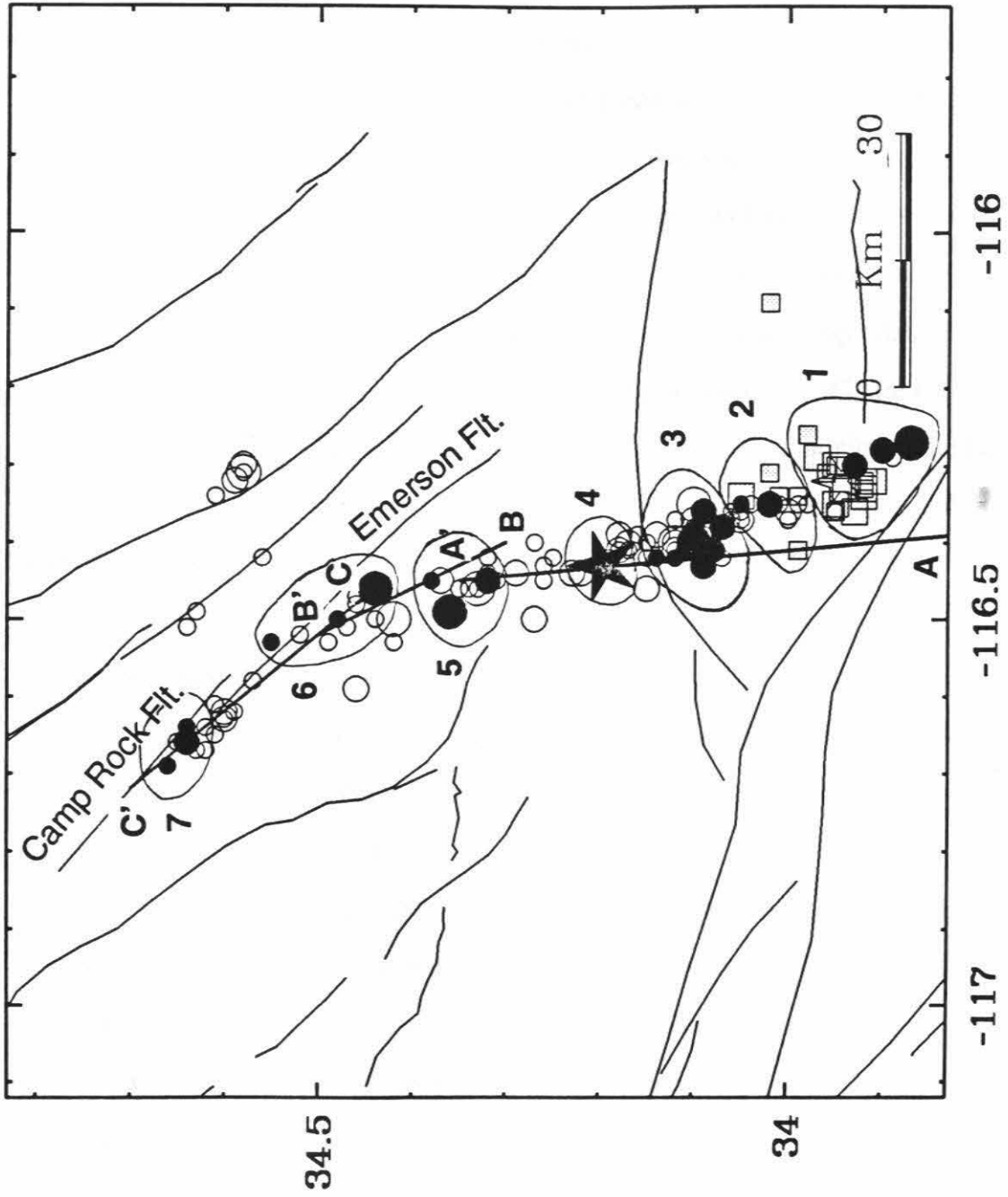


events to the south of the mainshock epicenter, including the aftershocks of the Joshua Tree earthquake, are similar in waveforms; their mechanisms determined with surface wave inversion are strike slip and similar to that of the mainshock of the Landers earthquake. The events to the north of the mainshock epicenter show dissimilar waveforms, and the mechanisms are very different suggesting heterogeneities of the stress field in the area. Only a few events occurred in the regions where large slip occurred during the mainshock. Almost 76% of the total energy of the aftershocks was released from the faults to the south of the mainshock epicenter. About 40% was from the region between the epicenters of the Landers and Joshua Tree earthquakes at a depth larger than 8 km, while 36% was from the south of the Joshua Tree epicenter at a depth equal or less than 10 km. For the Joshua Tree earthquake, most energy was released from the depths between 5 to 15 km. The ratio of cumulative seismic moment of the aftershocks to that of the mainshock is about 9/100 for the Joshua Tree earthquake, which is comparable to that of most events in California. The ratio for the Landers earthquake sequence is about 6/1000, which is much lower than the others.

## 6.2 Introduction

The June 28, 1992,  $M_w=7.3$ , Landers earthquake occurred at a depth of about 5-10 km in the southern Mojave Desert, California, and was preceded by the  $M_w=6.2$  Joshua Tree earthquake (Figure 6.1). The Joshua Tree earthquake occurred on 23 April, 1992 about 30 km to the south of the Landers earthquake. Two large aftershocks of the Landers earthquake occurred, one was 3 hours later near Big Bear Lake ( $M_w=6.2$ ) and the other was about a month later on or near the Pisgah fault ( $M=5.5$ ). These two earthquakes

Figure 6.1: Seismicity after the Joshua Tree earthquake for the period from 23 April to 27 June 1992 and after the Landers earthquake for the period from 28 June to 28 July 1992. The data are from the catalog of the Caltech-USGS Southern California Seismic Network (SCSN). The stars indicate the mainshocks of the Landers and Joshua Tree earthquakes. The open and solid circles indicate the aftershocks with  $M_L > 3.5$  recorded by Caltech-USGS SCSN and PFO UCSD/TERRAscope station, respectively, for the Landers earthquake. The shaded squares indicate the foreshock and aftershocks with  $M_L > 3.5$  for the Joshua Tree earthquake sequence. The bold lines indicate the profiles AA', BB', and CC'. The bold curves circle the events of different groups.



had their own set of aftershocks and were off the clusters of the Landers and Joshua Tree earthquakes.

The Landers earthquake caused an extensive surface break extending over 70 km with offset as large as 6.5 m. It is the largest event in Southern California since 1952. The aftershock zone extends 55 km to the north along a system of six different surficial faults and 40 km to the south of the mainshock's epicenter through the aftershock zone of the Joshua Tree earthquake. The mechanisms of the Landers and Joshua Tree earthquakes determined from moment tensor inversion of teleseismic long period surface waves (Kanamori et al. 1992) and 10-30 sec surface waves of TERRAScope data (Thio and Kanamori 1992), respectively, show similar strike-slip mechanisms (Figure 6.2b) which are consistent with those obtained from first-motion data. The deconvolution of the Landers earthquake seismogram using the empirical Green's function method suggested that the earthquake consists of two zones of large slip, hereafter called asperities, about 30 km apart (Kanamori et al. 1992). The slip distribution obtained by Wald et al. (1992) using strong motion data and surface offsets mapped in the field (Landers Earthquake Response Team, 1992) are in good agreement with this. The ratios of the energy to the moment indicates that the Landers earthquake belongs to the group of earthquakes with high stress drop and has a long repeat time (Kanamori et al. 1992).

In view of the unique characteristics of the Joshua Tree-Landers earthquake sequence, we examined the activity of the foreshocks and aftershocks to understand the entire rupture process of the earthquake sequence. Since the two large aftershock sequences, the Big Bear and Pisgah earthquakes, are off the main surficial ruptured faults, we only considered the earthquake sequences of the Landers and Joshua Tree.

Since the PFO station is the closest among all the TERRAScope stations to the

epicenters of the Landers and the Joshua Tree earthquakes, it recorded the most complete aftershock data. We investigated the data recorded at PFO and used the mechanisms, seismic moments and depths determined from moment tensor inversion using 10-30 sec surface wave of TERRAscope data (Thio and Kanamori 1992) to examine the correlation of the waveforms and mechanisms along the major fault zone. Since the depths are usually not determined very well, we examined the accuracy of the depths by comparing the amplitude ratios of surface waves to body waves of the events. We combined the mechanisms and seismic moments with the corrected depths to determine the distribution of energy released along the fault and depth.

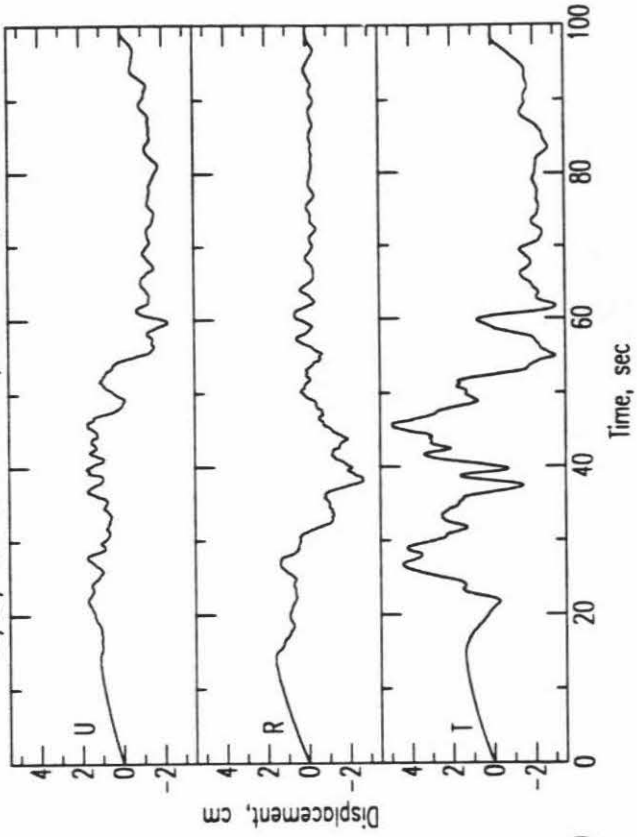
### 6.3 Data

For the Joshua Tree earthquake sequence, one foreshock and twenty four aftershocks with  $M_L \geq 3.5$  were recorded by the Caltech-USGS Southern California Seismic Network (SCSN) during the period from 23 April 1992 to the time of the mainshock of the Landers earthquake. Ninety one aftershocks with  $M_L \geq 3.5$  were recorded by SCSN during the period from 28 June to 28 July, 1992, for the Landers earthquake. Of these, fifty three events were recorded with the PFO UCSD/TERRAscope station in this area (Figure 6.1).

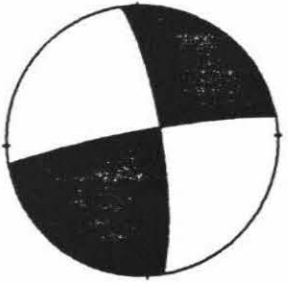
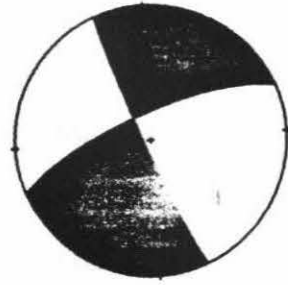
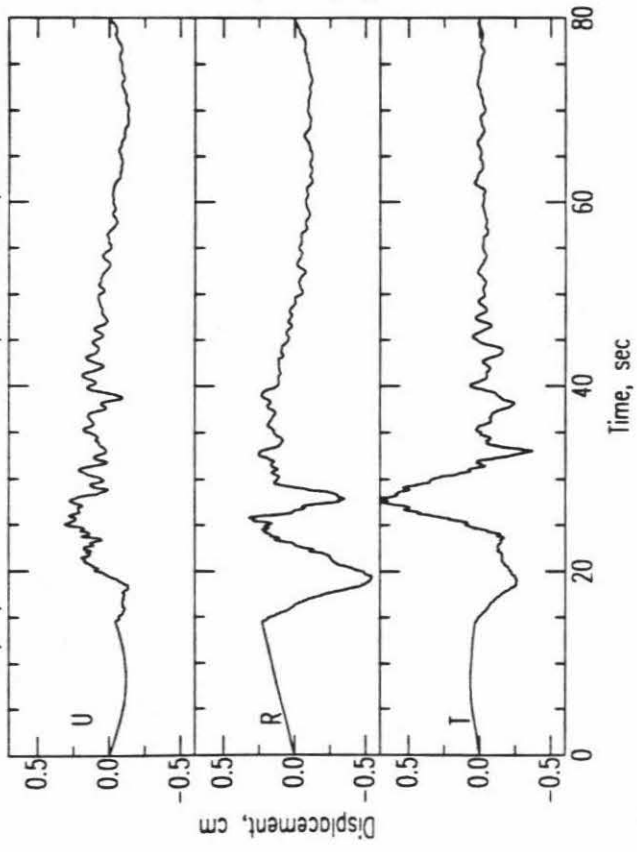
We rotated the original seismograms into the transverse and radial components, and integrated them to obtain ground motion displacement records. Figure 6.2a shows the displacement records at PFO station for the Joshua Tree earthquake, and the Landers earthquake. Since the very broadband channels clipped for these events, the data were retrieved from low-gain channels. Figure 6.2b shows the mechanisms of the Joshua Tree

Figure 6.2: (a) Rotated displacement records of the Landers and Joshua Tree earthquakes obtained from the low-gain channel of the PFO UCSD/TERRAscope station. (b) The mechanisms of the Landers and Joshua Tree earthquakes were determined by Kanamori et al. (1992) and Thio and Kanamori (1992).

06/28/1992 Landers Earthquake PFO Displacement



04/23/1992 Joshua Tree Earthquake PFO Displacement



a.

b.

and the Landers earthquakes determined from the moment tensor inversion of 10-30 sec surface waves of TERRAScope data (Thio and Kanamori 1992) and long-period surface waves of teleseismic data (Kanamori et al. 1992), respectively. The mechanisms are similar to those obtained from the first-motion data (Hauksson et al. 1992). The mechanisms and seismic moments of the events in this study used were determined from surface wave inversion using 10 to 30 sec surface wave of TERRAScope data (Thio personal communication, 1992). In most cases, the depth where the non-double couple component is minimized is close to the depth where the overall misfit measured by the RMS residual becomes minimum. If the two depths are very different, the average of the two is used for the depth of the event, but the solution is considered unreliable. The mechanisms, seismic moments and depths of the events determined from this method are listed in Table 6.1. For some events, the waveforms at PFO are available, but the mechanisms were not determined due to the noisy surface wave at other TERRAScope stations.

## 6.4 Results

### 6.4.1 Waveform and Mechanism Correlation

We classified the events of the Joshua Tree-Landers earthquake sequence into 7 groups according to the locations (Figure 6.1 and Table 6.1). In each group, we classified the events into several subgroups according to the waveforms recorded at PFO station. The classification was made by comparing the entire waveforms of the three components of the events. For convenience, we used the motions of P and S waves to distinguish the



Table 6.1. The origin time, location, fault parameters, seismic moments and depths of the Landers-Joshua Tree earthquake sequence in seven groups.

Table 6.1

No.	Date (y/m/d)	Time	Latitude (°N)	Longitude (°W)	Z (km)	Dip	Rake	Strike	M <sub>0</sub> (dyne-cm)
Group 1									
1	92/04/23	0225	33.94	116.33	12	86	20	76	3.5x10 <sup>22</sup>
2	92/04/23	1336	33.92	116.32	4	52	-13	-115	8.9x10 <sup>21</sup>
3	92/04/23	1806	33.94	116.30	13	85	7	87	3.2x10 <sup>21</sup>
4	92/04/23	1856	33.97	116.29	6	77	-14	-104	1.3x10 <sup>22</sup>
5	92/04/23	2352	33.98	116.26	4	75	-28	-101	3.2x10 <sup>21</sup>
6	92/04/25	0934	33.95	116.30	7	78	-22	-110	6.3x10 <sup>21</sup>
7	92/04/26	0626	33.92	116.33	4	50	-21	-114	5.0x10 <sup>22</sup>
8	92/04/27	0311	33.91	116.32	4	62	-51	-134	2.5x10 <sup>22</sup>
9	92/04/28	1113	33.92	116.32	5	48	-71	-151	8.9x10 <sup>21</sup>
10	92/04/28	1133	33.95	116.30	4	47	-56	-143	1.3x10 <sup>22</sup>
11	92/05/01	1338	33.92	116.33	10	39	-69	-140	4.5x10 <sup>21</sup>
12	92/05/02	1910	33.96	116.31	9	80	18	76	2.2x10 <sup>21</sup>
13	92/05/04	0116	33.93	116.36	9	43	-24	-138	1.3x10 <sup>22</sup>
14	92/05/04	1619	33.92	116.32	12	84	359	79	1.4x10 <sup>23</sup>
15	92/05/06	0238	33.92	116.34	10	24	-12	-104	7.1x10 <sup>22</sup>
16	92/05/18	0022	33.95	116.36	11	40	-30	-135	2.2x10 <sup>21</sup>
17	92/05/18	1544	33.95	116.35	5	40	-23	-126	1.4x10 <sup>23</sup>
18	92/06/29	1601	33.87	116.27	7	85	19	70	2.0x10 <sup>24</sup>
19	92/07/24	1814	33.90	116.28	8	84	-28	-105	2.5x10 <sup>23</sup>
20	92/07/25	0431	33.93	116.30	10	36	-42	-126	1.4x10 <sup>23</sup>
21	92/07/25	1702	33.94	116.31	15	54	4	-93	2.2x10 <sup>21</sup>
Group 2									
1	92/04/23	2256	33.99	116.34	13	85	4	36	3.2x10 <sup>21</sup>
2	92/04/24	0329	34.01	116.34	4	65	-30	-111	2.2x10 <sup>21</sup>
3	92/04/26	0308	34.02	116.31	15	56	-50	-147	1.6x10 <sup>21</sup>
4	92/04/26	1721	34.05	116.34	8	89	354	74	2.5x10 <sup>22</sup>
5	92/05/02	1246	33.99	116.41	5	89	330	70	4.5x10 <sup>21</sup>
6	92/06/30	1226	34.02	116.35	4	78	-35	-131	3.9x10 <sup>21</sup>
Group 3									
1	92/06/28	1236	34.14	116.42	16	72	-28	-112	1.2x10 <sup>24</sup>
2	92/06/28	1439	34.09	116.43	--	--	--	--	--
3	92/06/28	2023	34.12	116.42	26	69	-124	156	2.2x10 <sup>21</sup>
4	92/06/28	2213	34.05	116.35	9	86	25	48	5.3x10 <sup>21</sup>
5	92/06/29	1408	34.10	116.39	21	60	2	61	2.3x10 <sup>23</sup>

Table 6.1 Cont.

No.	Date (y/m/d)	Time	Latitude (°N)	Longitude (°W)	Z (km)	Dip	Rake	Strike	M <sub>0</sub> (dyne-cm)
6	92/06/29	1413	34.10	116.40	13	71	352	56	1.1x10 <sup>24</sup>
7	92/06/29	1431	34.09	116.35	8	57	-103	-165	2.1x10 <sup>21</sup>
8	92/06/29	1454	34.10	116.41	--	--	--	--	--
9	92/06/30	1130	34.09	116.41	18	87	10	73	1.5x10 <sup>22</sup>
10	92/06/30	1214	34.08	116.41	16	81	356	45	9.5x10 <sup>21</sup>
11	92/07/06	1200	34.09	116.36	8	82	-29	-117	2.8x10 <sup>22</sup>
12	92/07/06	1941	34.07	116.38	11	78	356	64	3.0x10 <sup>22</sup>
13	92/07/13	0500	34.08	116.41	--	--	--	--	--
Group 4									
1	92/07/20	0408	34.20	116.43	8	60	-6	-135	8.9x10 <sup>21</sup>
Group 5									
1	92/06/28	1240	34.36	116.49	--	--	--	--	--
2	92/06/30	1234	34.32	116.45	4	43	143	-51	4.9x10 <sup>21</sup>
3	92/07/02	0516	34.38	116.45	6	58	26	76	4.9x10 <sup>21</sup>
4	92/07/15	0018	34.33	116.46	3	54	201	28	6.3x10 <sup>21</sup>
Group 6									
1	92/06/28	1309	34.41	116.46	--	--	--	--	--
2	92/07/12	0535	34.55	116.53	4	72	-97	173	4.5x10 <sup>21</sup>
3	92/07/24	0723	34.48	116.50	20	65	-59	-163	3.2x10 <sup>21</sup>
Group 7									
1	92/06/29	2044	34.66	116.69	--	--	--	--	--
2	92/06/30	1726	34.64	116.66	5	53	-108	-177	1.2x10 <sup>22</sup>
3	92/06/30	2000	34.64	116.66	--	--	--	--	--
4	92/07/14	2036	34.64	116.64	1	5.6	5.1	-27	6.3x10 <sup>21</sup>

differences among the subgroups. However, some events with similar P-wave and S-wave motions were classified into different subgroups because of the difference in the later phases. Because of the structural complexity, there are still some minor differences between the events in the same subgroup. However, from the similarities of locations and waveforms, we expect that the events in the same subgroups have similar mechanisms.

There are 21 events in Group 1. Except for the event 5, 18, and 19, the locations of these events are within about 4 km radius of the epicenter of the Joshua Tree earthquake (Figure 6.3a). According to the waveforms at the PFO station, we classified them into five subgroups (Group 1a, 1b, 1c, 1d, and 1e). Figures 6.4a to 6.4e show the displacement waveforms of the events in Group 1. The events in Group 1a (Figure 6.4a: events 1, 3, 4, 6 and 12) show a downward P-wave motion and an S wave with negative (toward the epicenter) radial component and positive (counter-clockwise around the epicenter) transverse component. The events in Group 1b (Figure 6.4b: events 2, 6, 7, 15, 20 and 21) show similar P-wave and SH-wave motions but opposite SV-wave motion to those of the events in Group 1a. The events in Group 1c (Figure 6.4c: events 8, 9, and 10) show negative P-wave and S-wave motions on the three components. The events in this subgroup contain more long period component than the events in other subgroups with similar size. This suggests that these events have lower stress drops than others. The events in Group 1d (Figure 6.4d: events 11, 13, 16, and 17) show a small downward P-wave motion and an S-wave with positive radial component and negative transverse component. There are three events in Group 1e (Figure 6.4e: events 14, 18, and 19). Each of them is different from any other events in waveforms. Event 14 is a large aftershock of the Joshua Tree earthquake with  $M_w=4.7$ . Events 18 and 19 are two large aftershocks of

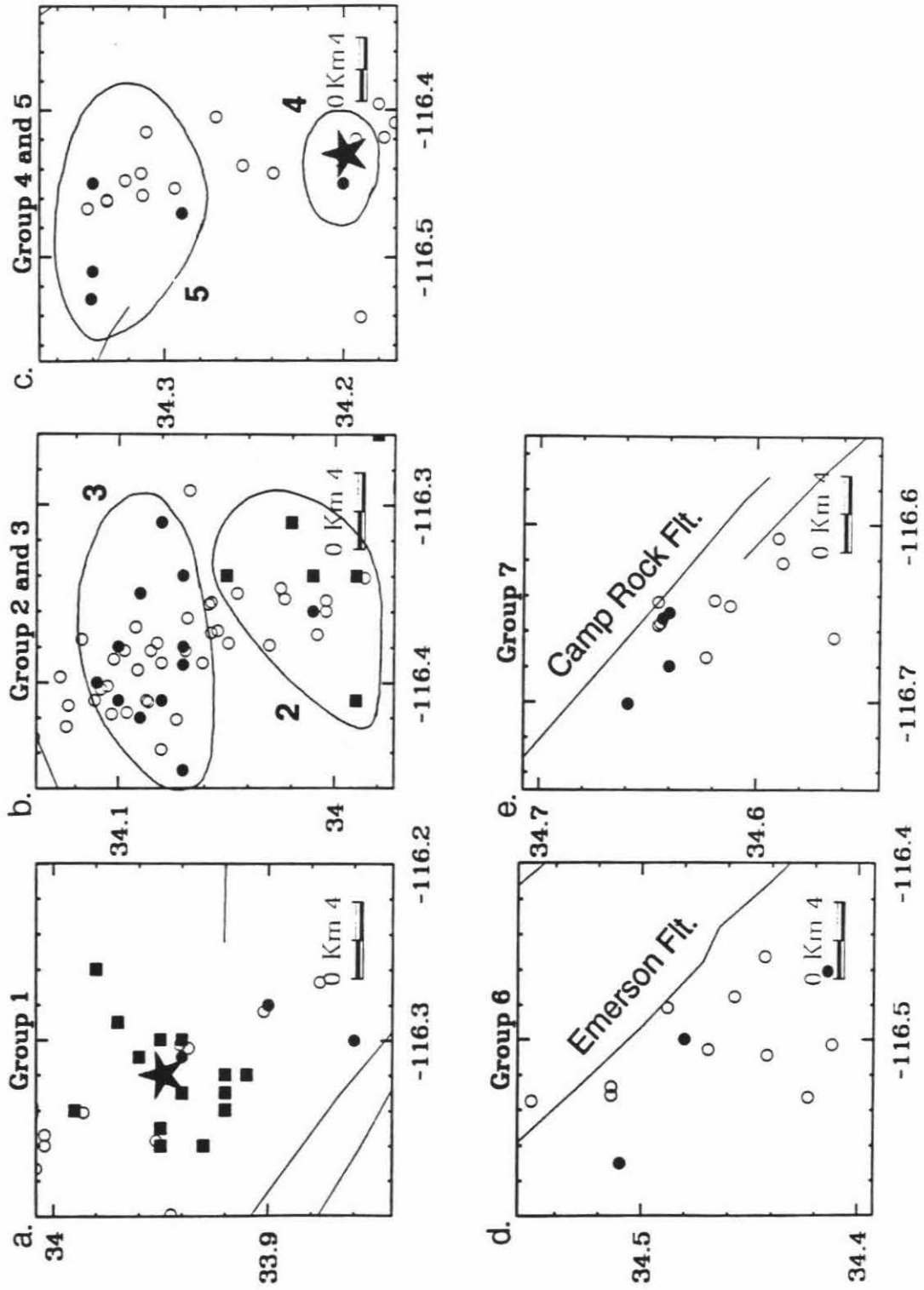
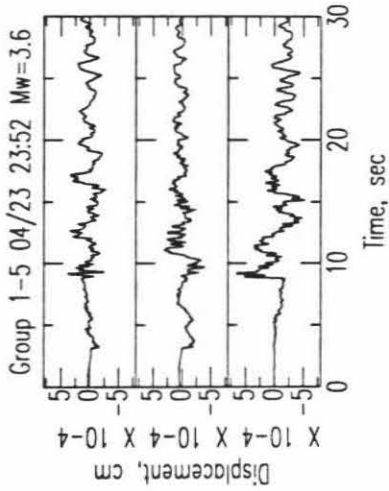
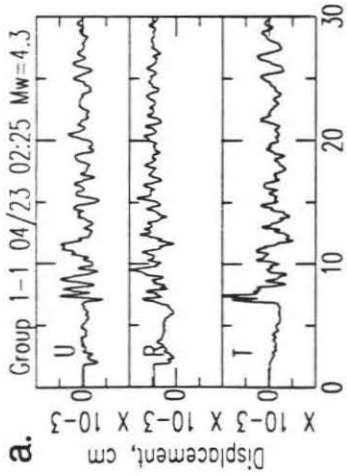
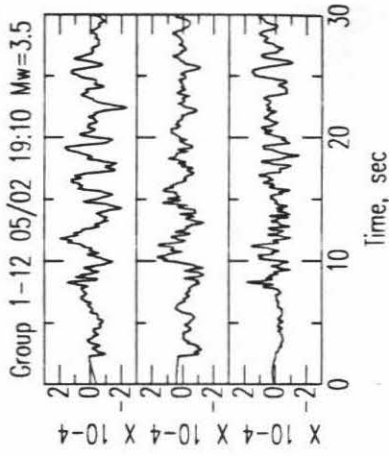
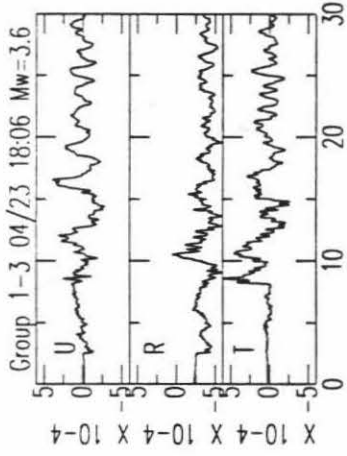
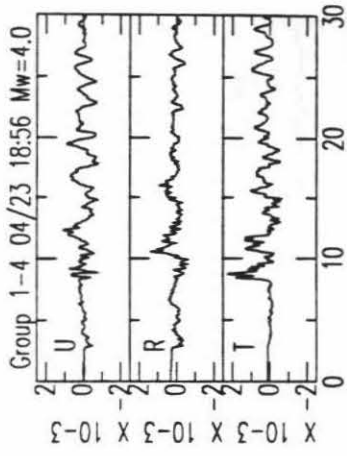
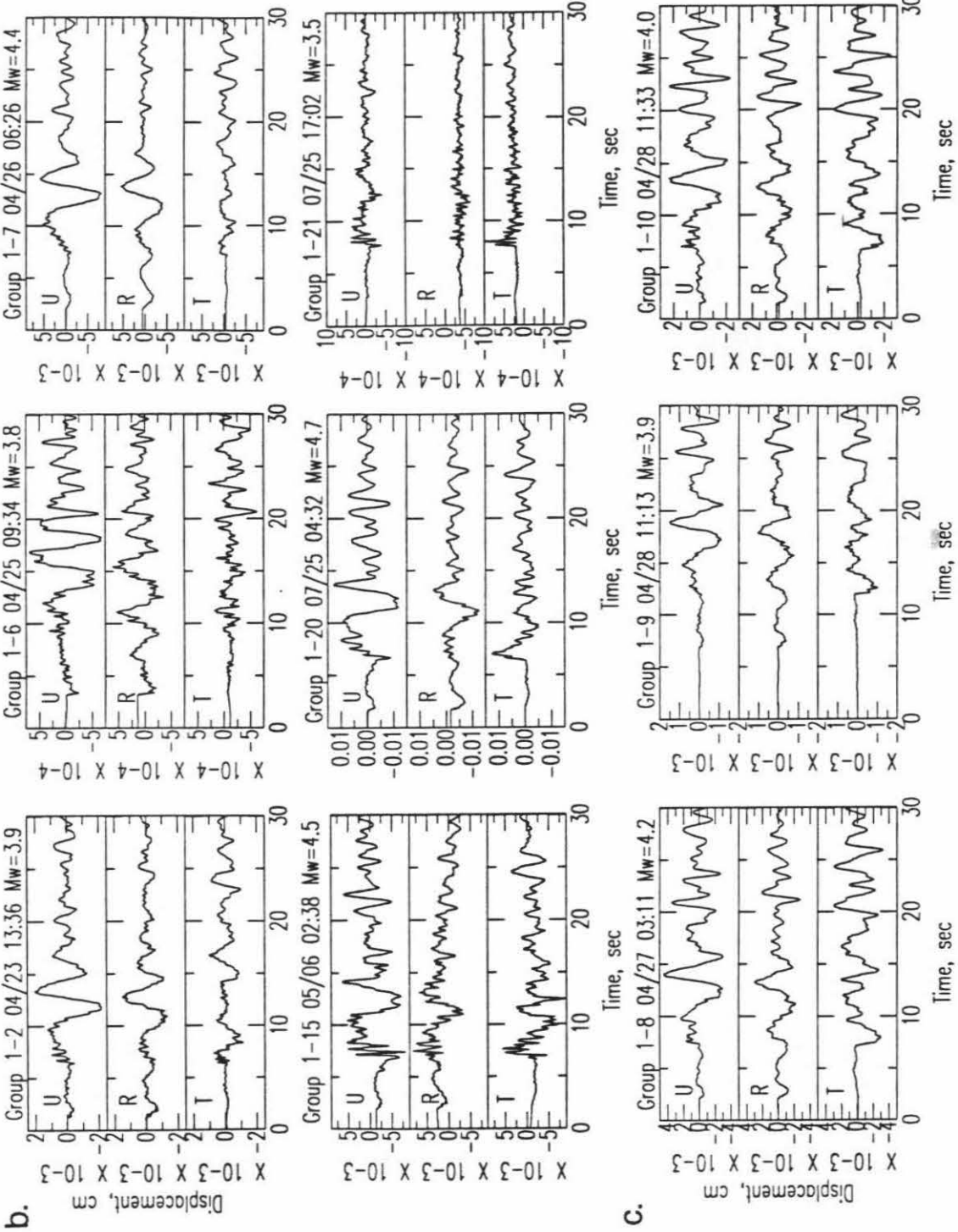


Figure 6.3 Locations of the events in seven groups

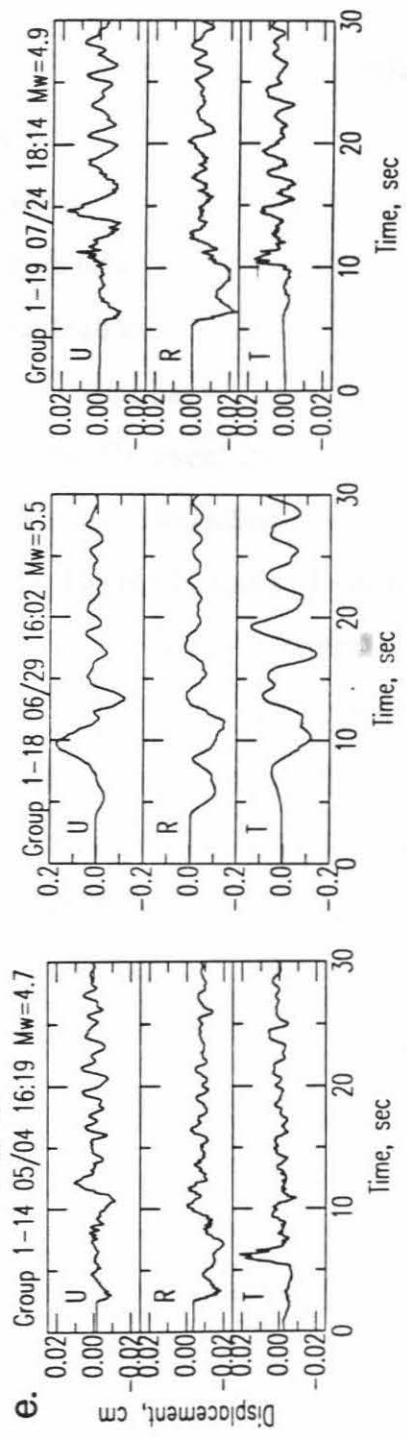
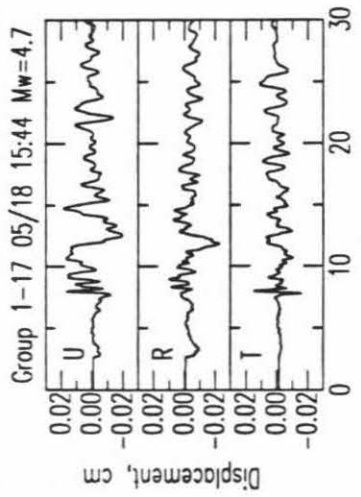
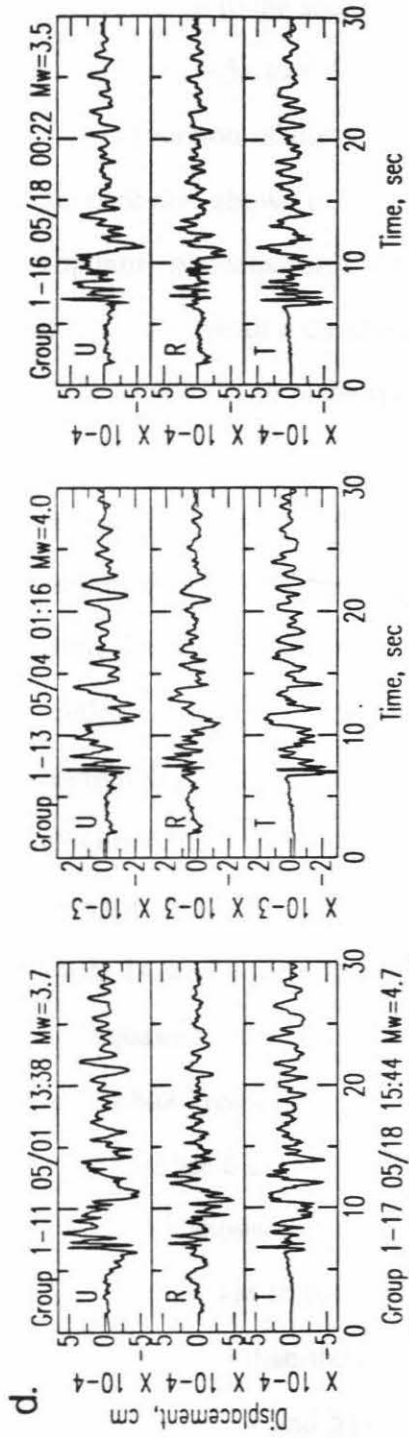
Figure 6.4: Rotated displacement records of the 21 aftershocks in 5 subgroups for Group 1. (a) Group 1a: events 1, 3, 4, 5, and 12; (b) Group 1b: events 2, 6, 7, 15, 20, and 21; (c) Group 1c: events 8, 9, and 10; (d) Group 1d: events 11, 13, 16, and 17; (e) Group 1e: events 14, 18, and 19.



a.





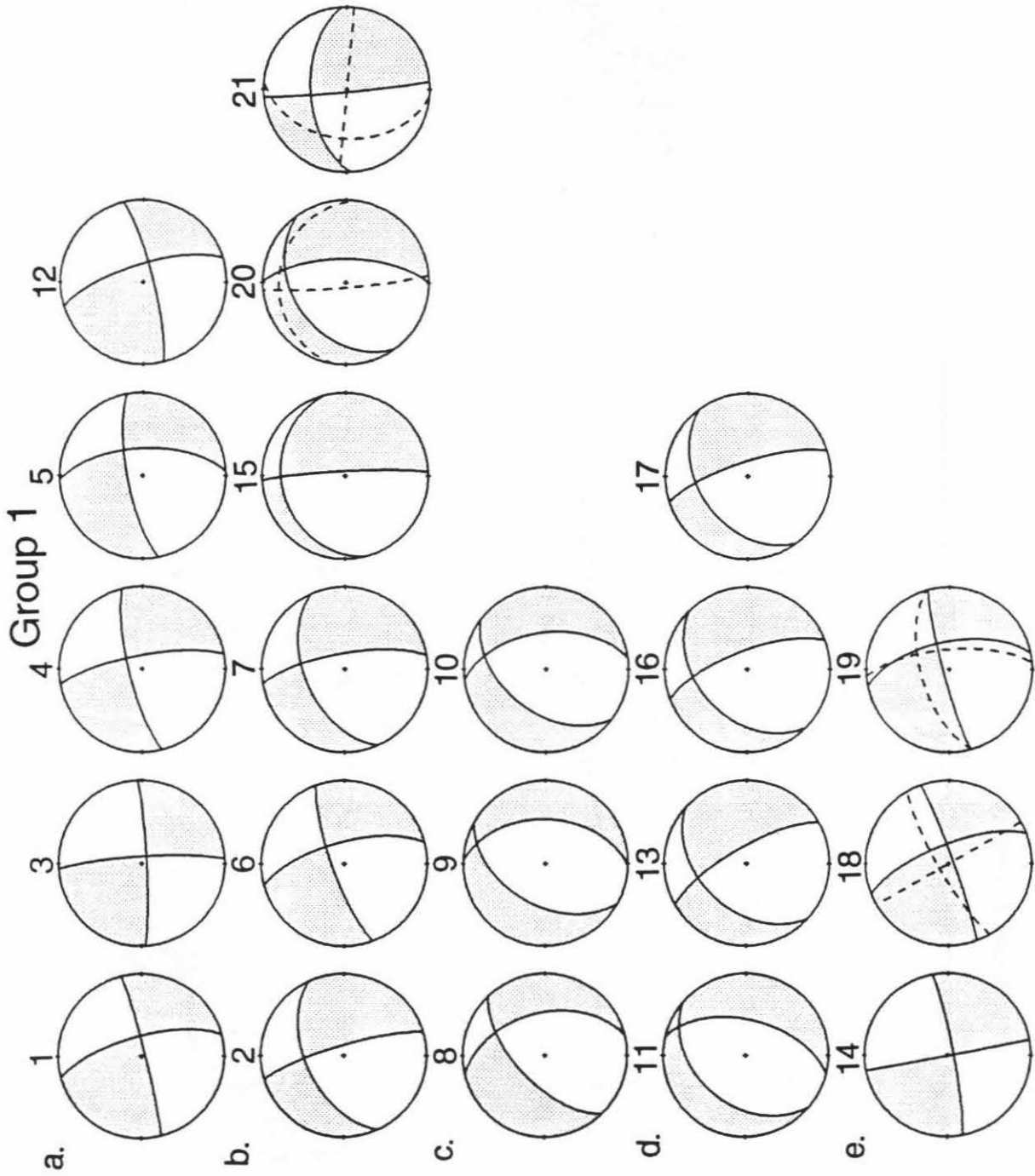


the Landers earthquake with  $M_w=5.5$  and 4.9, respectively. The locations of these two events are far to the south of the cluster of Group 1.

Figures 6.5a to 6.5e show the corresponding mechanisms determined from surface wave inversion of the 5 subgroups. For comparison, the mechanisms from first-motion data are also shown in Figure 6.5. The mechanisms of Group 1a show almost pure strike-slip motion mechanisms with near vertical dip angles (Figure 6.5a). Figure 6.5b shows the mechanisms with a combination of strike-slip and normal fault mechanisms. The north-south striking fault plane is near vertical, while the other fault plane has various dip angles. The event 15 has a very shallow plane dipping to the north. The event 20 shows more normal than strike-slip fault component. The mechanism of event 20 from first-motion data is similar to that of event 15 from surface wave inversion. The mechanisms of event 21 from first-motion and surface wave inversion are similar in strike but very different in dip angles. The mechanisms of Group 1c are very consistent (Figure 6.5c). They all show normal fault mechanisms. Except for event 11, the mechanisms of the events in Group 1d (Figure 6.5d) are similar to each other with normal fault mechanism with some strike-slip component. The mechanisms of the events in Group 1e are shown in Figure 6.5e. The event 14, and events 18 and 19 are the largest aftershocks of the Joshua Tree, and Landers earthquake sequence, respectively and the mechanisms of the events are similar to that of the Joshua Tree and Landers earthquakes.

There are 6 events in Group 2. The magnitudes of these events are between 3.5 to 4.2. Figure 6.6 shows the events in Group 2 in two subgroups. The locations of these events are about 10 km to the north of the hypocenter of the Joshua Tree earthquake. They are more scattered than the events in Group 1 (Figure 6.3b). The events in Group 2a (Figure 6.6a: events 2, 4 and 5) show a downward P-wave motion and negative and positive S-

Figure 6.5: The mechanisms determined by surface wave inversion (solid curves) and first-motion data (dashed curves) for the 21 events of Group 1. (a) Group 1a: events 1, 3, 4, 5, and 12; (b) Group 1b: events 2, 6, 7, 15, 20, and 21; (c) Group 1c: events 8, 9, and 10; (d) Group 1d: events 11, 13, 16, and 17; (e) Group 1e: events 14, 18, and 19.



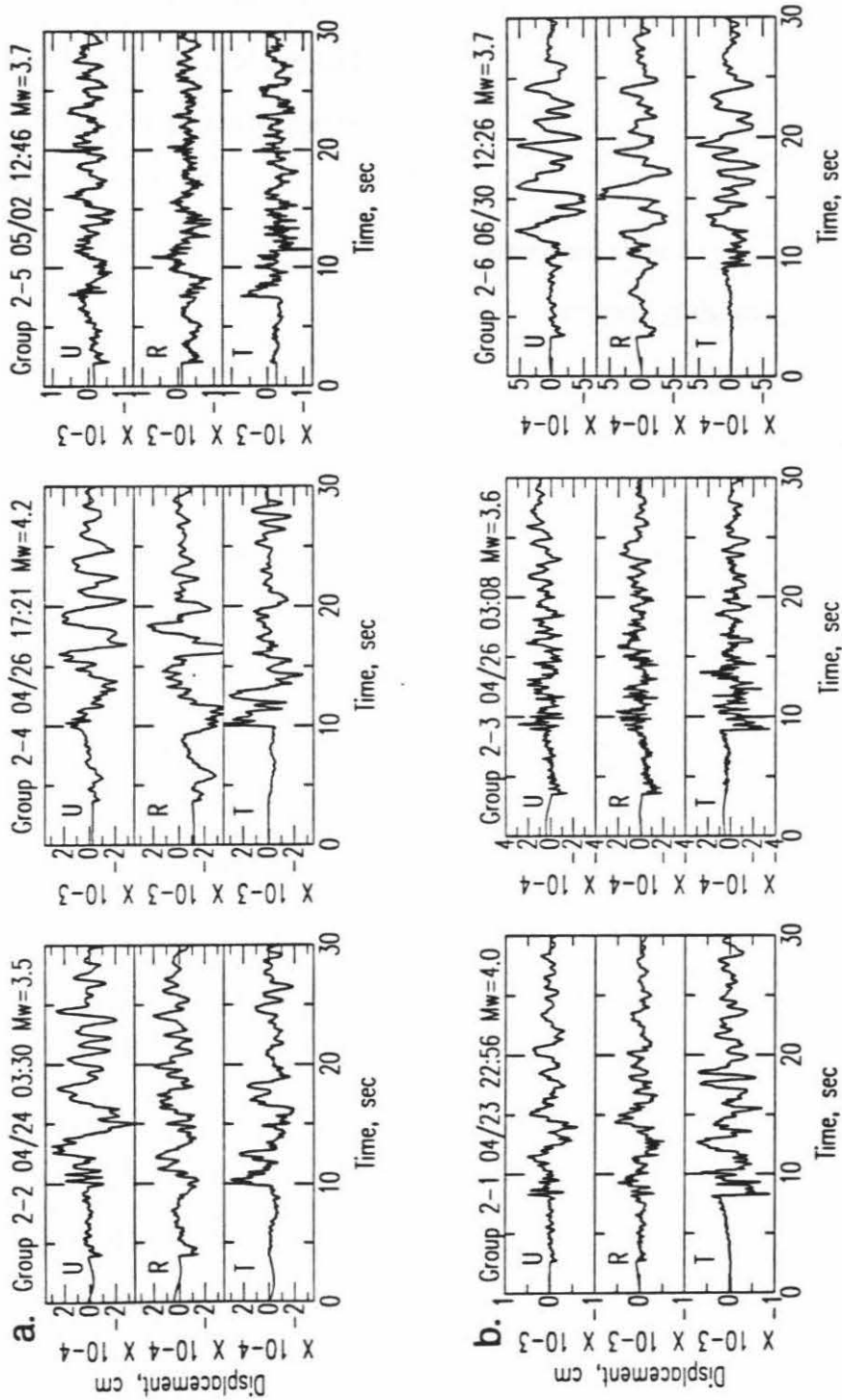


Figure 6.6: Rotated displacement records of the 6 aftershocks in 2 subgroups for Group 2. (a) Group 2a: events 2, 4, and 5; (b) Group 2b: events 1, 3 and 6.

wave in radial and transverse component, respectively. The events in Group 2b also show a downward P-wave motion but the S-wave motions in radial and transverse components are opposite to those of events in Group 2a. The waveforms of events 2 and 6 show more long period components than the other events in this group suggesting lower stress drops of these two events.

The mechanisms of the events in this group are shown in Figure 6.7. The locations of the events are more than 4 km apart and the mechanisms of the events in the same subgroup are not as similar as those of Group 1. The mechanisms of Group 2a are strike slip, while the mechanisms of Group 2b, except for event 1, show more normal fault component.

There are 13 events in Group 3. The waveforms of this group are shown in Figure 6.8 in 4 subgroups. They are the aftershocks of the Landers earthquake. The locations of these events are between the hypocenters of the Joshua Tree and Landers earthquakes (Figure 6.3c). The waveforms of the events in Group 3a (Figure 6.8a: events 1, 2, 9, and 11) show a downward P-wave motion and negative and positive S-wave motion in radial and transverse components, respectively. The noisy S-wave in the radial component of event 2 and 9 suggests that the PFO station is close to the node of SV wave. The events in Group 3a show different surface wave content even though they are almost identical in body wave. The P-wave and S-wave motions of Group 3b (Figure 6.8b: events 5, 6, 8, and 12) are similar to those of Group 3a. However, the later parts of the waveforms are different. The S-wave motions of the events in Group 3c (Figure 6.8c: events 3, 7, and 13) are similar to those of Group 3a, but the P-wave motions of the events are nodal. The waveforms of the events in Group 3d (Figure 6.8d: events 4 and 10) show similar P-wave and SV-wave motions but opposite SH-wave motion to those of Group 3a.

## Group 2

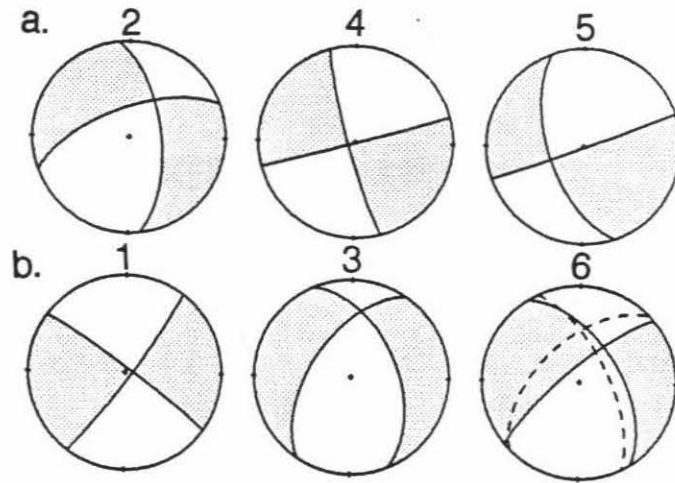
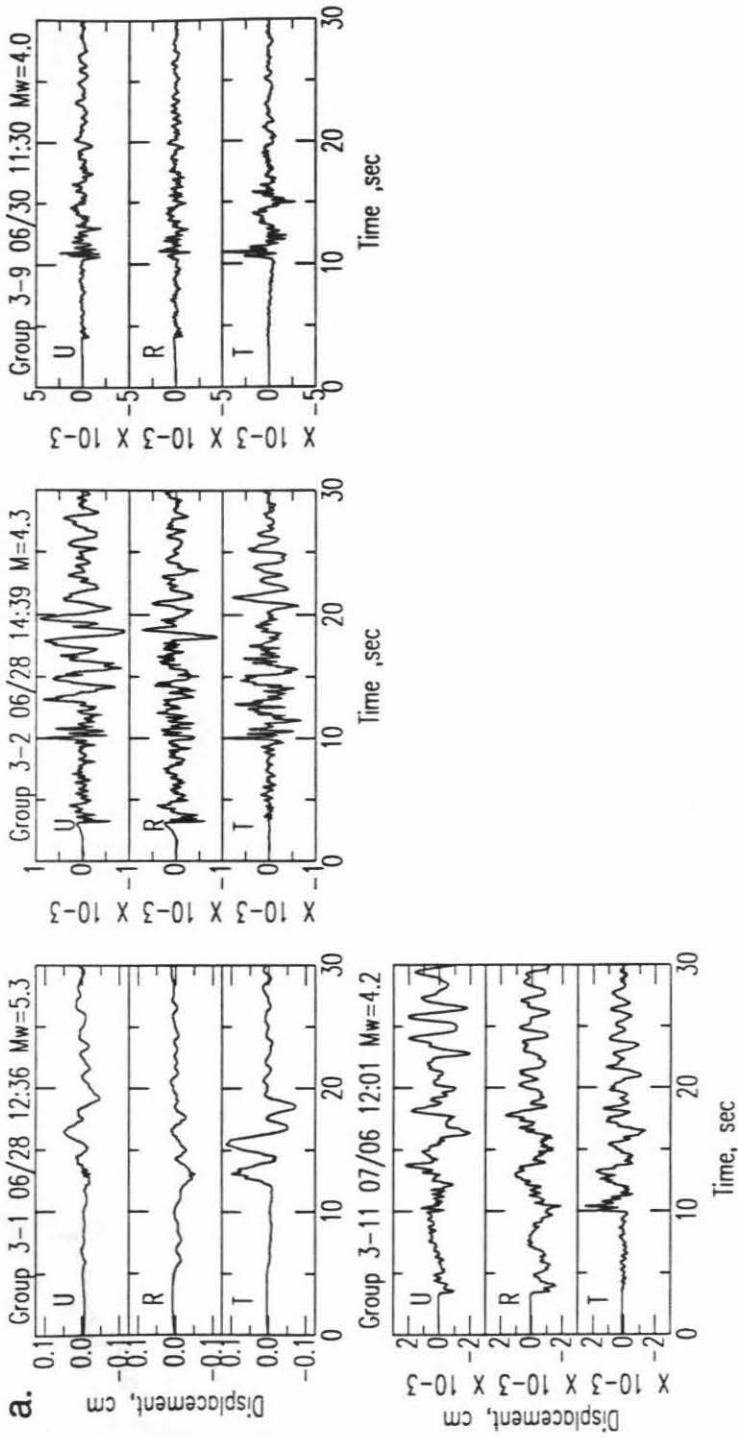
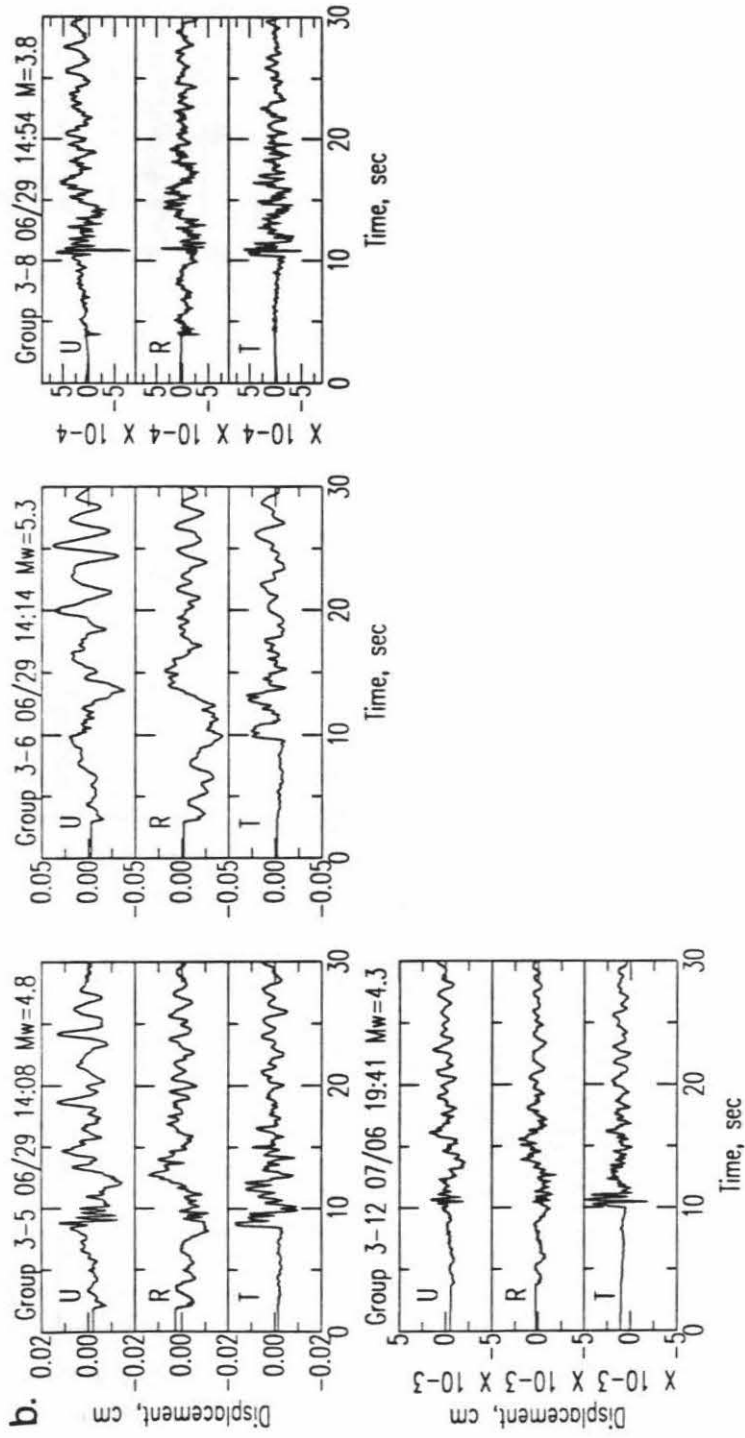


Figure 6.7: The mechanisms determined by surface wave inversion (solid curves) and first-motion data (dashed curves) for the 6 events of Group 2. (a) Group 2a: events 2, 4, and 5; (b) Group 2b: events 1, 3 and 6.

Figure 6.8: Rotated displacement records of the 13 aftershocks in 4 subgroups for Group 3. (a) Group 3a: events 1, 2, 9, and 11; (b) Group 3b: events 5, 6, 8, and 12; (c) Group 3c: events 3, 7, and 13; (d) Group 3d: events 4 and 10.







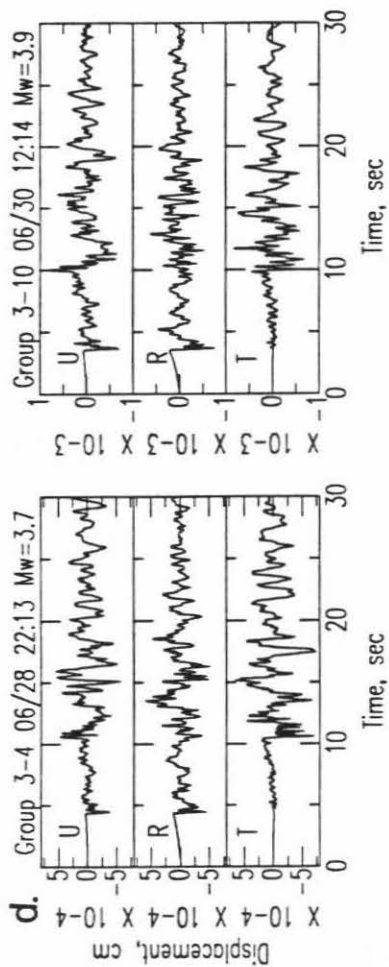
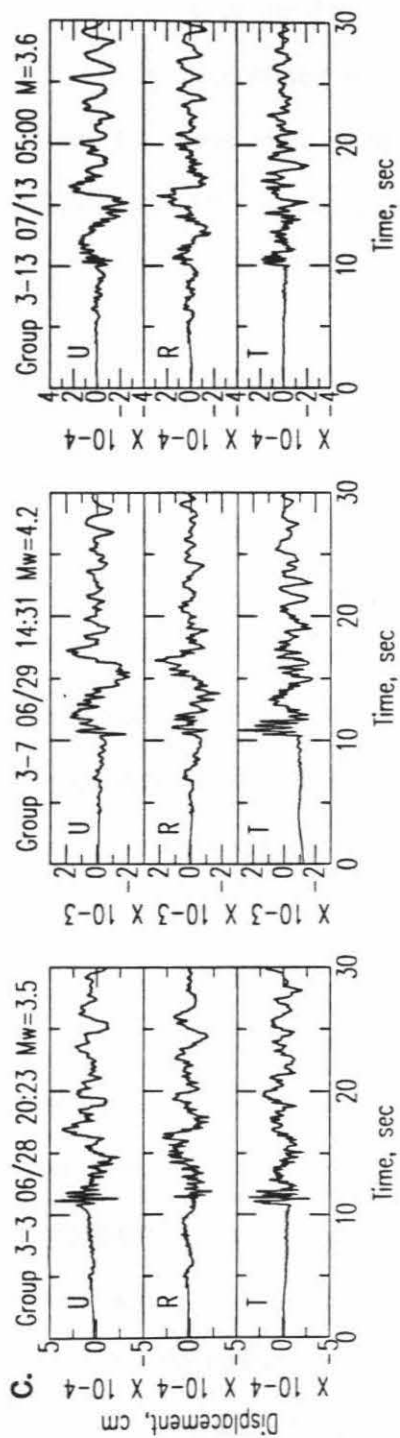


Figure 6.9 shows the mechanisms of the events in Group 3. Due to the noisy surface waves at most of the TERRAscope stations, the mechanisms of the events 2, 8 and 13 couldn't be determined by surface wave inversion. Only first-motion mechanisms are shown for these three events. The mechanisms of Group 3a show mostly strike-slip mechanisms which are quite consistent with those from first-motion data. The mechanism of event 2 was not determined by surface wave inversion. From the similarity of the locations and waveforms of event 2 and 9, we suggest that the mechanism of event 2 is similar to that of event 9. The mechanisms of Group 3b (Figure 6.9b) also show mostly strike-slip mechanisms, but the dip directions of the two nodal planes are opposite to those of Group 3a. Except for event 12, the mechanisms of the other events are consistent with the first-motion mechanisms. In view of the similarities of the waveforms and locations of the events, we prefer the mechanism from surface wave inversion for event 12. The mechanisms of Group 3c are shown in Figure 6.9c. They show north-south normal fault mechanisms which are very different from those of Group 3a and 3b. The first-motion mechanisms of event 13 show a normal fault mechanism with strike in NW direction. The mechanisms of the events in Group 3d (Figure 6.9d) show almost pure strike-slip mechanisms which are consistent with first-motion mechanisms.

There is only one event in Group 4 which is very close to the epicenter of the mainshock (Figure 6.3c). Since this is a small event with  $M_w=3.9$ , the waveforms of the event (Figure 6.10) are difficult to compare with those of the mainshock. However, the mechanism of this event (Figure 6.10) from surface wave inversion is similar to that of the mainshock.

The displacement waveforms of the events in Group 5 are shown in Figure 6.11. The locations of these events are to the north of the mainshock's epicenter (Figure 6.3c). They

## Group 3

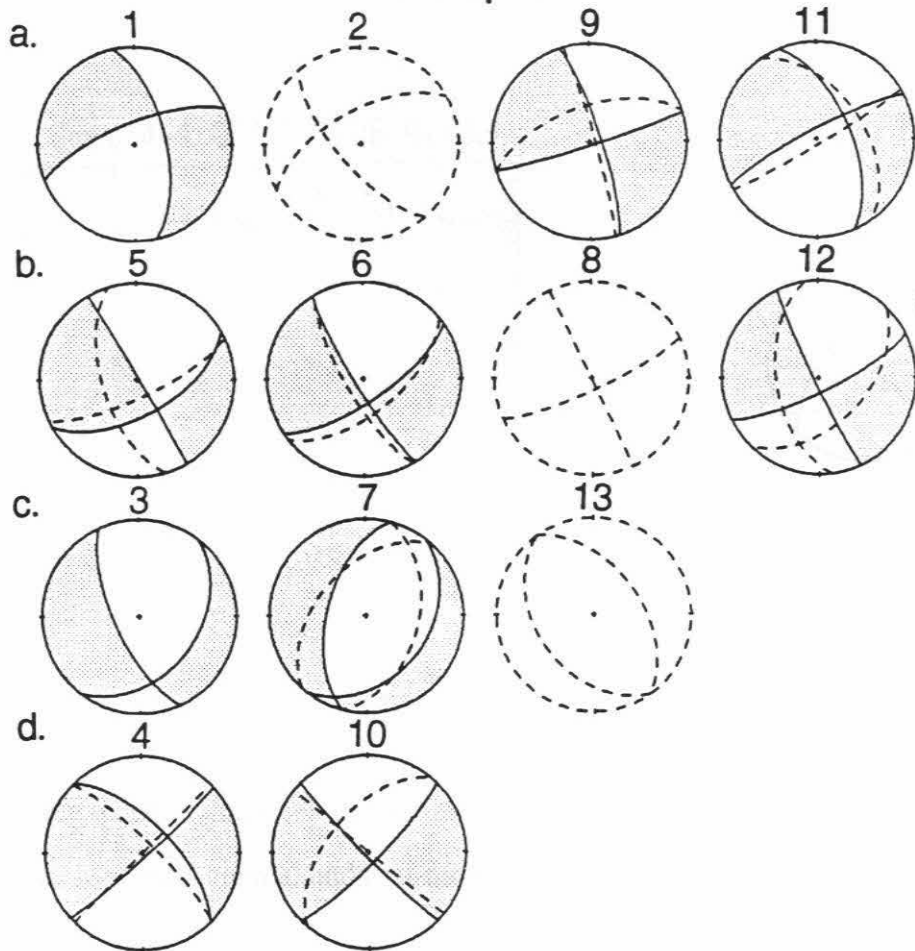


Figure 6.9: The mechanisms determined by surface wave inversion (solid curves) and first-motion data (dashed curves) for the 13 events of Group 3. (a) Group 3a: events 1, 2, 9, and 11; (b) Group 3b: events 5, 6, 8, and 12; (c) Group 3c: events 3, 7, and 13; (d) Group 3d: events 4 and 10.

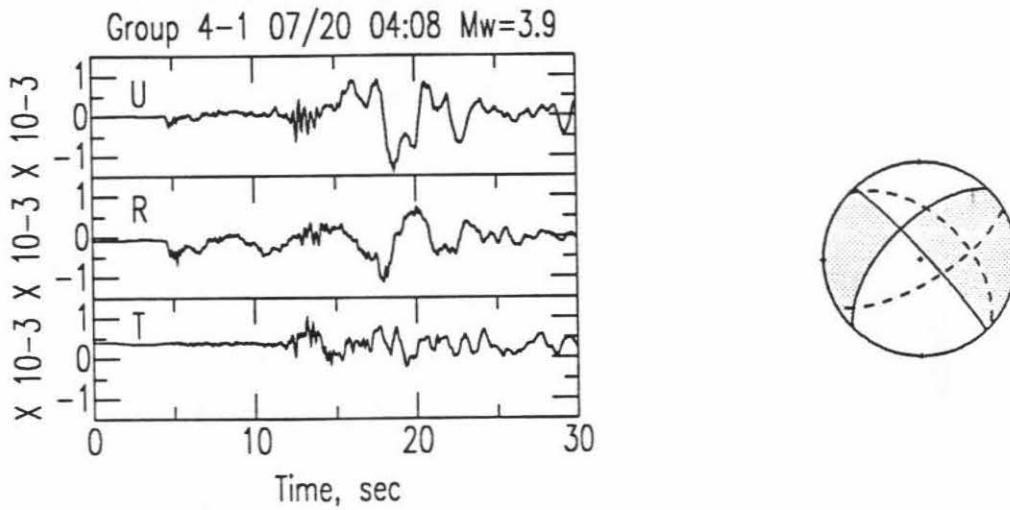


Figure 6.10: Rotated displacement records and the mechanisms determined from surface wave inversion (solid curves) and first-motion data (dashed curves) for the event of Group 4.

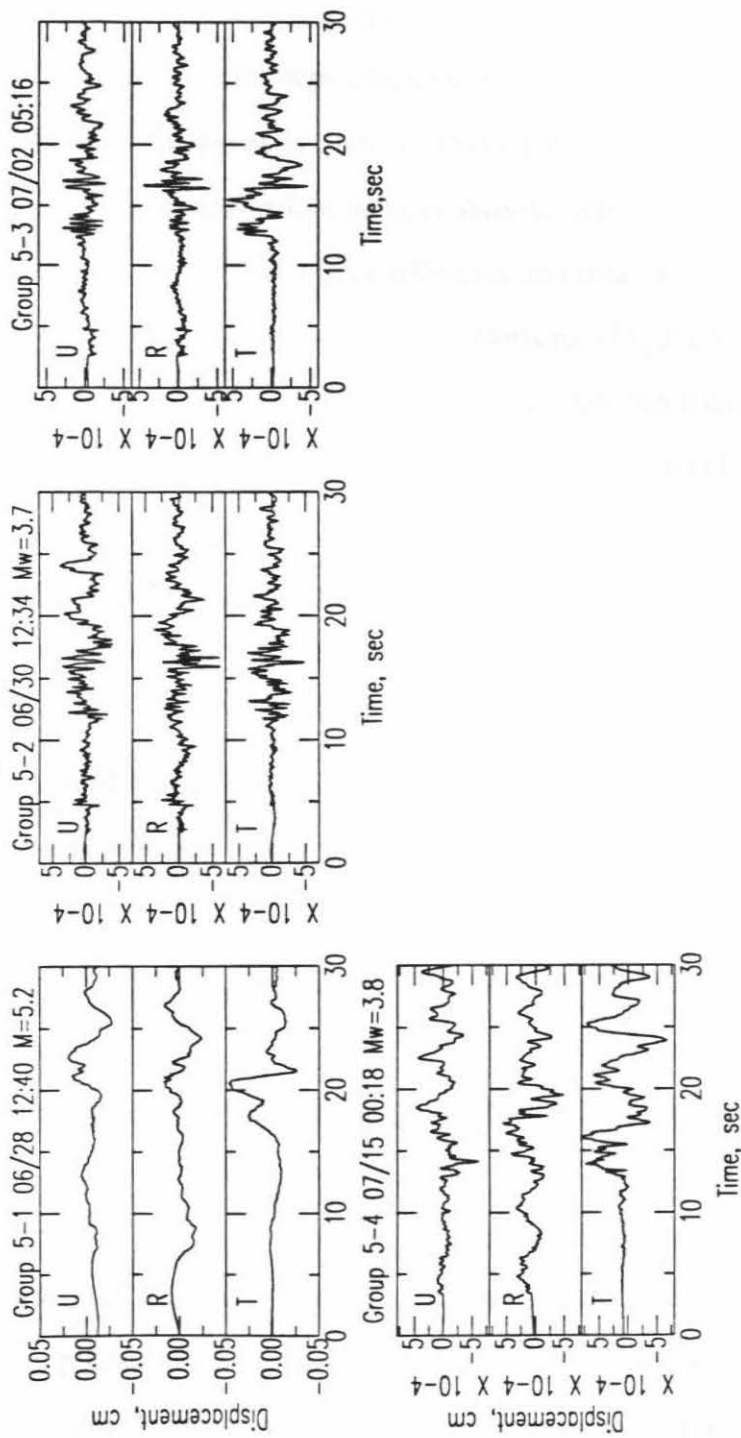


Figure 6.11: Rotated displacement records of the 4 aftershocks of Group 5.

are located in the transition zone of the Landers to the Homestead Valley faults. The waveforms of the events in Group 5a (Figure 6.11a: events 1, 2, and 3) are all different from each other. There is one large aftershock (event 1) with  $M_L=5.2$  in this group. Since the origin time of the event is close to that of the mainshock, the waveforms were contaminated by the mainshock at most of stations. The mechanism of this event is not available from surface wave inversion or first-motion data. The mechanisms of the events 2 and 3 show east-west thrust fault mechanisms (Figure 6.12). The first-motion mechanism of event 2 is very different from surface wave mechanism. Since this is a small event, the mechanism is difficult to determine. The mechanisms of event 4 show strike-slip with large east-west normal fault component. The mechanisms in this group are very different from those of the events located to the south of the mainshock's epicenter. The dissimilar waveforms and mechanisms in this group probably result from the different strike of the faults.

There are three events in Group 6. The locations of the events are along the Homestead Valley fault (Figure 6.3d). The waveforms of the events in Group 6 are all different from each other (Figure 6.13). Two mechanisms (events 2 and 3) shown in Figure 6.14 were determined from surface wave inversion and first-motion data. The surface wave mechanisms are very different from first-motion mechanisms. However, they are small events and show dissimilar waveforms to each other. It is difficult to determine which solution is better. The mechanisms from surface waves show a north-south striking normal fault.

There are four events in Group 7. The locations of these events are along the Emerson/Camp Rock fault (Figure 6.3e). They also show different waveforms from each other (Figure 6.15). Two mechanisms (events 2 and 4) were determined from surface wave



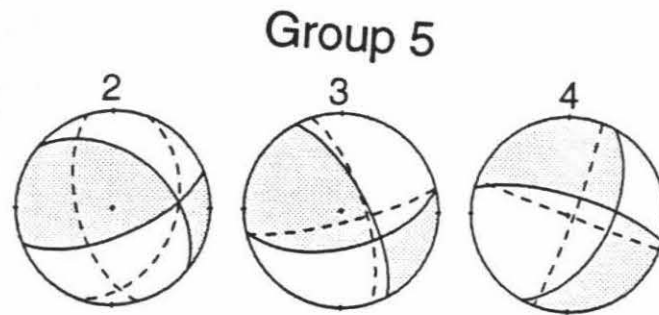


Figure 6.12: The mechanisms determined by surface wave inversion (solid curves) and first-motion data (dashed curves) for the 4 events in Group 5.

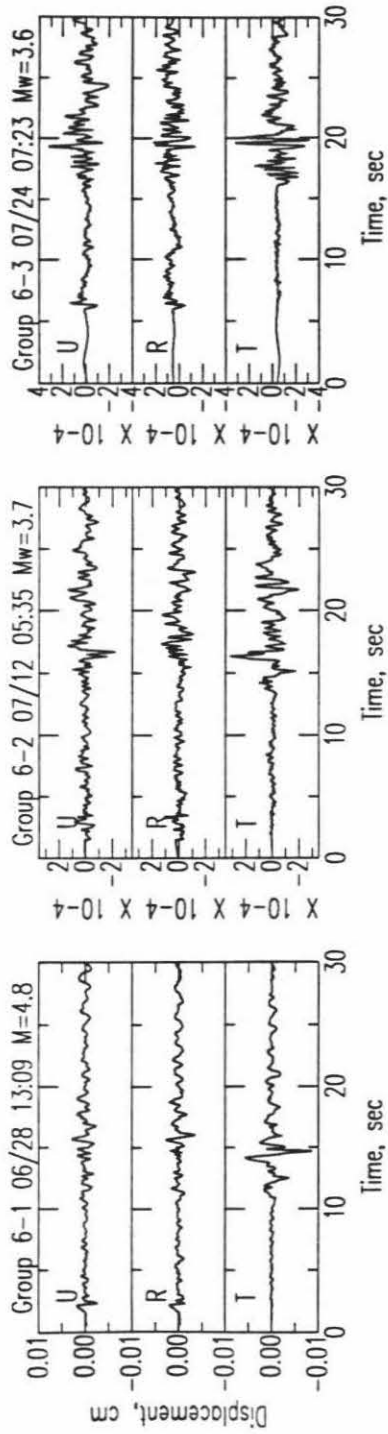


Figure 6.13: Rotated displacement records of the 3 aftershocks of Group 6.

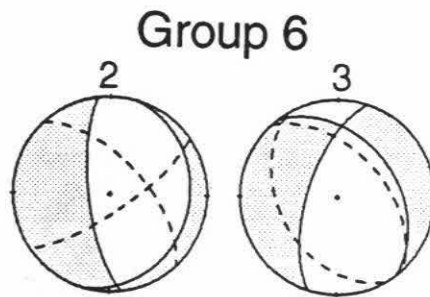


Figure 6.14: The mechanisms determined by surface wave inversion (solid curves) and first-motion data (dashed curves) for the 3 events in Group 6.

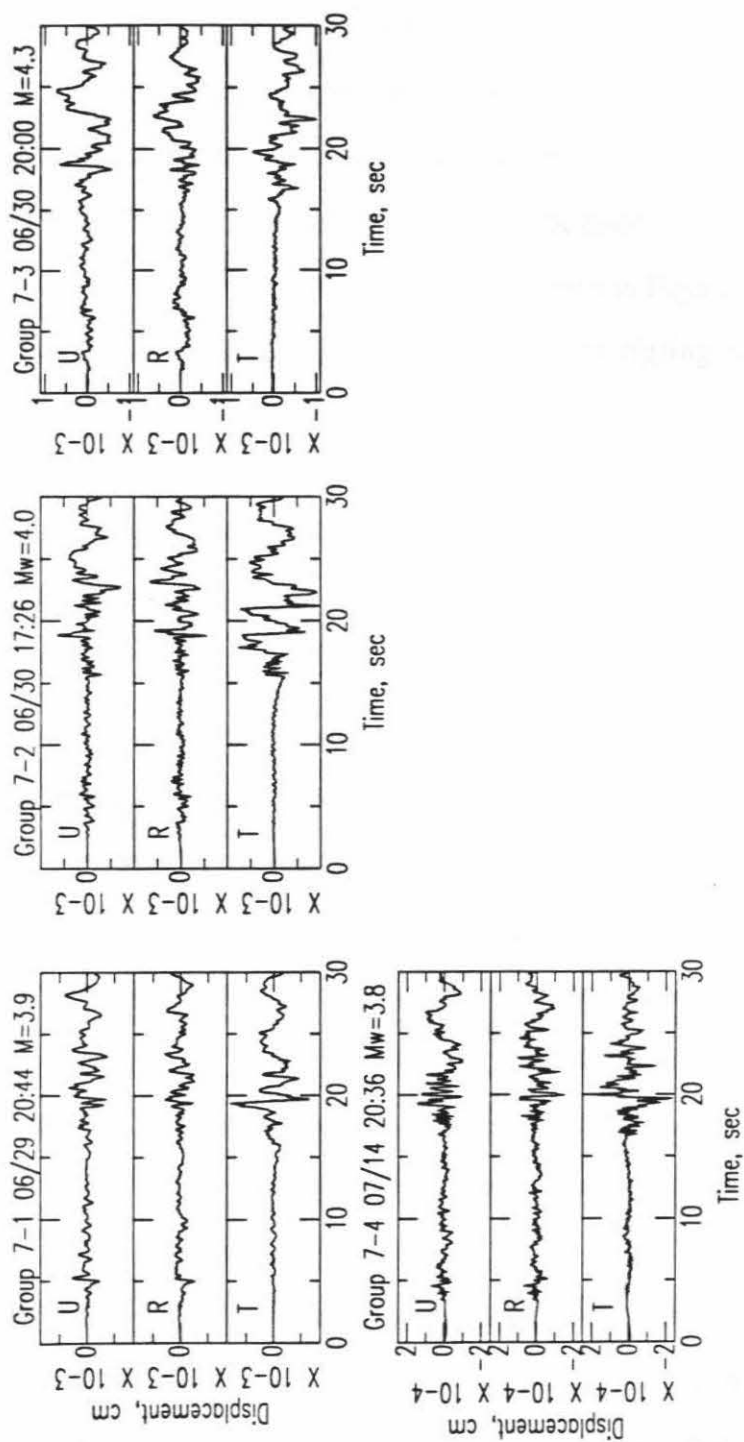


Figure 6.15: Rotated displacement records of the 4 aftershocks of Group 7.

inversion (Figure 6.16). The mechanism of event 2 is a north-south striking normal fault and is consistent with first-motion mechanism. The mechanism of event 4 has a fault plane with very shallow dip angle, while the other fault plane is nearly vertical ; and the mechanism is very different from first-motion mechanism. The first-motion mechanisms of event 1 and 4 are similar to each other. In general, the events in this group show dissimilar mechanisms, reflecting the dissimilar waveforms shown in Figure 6.15.

For some events, especially for the events interfering with large events, the mechanisms either from first-motion or surface wave inversion are not available. From the correlation of waveforms and mechanisms, we can infer the mechanism. The different frequency content of the waveforms of the event suggests the differences in stress drop. In general, the waveforms of the events located to the south of the mainshock's epicenter (Groups 1, 2, 3 and 4) are not very much different from each other and are similar to those of Joshua Tree and Landers earthquakes. The mechanisms are mostly strike-slip similar to those of the Joshua Tree and Landers earthquakes. Some of the events in this area showing normal fault mechanisms suggests the structural complexity along the fault. Some events with broader waveforms compared with the events with similar magnitude suggested the lower stress drops of the events. The waveforms and mechanisms of the events located to the north of the mainshock's hypocenter are very different from each other.

#### 6.4.2 Examination of Accuracy of Depth Determination

Since the details of the structure are not known very well, large uncertainties are usually involved in depth determination. We first compare the depth determined with different methods. Figure 6.17a, 6.17b, 6.17c show the hypocenters taken from the catalog of

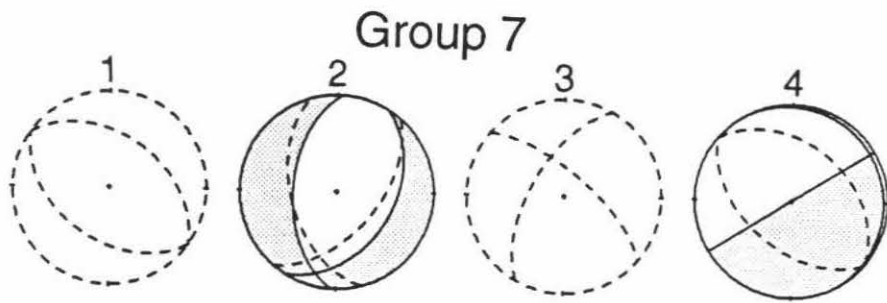
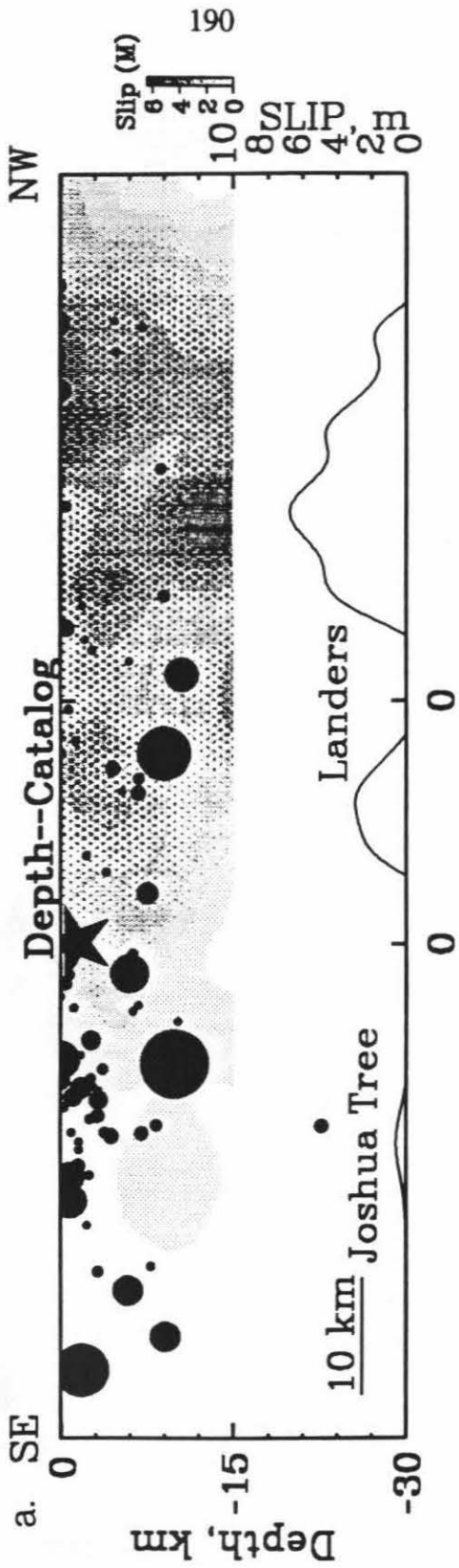
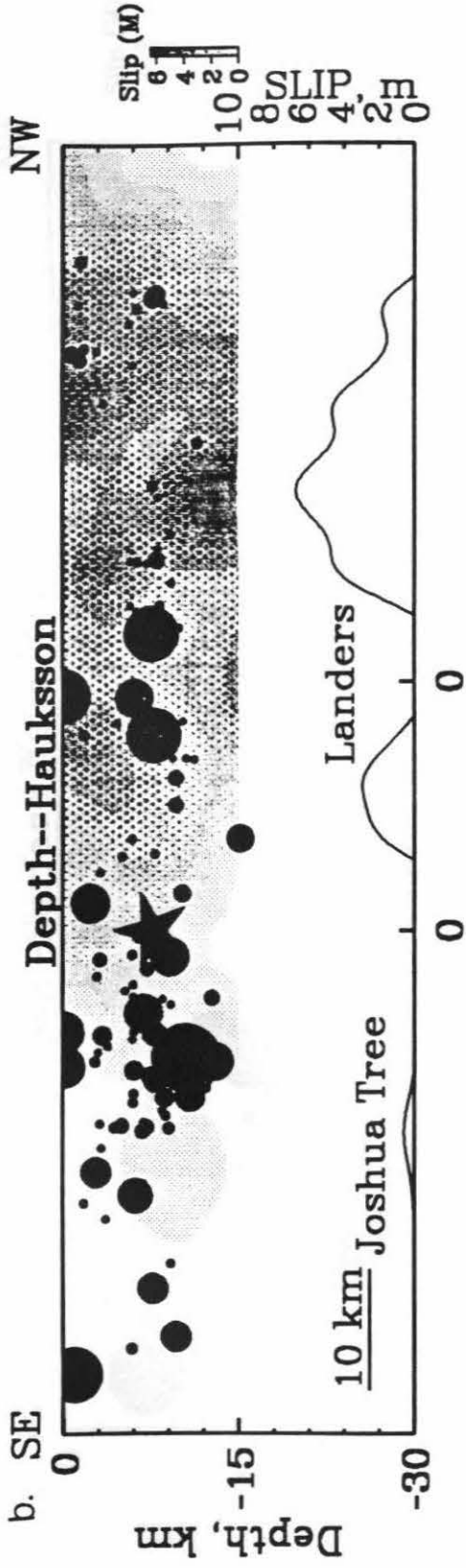


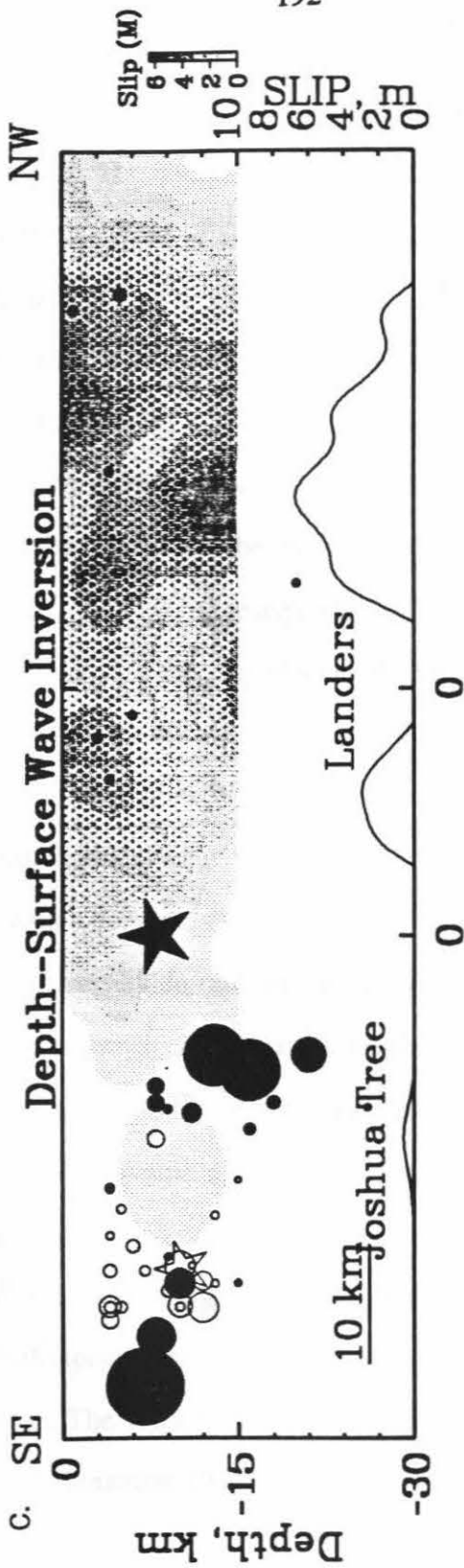
Figure 6.16: The mechanisms determined by surface wave inversion (solid curves) and first-motion data (dashed curves) for the 4 events in Group 7.

Figure 6.17: Depth distribution along AA', BB' and CC' shown in Figure 6.1 using the depths determined with different data set. The star indicates the hypocenter of the mainshock. The size of the symbol corresponds to the size of the event. The slip distributions obtained from TERRAScope (solid curves) and strong motion data (contour density plot) during the Joshua Tree and Landers earthquakes are also shown. (a) Depths from catalog of USGS-Caltech SCSN; (b) Depths from relocated catalog; (c) Depths from surface wave inversion. The shaded symbols indicate the Joshua Tree earthquake sequence.









SCSN, relocated by Hauksson (personal Communication, 1992), and determined by surface wave inversion, respectively, along the cross sections AA', BB', and CC' shown in Figure 6.1. The catalog data (Figure 6.17a) show that most of the events in the southeastern segment of the fault have depth less than 5 km. Some of the events were moved to a depth between 10 to 15 km after relocation by Hauksson. Some relocated events are very shallow near the surface. In general, the depths from SCSN catalog and Hauksson's relocated catalog are less than 15 km. The depths of some of the events determined by surface-wave inversion are larger than 15 km. Only a few events have depths less than 5 km. For the large shallow aftershocks in the relocated catalog and for the events between the two large asperities, TERRAScope data are not available.

To understand the depth variation of energy release during the earthquake sequence, we need to resolve the difference in depth exhibited in Figure 6.17a to 6.17c. We used the amplitude ratio of surface wave to body wave to examine the depth. As shown earlier, some events have similar body wave but different surface wave. Figure 6.18 shows an example which compares the transverse component of events 2, 11 and 9 of Group 3. The difference in amplitude ratio of surface wave to body wave between the events shown in Figure 6.18 suggests differences in depth.

To see how the surface wave amplitude changes with source depths, we computed synthetic seismograms using the mainshock mechanism for various source depths. Synthetic seismograms were computed using reflection-transmission matrices (Kennett and Kerry 1979) and the discrete wave number method (Bouchon 1981), assuming an anelastic layered half-space structure. The program written by Takeo (1987) was used for this computation. The velocity structure is the standard Southern California velocity structure (Hadley and Kanamori 1977).

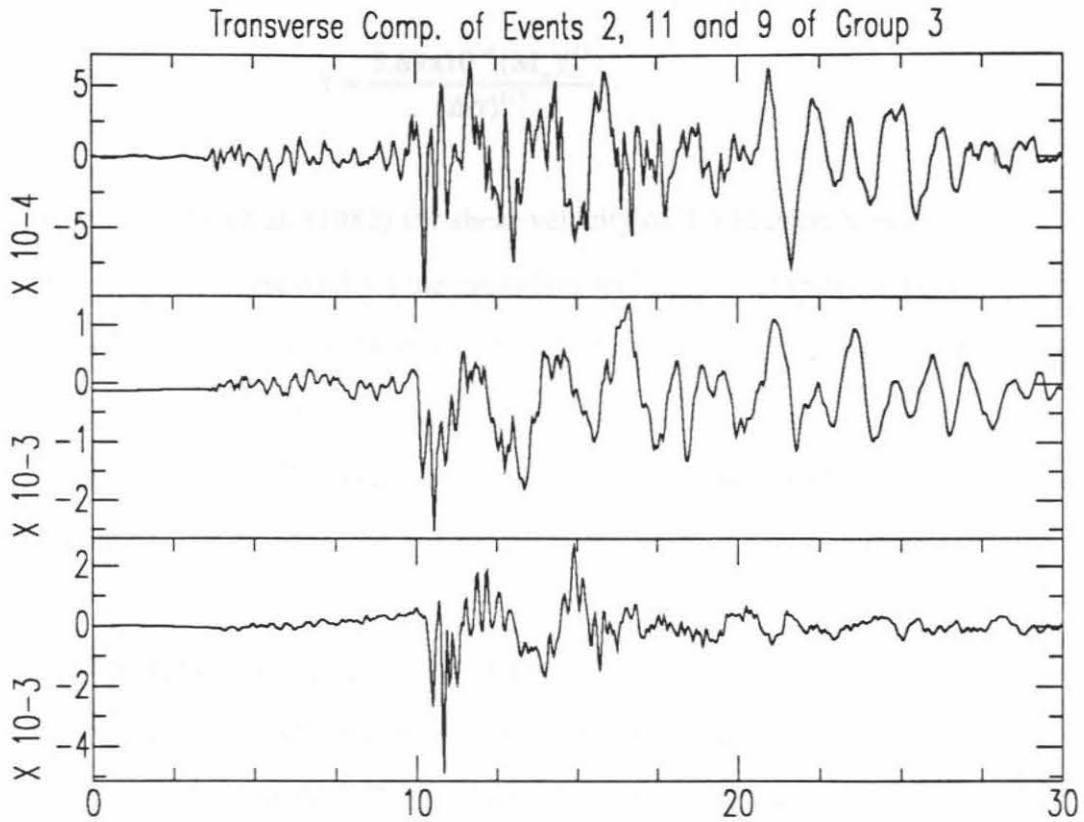


Figure 6.18: The example of seismograms with transverse component of event 1, 3 and 4 of Group 1. The differences in surface wave contents of the three events implies the differences in the depths.

To simulate seismograms for events with various magnitudes, we convolved the synthetic seismograms computed for an impulsive source with the source time function with a duration of

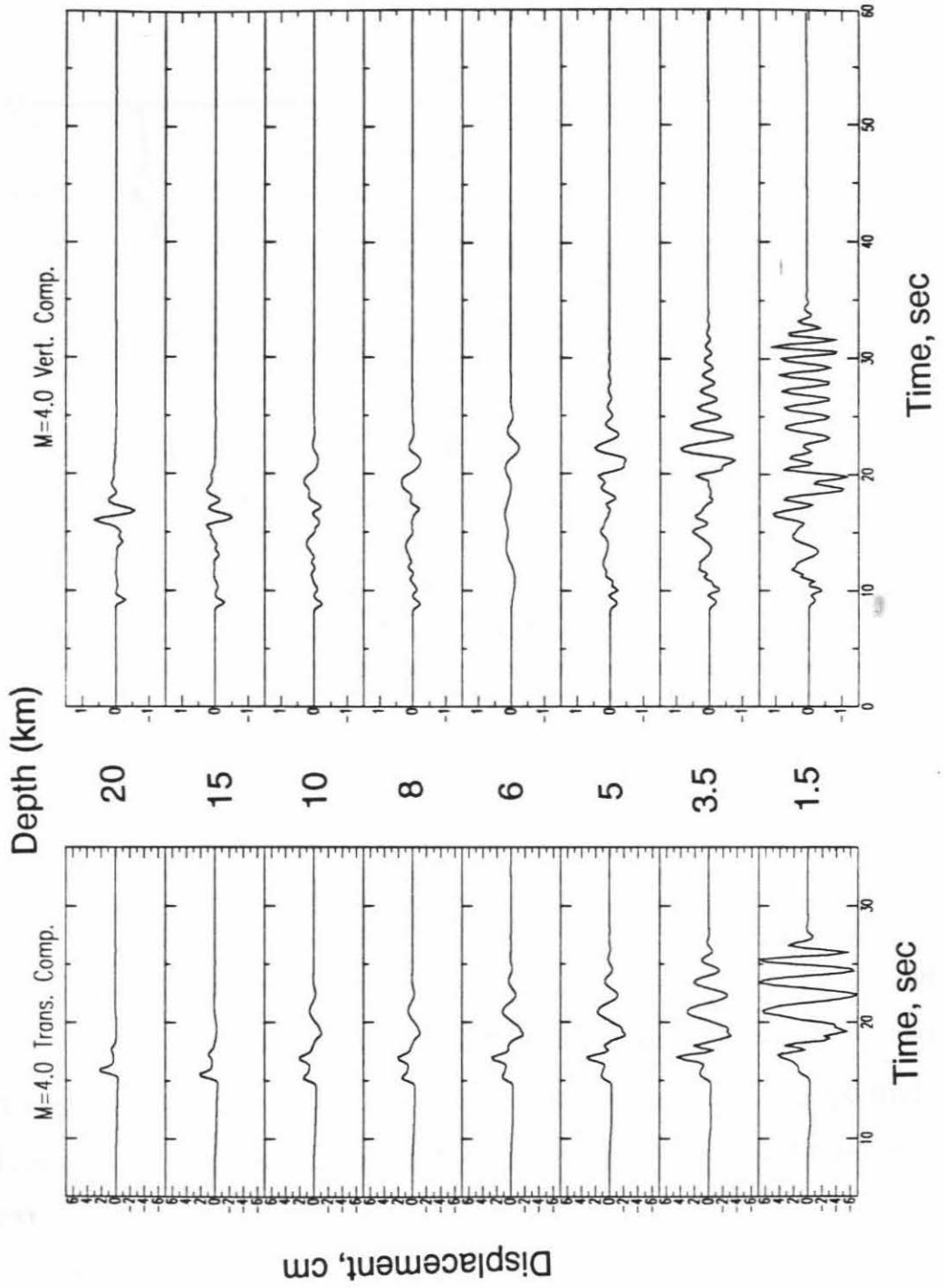
$$\tau = \frac{5.69 \times 10^{-8} (M_0)^{1/3}}{(\Delta\sigma)^{1/3}} \quad (2)$$

given by Cohn et al. (1982) for shear velocity of 3.5 km/sec, where  $\tau$  is in seconds,  $\Delta\sigma$  (bars) and  $M_0$  (dyne-cm) are the stress drop and seismic moment respectively. The seismic moment was computed from local magnitude using the relationship of  $\log M_0 = 1.5 M_L + 16.1$  (Thatcher and Hanks 1973).

Since most of the aftershocks have magnitude of about  $M_L=4$ , we computed the synthetic seismograms for  $M_L=4$ . A stress drop of 100 bar is assumed. Figure 6.19 shows the transverse and vertical components of synthetic seismograms for events with  $M_L=4$  at various source depths. For depths deeper than 15 km, almost no surface waves are seen on the record. We measured the amplitude ratio of surface to body waves of the synthetic waveforms and compared them with the observed amplitude ratio to examine the accuracy of the depths. Since there are only a few small events to the north of the mainshock epicenter and their mechanisms are different from each other, it is difficult to compare the observed and synthetic amplitude ratios for these events. Thus, we only compared the observed and synthetic amplitude ratios of the events to the south of the mainshock epicenter.

Figure 6.20 shows the amplitude ratios,  $R$ , of surface wave to SH wave amplitudes versus depths of these events determined from surface wave inversion. The solid curves indicate the synthetic amplitude ratio for magnitude  $M_L=4$ . The distance used in this

Figure 6.19: The synthetic seismograms for  $M_L=4.0$  with transverse and vertical components for various depths.



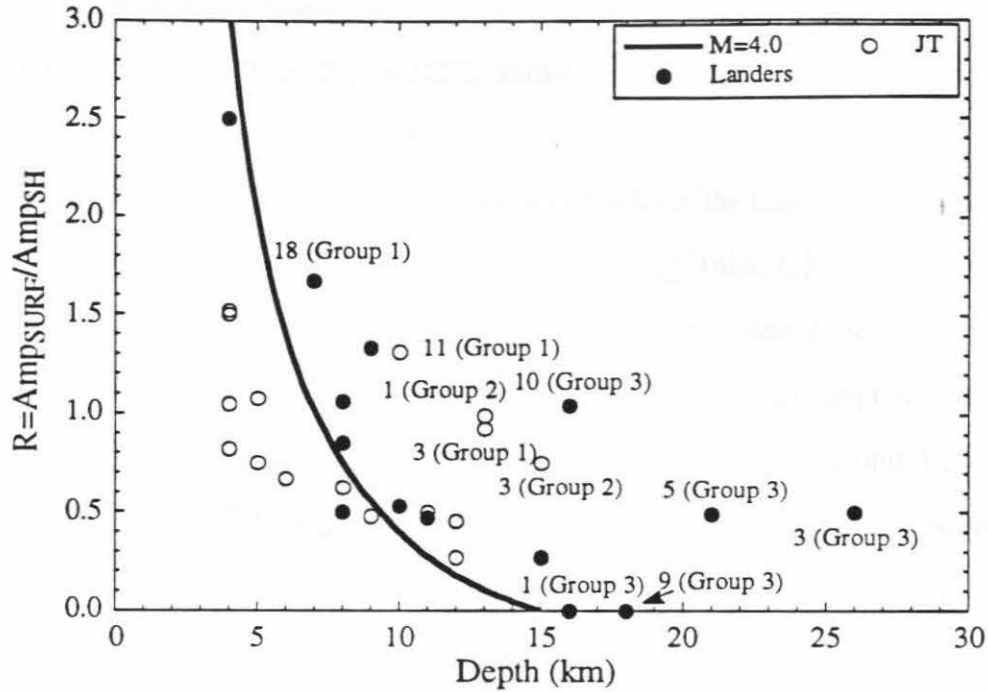


Figure 6.20: The amplitude ratio,  $R$ , of surface wave to SH wave versus depths from surface waves for the aftershocks to the south of the mainshock epicenter. The open and solid circles indicate the aftershocks of Landers and Joshua Tree earthquakes, respectively. The solid curve indicates the synthetic amplitude ratio curves for magnitude of 4, and stress drop of 100.



computation is 52 km, which is the average epicentral distance of these events to PFO station. Since the synthetic waveforms were computed for an event with  $M_L=4$ , the ratios for events with  $M_L \neq 4$  should be adjusted slightly. In general, the amplitude ratio of the events follow the trend of the synthetic amplitude ratio curve, but a few events deviated from the synthetic ratio significantly.

Figure 6.21 compares the depths of the aftershocks of the Landers earthquake estimated from the surface wave inversion and relocated catalog. Table 6.2 lists the data used. The depths from surface wave inversion are generally deeper than those from the relocated catalog. There are some events having significantly different depths with these two methods. The events 3 (Group 3), 5 (Group 3), 3 (Group 6), 9 (Group 3), 1 (Group 3), 10 (Group 3), and 18 (Group 1) have surface-wave depths (depth determined from surface waves) significantly larger than those determined by relocation. The events 2 (Group 6) and 4 (Group 7) have relocated depths larger than the surface-wave depths. Now we examine these events for which the depths determined with the two methods are significantly different.

Figure 6.20 shows that the depths of events 3(Group 3), 5 (Group 3), 9 (Group 3), 1 (Group 3), 10 (Group 3), and 18 (Group 1) determined from surface waves are considerably overestimated. This trend is consistent with the trend shown in Figure 6.21. We now examine each of these events. We compared the observed and synthetic amplitude ratios of these events to determine the reasonable depths of these events from relocated catalog and surface-wave inversion.

(1) Event 3 (Group 3)

Figure 6.20 suggests that the depth of this event should be around 10 km, which is close to the depth from the relocated catalog. However, if the depth is fixed at 10 km, the

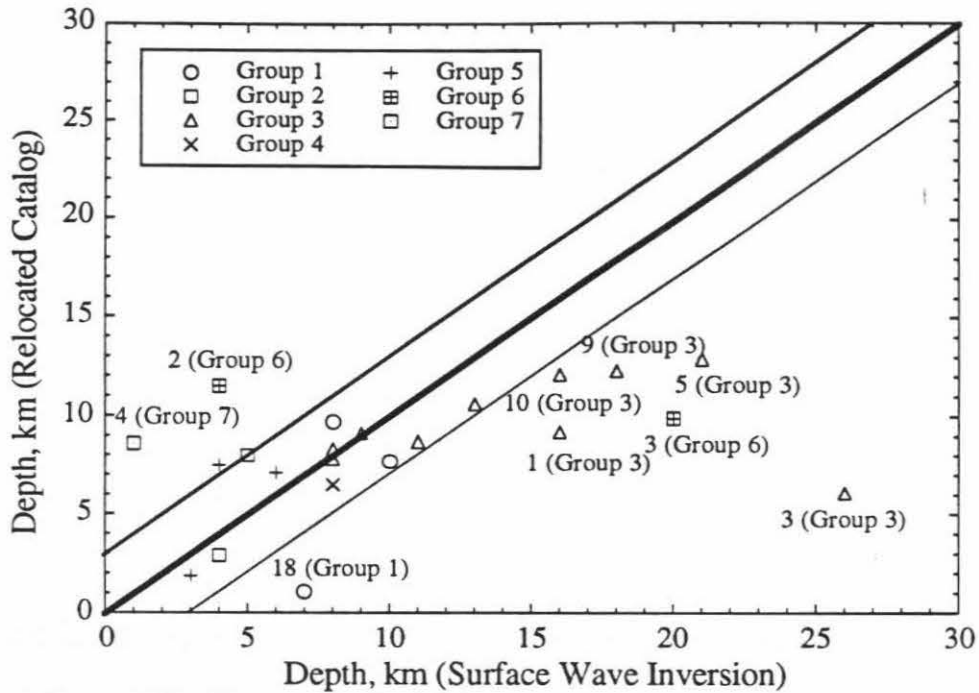


Figure 6.21: The comparison of the depths from the relocated catalog of Caltech-USGS SCSN and surface wave inversion for the aftershocks of the Landers earthquake in seven groups. The heavy solid line indicate the trend for consistent depths, and the two thin solid lines indicate the  $\pm 3$  km range.

Table 6.2. The depths of the Landers and Joshua Tree earthquake sequences.  $Z_s$ : depths from surface wave inversion;  $Z_R$ : depths from the relocated catalog of SCSN;  $Z_F$ : final depths after examination.

Table 6.2

No.	Date (y/m/d)	time	Latitude (°N)	Longitude (°W)	M <sub>w</sub>	Z <sub>S</sub> (km)	Z <sub>R</sub> (km)	Z <sub>F</sub> (km)
Group 1								
1	92/04/23	0225	33.94	116.33	4.3	12	--	12
2	92/04/23	1336	33.92	116.32	3.9	4	--	4
3	92/04/23	1806	33.94	116.30	3.6	13	--	8
4	92/04/23	1856	33.97	116.29	4.0	6	--	6
5	92/04/23	2352	33.98	116.26	3.6	4	--	4
6	92/04/25	0934	33.95	116.30	3.8	7	--	7
7	92/04/26	0626	33.92	116.33	4.4	4	--	4
8	92/04/27	0311	33.91	116.32	4.2	4	--	4
9	92/04/28	1113	33.92	116.32	3.9	5	--	5
10	92/04/28	1133	33.95	116.30	4.0	4	--	4
11	92/05/01	1338	33.92	116.33	3.7	10	--	8
12	92/05/02	1910	33.96	116.31	3.5	9	--	9
13	92/05/04	0116	33.93	116.36	4.0	9	--	9
14	92/05/04	1619	33.92	116.32	4.7	12	--	12
15	92/05/06	0238	33.92	116.34	4.5	10	--	10
16	92/05/18	0022	33.95	116.36	3.5	11	--	11
17	92/05/18	1544	33.95	116.35	4.7	5	--	5
18	92/06/29	1601	33.87	116.27	5.5	7	1.1	1.1
19	92/07/24	1814	33.90	116.28	4.9	8	9.7	8
20	92/07/25	0431	33.93	116.30	4.7	10	7.7	10
21	92/07/25	1702	33.94	116.31	3.5	15	8.6	15
Group 2								
1	92/04/23	2256	33.99	116.34	3.6	13	--	8
2	92/04/24	0329	34.01	116.34	3.5	4	--	4
3	92/04/26	0308	34.02	116.31	3.4	15	--	8
4	92/04/26	1721	34.05	116.34	4.2	8	--	8
5	92/05/02	1246	33.99	116.41	3.7	5	--	5
6	92/06/30	1226	34.02	116.35	3.7	4	2.9	4
Group 3								
1	92/06/28	1236	34.14	116.42	5.3	16	9.2	16
2	92/06/28	1439	34.09	116.43	--	--	7.7	7.7
3	92/06/28	2023	34.12	116.42	3.5	26	6.1	10
4	92/06/28	2213	34.05	116.35	3.7	9	9.1	9
5	92/06/29	1408	34.10	116.39	4.8	21	12.9	21
6	92/06/29	1414	34.10	116.40	5.3	13	10.6	13
7	92/06/29	1431	34.09	116.35	3.5	8	8.3	8
8	92/06/29	1454	34.10	116.41	--	--	8.9	8.9

Table 6.2 Cont.

No.	Date (y/m/d)	time	Latitude (°N)	Longitude (°W)	M <sub>w</sub>	Z <sub>S</sub> (km)	Z <sub>R</sub> (km)	Z <sub>F</sub> (km)
9	92/06/30	1130	34.09	116.41	4.1	18	12.3	18
10	92/06/30	1214	34.08	116.41	3.9	16	12.1	12.1
11	92/07/06	1201	34.09	116.36	4.2	8	7.8	8
12	92/07/06	1941	34.07	116.38	4.3	11	8.7	11
13	92/07/13	0500	34.08	116.41	--	--	8.0	8
Group 4								
1	92/07/20	0408	34.20	116.43	3.9	8	6.5	8
Group 5								
1	92/06/28	1240	34.36	116.49	--	--	6	6
2	92/06/30	1234	34.32	116.45	3.7	4	7.5	4
3	92/07/02	0516	34.38	116.45	3.7	6	7.1	6
4	92/07/15	0018	34.33	116.46	3.8	3	1.9	3
Group 6								
1	92/06/28	1309	34.41	116.46	--	--	10.5	10.5
2	92/07/12	0535	34.55	116.53	3.7	4	11.5	4
3	92/07/24	0723	34.48	116.50	3.6	20	9.9	9.9
Group 7								
1	92/06/29	2044	34.66	116.69	--	--	1.6	1.6
2	92/06/30	1726	34.64	116.66	4.0	5	8.0	5.0
3	92/06/30	2000	34.64	116.66	--	--	7.7	7.7
4	92/07/14	2036	34.64	116.64	3.8	1	8.6	8.6

inversion shows a very large non-double couple component and a very large variance. We have not found the cause of this problem yet. We used the depth of 10 km for this event.

(2) Event 5 (Group 3)

Figure 6.20 suggests a depth of about 10 km, while the relocated depth is 12.9 km. Since the magnitude of this event is 4.8, the difference between 10 and 12.9 km is insignificant considering the size of its rupture zone. We assigned the depth determined by relocation to this event.

(3) Event 9 (Group 3)

As shown in Figure 6.20, the ratio  $R$  for this event is very small, suggesting that the depth is probably 15 km or larger. The relocated depth is 12.3, and the surface-wave depth is 18 km. We used the surface-wave depth for this event.

(4) Event 1 (Group 3)

This is a large event ( $M_w=5.3$ ), and the difference between the relocated depth, 9.2 km, and the surface-wave depth, 16 km, is not significant considering the finiteness of the source. Since the ratio  $R$  for this event is very small, suggesting that the depth of the event is probably larger than 15 km, we used the surface-wave depth for this event.

(5) Event 10 (Group 3)

Figure 6.20 suggests a depth of 8 km, which is much shallower than the surface-wave depth, 16 km. We used the depth determined from relocation, 12.1 km, for this event.

(6) Event 18 (Group 1)

Since the magnitude of this event is very large,  $M_w=5.5$ , the difference between the relocated depth, 1.1 km, and the surface-wave depth, 7 km, is not significant. We used the depth of 1.1 for this event.

For events in Groups 5, 6 and 7, we did not compute the synthetic amplitude ratio curve, and considered only the relative depths. The observed amplitude ratios suggest that the depths of the events in Group 5 increase in the order of events 4, 3, 2, and 1. For Group 6, the depth should increase in the order of events 2, 3 and 1. The events 1, 2 and 3 of Group 7 have similar ratios of surface wave to body wave amplitude, suggesting that they have about the same depth. The event 4 of Group 7 shows a relatively small R, suggesting that it is deeper than events 1, 2 and 3. Considering the relative depths, and the depths determined from surface wave inversion and relocation we adjusted the depths of these events as listed in Table 6.2

We also examined the depths of the Joshua Tree aftershocks determined from surface wave inversion. Figure 6.20 suggests that the events 3 and 11 of Group 1, and events 1 and 3 of Group 2, are shallower than those indicated by surface-wave inversion. The depth of these events is probably about 8 km. For these events for which the depths were not determined by surface wave inversion, we used the depths from relocation as long as the amplitude ratios of these events are reasonable for the relocated depths.

#### 6.4.3 Variation of the Energy Release and Mechanism on the Fault Plane

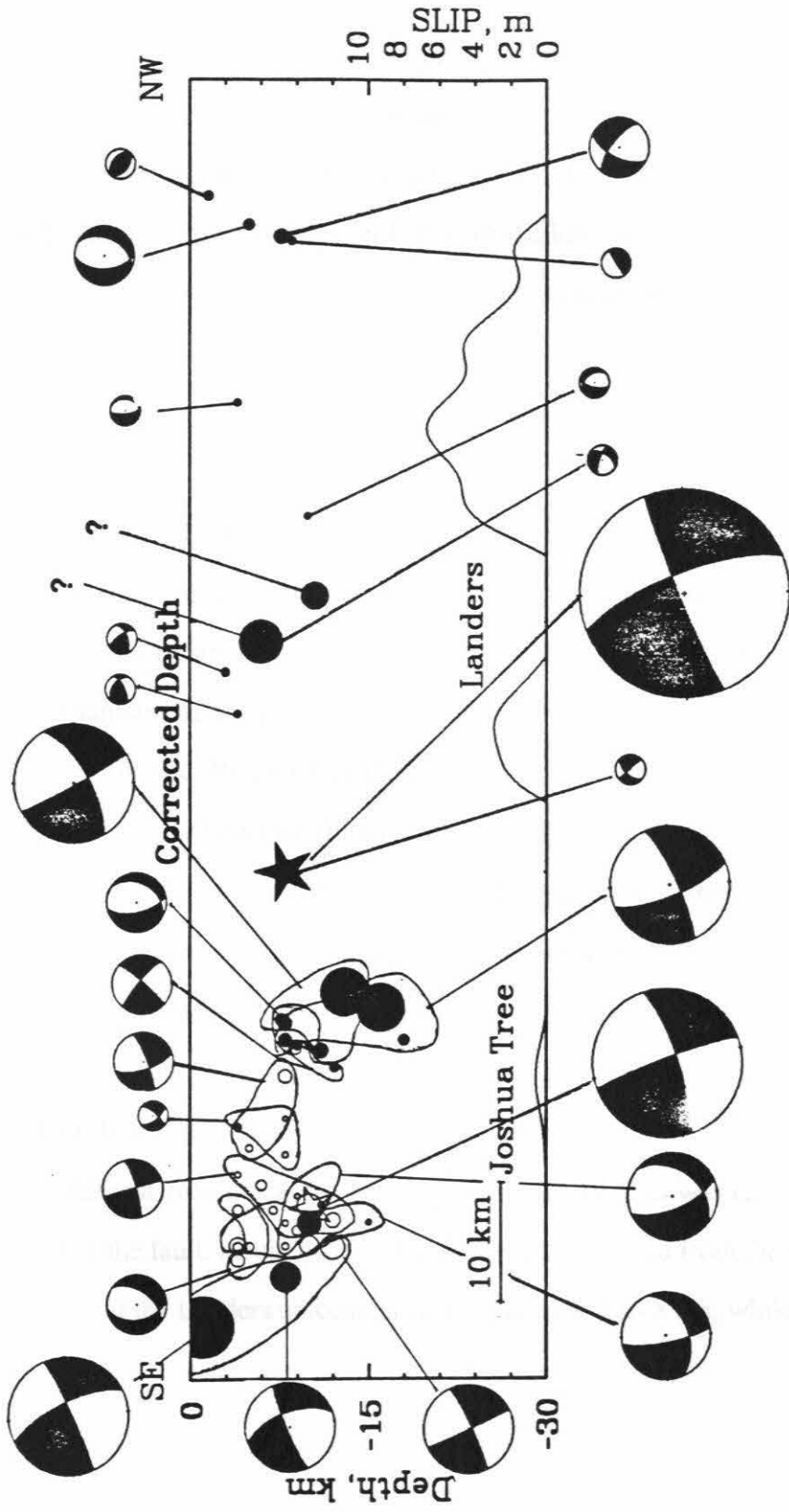
As shown in the previous section, with some adjustments in the depth, the depths of the Landers sequence determined by Hauksson's relocation and those of the Joshua Tree sequence determined by surface-wave inversion provide a good overall picture of the depth distribution of the mainshock and aftershocks of the Landers-Joshua Tree earthquake sequence. Here we refer to Figure 6.17b and 6.17c and examine the relation between the energy release pattern during the aftershock sequence and the slip during the mainshock.

The size of the symbol shown in Figure 6.17b and 6.17c corresponds to the ruptured area of the event using the relation  $S = \left(\frac{M_o}{\xi}\right)^{\frac{2}{3}}$ , where  $S$  and  $M_o$  are the fault area (in  $\text{cm}^2$ ) and seismic moment (in dyne-cm), and  $\xi = 1.3 \times 10^7$  dyne/ $\text{cm}^2$  is a constant (Abe 1975; Kanamori 1977). Figure 6.17b and 6.17c also show the slip distribution during the mainshock determined by Wald et al. (1992) using strong motion data and Kanamori et al. (1992) using TERRAScope data. The slip distribution for the Joshua Tree earthquake determined by deconvolution of TERRAScope records at GSC, PFO and PAS is sketched in. The Joshua Tree earthquake ruptured to the north for about 15 km and has the maximum slip of about 0.7 m, which is very small compared with the maximum slip of 6.5 m of the Landers earthquake. Most of the events occurred to the south of the Landers mainshock epicenter, especially between the epicenters of the Landers and Joshua Tree earthquakes. The events near the Joshua Tree earthquake surround the rupture zone of the Joshua Tree earthquake. The events to the north of the Landers mainshock surround the two asperities of the Landers earthquake. There are 3 large aftershocks with magnitudes larger than 4.5 located in the region between the two asperities. This observation is in a good agreement with the recent studies (e.g., Mendoza and Hartzell 1988; Schwartz et al. 1989; Choy and Dewey 1988; Houston and Engdahl 1989) which show that aftershocks generally do not occur in the regions of large slip during the mainshock.

Figure 6.22 shows the average mechanism of each subgroup of Group 1, 2, 3 and the mechanisms of the each event in Group 4, 5, 6, and 7 along the profiles AA', BB' and CC'. The events are plotted at the depth adjusted in the previous section. The size of the focal sphere is proportional to the total seismic moment of the events in each subgroup or each event. The events of Group 1a are almost pure strike slip. The events in Group 1b are strike slip mechanisms with some normal fault component. The events of Group 1c are



Figure 6.22: The corrected depths and spatial variation of the mechanism along the strike of the fault. The mechanism represents the average mechanism of each subgroup. The size of the focal sphere is proportional to the total seismic moment of the subgroup. The stars represent the hypocenters of the preshock and mainshock. The solid and shaded symbols indicate the Landers and Joshua Tree earthquake sequences.



shallow, about 4 km deep. The average mechanism of these events is a normal fault mechanism. They have long-period waveforms, and probably low stress drops. The events of Group 1d are close to the hypocenter of the Joshua Tree earthquake, and also have a normal fault mechanism. Group 1e consists of three large aftershocks. One large aftershock, event 18 of Group 1, is very shallow. Although the Joshua Tree earthquake did not rupture the surface, this event may have caused surface break in this area. Most of the energy in Group 1 was from the Group 1e.

The average mechanism of the 2 subgroups of Group 2 is similar. The energy released from Group 2 is less than that from Group 1. The events of Group 3a and Group 3b show a near vertical distribution extending to a depth of about 15 km. The mechanisms of these two subgroups are strike-slip with a different dip direction of a north-south striking fault plane. Some small events located in the area of Group 3a and 3b show normal fault mechanisms at a depth of about 8 km. Most of the energy of Group 3 was released from Group 3a and 3b. Most of the events to the south of the mainshock hypocenter show strike-slip mechanisms similar to that of the mainshock. The events to the north of the mainshock epicenter surrounding the two asperities show dissimilar waveforms with different mechanisms, suggesting heterogeneities in the stress field in the area surrounding the two asperities. There are two large aftershocks located in the region between the two large asperities. Unfortunately, no mechanism solutions are available for these two events. Their dissimilar waveforms suggest that the mechanisms of these two events are different.

Almost 76% of the total energy of the aftershocks was released from the southeastern part of the fault. About 40% of the energy was released from the region between the Joshua Tree and the Landers epicenters at depths larger than 8 km, while 36% was from the events

to the south of the Joshua Tree epicenter at a depth equal to or less than 10 km. For the Joshua Tree earthquake, most energy was released from depths between 5 to 15 km.

We compared the cumulative seismic moments of the aftershocks to that of the mainshock for the Joshua Tree and Landers earthquake sequences to other 14 earthquake sequences in California. The method is similar to that of Ma and Kanamori (1991). The ratio of most of the sequences in California is between 1 and 1/100. The ratio for the Joshua Tree earthquake sequence is about 9/100, which is comparable to that of most events in California. The ratio for the Landers earthquake sequence is about 6/1000, which is close to that of the 1988 Pasadena earthquake sequence, and is much lower than the others.

## 6.5 Conclusions

The June 28, 1992 Landers earthquake is the largest earthquake to occur in California since 1952. This earthquake caused extensive surface rupture and involved at least five principal faults. The preshock, the Joshua Tree earthquake, occurred about 30 km to the south of the mainshock's epicenter. The TERRAScope stations recorded on-scale waveforms for some of the aftershocks of the Landers and Joshua Tree earthquakes. We investigated the waveforms of broadband seismograms of the aftershocks ( $M_w \geq 3.5$ ) of the Joshua Tree and Landers earthquakes recorded at the PFO station (UCSD/TERRAScope station). We also examined the accuracy of depth determination using the amplitude ratios of surface to body waves.

Similarity of waveforms and locations suggests similarity of mechanisms. The events to the south of the mainshock epicenter are similar in waveforms. The mechanisms from

surface-wave inversion are strike slip similar to that of the mainshock. The events to the north of the mainshock epicenter show dissimilar waveforms and mechanisms.

We found a near vertical distribution of the aftershocks extending to a depth of about 15 km. One large aftershock with a very shallow depth to the south of the Joshua Tree epicenter may have ruptured the surface. Only a few events occurred in the regions where large slip occurred during the mainshock of the Landers and Joshua Tree earthquakes.

Almost 76% of the total energy of the aftershocks was released from the faults to the south of the Landers mainshock epicenter. About 40% of the energy was from the region between the Joshua Tree and Landers earthquakes at depths larger than 8 km, while 36% of that was from the aftershocks to the south of Joshua Tree epicenter at depths equal to or less than 10 km. For the Joshua Tree earthquake, most energy was released from depths between 5 to 15 km.

The ratio of cumulative seismic moment of the aftershocks to that of the mainshock for Joshua Tree earthquake is about 9/100, which is comparable to that of most events in California. The ratio for the Landers earthquake sequence is about 6/1000, which is close to that of the 1988 Pasadena earthquake sequence, and is much lower than the others.

## Conclusions of Part II

Seismic waves carry information of not only the source of the earthquake but also the path. Modern broadband instruments provide high-quality waveform data for local events with magnitudes from 1.5 to 7, or even larger. These high-quality waveform data can be used to study details of earthquake sequences. In Part II of this thesis, I investigated the waveforms recorded by TERRAScope, a broadband wide-dynamic range seismic network in southern California, for the 1988 Pasadena, 1991 Sierra Madre and 1992 Joshua Tree-Landers earthquake sequences.

In general, similarity of waveforms suggests similar location and mechanism of the events. Grouping the events from these three sequences by waveform similarity, we confirmed that a good correlation exists between waveforms and mechanisms for the events at similar locations. This correlation allowed us to estimate the mechanisms of the events for which mechanism determination cannot be made using the conventional methods. For very small earthquakes, first-motion data are often too incomplete to determine the mechanism. Also during the aftershock sequence of a major earthquake, waveforms of successive events often interfere with each other making mechanism determinations using the standard methods (e.g., first-motion method, surface wave inversion, and waveform modeling) difficult. Even in these cases, correlation of waveforms at a few selected stations can be used to determine the mechanisms. Using the waveform correlation

method, I could obtain a more complete picture of the aftershock sequence of the 1988 Pasadena earthquake and the 1991 Sierra Madre earthquake than that obtained by the traditional method alone.

For the earthquakes which occurred close to a TERRAScope station (e.g., the 1988 Pasadena and 1991 Sierra Madre earthquakes) the observed waveforms provide approximate source time functions which allow us to determine the overall source mechanisms, stress drops of the events and attenuation characteristics,  $Q^{-1}$ , of the crust. The mechanism determined from the first-motion data represents the fault motion in the beginning of an earthquake, but not necessarily the overall fault motion. Broadband data provide important information on the temporal change in the mechanism. In the study of the 1988 Pasadena earthquake and the 1991 Sierra Madre earthquake sequences, I determined the overall focal mechanisms and seismic moments using broadband waveform data combined with the first-motion data from the Southern California Seismic Network (SCSN). An inversion method to determine the mechanisms from broadband data was developed. Using this method, we could examine temporal variations of mechanisms during faulting. In most cases, the first-motion mechanism was consistent with that determined from waveforms, suggesting that the mechanism did not change during faulting. In a few cases, however, a significant change in the mechanism was observed.

The stress drops are 800 to 1500 and 500 bars for the Pasadena and the Sierra Madre earthquakes, respectively, which are larger than those of most earthquakes which are between 10 and 100 bars. This result is consistent with that obtained by Kanamori and Allen (1986) who found that stress drops of earthquakes which occur on faults with long repeat times are higher than those on faults with short repeat times. The large aftershocks of the 1991 Sierra Madre earthquake have relatively low stress drops. This is consistent

with the result obtained by Kanamori et al. (1993) who found that stress drops in most aftershocks are lower than that of the mainshock. Although we do not know exactly where aftershocks occur, some of them probably occur on the fault plane where the mainshock slippage occurred; these aftershocks have had a very short time to heal, hence a low stress drop.

The average  $Q_{\beta}$  values along the paths from the hypocenters of the Pasadena and the Sierra Madre earthquakes are 80 and 130, respectively. These  $Q$  values reflect the degree of fracture in the fault zone and shallow crust. As more TERRAScope stations are installed and more earthquake data become available, we will be able to map the regional variation of  $Q_{\beta}$ , from which we will be able to obtain a better picture of mechanical conditions of fault zones in southern California.

The ratios of the cumulative aftershock seismic moment to the mainshock seismic moment are about 1/1000 and 1/50, respectively, for the 1988 Pasadena and the 1991 Sierra Madre earthquake sequences. These values are relatively small compared with that, 1 to 1/100, for most events in California. This result suggests that, in high-stress drop events like the Pasadena and the Sierra Madre earthquakes, the strain had accumulated near the main asperity and, during the main shock, almost all the energy was released there leaving little energy for aftershocks.

For the 1992 Joshua Tree-Landers earthquake sequence, the complete waveform data recorded by TERRAScope allowed us to examine the accuracy of depth determination from the amplitude ratio of surface to body waves. After having adjusted the depths determined from travel times and surface-wave inversions, we could determine the variation of the energy release and the mechanisms on the fault plane. We found that only a few events occurred in the areas where large slip occurred (asperities) during the mainshock. The



events near the asperities have dissimilar waveforms suggesting different mechanisms and a heterogeneous stress field. At one location, a near vertical distribution of the aftershock activity extending to a depth of 15 km, or even deeper, was found. Also some events, mostly shallow, have very long-period waveforms compared with the events with similar size, suggesting that they are very low-stress-drop events occurring in a shallow crust.

## References of Part II

- Abe, K. Reliable estimation of the seismic moment of large earthquakes, *J. Phys. Earth.*, **23**, 381-390, 1975.
- Blackman R. B. and J. W Tukey. The measurement of power spectra. *Dover Publication Inc.*, 190 pp, 1958.
- Bouchon, M. A simple method to calculate Green's functions for elastic layered media, *Bull. Seismol. Soc. Am.*, **71**, 959-971, 1981.
- Brune, J. N., Tectonic stress and the spectra of seismic shear waves from earthquake, *J. Geophys. Res.*, **75**, 4997-5009, 1970.
- Choy, G. L., and J. W. Dewey. Rupture process of an extended earthquake sequence: teleseismic analysis of the Chilean earthquake of March 3, 1985, *J. Geophys. Res.*, **93**, 1103-1118, 1988.
- Cohn, S. N., Hong, T. L., D. V. Helmberger. The Oroville earthquakes: A study of source characteristics and site effects, *J. Geophys. Res.*, **87**, 4585-4594, 1982.
- Dreger, D. S. and D. V. Helmberger. Source parameters of the Sierra Madre earthquake from regional and local body waves, *Geophys. Res. Lett.*, **18**, 2015-2018, 1991.
- Dreger, D. Modeling earthquakes with local and regional broadband data, Pasadena, California Institute of Technology, *Ph.D. thesis*, 203 pp, 1992.
- Eshelby, J. D. The determination of the elastic field of an ellipsoidal inclusion and related problems, *Proc. Roy. Soc. London, Series A*, **241**, 376-396, 1957.
- Futterman, W. I. Dispersive body waves. *J. Geophys. Res.* **67**, 5279-5291, 1962.
- Ganley, D. C. and E. R. Kanasevich. Measurement of absorption and dispersion from check shot surveys, *J. Geophys. Res.* **85**, 5219-5226, 1980.

- Hadley D. and H. Kanamori. Seismic structure of the transverse ranges, California, *Geol. Soc. Am. Bull.*, **88**, 1469-1478, 1977.
- Hartzell, S. Earthquake aftershocks as Green's functions., *Geophys. Res. Lett.* **5**, 1-5, 1978.
- Hauksson, E. The 1991 Sierra Madre Earthquake Sequence in Southern California: Seismological and Tectonic Analysis, submitted to *J. Geophys. Res.*, 1992.
- Hauksson, E. and L. M. Jones. The 1991 ( $M_L=5.8$ ) Sierra Madre earthquake in Southern California Seismological and Tectonic Analysis, *EOS*, **72**, 1991.
- Hauksson, E., L. Jones, T. Heaton, K. Hutton, J. Mori, S. Hough, H. Kanamori, and H.-K. Thio. The Landers and Big Bear earthquakes in Eastern San Bernardino County: June 28, 1992, Preliminary Report of the Southern California Seismic Network, 6/28/1992.
- Houston, H. and E. R. Engdahl. A comparison of the spatio-temporal distribution of moment release for the 1986 Andreanof Islands earthquake with relocated seismicity, *Geophys. Res. Lett.*, **16**, 1421-1424, 1989.
- Jones, L. M., K. E. Sieh, E. Hauksson, and L. K. Hutton. The 3 December 1988, Pasadena, California, earthquake: evidence for strike-slip motion on the Raymond fault, *Bull. Seismol. Soc. Am.*, **80**, 474-482, 1990.
- Kanamori, H., and D. L. Anderson. Theoretical basis of some empirical relations in seismology, *Bull. Seismol. Soc. Am.*, **65**, 1073-1095, 1975.
- Kanamori, H. Seismic and aseismic slip along subduction zones and their tectonic implications, in *Island Arcs, Deep Sea Trenches and Back-Arc Basins*, edited by M. Talwani and W. C. Pittman, 163-174, Maurice Ewing Series, American Geophysical Union, Washington, D. C., 1977.
- Kanamori, H., and C. R. Allen. Earthquake repeat time and average stress drop, in Maurice Ewing Volume 6, *Earthquake Source Mechanisms*, edited by S. Das and C. H. Scholz, 227-235, American Geophysical Union, Washington D. C., 1986.

- Kanamori, H. Pasadena very-broad band system and its use for realtime seismology, extended abstract for the U. S.-Japan Seminar for Earthquake Research, Morro Bay, California, Sept. 11-15, 1988, *U.S.G.S. Open-file Report.*, 1989.
- Kanamori, H., J. Mori, and T. H. Heaton. The 3 December 1988 Pasadena earthquake (M=4.9) recorded with the very broadband system in Pasadena, *Bull. Seismol. Soc. Am.*, **80**, 483-487, 1990.
- Kanamori, H., E. Hauksson and T. H. Heaton. Experiment towards realtime seismology using TERRAScope: the 1991 Sierra Madre earthquake, *EOS*, **67**, 1991.
- Kanamori H. and J. Given . Use of long-period surface waves for rapid determination of earthquake-source parameters, *Phys. Earth Planet. Inter.*, **27**, 8-31, 1981.
- Kanamori, H., H. Thio, D. Dreger, E. Hauksson, and T. Heaton. Initial investigation of the Landers, California, earthquake of 28 June 1992 using TERRAScope, submitted to *Geophys. Res. Lett.*, 1992.
- Kanamori, H., J. Mori, E. Hauksson, T. H. Heaton, L. K. Hutton, and L. M. Jones. Determination of earthquake energy release and  $M_L$  using TERRAScope (submit to *Bull. Seism. Soc. Am.*), 1993.
- Kennett, L. N., and N. J. Kerry. Seismic waves in a stratified half-space, *Geophys. J. R. Astror. Soc.*, **57**, 557-583, 1979.
- Ma, K.-F. and H. Kanamori. Aftershock sequence of the 3 December 1988 Pasadena earthquake, *Bull. Seism. Soc. Am.*, **81**, 2310-2319, 1991.
- Magistrale H. W. Three-dimensional velocity structure of southern California, Pasadena, California Institute of Technology, *Ph.D. thesis*, 294 pp, 1990.
- Mendoza, C. and S. H. Hartzell. Aftershock patterns and main shock faulting, *Bull. Seismol. Soc. Am.*, **78**, 1438-1449, 1988.

- Reasenber, P. and D. Oppenheimer. FPFIT, FPLOT, and FPPAGE: Fortran computer programs for calculating and displaying earthquake fault-plane solutions, *U.S.G.S. Open-file Report*, 85-739, 1985.
- Schwartz, S. Y., J. W. Dewey, and T. Lay. Influence of fault plane heterogeneity on the seismic behavior in the Southern Kuriles Islands arc, *J. Geophys. Res.*, **94**, 5637-5649, 1989.
- Takeo, M. An inversion method to analyze the rupture processes of earthquakes using near-field seismograms, *Bull. Seismol. Soc. Am.*, **77**, 490-513, 1987.
- Thatcher, W., and T.C. Hanks. Source parameters of southern California earthquakes, *J. Geophys. Res.*, **78**, 8547-8576, 1973.
- Thio, H. K., and H. Kanamori. Moment tensor inversions in Southern California using surface waves recorded by TERRAScope (abstract) *EOS*, **73**, 376, 1992.
- Wald, D. J. Strong motion and broadband teleseismic Analysis of the 1991 Sierra Madre, California, earthquake, *J. Geophys. Res.*, 11033-11046, 1991.
- Wald, D. J., D. V. Helmberger, H. K. Thio, D. Dreger, and T. H. Heaton. On developing a single rupture model for the 1992 Landers, California earthquake consistent with static, broadband teleseismic, regional and strong motion data sets (abstract). *EOS*, **73**, 358, 1992.